EUSKAL HERRIKO UNIBERTSITATEA
THE UNIVERSITY OF THE BASQUE COUNTRY

Department of Electricity and Electronics

eman ta zabal zazu
Universidad del País Vasco
Euskal Herriko Unibertsitatea

CAMPUS OF
INTERNATIONAL
EXCELLENCE

Atomistic *ab initio* study of optical excitations in nanoplasmonic systems as probed by light and fast electrons

---

Thesis by

Bruno Candelas Peñalba

Supervised by

Prof. Nerea Zabala Unzalu
and
Prof. Javier Aizpurua Iriazabal

Donostia-San Sebastián, Julio de 2025

ACKNOWLEDGMENTS

Ha llovido mucho desde que comencé con esta tesis, en un mundo en el que las pandemias eran todavía cosa de película. En todo este tiempo, he conocido a mucha gente sin cuyo apoyo esta tesis no habría salido adelante. A todos ellos quiero dedicar las siguentes páginas.

En primer lugar, quisiera agradecer a mis supervisores, Javi y Nerea, el haberme dado la oportunidad de realizar esta tesis. Ha sido un viaje largo y con algunas curvas, pero creo que al final nos ha quedado un trabajo del que podemos estar orgullosos. Gracias por vuestro apoyo y por vuestra guía.

Quiero agradecer a mis compañeros en el grupo de Teoría de la Nanofotónica, pasados y presentes, por todos los momentos que hemos compartido. En especial a los que estuvisteis conmigo desde el principio y me enseñasteis cómo sobrevivir a un doctorado. A Álvaro y Antton, que habéis sido como mis hermanos mayores durante buena parte de estos casi seis años. Gracias por los cientos de consejos que me habéis dado, y por estar siempre ahí dentro y fuera del CFM. A Mattin, con quien no he coincididido tanto como me habría gustado, pero siempre ha sido un placer. Sin tu ayuda las figuras más bonitas de esta tesis no habrían sido posibles. A Carlitos, el más pelón, fuente infinita de cultura y rigor académico. A Adrián, con su gracia natural, que me ha acabado adelantando por la derecha. A Jonathan, siempre imperturbable incluso cuando el techo se le cae encima. A Roberto, mi químico de confianza y mi mejor fuente de noticias de actualidad. A Xabi, el más serio y formal, pero que luego no se pierde una casa rural. A Benji, que llegó como quién dice ayer a revolucionar el gallinero, y ya es el que más charlas ha dado, el que más postres ha traído, y el que más unboxings ha hecho. También a Rubén, el alma del grupo, cuyo trabajo infatigable hace que todo siga rodando. A todos los demás: Isa, Mario, Edu, Fer, Nikos, Aurelian, Unai, José Luis, Sofia... ¡A ver cuándo hacemos el próximo group meeting!

Más allá del grupo de investigación, también quiero dar las gracias a toda la gente excelente con la que he tenido la oportunidad de convivir en el entorno del CFM. A Martín, mi más fiel compañero de cafés, comidas, magics y fiestas. El único que ha estado ahí durante todo (todo) el doctorado. No podría haber deseado mejor compañía. ¡Ánimo, que no te queda nada! A Iker, mi ingeniero favorito, que llegó medio despistado al máster de Quantum Technologies, y para cuando imprima esto ya será un doctor en pleno derecho. ¡Tú sí que eres un león, y no esos matados del Athletic! A Jon, el tertuliano más duro, que me ha hecho sudar en tantos debates.

A María, la más animada, siempre proponiendo planes y alegrándonos el día. A Josu, tranquilo y confiable, siempre dispuesto a una pachanga. A Mikel, que lo tiene todo: músico, poeta, imitador... ¡Hasta de física sabe! A Txemikel, maestro de asados y euskaldun adoptivo. Gracias también a muchos más: Alberto, Joseba, Raulillo, Carmen, Jorge, Cris (¡las dos!), Enrique, Sebas, Melillo, Miriam, Miguel Ángel, Asier, David, Rubén... Sois tantos que seguro que me dejo a alguien. Ha sido un privilegio compartir con vosotros estos años.

Of course, these acknowledgments would not be complete without mentioning the people in the Computational Electronic Structure Theory group at Aalto University. I am especially grateful to Patrick and Tuomas for welcoming me with open arms and hosting my stay in Finland. Such a different climate and culture were not always easy to endure, but it would for sure have been much harder without the excellent people I got to know there. Prajwal, Joakim, Matthias, Nitik, Han, Pascal, Jarno, Hilda, and all, thank you! I wish I could visit you again someday (but hopefully in summer this time).

I would also like to thank those who helped me overcome the scientific challenges I've encountered throughout the PhD. Especially, thanks to the developers of the PyNAO code, Marc, Peter and Daniel, for all your advices at the beginning when I was just learning the ropes. Also thanks to Robert and Michael for answering the doubts of a complete stranger on the GPAW forum. Gracias también al equipo de supercomputación del DIPC, siempre tan bien dispuestos. Hacéis una labor inmejorable.

Por último y más importante, quiero dar gracias a mi familia, por su apoyo incondicional y por aguantarme en casa durante todo este tiempo. A mi hermano Pablo, con quien lo he compartido todo, por ayudarme siempre a desconectar. A mi padre, Ramón, un auténtico crack, a quien siempre he admirado. Gracias por todo lo que me has enseñado, y por todo lo que aún queda por enseñar. Y en especial, a mi madre, Miriam, mi primera referencia en el mundo de la física, cuyos pasos he tratado de seguir dignamente, y la segunda persona que más intensamente ha vivido esta tesis, sus alegrías y sus penas.

LABURPENA

Giza historia osoan zehar, gure behaketa-gaitasunak begi hutsez hauteman genezakeenera mugatuak egon dira. XVII. mendean, optikan egindako aurrerapenei esker, kosmosa aztertzeko gai ziren teleskopioak garatu ziren, eta baita bizitzaren oinarrizko mekanismoak argitzea ahalbidetu zuten mikroskopioak ere. Mikroskopia optikoak biologian eta medikuntzan ekarpen nabarmenak egin dituen arren, Abberen difrakzio-mugak tresna hauen bereizmena murrizten du [1]. Izan ere, argiaren uhin-izaera dela eta, uhin-luzeraren erdia baino distantzia laburragoaz banandutako ezaugarriak ezin dira bereizi lente optiko konbentzionalen bidez. Maiztasun optikoen kasuan, difrakzio-muga hau ehunka nanometroetan dago kokatuta. Beraz, mikroskopia-teknika alternatiboak behar dira nanoeskalako objektuak behatu eta manipulatzeko. Metodo horien bilaketa eta aplikazioa nanofotonikaren oinarrian dago.

Testuinguru horretan, nanopartikula eta gainazal metalikoak nanofotonikaren erdigune bilakatu dira, plasmoiak jasateko gaitasuna baitute. Plasmoiak elektroi-hodeiaren oszilazio kolektiboak dira, argiaren uhin elektromagnetikoekin akoplatu daitezkeenak. Modu hauen bitartez, posible da argi erasotzailearen eremu elektromagnetikoa areagotzea eta uhin-luzera baino txikiagoak diren eskualdetan lokalizatzea [2]. Ezaugarri berezi horiek nanopartikula plasmonikoak osagai giltzarriak bihurtzen dituzte espektroskopiako eta mikroskopiako hainbat teknikatan, hala nola gainazalak areagotutako Raman espektroskopian (ingelesez *Surface-Enhanced Raman Spectroscopy*, SERS) [3] edo gainazalak areagotutako fluoreszentzian (*Surface-Enhanced Fluorescence*) [4]. Horrez gain, egitura plasmonikoek etorkizun handiko aplikazioak dituzte hainbat eremutan, adibidez biomedikuntzan [5] edo telekomunikazioetan [6, 7].

Normalean, nanopartikula plasmonikoen erantzun optikoa zehazki deskribatzen da Maxwell-en ekuazioen bidez, elektromagnetismo klasikoaren esparruan [8]. Hala ere, nanofabrikazioaren aurrerapen etengabeek gailuen miniaturizazioa molekula bakarreko eskalara bultzatu dute [9], non efektu kuantikoak —besteak beste elektroien tunel-efektua [10–13], erantzun optikoaren ez-lokaltasuna [14–16], edo elektroien isurpena (*spill-out*) [17, 18]— agertzen hasten diren elektroien uhin-izaeraren ondorioz. Fenomeno horiek guztiak kontuan hartzeko, mekanika kuantikoan oinarritutako materiaren erantzun optikoaren deskribapena behar da. Zoritxarrez, dauzkagun ordenagailuekin, ezinezkoa da Schrödingerren ekuazioa zuzenean ebaztea elektroi gutxi batzuk baino gehiago dituzten sistementzat. *Ab*

initio metodoek problema sinplifikatzen dute magnitude fisiko garrantzitsuak elektroi dentsitatetik eratorriz, gorputz anitzeko uhin-funtzioa erabili ordez, eta, beraz, tresna oso arrakastatsuak dira nanostestrukturen erantzun optikoa adierazteko [19–21].

Zehazki, tesi honetan denboraren mendeko dentsitatearen funtzionalaren teoria (*time-dependent density-functional theory*, TDDFT) erabiliko dugu egitura nanometrikoen erantzun optikoa deskribatzeko. Nanopartikularen xehetasunak atomoaren mailan kontuan hartzen ditu metodologia honek, eta eremu hurbilaren banaketa eta puntu beroen eraketa, azpiko eremu plasmonikoen efektua areagotuz [22], zehazki deskribatzea ahalbidetzen du. Nanofotonikaren arloan TDDFT hainbat fenomeno desberdin aztertzeko erabili da, hala nola karga-transferentzia lotura metalikoetan [23], metalezko nanopartikulen eta molekulen arteko akoplamendu sendoa (*strong coupling*) [24, 25], eramaile beroen sorrera metalezko nanopartikuletan [26], edo pikobarrunbeen erantzun optikoa [27].

Aipatutako abantailen ondorioz, TDDFT atomistikoa bereziki egokia da nanoegitura plasmonikoen eta igorle kuantikoen (hala nola molekula organikoak edo puntu kuantiko erdieroaleak) arteko elkarrekintzak ikertzeko. Azken urteotan, barrunbe plasmoniko eta igorle kuantikoez osatutako sistema hibridoek arreta handia erakarri dute, igorle kuantikoaren propietateak barrunbeak sortutako eremu elektromagnetiko biziekin akoplatuz alda daitezkeelako. Akoplamendu sendoko erregimenean, elkarrekintza horrek polaritoi izeneko [28] argi-materia egoera hibridoak sortzen ditu, energia-maila doigarriak dituztenak eta materiaren propietate kimikoak alda ditzaketenak [29, 30]. Ondorioz, sistema horiek aplikazio ugari aurkitu dituzte fotokimikan [31–33], fotoi bakarreko igorpenean [34], elektrolumineszentzian [35], eta elektroien garraioan [36], besteak beste. Akoplamendu sendoko muturreko kasuetan, hala nola nanobarrunbe plasmonikoetan molekula bakarrak kokatzean sortzen direnetan, sistemaren eskala txikiak mekanika kuantikoan oinarritutako tratamendu zehatza eskatzen du, barrunbearen ezaugarri atomistikoak kontuan hartzen dituena, eta TDDFT atomistikoaren metodologiak eskaera horiek guztiak modu naturalean betetzen ditu.

Nanopartikula plasmonikoen beste aplikazio giltzarri bat molekulen seinale bibrazionala areagotzeko gaitasunean datza, SERS teknikan bezala, non eremu plasmonikoek 10^8-ko edo gehiagoko areagotze-faktoreak eragin ditzaketeen, molekula bakarren detekzioa ahalbidetuz [37, 38]. SERS-ek aplikazio ugari bultzatu ditu [3, 39, 40], eta berezko esparru oparo batean bilakatu da. Nahiz eta TDDFT metodo atomistikoak maiz erabiltzen diren SERS konfigurazioak aztertzeko beren doitasun eta moldakortasunagatik [41], kalkulu horiei lotutako konputazio-kostu handia dela eta, normalean sistema errealen eredu sinplifikatuak erabiltzera dira. Hori bereziki egia da sistema periodikoak aztertzen direnean, hala nola monogeruza automihiztatuak (*self-assembled monolayers*, SAMs) [42] edo nanopartikula-ispiluan (*nanoparticle-on-mirror*) izeneko konfigurazioak [43], sarritan molekula bakar batez edo eskukada batez osatutako sistema finitu gisa modelatzen direnak [44, 45]. Tesi honetan, hurbilketa horien egokitasuna ebaluatzen dugu, metalezko gainazaletan adskribatutako molekula-monogeruzen eredu periodikoen zein finituen espektroak konputatuz.

Nanoegitura plasmonikoak ezaugarritzeko teknika erabilienetako bat Elektroien Energia-Galera Espektroskopia (*Electron Energy-Loss Spectroscopy*, EELS) da, non elektroi-zunda bat lagin batekin elkarregitean galtzen duen energia neurtzen den. Teknika honek abaintail handiak eskaintzen ditu. Bereizmen espektral eta espazial bikainak izateaz gain [46–49], erantzunaren espektro osoa eskuratzeko gaitasuna eskaintzen du, modu plasmoniko "ilunak" eta nanoegituraren barrualdera mugatutako moduak barne, espektroskopia optiko konbentzionalekin kitzikatzen ez direnak [50–52]. Azken urteotan, elektroi-sorta azkarrek kitzikatutako metalezko nanopartikula txikien gainazaleko plasmoi lokalizatuen (*localized surface plasmon*, LSP) azterketak arreta handia erakarri du [53–55], eta ikerketa batzuek nabarmendu dute TDDFT atomistikoaren gaitasuna egitura hauen erantzuna simulatzeko. Hala ere, elektroi sorta sarkorrek nanopartikularen bolumenaren barruan mugatutako elektroi-dentsitatearen oszilazio kolektiboak ere kitzikatu ditzakete, hots, konfinatutako bolumeneko plasmoiak (*confined bulk plasmons*, CBPs) [52, 56]. Modu horiek arreta mugatua jaso dute argiarekin duten akoplamendua eraginkorra ez delako [57], eta oraindik garatzear dago nanopartikula txikietan CBP-en elektroi sorta sarkorren bidezko kitzikapenaren erabateko ulermena. Tesi honetan, frogatzen dugu metodo atomistikoek zehazki deskribatu ahal dutela metalezko nanopartikula txikien erantzun plasmoniko osoa, elektroien ibilbidea nanopartikulatik urrun pasatzen denean eta baita ibilbide sarkorrentzat ere. Gure analisia biribiltzeko, kalkulu osagarriak egin ditugu, eredu hidrodinamiko klasiko batean [58, 59] zein *jellium* TDDFT eredu batean [60, 61] oinarritutak.

Tesi honek nanofotonikan interes handia duten sistema plasmoniko kanonikoen hautespen baten azterketa atomistikoa aurkezten du, nano- eta piko-eskalen arteko interfazean agertzen diren efektu kuantikoen oinarrizko ulermen sakonagoa lortzeko helburuarekin, egitura atomistikoaren garrantzia azpimarratuz. Tesia honela dago egituratuta:

1. kapituluan, nanoeskala mailan argia eta materiaren arteko interakzioan agertzen diren fenomenoak eta oinarrizko kontzeptuak berrikusten ditugu. Hasteko, metalezko nanopartikula esferikoen eta dimeroen erresonantzia plasmonikoen deskribapen elektromagnetiko klasikoa erabiliz, tesian zehar agertuko diren plasmoi mota desberdinak aurkezten ditugu. Horrez gain, molekulen eta metal–molekula sistema hibridoen kitzikapenak aurkezten dituge ere, eta akoplamendu sendoaren fenomenoa azaltzen dugu. Halaber, tesi honetan kontuan hartutako hiru espektroskopia-tekniken azalpen laburra ematen dugu: espektroskopia optikoa, EELS eta SERS.

2. kapituluak tesi honetan erabili ditugun metodologia teorikoak aurkezten ditu. Hasteko, TDDFT atomistikoaren oinarri teorikoak azaltzen ditugu, aztertutako sistemen eta argiaren edo elektroi-sorten arteko elkarrekintza modelatzeko erabili duguna. Ondoren, sistema periodikoen Raman espektroa kalkulatzeko erabili dugun perturbazio-teorian oinarritutako metodologia azaltzen dugu. Bestalde, aurkezten dugu metodologia bat, optimizazio Bayesiarrean oinarritzen dena, metalezko gainazaletan adsorbatutako molekula-monogeruzenen ergia baxueneko konfigurazioak bilatzeko erabiltzen duguna.

3. kapituluan, sistema hibrido baten espektro optikoa aztertzen dugu, bi

zilarrezko nanopartikulen arteko barrunbean porfina molekula bat kokatuz osatua. Ezaugarri atomistikoek akoplamendu elektromagnetikoaren indarrean duten eraginean zentratzen gara, bereziki bi konfigurazio desberdinen konparaketa eginez, aurpegi–aurpegi eta punta–punta deiturikoak. Gure emaitzek agerian uzten dute sistemaren erresonantzia plasmonikoa bi polaritoietan banatzen dela, akoplamendu elektromagnetikoaren ondorioz. Espektro optikoa oszilatzaile harmoniko akoplatuen eredu batekin konparatuz, ikusten dugu argia eta materiaren arteko akoplamendua aztertutako barrunbeen zabalera guztietarako akoplamendu sendoko erregimenean dagoela, eta barrunbearen konfigurazio geometrikoak eragin nabarmena daukala. Horrez gain, konfigurazioak beste fenomeno kuantikoen agerpena determinatzen du ere, halaber, karga-transferentziako plasmoiak (*charge transfer plasmons*, CTP) energia baxuetan, aurpegi–aurpegi konfigurazioan bakarrik ikusten direnak. Oro har, azterketa honek agerian uzten du morfologia atomistikoaren garrantzia nanobarrunbe plasmonikoen muturreko kasuetan.

4. kapitulua sodiozko nanopartikula txikien elektroien energia-galera probabilitatearen espektroan zentratzen da, batez ere elektroien ibilbideak partikula zeharkatzen duenean. Urruneko elektroiek kitzikatutako gainazaleko plasmoiez gain, erakusten dugu elektroi sarkorrek konfinatutako bolumeneko plasmoiak eta energia handiagoko gainazaleko erresonantziak kitzikatzen dituztela baita ere. Eredu hidrodinamiko osagarri batetik eratorritako elektroien energia-galera probabilitaterako adierazpen analitikoen laguntzaz, espektro atomistikoaren gailurrak osatzen dituzten CBP modu ongi definituak identifikatzen ditugu, eta elektroien ibilbidearen talka-parametroak bere kitzikapenean duen eragina aztertzen dugu. Horrez gain, *jellium* TDDFT eredu baten laguntzarekin, maila handiagoko gainazaleko erresonantziak Bennett plasmoiak bezala identifikatzen ditugu. Ikerketa honek CBP-en eta Bennett plasmoien portaeraren ulermen sakonagoa eskaintzen du, eta ez-lokaltasuna kontuan hartzen duten eredu teoriko desberdinen arteko adostasun kualitatiboak —eta baita kuantitatiboak ere— sodiozko nanopartikuletan aztertutako fenomenoen sendotasuna azpimarratzen du. Gainera, gure karakterizazio kontzeptualak hainbat nanoegituratan esperimentalki behatutako bolumeneko plasmoien urdinerazko lerrakuntzak azaltzen lagundu dezake, eta nanopartikula metalikoen EELS-n ezaugarri plasmonikoen analisi eta ustiapen sakonago baterako oinarriak ezartzen ditu.

Azkenik, 5. kapituluak TDDFT azterketa atomistikoa aurkezten du, Au(111) gainazal batean adsorbatutako 4’-zianobifenil-4-tiol molekulen monogeruza automihiztatuena. Lehenik, optimizazio Bayesiarrean oinarritutako metodologia bat aplikatzen dugu monogeruza egitura egonkorrenak identifikatzeko. Honek tokiko energia-minimo batzuk itzultzen ditu, gero erlaxatzen direnak monogeruza-konfigurazio egokienak aurkitzeko. Haien Raman espektroak konparatuz, egitura atomistikoa eta molekulen arteko elkarrekintza zehazki modelatzearen garrantzia aztertzen dugu. Estaldura-dentsitate desberdinak dituzten monogeruzentzat prozesua errepikatuz, efektu kolektiboen agerpena ikusten dugu Raman espektroan, eta bibrazio-modu ezberdinen maiztasunen aldaketak aztertzen ditugu. Bukatzeko, adatomoen bidezko konfigurazio alternatibo bat ikertzen dugu, metalezko gainazalaren berreraikuntzak espektroei nola eragin diezaiekeen aztertzeko. Oro har, aurkeztutako metodologiak monogeruzen egituraren modelatze zehatza ahalbidetzen du, aldi berean molekulen arteko elkarrekintzak modu naturalean kontuan hartuz, estaldura-dentsitate handiko monogeruzen simulazio zehatzagoak egiteko bidea erraztuz.

Gure ustez, hemen aurkezten diren aurkikuntzek argiaren eta materiaren arteko elkarrekintzaren muturreko kasuetan efektu kuantiko eta atomistikoen eragina sakonago ulertzen lagundu ditzakete, sistema nanofotonikoak aztertzeko *ab initio* metodo atomistikoen eraginkortasuna are gehiago balioztatuz.

LIST OF ABBREVIATIONS

au	Atomic units
ASE	Atomic Simulation Environment
BDP	Bonding dipolar plasmon
BEM	Boundary Element Method
BOSS	Bayesian Optimization Structure Search
BPDT	Biphenyl-4,4’-dithiol
BQP	Bonding quadrupolar plasmon
CTP	Charge-transfer plasmon
CTP’	Higher-order charge-transfer plasmon
CBP	Confined bulk plasmon
CN-BPT	4’-cyanobiphenyl-4-thiol
DFT	Density-functional theory
DOS	Density of states
DP	Dipolar plasmon
DS	Search process using damping and symmetries
DSC	Search process using damping, symmetries, and the cost function
DSR	Search process using damping, symmetries, and the space restriction
DSCR	Search process using damping, symmetries, the cost function, and the space restriction
DZP	Double-zeta polarized
EEL	Electron energy loss
EELS	Electron energy-loss spectroscopy
eLCB	exploration-modified lower confidence bound
FCC	Face-centered cubic
GGA	Generalized gradient approximation
GP	Gaussian process
GPAW	Grid-based projector-augmented waves
HCP	Hexagonal close-packed
HDM	Hydrodynamic model
HOMO	Highest occupied molecular orbital
HOP	Higher-order LSPs

IR	Infrared
KS	Kohn–Sham
LCAO	Linear combination of atomic orbitals
LDA	Local-density approximation
LP	Lower polariton
LSP	Localized surface plasmon
LSPP	Localized surface plasmon polariton
LUMO	Lowest unoccupied molecular orbital
MNP	Metallic nanoparticle
MNPBEM	Metallic nanoparticles using a boundary element method
MP	Multipole plasmon
NAO	Numerical atomic orbitals
NEXAFS	Near-edge X-ray absorption fine-structure
NP	Nanoparticle
PAW	Projector-augmented wave
PBE	Perdew-Burke-Ernzerhof exchange–correlation functional
PDOS	Projected density of electronic states
PES	Potential Energy Surface
PyNAO	Python Numerical Atomic Orbitals
QE	Quantum emitter
QP	Quadrupolar plasmon
SAM	Self-assembled monolayer
SERS	Surface enhanced Raman spectroscopy
SI	International system of units
SIESTA	Spanish initiative for electronic simulations with thousands of atoms
SPP	Surface plasmon polariton
STEM	Scanning Transmission Electron Microscopy
TDDFT	Time-dependent density-functional theory
TEM	Transmission Electron Microscopy
UP	Upper polariton

LIST OF SYMBOLS

Chapter 1

a	Radius of a spherical nanoparticle
b	Impact parameter of the probe electrons
$\mathbf{B}$	Magnetic field
c	Speed of light in vacuum
D	Gap size of a cavity formed by two plasmonic nanoparticles
$\mathbf{D}$	Electric displacement field
e	Electric charge of an electron
E, E_0	Energy, ground-state energy
$\mathbf{E}, \mathbf{E}^{\mathrm{ext}}, \mathbf{E}^{\mathrm{ind}}$	Electric field, external electric field, induced electric field
$\mathbf{E}_0, \mathrm{E}_0$	Electric field amplitude
$\mathbf{E}^{\mathrm{e}}$	Electric field generated by the probing electron
$\mathrm{F}^{\mathrm{ind}}$	Induced force acting on the probing electron
g	Plasmon–exciton coupling strength
$h, \hbar$	Planck's constant, reduced Planck's constant
$\mathbf{H}$	Magnetizing field
$\mathbf{J}_{\mathrm{ext}}, \mathbf{J}_{\mathrm{s}}$	External current density, surface current density
$k, \mathbf{k}$	Wavenumber, wavevector
k_B	Boltzmann constant
$m_{\mathrm{e}}, m_{\mathrm{e}}^*$	Electron mass, effective electron mass
n, n_0	Electron density, static electron density
$\hat{\mathbf{n}}$	Normal vector to a surface
$\mathbf{p}, \mathbf{P}$	Induced dipole moment, polarization vector
$\mathbf{r}$	Position vector
t	Time
T	Temperature

v_F	Fermi velocity of the electrons
$v, \mathbf{v}$	Electron velocity, electron velocity vector
$\mathbf{v}_\mathrm{h}$	Hydrodynamical velocity
V	Volume of a system
V_e	Effective volume of the optical mode
W	Electron energy loss
Y_ℓ^m	Scalar spherical harmonics
(x, y, z)	Cartesian coordinates
(r, θ, φ)	Spherical coordinates
$\alpha_\mathrm{s}, \alpha_\mathrm{hyb}$	Polarizability of a sphere, polarizability of the hybrid cavity–emitter system
$\alpha^0_\mathrm{ex}, \alpha^0_\mathrm{pl}$	Oscillator strength of the emitter and of the plasmonic cavity
β_h	Compressibility of the electron gas
γ_h	Hydrodynamical damping coefficient
$\gamma_\mathrm{ex}, \gamma_\mathrm{pl}$	Damping rate of the exciton and of the plasmonic cavity
γ_p	Phenomenological Drude damping coefficient
Γ_EELS	Electron energy loss probability
$\delta(x)$	Dirac delta function
ε	Relative electric permittivity or dielectric function
ε_0, μ_0	Electric permittivity of vacuum, magnetic permeability of vacuum
λ	Wavelength
μ_t	Transition dipole moment
ν_n	Frequency of vibrational state n
$\rho_\mathrm{ext}, \rho_\mathrm{s}$	External electric charge density, surface electric charge density
$\rho_n^{aS/S}$	Anti-Stokes to Stokes ratio
$\sigma_\mathrm{abs}, \sigma_\mathrm{ext}, \sigma_\mathrm{sca}$	Absorption, extinction, and scattering cross-sections
$\mathrm{d}\sigma_n^{(a)S}/\mathrm{d}\Omega$	(anti-)Stokes differential scattering cross section
$\phi, \phi^\mathrm{ext}, \phi^\mathrm{ind}$	Electrostatic potential, external electrostatic potential, and induced electrostatic potential
ω_p	Plasma frequency
ω_bulk	Bulk plasmon frequency
$\omega_\mathrm{ex}, \omega_\mathrm{pl}$	Resonance frequency of the emitter and of the plasmonic cavity
ω_ℓ	Multipolar resonance frequency of the ℓth order LSPP
ω_sp	Surface plasmon frequency
ω_spp	Surface plasmon polariton frequency
ω_BDP	Bonding dipole plasmon frequency
Ω	Solid angle

Ω_R	Mode splitting
$\Vert$	Direction parallel to the interface

Chapter 2

$\mathbf{a_1}, \mathbf{a_2}, \mathbf{a_3}$	Primitive lattice vectors
$\hat{a}^\dagger (\hat{a})$	Bosonic creation (annihilation) operator
$\boldsymbol{\mathcal{A}}$	Magnetic vector potential
$\mathbf{b_1}, \mathbf{b_2}, \mathbf{b_3}$	Primitive vectors of the reciprocal lattice
$\hat{c}^\dagger (\hat{c})$	Fermionic creation (annihilation) operator
d_E	Euclidean distance between two points of the objective function domain $d_\mathrm{E} = \lvert x - x' \rvert$
$\mathcal{D} = (\mathbf{x}, \mathbf{y})$, $\mu_\mathcal{D}$, $K_\mathcal{D}$	Dataset of observations $\mathbf{y}$ at points $\mathbf{x}$, conditioned mean function, conditioned covariance function
E_H, E_xc	Hartree energy, exchange–correlation energy
$\mathcal{E}_\mathrm{xc}$	Exchange–correlation energy density
$\mathbb{E}[X]$	Expected value of random variable X
$f(x)$	Objective function
f_i	Occupation term of state i
f^a	Atomic orbitals in the LCAO basis set
$F[n]$	Universal Hohenberg–Kohn functional
F^μ	Dominant product functions
$g_{nm\mathbf{k}}^{\nu\mathbf{q}}$	Electron–phonon coupling matrix elements
$\mathbf{G}$	Reciprocal lattice vectors
$\mathcal{GP}(f;\mu,K)$	Gaussian process
$\hat{H}, \hat{H}_\mathrm{KS}$	Schrödinger Hamiltonian, effective Kohn–Sham Hamiltonian
$\hat{H}_0, \hat{H}_\mathrm{e}, \hat{H}_\nu$	Unperturbed Hamiltonian of the electrons and ions, electronic Hamiltonian, ionic Hamiltonian
$\hat{H}_\mathrm{R}, \hat{H}_{\mathrm{e}\nu}, \hat{H}_{\mathrm{e}\gamma}$	Perturbative Raman Hamiltonian, electron–phonon coupling Hamiltonian, electron–light interaction Hamiltonian
$K(x, x')$, $K_{M(\nu)}$, K_SE	Covariance function, Matérn covariance function, squared exponential covariance function
K_Hxc	Hartree–exchange–correlation kernel
l_s	Length scale of a covariance function
ℓ_CO	C-O bond length
$\mathbf{m}$, $\mathbf{C}$	Mean vector and covariance matrix of observations $\mathbf{y}$
M	Nuclear mass

$p(X)$	Probability distribution of variable X
$\mathbf{p}^{\text{ind}}, p_j^{\text{ind}}$	Induced dipole moment, induced dipole moment along the j direction
$\hat{\mathbf{p}}$	Momentum operator
$P_{i\to f}^{(3)}$	Transition probability within third-order perturbation theory
$\mathbf{q}$	Phonon momentum
$\mathbb{R}$	Real space
$R_{\alpha\beta}^{\nu}$	Raman tensor components
$T_{\text{s}}, \hat{T}$	Kinetic energy of the noninteracting system, kinetic energy operator
$\text{Tr}[\ ]$	Trace
$\mathbf{T}$	Bravais lattice vector
$\mathbf{u}_{\text{in(out)}}$	Polarization vector of the input (output) electromagnetic field
$V_{\text{eff}}, V_{\text{ext}}, V_{\text{H}}, V_{\text{xc}}, V_{\text{Hxc}}$	Effective Kohn–Sham potential, external potential, Hartree potential, exchange–correlation potential, Hartree–exchange–correlation potential
V_{μ}^{ab}	Product vertex coefficients
X	Real domain of the objective function
X_a^n	LCAO expansion coefficients
Z	Atomic number
$\alpha(x;\mathcal{D})$, $\alpha_{\text{EI}}(x;\mathcal{D})$, $\alpha_{\text{eLCB}}(x;\mathcal{D})$	Acquisition function, expected improvement acquisition function, exploration-modified lower confidence bound acquisition function
$\hat{\boldsymbol{\alpha}}$	Optical polarizability tensor
δn	Induced electron density
δV_{ext}	Time-dependent part of the external potential
$\delta V_{\text{eff}}, \delta V_{\text{Hxc}}$	Variations of the Kohn–Sham effective and Hartree–exchange–correlation potentials
ϵ_i	Kohn–Sham eigenenergies
η	Artificial spectral broadening
λ_{os}	Output scale
$\mu(x)$	Mean function
μ_c	Chemical potential
ρ	Correlation
σ, σ^2	Standard deviation, variance
ϕ_i	Kohn–Sham wavefunctions
$\Phi = f(x)$	Value of the objective function f
χ, χ_0	Response function, noninteracting response function

X	Domain of the objective function f
ψ	Wavefunction
ψ_a, ψ_b	Intermediate electronic states
Ψ_a, Ψ_b	Intermediate states
$\Psi_i,\ \Psi_f$	Initial state, final state
$\omega_{\mathrm{in(out)}}$	Frequency of the input (output) electromagnetic field

Chapter 3

$E_{\mathrm{DFT}}, E_{\mathrm{shift}}$	Total energy of the system before and after the molecular level shifting
E_f	Fermi energy
$\hat{H}_{\mathrm{shift}}$	Kohn–Sham Hamiltonian including the molecular level shifting
$n^I_{mm}, \Delta^I_{mm'}$	Occupation of the orbital m of the atom I and the local potential shift applied to it
$p_z^{\mathrm{Re}}, p_z^{\mathrm{Im}}$	Real and imaginary parts of the z-component of the induced dipole moment
$P^I_{mm'}, \varphi^I_m$	Localized projectors for computing the local populations, projector functions
r_c	Cutoff radius used for computing the projector functions
$\delta n_{\mathrm{Re}}, \delta n_{\mathrm{Im}}$	Real and imaginary parts of the induced charge density
$\delta\theta$	Phase difference between the molecule and the MNPs
Δ	Magnitude of the molecular level shifting
$\varepsilon_{\mathrm{e}}, \varepsilon_{\mathrm{scr}}$	Relative permittivity of the emitter, $\epsilon_{\mathrm{scr}} = (2\epsilon_0 + \epsilon_{\mathrm{e}})/(3\epsilon_0)$
θ_j	Phase of component j
ω_0	Frequency of the incident monochromatic field

Chapter 4

a_0	Bohr radius
n_+	Uniform positive jellium background charge
r_{s}	Wigner-Seitz radius
$R_q, \Delta R_q$	Accumulated charge ratio, difference between R_q and the homogeneous charge reference

Chapter 5

A	Area of the unit cell, $A = a_1' a_2'$
$\mathbf{a}_1', \mathbf{a}_2'$	Primitive vectors of the overlayer lattice
E_{ads}, E_{SAM}, E_{mol}, E_{slab}	Adsorption energy, total energies of the SAM, of the bare molecule, and of the gold slab
E'_{ads}	Damped adsorption energy
$E^{\mathrm{BOSS}}_{\mathrm{ads},n}$, $E^{\mathrm{DFT}}_{\mathrm{ads},n}$, $E^{\mathrm{DFT,\ rel}}_{\mathrm{ads},n}$	Adsorption energies for the nth local minimum as: predicted by BOSS, computed with DFT, computed with DFT after relaxation
$d_{\mathrm{cut}}, \mathrm{A}_{\mathrm{cost}}, s$	Parameters defining the cost function
d_{min}	Minimal distance between atoms of different building blocks for a given configuration
$d^{\theta}_{ij}, d^{\mathrm{s}}_{ij}, d^{\mathrm{norm}}_{ij}$	Matrix elements of the: angular distance matrix, positional distance matrix, normalized distance matrix
f_{cost}	Cost function
$I_{IR,n}$, p_n	Infrared intensity and infrared transition dipole moment of vibrational mode n
r_{d}	Separation between dipoles (molecules)
$\alpha, \beta, \gamma_1, \gamma_2$	Angular variables in the BOSS rotational search
$\alpha', \beta_1, \beta_2, \gamma_1', \gamma_2'$	Angular variables in the adatom-mediated geometry BOSS rotational search
δI	Euclidean distance between two Raman spectra
$\delta \mathrm{E}$	Decrease in energy during relaxation
Δ_I	Maximal Euclidean distance
Δ_N	Convergence parameter for the BOSS search process
$\delta \nu_n$	Frequency shift of vibrational mode n
θ_1, θ_2	Angles between $\mathbf{a}_1$ and $\mathbf{a}_1'$, and between $\mathbf{a}_2$ and $\mathbf{a}_2'$

Appendix B

$n^{\mathrm{e}}(\mathbf{r})$	Charge density of the probe
$r_<, r_>$	$r_< = \min(r, r')$, $r_> = \max(r, r')$
$\tilde{\beta}$	Local compressibility of the electron gas
$\Gamma^{\mathrm{bulk}}_{\ell m}$, $\Gamma^{\mathrm{Begr}}_{\ell m}$, $\Gamma^{\mathrm{ext}}_{\ell m}$	Bulk, Begrenzung, and external terms in the energy-loss probability
$\Gamma^{\mathrm{Begr,i}}_{\ell m}$, $\Gamma^{\mathrm{Begr,o}}_{\ell m}$	Inner and outer Begrenzung terms
μ_h	$\mu_{\mathrm{h}}(\omega) = \frac{1}{\beta_{\mathrm{h}}} \sqrt{\omega(\omega + i\gamma) - \omega_{\mathrm{p}}^2}$
$\tilde{\omega}_{\mathrm{p}}(\mathbf{r})$	Local plasmon frequency

Appendix C

C_n^{AB}	Dispersion coefficients for the atomic pair $\{$A,B$\}$
$E_{\mathrm{c}}^{\mathrm{vdW}}[n]$, $E_{\mathrm{c}}^{\mathrm{GGA}}[n]$, $E_{\mathrm{c}}^{\mathrm{nl}}[n]$	Van der Waals, GGA, and dispersive correlation energies
$E_{\mathrm{xc}}^{\mathrm{LDA}}[n]$, $E_{\mathrm{xc}}^{\mathrm{GGA}}[n]$	LDA and GGA exchange–correlation energies
$\mathcal{E}_{\mathrm{c}}(n)$, $\mathcal{E}_{\mathrm{x}}(n)$	Correlation and exchange energy densities
$\mathcal{E}_x^{\mathrm{LDA}}$, $\mathcal{E}_{\mathrm{x}}^{\mathrm{GGA}}$	LDA and GGA exchange energy densities
d_{d}	Parameter controlling the steepness of the damping function f^{dmp}
f^{dmp}	Damping function
$F_{\mathrm{x}}(s_{\mathrm{g}})$	Exchange enhancement factor
R_{AB}	Distance between atom A and atom B
s_{g}	Reduced density gradient
s_{n}	Global scaling parameter
$\xi(\mathbf{r},\mathbf{r}')$	General non-local function

Appendix D

$C_{i\alpha}$	Coefficients of the expansion of KS eigenorbital ϕ_i
E_{cut}	Cutoff energy for truncating a basis set of plane waves
$H_{\alpha\beta}$, $S_{\alpha\beta}$	Matrix elements of the KS Hamiltonian and of the overlap matrix
$R_{I\ell n}$, $\mathbf{R}_I$	Radial part of the atomic orbitals, position of atom I
$\varphi_\alpha(\mathbf{r})$	Functions in a basis set
$\varphi_{\mathbf{G}}(\mathbf{r})$	Functions in a basis set of plane waves
$\varphi_{In\ell m}(\mathbf{r})$	Functions in a basis set of atomic orbitals

Appendix E

$n^{\mathrm{AE}}, n_{\mathrm{v}}$	All-electron density, pseudo valence density
P_{ni}^a, $\lvert\tilde{p}_i^a\rangle$	Coefficients of the expansion of $\lvert\tilde{\phi}_n\rangle$ into the $\lvert\tilde{\varphi}_i^a\rangle$, smooth projector functions
r_c^a	Cutoff radii defining the augmentation spheres
$R_{n\ell}^{\mathrm{AE}}(r)$	Radial part of the all-electron eigenfunctions

$R_\ell^{\mathrm{P}}(r)$	Radial part of the pseudo wavefunctions
$\hat{\mathcal{T}}$, $\hat{\mathcal{T}}^a$	Transformation relating the KS and auxiliary wavefunctions, localized atom-centered transformations
$V_{(\mathrm{sc})\ell}^{\mathrm{P}}(r)$, $V_\ell^{\mathrm{P}}(r)$	Pseudopotential, unscreened pseudopotential
Z_V	Number of valence electrons
$\epsilon_{n\ell}$	All-electron eigenenergies
$\lvert\phi_n\rangle$, $\lvert\tilde{\phi}_n\rangle$	KS wavefunctions, auxiliary smooth wavefunctions
$\lvert\varphi_i^a\rangle$, $\lvert\tilde{\varphi}_i^a\rangle$	Partial waves, auxiliary smooth partial waves

Appendix F

$\mathcal{N}(x;\mu,\sigma)$	Gaussian distribution
$\mathcal{N}(\mathbf{x};\boldsymbol{\mu},\mathbf{\Sigma})$, $\boldsymbol{\mu}$, $\mathbf{\Sigma}$	Multivariate Gaussian distribution, mean vector, covariance matrix
$p_{X,Y}(x,y)$	Joint probability distribution of variables X and Y
$p_{Y\vert X}(y\vert x)$	Conditional probability distribution of variable Y on X
$p_X(x)$	Marginal probability distribution of variable X

Contents

Appendices

INTRODUCTION

Throughout most of human history, our observational capabilities have been limited to what we could perceive with the naked eye. It was not until the 17th century that advancements in optics enabled the development of telescopes for exploring the cosmos, and microscopes for unveiling the fundamental mechanisms of life. Despite the remarkable contributions of optical microscopy to biology and medicine, the resolution of these instruments remains constrained by Abbe's diffraction limit [1]. Indeed, due to the wave nature of light, features separated by less than half the wavelength, which for optical frequencies means hundreds of nanometers, cannot be resolved using conventional optical lenses. Therefore, alternative microscopy techniques are required in order to observe and manipulate objects at the nanoscale. The pursuit and application of such methods lies at the core of the field of nanophotonics.

In this context, metallic nanoparticles and surfaces have become central to nanophotonics owing to their ability to support *plasmons* —collective oscillations of the electron cloud that can couple to incident electromagnetic radiation. This interaction produces hybrid modes that exhibit pronounced field enhancement and spatial localization when excited by light or fast electron beams [2]. These unique properties make plasmonic nanoparticles key components in various spectroscopy and microscopy techniques, such as Surface-Enhanced Raman Spectroscopy [3] or Surface-Enhanced Fluorescence [4], with promising applications across diverse areas including biomedicine [5] and telecommunications [6, 7].

Typically, the optical response of plasmonic nanoparticles is accurately described by Maxwell's equations within the framework of classical electromagnetism [8]. However, continuous advances in nanofabrication have pushed the miniaturization of devices down to the single-molecule scale [9], where quantum effects —such as electron tunneling [10–13], nonlocal response [14–16], and electronic spill-out [17, 18]— begin to emerge due to the wave-like behavior of electrons. Addressing these quantum phenomena requires a quantum-mechanical description of the response of matter to light. Unfortunately, directly solving the many-electron Schrödinger's equation is computationally prohibitive for systems with more than a few electrons. *Ab initio* methods simplify the problem by deriving all the relevant physical quantities from the electron density rather than from the many-body wavefunction, and have therefore become highly successful tools for addressing the optical response of nanostructures [19–21]. In particular, time-dependent density-functional theory (TDDFT) at the atomistic level allows for an accurate description of how the atomistic details of a nanoparticle can determine the presence of hot spots, further enhanced by the underlying plasmonic fields [22]. This methodology has been used for studying phenomena such as charge transfer in metallic junctions [23], strong coupling between metallic nanoparticles and molecules [24, 25], hot-carrier generation in metallic nanoparticles [26], or the extreme field enhancement in picocavities [27], among others.

The aforementioned advantages make atomistic TDDFT particularly well suited for investigating interactions between plasmonic nanostructures and quantum emitters, such as organic molecules or semiconductor quantum dots. In recent years, hybrid emitter–plasmonic cavity systems have attracted significant attention, because the properties of the quantum emitter can be modified via coupling with the intense electromagnetic fields present at plasmonic hot-spots. In the strong-coupling regime, this interaction gives rise to hybrid light–matter states known as polaritons [28], which exhibit tunable energy levels and can alter the chemical properties of matter [29, 30]. Consequently, such systems have found applications in photochemistry [31–33], single-photon emission [34], electroluminescence [35], and exciton transport [36], among others. In extreme cases of strong-coupling, such as those involving single molecules in plasmonic nanogaps, the small scale of the system requires a detailed quantum-mechanical treatment including the atomistic features of the cavity, all of which are naturally addressed within the atomistic TDDFT formalism.

Another key application of plasmonic nanoparticles lies in their ability to amplify the vibrational signal of molecules as in Surface-Enhanced Raman Spectroscopy (SERS), achieving signal enhancement factors of up to 10^8 or more, thereby enabling single-molecule detection [37, 38]. SERS has driven a myriad of promising applications [3, 39, 40], becoming a thriving field on its own. Although atomistic TDDFT methods are commonly employed to model SERS configurations due to their accuracy and versatility [41], the computational cost associated with these calculations often forces researches to employ simplified models of the actual systems. This is particularly true for systems that, in reality, are large enough to be considered periodic, such as self-assembled monolayers [42] or nanoparticle-on-mirror configurations [43], which are frequently modeled as finite systems consisting of one or a handful of molecules [44, 45]. In this thesis, we assess the suitability of such approximations by computing the spectra of both periodic and finite models of molecular monolayers adsorbed on metallic surfaces.

One of the most widely used techniques for characterizing plasmonic nanostructures is Electron Energy-Loss Spectroscopy, which involves measuring the energy lost by fast probing electrons as they interact with the sample. The advantages of this technique lie not only on its exceptional spatial and spectral resolution [46–49], but also on its ability to access the full spectral response, including the so-called plasmonic “dark modes” and modes confined to the interior of the nanostructure, which are not excited by conventional light [50–52]. In recent years, localized surface plasmons in small metallic nanoparticles excited by fast electron beams have received significant attention [53–55], with studies highlighting the capability of atomistic *ab initio* methods to model their excitation [22]. However, penetrating electron beams are also capable of exciting longitudinal collective oscillations of the electron density confined within the volume of the nanoparticle, known as confined bulk plasmons [52, 56]. These modes have received limited attention due to their inefficient coupling with light [57], and a complete understanding of their excitation by penetrating electron beams in small nanoparticles has yet to be fully developed. Here, we demonstrate how atomistic *ab initio* methods can accurately capture the full plasmonic response of small metallic nanoparticles as probed by both aloof and penetrating electrons. We complement our analysis with auxiliary calculations based on a classical hydrodynamic model [58, 59] and a jellium TDDFT model [60, 61].

This thesis presents an atomistic *ab initio* study of a selection of canonical plasmonic systems of great interest in nanophotonics, aiming to achieve a deeper fundamental understanding of the quantum effects emerging at the interface between the nano- and pico-scales, with particular emphasis on the atomistic structure. The thesis is structured as follows.

In Chapter 1, we review the fundamental concepts and phenomena arising from light–matter interactions at the nanoscale, focusing on the classical electromagnetic description of plasmonic resonances in spherical metallic nanoparticles and dimers, as well as on excitations in molecules and hybrid metal–molecule systems. We also introduce the three spectroscopy techniques considered throughout this thesis: optical spectroscopy, Electron Energy-Loss Spectroscopy, and Surface-Enhanced Raman Spectroscopy.

Chapter 2 outlines the theoretical framework of atomistic TDDFT, which is used to model the interaction of the studied systems with light and electron beams. Additionally, we introduce the method for computing the Raman spectra of periodic systems, based on perturbation theory. We also present a Bayesian Optimization procedure designed for obtaining the minimum energy configurations of nanoscale systems, such as molecular adsorbates on metallic surfaces.

In Chapter 3, we analyze the optical absorption spectrum of a hybrid system consisting of a porphine molecule placed in the cavity formed by a silver nanoparticle dimer. We show that the light–matter coupling strength, which exceeds the strong-coupling threshold across the entire range of studied gap sizes, is significantly affected by the geometrical configuration of the cavity. This configuration also determines the emergence of charge-transfer modes and electronic quenching phenomena at narrow gaps.

Chapter 4 focuses on the electron energy-loss probability spectrum of small sodium nanoparticles, particularly under penetrating electron trajectories. In addition to localized surface plasmons excited by aloof electrons, we identify and characterize confined bulk plasmons and higher-order surface resonances, so-called Bennett plasmons. By comparing the results obtained with atomistic TDDFT to auxiliary calculations using hydrodynamic and jellium TDDFT models, we construct a detailed picture of the complex resonance structure of these modes.

Finally, Chapter 5 presents a TDDFT study of a self-assembled monolayer of 4'-cyanobiphenyl-4-thiol molecules on an Au(111) surface. We first apply a methodology based on Bayesian optimization to identify the most stable monolayer structures. Then we analyze how the molecular orientation, the surface coverage density, and the emergence of adatom-mediated configurations influence the Raman spectrum.

We believe that the findings presented herein can contribute to a deeper understanding of quantum and atomistic effects in extreme cases of light–matter interaction, further validating the effectiveness of atomistic *ab initio* methods for studying nanophotonic systems.

CHAPTER 1

THEORETICAL CONCEPTS AND SPECTROSCOPIC TECHNIQUES

In this thesis, we analyze the electromagnetic interaction of several canonical systems in nanophotonics with different types of illumination. The aim of this chapter is to provide an introduction to key concepts and phenomena arising in light–matter interaction at the nanoscale, in order to set a conceptual basis for the studies described in the next chapters.

We start with a brief summary of the classical electrodynamics formalism in Section 1.1, where we present Maxwell's equations and the main approximations considered in this thesis. We emphasize that the classical linear optical response of a bulk material can usually be described by its local permittivity, with the electromagnetic field fulfilling a set of boundary conditions at the interfaces between materials. In Section 1.2, we explain the emergence of collective oscillations of electrons, or plasmons, in different metallic nanostructures within the classical formalism. Next, we describe briefly the main excitations occurring in molecules in Section 1.3, and in Section 1.4 we introduce the coupling between plasmons and molecular excitations, defining the weak- and strong-coupling regimes. This will be followed by a short overview of two related spectroscopy techniques: Surface-Enhanced Raman Spectroscopy (SERS, in Section 1.5), which uses the field enhancement of plasmonic nanoparticles for boosting the vibrational signal from molecules, and Electron Energy-Loss Spectroscopy (EELS, in Section 1.6), widely used for probing plasmonic nanoparticles with the fast electrons in Scanning Transmission Electron Microscopy (STEM).

1.1 Optical response in classical electromagnetism

Within the framework of classical electromagnetism, the interaction of an electromagnetic field with a material can be described by Maxwell's equations (in SI units) [8, 62]:

$$\nabla \times \mathbf{E}(\mathbf{r},t) = -\frac{\partial}{\partial t}\mathbf{B}(\mathbf{r},t), \tag{1.1a}$$

$$\nabla \times \mathbf{H}(\mathbf{r},t) = \frac{\partial}{\partial t}\mathbf{D}(\mathbf{r},t) + \mathbf{J}_{\mathbf{ext}}(\mathbf{r},t), \tag{1.1b}$$

$$\nabla \cdot \mathbf{D}(\mathbf{r},t) = \rho_{\text{ext}}(\mathbf{r},t), \tag{1.1c}$$

$$\nabla \cdot \mathbf{B}(\mathbf{r},t) = 0, \tag{1.1d}$$

where $\mathbf{E}(\mathbf{r},t)$, $\mathbf{B}(\mathbf{r},t)$, $\mathbf{D}(\mathbf{r},t)$, and $\mathbf{H}(\mathbf{r},t)$ are the macroscopic electric, magnetic, displacement, and magnetizing fields, respectively, and $\rho_{\text{ext}}(\mathbf{r},t)$ and $\mathbf{J}_{\mathbf{ext}}(\mathbf{r},t)$ are the external charge and current density that act as sources of electromagnetic fields. For nonmagnetic materials such as the ones considered in this thesis, the magnetic and magnetizing fields are directly related as $\mathbf{B}(\mathbf{r},t) = \mu_0 \mathbf{H}(\mathbf{r},t)$, where μ_0 is the permeability of vacuum. In the linear-response regime, and assuming an isotropic and homogeneous medium, the displacement and electric fields are linked by the constitutive relationship:

$$\mathbf{D}(\mathbf{r},t) = \varepsilon_0 \int_{-\infty}^{\infty}\int_{-\infty}^{\infty} d\mathbf{r}'dt'\varepsilon(\mathbf{r}-\mathbf{r}',t-t')\ \mathbf{E}(\mathbf{r}',t'), \tag{1.2}$$

where ε_0 is the vacuum permittivity, and $\varepsilon(\mathbf{r}-\mathbf{r}',t-t')$ is the dielectric function describing the optical excitations in the material. Though in principle the dielectric function is a matrix and the response depends on the direction of excitation, here we will only consider isotropic media and assume that the response is a scalar. This expression is nonlocal both in space and time, as it relates the displacement vector $\mathbf{D}$ at position $\mathbf{r}$ and time t to the value of the electric field $\mathbf{E}$ at all positions $\mathbf{r}'$ and times $t' < t$. This relationship can also be expressed in the domain of the angular frequency ω by doing the Fourier transform:

$$\mathbf{D}(\mathbf{r},\omega) = \varepsilon_0 \int_{-\infty}^{\infty} d\mathbf{r}'\varepsilon(\mathbf{r}-\mathbf{r}',\omega)\ \mathbf{E}(\mathbf{r}',\omega). \tag{1.3}$$

The spatial nonlocality of the dielectric function significantly modifies the optical response of metallic nanostructures with characteristic dimensions smaller than ~ 10 nm [14]. In the results presented in this thesis, which are computed within the time-dependent density-functional theory (TDDFT) framework (see Chapter 2), nonlocal effects are naturally accounted for. However, incorporating them into the classical formalism is not straightforward, and in the classical description of the optical response we will limit ourselves to a local model of the

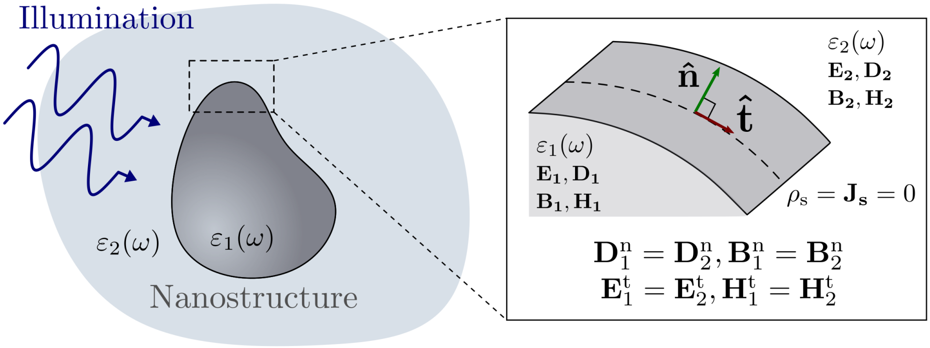

Figure 1.1: Schematics of a neutral bounded nanostructure in the piecewise-constant approximation. The dielectric function is $\varepsilon_1(\omega)$ inside the nanostructure and $\varepsilon_2(\omega)$ in the surrounding medium, and changes abruptly at the interface. The inset displays a close-up on the interface. The normal ($\hat{\mathbf{n}}$) and tangential ($\hat{\mathbf{t}}$) unit vectors are depicted, as well as the continuity conditions for the different electromagnetic fields.

permittivity, which is usually accurate to qualitatively describe the interaction between metallic nanoparticles and light. The local-response approximation assumes that the displacement vector at a position $\mathbf{r}$ only depends on the electric field at the same position, so that the dielectric function becomes

$$\varepsilon(\mathbf{r}-\mathbf{r}',\omega) = \varepsilon_0\varepsilon(\mathbf{r},\omega)\ \delta(\mathbf{r}-\mathbf{r}'), \tag{1.4}$$

where $\delta(\mathbf{r}-\mathbf{r}')$ is the Dirac delta function. The constitutive relation then becomes

$$\mathbf{D}(\mathbf{r},\omega) = \varepsilon_0\varepsilon(\mathbf{r},\omega)\ \mathbf{E}(\mathbf{r},\omega) = \varepsilon_0\ \mathbf{E}(\mathbf{r},\omega) + \mathbf{P}(\mathbf{r},\omega), \tag{1.5}$$

where $\mathbf{P}(\mathbf{r},\omega)$ is the electric polarization, defined as the dipole moment per unit volume at point $\mathbf{r}$. In the case of bulk materials, this relationship can be further simplified by assuming a dielectric permittivity that is homogeneous in space, $\varepsilon(\mathbf{r},\omega) = \varepsilon(\omega)$.

1.1.1 Boundary conditions

In this thesis, we focus our analysis on bounded nanostructures, as the one depicted in Fig. 1.1. These systems are composed by different materials, each with its own optical properties, and therefore the spatial dependence of the permittivity is unavoidable. The simplest approach for solving Eqs. (1.1a)–(1.1d) in such systems is the so-called piecewise-constant approximation [63], in which $\varepsilon(\mathbf{r},\omega)$ is considered to be constant inside each material, and varies abruptly at the interfaces. For example, if our system consists of two materials indexed by numbers 1 and 2, the permittivity can be expressed with the piecewise function

$$\varepsilon(\mathbf{r},\omega) = \begin{cases} \varepsilon_1(\omega) & \text{in material 1,} \\ \varepsilon_2(\omega) & \text{in material 2.} \end{cases} \tag{1.6}$$

In order to satisfy Maxwell's equations at the interface, the following set of boundary conditions must be fulfilled [8]

$$\hat{\mathbf{n}} \cdot (\mathbf{D_2} - \mathbf{D_1}) = \rho_\mathrm{s}, \tag{1.7a}$$
$$\hat{\mathbf{n}} \cdot (\mathbf{B_2} - \mathbf{B_1}) = 0, \tag{1.7b}$$
$$\hat{\mathbf{n}} \times (\mathbf{E_2} - \mathbf{E_1}) = 0, \tag{1.7c}$$
$$\hat{\mathbf{n}} \times (\mathbf{H_2} - \mathbf{H_1}) = \mathbf{J_s}, \tag{1.7d}$$

where $\hat{\mathbf{n}}$ is the unit vector perpendicular to the interface, pointing from material 1 to material 2, and ρ_s and $\mathbf{J_s}$ are the external surface charge and surface current densities, respectively. Since the systems considered in this thesis are neutral, no free charges or currents at the interfaces will be considered, and therefore the conditions above can be simplified by taking $\rho_\mathrm{s} = \mathbf{J_s} = 0$. In such a case, Eqs. (1.7a)–(1.7d) impose the continuity of the normal components of the **D** and **B** fields, as well as the continuity of the tangential components of the **E** and **H** fields. Notably, this means that the normal component of the electric field **E** will be strongly discontinuous at the interfaces due to the abrupt change in the permittivity.

1.1.2 The nonretarded approximation

When the size of the considered structures is much smaller than the wavelength of the incident light, retardation effects in the electromagnetic interaction caused by the finite speed of light can be neglected. In such cases, one can use the so-called nonretarded or quasi-static approximation, in which the speed of light is considered to be infinite ($c \to \infty$). This allows us to express the total electromagnetic field as the gradient of a scalar function

$$\mathbf{E}(\mathbf{r},\omega) = -\nabla\phi(\mathbf{r},\omega). \tag{1.8}$$

The scalar function $\phi(\mathbf{r},\omega)$ is known as the electrostatic potential. The total electromagnetic field can be decomposed as a sum of the external electric field, $\mathbf{E}^\mathrm{ext}(\mathbf{r},\omega)$, and the field induced by the nanostructure, $\mathbf{E}^\mathrm{ind}(\mathbf{r},\omega)$. The external field may be due to an electromagnetic wave or an electron beam, for example. The induced field is caused by the induced charges and currents produced at the nanostructures as a result of the external drive. Similarly, the electrostatic potential can also be separated into the external and induced potentials, $\phi(\mathbf{r},\omega) = \phi^\mathrm{ext}(\mathbf{r},\omega) + \phi^\mathrm{ind}(\mathbf{r},\omega)$. From Eq. (1.1c), one can conclude that the external potential must satisfy Poisson's equation:

$$\nabla^2\phi^\mathrm{ext}(\mathbf{r},\omega) = \rho_\mathrm{ext}, \tag{1.9}$$

while the induced potential satisfies Laplace's equation:

$$\nabla^2 \phi^{\mathrm{ind}}(\mathbf{r},\omega) = 0. \tag{1.10}$$

The boundary conditions at the interface between two materials are also simplified in the nonretarded approximation, and can be expressed as

$$\phi^1(\mathbf{r},\omega) = \phi^2(\mathbf{r},\omega), \tag{1.11a}$$

$$\epsilon_1(\omega)\ \hat{\mathbf{n}} \cdot \nabla\phi^1(\mathbf{r},\omega) = \epsilon_2(\omega)\ \hat{\mathbf{n}} \cdot \nabla\phi^2(\mathbf{r},\omega), \tag{1.11b}$$

where ϕ^j is the electrostatic potential in material j. The nonretarded approximation will be a useful framework to describe the optical response of small nanostructures and clusters, which is the object of this thesis.

1.2 Nanoplasmonics

Conduction electrons in metallic nanoparticles behave as an homogeneous gas of free particles, which can sustain collective surface charge density oscillations at certain resonance frequencies depending on the material. The quanta of these charge oscillations are called plasmons, and are a key feature in the interaction of metallic nanostructures with light. Their capacity to produce extremely enhanced and confined electromagnetic near-fields is crucial in nanophotonics, and has led to the development of a plethora of applications. Before discussing the main applications and the methods employed for the characterization of plasmonic systems, we will briefly go over the basic types of plasmons emerging from the classical description of metallic nanostructures. Although we will be focusing on the plasmons emerging in bounded nanoparticles and dimers, we also describe plasmons supported by infinite and semi-infinite metallic systems in order to properly understand the underlying physical concepts in the optical response of metals.

1.2.1 The Drude model

The simplest description of the response of the conduction electrons in a metal to an external electric field is given by the Drude model [62, 64, 65], which considers that the electronic structure of the material is given by a classical homogeneous electron gas. In response to an external oscillating electric field $\mathbf{E}(t) = \mathbf{E}_0 \mathrm{e}^{-i\omega t}$, the displacement $\mathbf{r}(t)$ of an electron with effective mass m_{e}^* and charge e from its equilibrium position is given by the equation of motion

$$m_{\mathrm{e}}^* \ddot{\mathbf{r}}(t) + m_{\mathrm{e}}^* \gamma_{\mathrm{p}} \dot{\mathbf{r}}(t) = e\mathbf{E}_0 \mathrm{e}^{-i\omega t}, \tag{1.12}$$

where γ_{p} is a phenomenological damping coefficient accounting for the losses caused by collisions with the lattice nuclei and other processes. By inserting the ansatz $\mathbf{r}(t) = \mathbf{r}_0 \mathrm{e}^{-i\omega t}$ into Eq. (1.12), one can obtain the displacement of the electrons in the frequency domain

$$\mathbf{r}_0(\omega) = -\frac{e}{m_\mathrm{e}^* \omega(\omega + i\gamma_\mathrm{p})}\mathbf{E}_0(\omega). \tag{1.13}$$

As a consequence of the displacement of the homogeneous electron gas, the external electric field induces a polarization $\mathbf{P}(\omega) = ne\mathbf{r}_0(\omega)$, where n is the average electron density. By using the relation in Eq. (1.5), one can obtain the expression for the local frequency-dependent permittivity in the Drude model

$$\varepsilon(\omega) = 1 - \frac{\omega_\mathrm{p}^2}{\omega(\omega + i\gamma_\mathrm{p})}, \tag{1.14}$$

where ω_p is the plasma frequency of the metal, defined as

$$\omega_\mathrm{p} = \sqrt{\frac{ne^2}{\varepsilon_0 m_\mathrm{e}^*}}. \tag{1.15}$$

Despite its simplicity, the Drude model provides an accurate description of the response at low excitation energies, and allows for the understanding of the main phenomena in optical spectroscopy of metals, such as the emergence of surface plasmons. The model can be improved by adding a background screening ε_∞ in order to account phenomenologically for the polarizability of bounded electrons, such as the d shells in silver and gold, metals which are ubiquitous in nanophotonics, though this is not necessary for simple metals like sodium, where such bound electrons do not affect the response.

1.2.2 Bulk Plasmon Polaritons

Let us consider a bulk metal infinitely extended in every direction. This system sustains longitudinal waves of electronic density propagating in the infinite metal, known as bulk or volume plasmons. In these modes, the electrons move collectively in the direction of the propagation, producing an oscillation of the charge density and an oscillating polarization $\mathbf{P}$, as depicted in Fig. 1.2a. Assuming a local permittivity and in the absence of external charges, the electric field must follow the equation $\nabla \cdot (\varepsilon(\mathbf{r},\omega)\mathbf{E}(\mathbf{r},\omega)) = 0$ (from Eq. (1.1c)). Since longitudinal waves must satisfy $\nabla \cdot \mathbf{E}(\mathbf{r},\omega) \neq 0$, they can only exist in an homogeneous material when $\varepsilon(\omega) = 0$ [66, 67], which, assuming a Drude-like dielectric function [Eq. (1.14)] with negligible losses ($\gamma_\mathrm{p} \approx 0$), leads to the bulk plasmon frequency

$$\omega_\mathrm{bulk} = \omega_\mathrm{p}. \tag{1.16}$$

Additionally, an infinite bulk metal can also support propagating transverse modes called bulk plasmon polaritons. By introducing solutions of the form $\mathbf{E}(\mathbf{r},t) = \mathbf{E}_0 e^{i\mathbf{k}\cdot\mathbf{r}} e^{-i\omega t}$ and $\mathbf{B}(\mathbf{r},t) = \mathbf{B}_0 e^{i\mathbf{k}\cdot\mathbf{r}} e^{-i\omega t}$ into Eqs. (1.1a)–(1.1d), and assuming there are no free charges, we observe that nontrivial solutions are only possible when

$$\omega = \frac{ck}{\sqrt{\varepsilon(\omega)}}, \tag{1.17}$$

where the wavenumber k is the magnitude of the wavevector $\mathbf{k}$. If we model the response of the bulk material with a Drude-like dielectric function [Eq. (1.14)], the condition reduces to

$$\omega = \sqrt{\omega_{\mathrm{p}}^2 + c^2k^2}, \tag{1.18}$$

which means that propagating modes in an infinite bulk metal can only exist at frequencies $\omega \geq \omega_{\mathrm{p}}$. Furthermore, the dispersion relation in Eq. (1.18) illustrates that bulk plasmon polaritons are a result of the hybridization between light and electronic oscillations, as they present features of both photons and plasmons. When the wavevector is small ($k \to 0$), the propagating modes have a primarily electronic character, whereas at the long wavevector ($k \to \infty$) limit their dispersion is equivalent to that of light in vacuum ($\omega = ck$).

1.2.3 Surface Plasmon Polaritons

In order to observe the effect of the material boundary, we consider the simple case of a semi-infinite ($z > 0$) metal in contact with vacuum ($\varepsilon = 1$) along a planar interface. In this configuration, a new type of plasmon arises, consisting of charge density oscillations propagating along the metal–vacuum interface and bound to the metal surface, so-called surface plasmons. By solving Laplace equation for the induced potential and imposing the continuity of the displacement field $\mathbf{D}$ at the interface, it can be proved that the resonance condition of the surface plasmon in the nonretarded approximation is determined by $\varepsilon(\omega) = -1$ [68]. Assuming a lossless ($\gamma_{\mathrm{p}} \approx 0$) Drude-like dielectric function for the metal [Eq. (1.14)], this yields the surface-plasmon frequency

$$\omega_{\mathrm{sp}} = \frac{\omega_{\mathrm{p}}}{\sqrt{2}}. \tag{1.19}$$

In addition to these purely electronic modes, metal–vacuum interfaces also support hybrid modes called surface plasmon polaritons (SPPs), which propagate along the metal–vacuum interface and are characterized by electromagnetic fields evanescent in the z direction (perpendicular to the interface), this is, decaying exponentially instead of quadratically, as depicted in Fig. 1.2b. Such fields are characterized by the expression [62]

$$\mathbf{E}_j(\mathbf{r}) = \begin{pmatrix} \mathrm{E}_{j,\parallel} \\ \mathrm{E}_{j,z} \end{pmatrix} e^{ik_\parallel r_\parallel - i\omega t} e^{-k_{j,z}|z|}, \tag{1.20}$$

where $j = 1, 2$ denotes both semi-infinite metal ($z < 0$) and vacuum ($z > 0$) spaces, and $k_\parallel$ and k_z are the wavevector components in the directions parallel and perpendicular to the interface, respectively. By imposing the continuity of the parallel component of $\mathbf{E}$ and the perpendicular component of the displacement

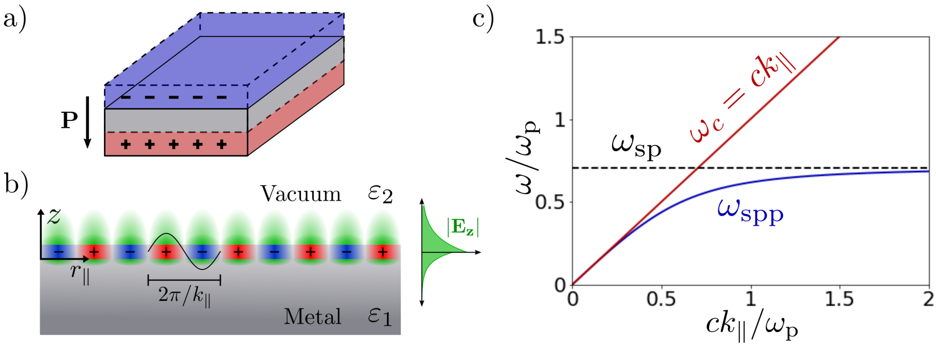

Figure 1.2: a) Sketch of a longitudinal bulk plasmon in an infinite bulk metal. The bulk plasmon is a longitudinal collective oscillation of the free electron gas in the metal producing an oscillating polarization $\mathbf{P}$. b) Sketch of a SPP with wavenumber $k_\parallel$ propagating along the metal–vacuum interface. The propagating positive (negative) surface charge density is represented in red (blue), and the perpendicular component of the evanescent electromagnetic field is depicted in green. The plot on the right shows the exponential decay of the evanescent field. c) Dispersion relation of the SPPs (blue line) given by Eq. (1.22), and of light in vacuum (red line). The surface plasmon frequency ω_sp is represented by the black dashed line.

vector $\mathbf{D}_j = \varepsilon_j \mathbf{E}_j$, one obtains the following dispersion relation for the parallel wavevector component (depicted in Fig. 1.2c) [62]

$$k_\parallel^2 = \frac{\varepsilon_1 \varepsilon_2}{\varepsilon_1 + \varepsilon_2} \frac{\omega^2}{c^2}. \tag{1.21}$$

By introducing the dielectric functions for vacuum ($\varepsilon_2 = 1$) and for a lossless Drude metal [Eq. (1.14)], the dispersion relation becomes [62, 68]

$$\omega_\mathrm{spp}^2(k_\parallel) = \frac{\omega_\mathrm{p}^2}{2} + c^2 k_\parallel^2 - \sqrt{\frac{\omega_\mathrm{p}^4}{4} + c^4 k_\parallel^4}. \tag{1.22}$$

This dispersion relation is represented in Fig. 1.2c, and evidences the hybrid nature of the SPPs. In the small wavevector limit ($k_\parallel \to 0$), the SPP frequency ω_spp (blue line) approaches the dispersion line of light in free space $\omega_c = ck_\parallel$ (red line), and thus SPPs behave as photons. On the other hand, in the large wavevector limit ω_spp asymptotically tends to the surface-plasmon frequency $\omega_\mathrm{sp} = \omega_\mathrm{p}/\sqrt{2}$ (black-dashed line), indicating that SPPs acquire an electronic character.

Close to the surface-plasmon frequency, SPPs show electromagnetic fields exponentially decaying as one moves away from the surface, as sketched in Fig. 1.2b (right-hand side), which allows for sub-wavelength confinement of light to a thin region around the interface. However, the dispersion relation of SPPs never crosses the light line, as we can observe in Fig. 1.2c, and therefore the energy and momentum conservation rules prevent their excitation by a plane wave traveling in vacuum. In order to overcome this momentum mismatch and excite SPPs with light, several strategies for providing the required additional momentum have been proposed, such as placing sharp metallic tips above the metal–vacuum interface [69], using evanescent fields generated with optical prisms [70, 71], or modifying the metallic surface by adding gratings or roughness [72].

1.2.4 Localized Surface Plasmon Polaritons

The momentum mismatch between light and surface plasmon polaritons in a semi-infinite metallic surface can be overcome when one considers finite metallic nanoparticles (MNPs) instead, as the finite geometry of a MNP provides the extra momentum needed for the energy–momentum exchange between light and collective electronic excitations. In this situation, the oscillations of free electrons are confined in the three dimensions instead of propagating, and therefore plasmon resonances in finite MNPs are called localized surface plasmon polaritons (LSPPs). While in infinite interfaces the SPP resonances have a continuous dispersion relationship, finite nanoparticles only support LSPPs at discrete resonance energies. For simplicity, in later chapters we will refer to LSPPs as “localized surface plasmons” (LSPs), as it is often done in the literature.

The emergence of LSPPs can be easily understood by analyzing the response of the canonical metallic nanoparticle, a spherical particle of arbitrary radius a surrounded by vacuum. In 1908, Gustav Mie demonstrated that the electromagnetic field scattered by such a particle can be expressed as a sum of different electric and magnetic multipoles, where each multipole corresponds to a different field distribution [73]. Luckily, this complex optical response is simplified when the size of the nanoparticle (with radius a) is much smaller than the wavelength of the optical oscillations, this is, $\lambda = \frac{2\pi}{k} = \frac{2\pi c}{\omega} \gg a$, as one can then use the nonretarded approximation (see Section 1.1). Following this approximation, the induced electrostatic potential ϕ^{ind} can be obtained by solving Laplace’s equation (1.10) in spherical coordinates (r, θ, φ), given by an expansion in terms of a spherical harmonics basis set $Y_\ell^m(\theta, \varphi) \to Y_\ell^m(\Omega)$, where Ω is the solid angle [8]:

$$\phi^{\mathrm{ind}}(\mathbf{r}, \omega) = \sum_{\ell=0}^{\infty} \sum_{m=-\ell}^{\ell} \left(A_\ell r^\ell + B_\ell r^{-(\ell+1)} \right) Y_\ell^m(\theta, \varphi), \tag{1.23}$$

where A_ℓ and B_ℓ are the coefficients of the ℓ-multipolar expansion. Imposing the finiteness of ϕ^{ind} at the origin and at infinity and applying the boundary conditions at the spherical interface, expressed by Eqs. (1.11a)–(1.11b), completely determines the induced potential in the entire space, inside and outside the spherical closure [21]:

$$\phi^{\mathrm{ind}}(\mathbf{r}, \omega) = \sum_{\ell=0}^{\infty} \sum_{m=-\ell}^{\ell} b_{\ell m}(\omega) Y_\ell^m(\theta, \varphi) \times \begin{cases} r^\ell / a^\ell & r \leq a \\ a^{\ell+1} / r^{\ell+1} & r \geq a \end{cases}, \tag{1.24}$$

with

$$b_{\ell m}(\omega) = \frac{-a[\varepsilon(\omega)-1]}{\ell+1+\ell\varepsilon(\omega)} \int d\Omega [Y_\ell^m(\theta,\varphi)]^* \frac{\partial}{\partial r}\phi^{\rm ext}(\mathbf{r},\omega)\bigg|_{r=a}, \qquad (1.25)$$

where the integral extends over the solid angle $\Omega = (\theta, \varphi)$. Without an external excitation ($\phi^{\rm ext} = 0$), the coefficients $b_{\ell m}(\omega)$ are null except at the poles in Eq. (1.25), so that the resonance conditions of the LSPPs sustained by a spherical MNP of radius a surrounded by vacuum are given by

$$\ell + 1 + \ell\varepsilon(\omega) = 0. \qquad (1.26)$$

Assuming a lossless Drude-like dielectric function characterizing the spherical nanoparticle [as in Eq. (1.14)], the multipolar resonance frequencies of LSPPs in the nonretarded approximation are given by

$$\omega_\ell = \omega_{\rm p}\sqrt{\frac{\ell}{2\ell+1}}, \qquad (1.27)$$

where ℓ is the multipole order of the LSPP resonance.

Though these resonance frequencies are in principle independent of the particle size, this assumption is no longer valid for large MNPs [74, 75], for which retardation effects become significant, neither for very small nanoparticles [17, 76], due to the emergence of quantum-size effects. On the other hand, the LSPP resonance approaches the frequency of the surface plasmon in the large-ℓ limit ($\omega_{\ell\to\infty} \approx \omega_{\rm p}/\sqrt{2}$). This occurs because the wavelength of the excited LSPPs decreases with ℓ as $\lambda \sim 2\pi a/\ell$, and therefore in the large-ℓ limit the nanoparticle surface can be interpreted as a flat interface.

Let us now consider the response of such a spherical nanoparticle to an incident monochromatic plane wave polarized along the z direction, expressed as $\mathbf{E}^{\rm ext}(\mathbf{r},\omega) = {\rm E}_0^\omega \, e^{i\mathbf{k}\cdot\mathbf{r}} \, \hat{z}$ in the frequency domain. Within the nonretarded approximation, one can neglect the spatial variation of the external electric field along the nanoparticle $\mathbf{E}^{\rm ext}(\mathbf{r},\omega) = {\rm E}_0^\omega \, \hat{z}$. Such an external field polarizes the metallic spherical particle along the z direction, concentrating charges of opposite signs at the top and bottom sides of the nanoparticle as depicted in Fig. 1.3a. Since the electric field associated with a plane wave oscillates in time, the free-electron gas will also oscillate in time, with a phase difference of $\pi/2$ with respect to the incident field. This charge distribution presents a clear dipolar character and thus the resonant excitation of this collective oscillation corresponds to the LSPP mode with $\ell = 1$ or dipolar plasmon (DP), which, according to Eq. (1.27), is activated when the frequency of the incident field is $\omega_{\rm DP} = \omega_{\rm p}/\sqrt{3}$.

The previous prediction can be demonstrated by considering a plane-wave illumination in Eq. (1.25). For the external potential associated with such wave, $\phi^{\rm ext}(\mathbf{r},\omega) = -{\rm E}_0 \; r \; \cos(\theta)$ in spherical coordinates, the integral in Eq. (1.25) has an analytic solution, and vanishes except for $\ell = 1$, which means that only the DP resonance is excited in such a situation. The induced electric field can be calculated

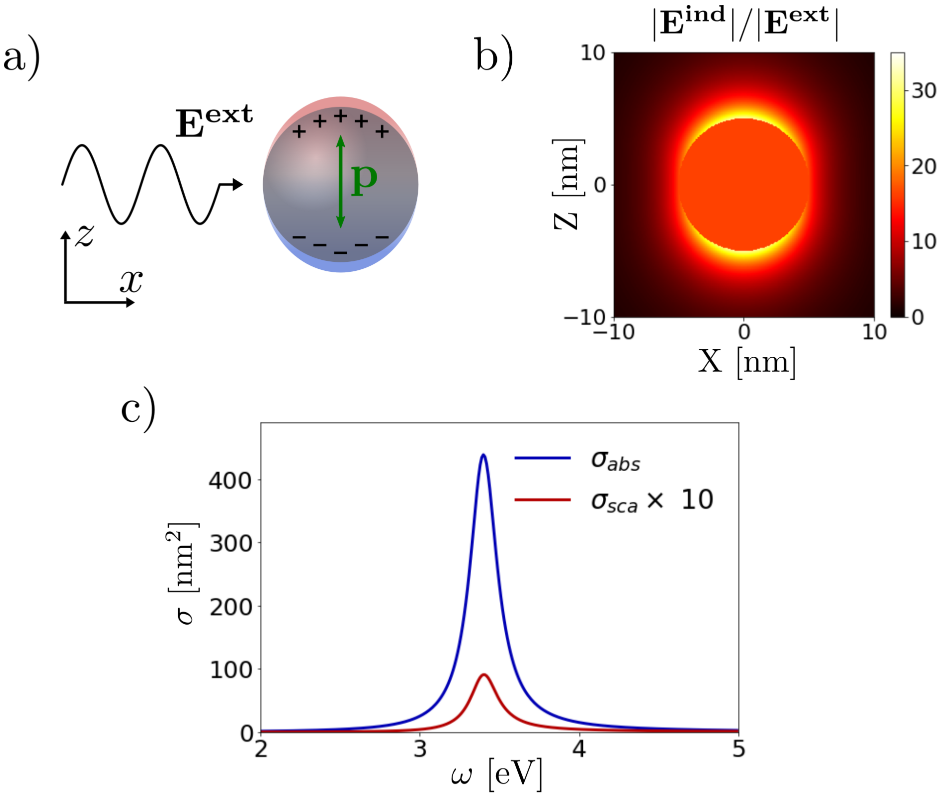

Figure 1.3: a) Sketch of the charge density induced on a spherical MNP by a plane-wave polarized along the z direction, with the oscillating dipole moment $\mathbf{p}$ induced at the nanoparticle represented in green. b) Map of the induced electric field enhancement from Eq. (1.28), for a Na MNP with radius $a = 5$ nm, characterized by a Drude-like dielectric function [Eq. (1.14)] with $\omega_{\mathrm{p}} = 5.89$ eV, and $\gamma_{\mathrm{p}} = 0.21$ eV, at the resonance frequency of the dipolar mode $\omega_{\mathrm{DP}} = 3.40$ eV. c) Spectra of the absorption (blue) and scattering (red) cross sections of the same Na MNP as in b). The scattering cross section is multiplied by 10 for visibility.

inside and outside the sphere from the gradient of the induced potential [62]:

$$\mathbf{E}^{\mathrm{ind}}(\mathbf{r},\omega) = -\nabla\phi^{\mathrm{ind}}(\mathbf{r},\omega) = \begin{cases} -\mathrm{E}_0 \frac{\varepsilon(\omega)-1}{\varepsilon(\omega)+2}\ \hat{\mathbf{z}} & \text{if } r < a \\ \\ \mathrm{E}_0 \frac{\varepsilon(\omega)-1}{\varepsilon(\omega)+2} \frac{a^3}{r^3} \left(2\cos(\theta)\ \hat{\mathbf{r}} + \ \sin(\theta)\ \hat{\boldsymbol{\theta}} \right) & \text{if } r > a \end{cases}, \tag{1.28}$$

with $\hat{\mathbf{r}}$ and $\hat{\boldsymbol{\theta}}$ the unit vectors along the radial and tangential directions, respectively. Indeed, inserting a lossless Drude-like dielectric function [Eq. (1.14)] one can observe that the induced field diverges at the DP frequency, $\omega_{\mathrm{DP}} = \omega_{\mathrm{p}}/\sqrt{3}$. Note also that, since $\hat{\mathbf{z}} = \cos\theta\ \hat{\mathbf{r}} - \ \sin\theta\ \hat{\boldsymbol{\theta}}$, the tangential component of the electric field is continuous at the interface, unlike the perpendicular component.

As a reference, we plot in Fig. 1.3b a map of the electric field enhancement $|\mathbf{E}^{\text{ind}}|/|\mathbf{E}^{\text{ext}}|$ for a sodium MNP of radius $a = 5$ nm, characterized by a Drude-like dielectric function [Eq. (1.14)] with parameters $\omega_{\text{p}} = 5.89$ eV and $\gamma_{\text{p}} = 0.21$ eV [77], at its DP frequency $\omega_{\text{DP}} = 3.40$ eV. Notice that the induced field is constant inside the MNP, but it varies sharply outside, presenting values much larger than the incident field close to the surface. This figure illustrates the ability of LSPPs to concentrate the electromagnetic field into space regions much smaller than the wavelength of the incident field (~ 400 nm in this case), thus allowing for beating the diffraction limit.

Interestingly, the induced electric field outside the sphere in the quasi-static approximation is identical to the field created by a point-dipole located at the center of the MNP [62]. Therefore, in cases when one is only concerned by the field outside the MNP, the particle can be considered as a point dipole $\mathbf{p}(\omega) = \alpha_{\text{s}}(\omega)\mathbf{E}^{\text{ext}}$ with polarizability

$$\alpha_{\text{s}}(\omega) = 4\pi\varepsilon_0 \, a^3 \frac{\varepsilon(\omega) - 1}{\varepsilon(\omega) + 2}. \tag{1.29}$$

Oscillating dipoles emit light into the far field, which makes MNPs excellent candidates for optical nanoantennas [78]. Furthermore, this means that plasmonic nanoparticles supporting LSPPs present a characteristic fingerprint in far-field spectroscopy, enabling their identification and characterization.

The scattering cross section of the radiating dipole, which is equal to the total power radiated to the far field divided by the intensity of the exciting plane wave, is given by [74]

$$\sigma_{\text{sca}}(\omega) = \frac{1}{6\pi\varepsilon_0^2} \left(\frac{\omega}{c}\right)^4 |\alpha_{\text{s}}(\omega)|^2. \tag{1.30}$$

The extinction cross section, corresponding to the total power dissipated by the MNP, is given by [74, 79]

$$\sigma_{\text{ext}}(\omega) = \frac{\omega}{c\varepsilon_0} \text{Im}\left\{\alpha_{\text{s}}(\omega)\right\}. \tag{1.31}$$

The extinction cross section can also be expressed as $\sigma_{\text{ext}}(\omega) = \sigma_{\text{sca}}(\omega) + \sigma_{\text{abs}}(\omega)$, where $\sigma_{\text{abs}}(\omega)$ is the absorption cross section, corresponding to the power absorbed by the MNP. Since for very small nanoparticles $\sigma_{\text{sca}}(\omega) \ll \sigma_{\text{ext}}(\omega)$, we will from now on consider $\sigma_{\text{abs}}(\omega) \approx \sigma_{\text{ext}}(\omega)$. The absorption and scattering cross sections for the sodium nanoparticle considered in Fig. 1.3b are displayed in Fig. 1.3c.

Even though we have been focused on spherical nanoparticles so far, nanoparticles of arbitrary shape can also sustain LSPPs, presenting qualitatively similar strongly enhanced and localized near-fields. However, all the plasmonic properties (resonance frequency, field enhancement, emission pattern, etc.) greatly depend on the characteristics of the nanoparticle, such as the shape, size and the material they are made of [80–83]. This great tunability of the plasmon properties allows for designing MNPs tailored for specific applications, and is a key reason behind the prominence of plasmonic nanoparticles in the field of nanophotonics.

Unfortunately, analytically solving Maxwell's equations is not viable in general for complex nanoparticle shapes, and numerical methods are required in such cases. Some of the most popular numerical methods for computing the classical electrodynamical response of metallic nanostructures are the Finite-Difference Time-Domain method [84] and the Finite-Element Method [85], which involve a discretization of Maxwell's equations in both time and space, or the Discrete-Dipole Approximation method [86], in which the system is described as being composed by an array of discrete elements responding as polarizable dipoles to the local electric field. Since these methods require the spatial discretization of the entire geometry, their computational cost scales with the volume of the system. In contrast, the Boundary Element Method (BEM) [87, 88] reformulates the solutions of Maxwell's equations in the presence of abrupt dielectric interfaces in terms of surface integrals involving surface charges and currents acting as sources of the induced electromagnetic field. This means that, instead of the whole volume, only the material interfaces need to be discretized, which allows for a better scaling with the size of the system.

1.2.5 Plasmons in metallic dimers

Designing individual nanoparticles is not the only way to engineer specific plasmonic properties. If two MNPs are placed in close proximity, their plasmonic modes hybridize due to the Coulomb interaction between them [89, 90], forming new modes in which the free electrons in both nanoparticles oscillate collectively, as illustrated in Fig. 1.4a. Crucially, the accumulation of charges at the facing surfaces across the gap leads to field enhancements much larger than those in an isolated nanoparticle [91–93], creating so-called electromagnetic "hot-spots".

On top of the versatility inherent to plasmonic nanoparticles, plasmonic dimers offer an additional degree of tunability, because both their LSPP resonance frequencies and field enhancements also depend on the surface-to-surface gap separation D. In Fig. 1.4b, we illustrate this dependency by plotting the absorption cross section $\sigma_{\text{abs}}(\omega)$ for a dimer of MNPs as the gap size D is varied in the $[1, 4]$ nanometer range. We consider the same sodium MNPs as in the previous section, and an incident electric field polarized along the dimer axis. The results presented in the figure are obtained with the MNPBEM [88] toolbox for the simulation of the optical response of metallic nanoparticles using the BEM approach. The main feature in the absorption spectra corresponds to the bonding dipolar plasmon (BDP), whose resonance frequency ω_{BDP} shifts from ~ 3.2 eV to ~ 2.7 eV as the gap narrows from 4 nm to 1 nm. The BDP is formed by the hybridization of the DPs of each nanoparticle, and its induced charge distribution, which is schematically depicted in Fig. 1.4a, is characterized by dipoles at each nanoparticle, with strong charge concentrations at the facing surfaces. In narrow gap geometries, it is also possible to excite the bonding quadrupolar plasmon (BQP) at ~ 3.5 eV, which can be understood as the hybridization of the DP of one MNP with the quadrupolar ($\ell = 2$) plasmon of the other one [90].

Figure 1.4c shows a map of the electric field enhancement $|\mathbf{E}^{\text{ind}}|/|\mathbf{E}^{\text{ext}}|$ in the

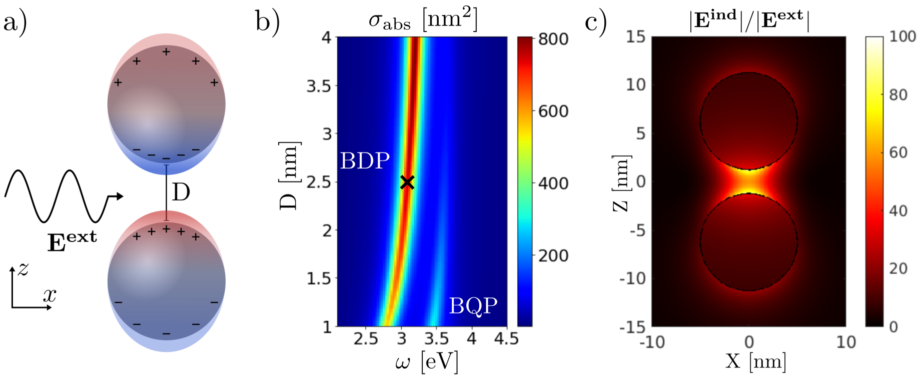

Figure 1.4: a) Schematic representation of the charge density induced on a dimer of MNPs by an incident plane wave polarized along the dimer axis at the frequency of the BDP mode. b) Absorption cross section $\sigma_{\mathrm{abs}}(\omega)$ of a dimer of two Na MNPs with radius $a = 5$ nm, characterized by a Drude-like dielectric function [Eq. (1.14)] with $\omega_{\mathrm{p}} = 5.89$ eV and $\gamma_{\mathrm{p}} = 0.21$ eV, as a function of the gap size D and the excitation energy. c) Map of the induced field enhancement $|\mathbf{E}^{\mathrm{ind}}|/|\mathbf{E}^{\mathrm{ext}}|$ in the $y = 0$ plane for the same dimer as in b), with D = 2.5 nm and at the BDP frequency $\omega_{\mathrm{BDP}} = 3.1$ eV, marked with a black cross in b).

cross section of the dimer plane ($y = 0$) for D = 2.5 nm at the BDP frequency $\omega_{\mathrm{BDP}} = 3.1$ eV. The induced fields are confined to the gap region, with field enhancement larger than that obtained for the single nanoparticle of Fig. 1.3b. It is possible to achieve even more dramatic field enhancements for narrower gaps. However, when gaps become too narrow, at around D ≤ 1 nm, the quantum nature of electrons starts to reverse this trend, as electron tunneling between the particles becomes possible. This decreases the accumulation of charges at the facing surfaces, which causes a quenching of the BDP resonance [10].

Furthermore, when electrons flow through the gap, another set of modes so-called charge-transfer plasmons (CTPs) can be activated. Direct physical contact is not strictly required for the emergence of CTPs, as long as electrons can move from one nanoparticle to the other, via electron tunneling [11, 12] as mentioned above, or through conductive molecular junctions [94, 95], as we will study in Chapter 3. Classical frameworks usually assume well-defined interfaces and electrons confined inside the MNPs, which prevents the excitation of these modes. One possible solution to capture this behavior is to effectively account for electron tunneling by placing an effective conductive material at the gap [96], introducing this quantum-mechanical effect within the classical electrodynamics framework. On the other hand, the real MNPs' interfaces are not sharp, unlike in the classical electrodynamics description, as there is a spill-out of the electronic charge density [18, 97]. Electronic spill-out is properly accounted for within a quantum mechanical description of the electron gas at the boundaries. This approach allows for naturally describing the electron tunneling, as the electronic clouds of both nanoparticles overlap when gap sizes are subnanometric, thus permitting the flow of charge before physical contact

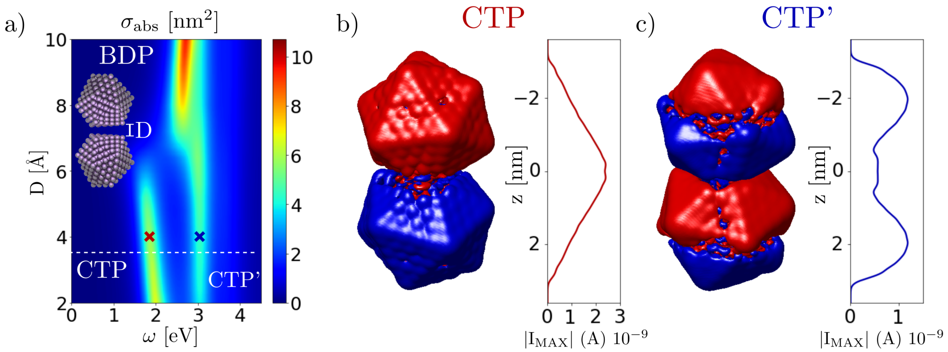

Figure 1.5: a) Absorption cross section $\sigma_{\mathrm{abs}}(\omega)$ as a function of the excitation energy ω and the gap size D, defined as the minimum distance between atoms of different MNPs, for a dimer of Na_{380} nanoparticles as depicted in the inset. The dashed line represents the point of contact between the MNPs, this is, when the gap size is equal to the atom–atom distance in the MNPs. b) Isosurface of the imaginary part of the induced charge density distribution for the CTP mode, for $\omega = 1.82$ eV and D = 4 nm, marked with a red cross in a). The corresponding modulus of the electron current flowing through a fixed-z plane is plotted to the right. c) Isosurface of the imaginary part of the induced charge density distribution for the CTP' mode, for $\omega = 3.02$ eV and D = 4 nm, marked with a blue cross in a), accompanied by the corresponding electron current plot.

occurs. On top of this, when such small characteristic sizes are considered, the real atomistic shape of the studied nanoparticles becomes very relevant [22, 27].

One way to account for all these effects and additional quantum phenomena is by using purely quantum-mechanical descriptions of the electron gas response, such as *ab initio* methods [98] as described in Sections 2.1 and 2.2. In order to illustrate the characteristics of CTPs in MNP dimers, we have computed the optical response of a dimer of Na_{380} nanoparticles with this methodology. In Fig. 1.5a, we show the absorption cross section $\sigma_{\mathrm{abs}}(\omega)$ for narrow gaps (0.2 nm $\leq$ D $\leq$ 1 nm), defined as the minimum distance between atoms of different MNPs. For D $\gtrsim$ 0.8 nm, the system follows the same trends as the classical response depicted in Fig. 1.4b, with a predominant BDP mode at around $\omega \approx 3.0$ eV red-shifting as the gap closes. At D $\approx$ 0.8 nm, however, the BDP resonance begins to quench due to the aforementioned electron tunneling, and already fades away for $D \approx 0.7$ nm. As the gap further closes, two distinct charge transfer modes emerge, one starting at $\omega \approx 1.7$ eV and blue-shifting to almost 2 eV, labeled CTP, and another one remaining at $\omega \approx 3$ eV, labeled CTP'.

The induced charge densities corresponding to these modes are depicted in Figs. 1.5b and 1.5c, together with the maximal induced electron currents. The CTP mode is characterized by a dipolar charge distribution across the whole dimer, with nonzero net charges of opposite sign at each nanoparticle. Since isolated MNPs are charge neutral, this indicates the flow of electrons through the gap, which is corroborated by the maximum of induced current being placed at the junction. In fact, it may be useful to understand the CTP as the dipolar mode of a single rod

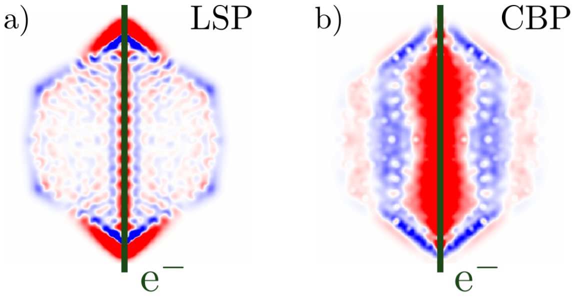

Figure 1.6: Induced charge density maps corresponding to (a) a localized surface plasmon (LSP) and (b) a confined bulk plasmon (CBP) excited by an electron beam penetrating an atomistic Na_{2057} nanoparticle, obtained within the *ab initio* framework described in Section 2.2. The dark green lines represent the electron trajectories.

[23]. The induced density of the CTP' mode resembles the BDP one, with dipolar charge distributions on each MNP, but the induced current plot shows significant values at the junction, which evidences the charge-transfer nature of the mode. Thus, it is possible to interpret the observed induced charge density as the second optically active mode of a single rod [99].

1.2.6 Confined Bulk Plasmons

Bounded metallic nanostructures can also sustain confined bulk plasmons (CBPs), resonant oscillations of the electron density inside the volume of the nanostructure above the plasma frequency [52]. These resonances are characterized by induced charge densities distributed through the entire nanoparticle volume, as observed in Fig. 1.6. In the canonical spherical MNP, they can be considered as stationary radial charge waves due to the interference between bulk plasmons that are bounced back at the spherical interface. These plasmons can be effectively excited by electron beams penetrating the MNPs in STEM-EELS, as we show in Chapter 4. CBPs were first observed experimentally in semi-infinite structures such as thin films made of Ag [56], K [100], and Mg [101], or in nanowires made of Bi [102] and Ge [103]. More recently, they have also been observed in several finite MNPs, including Bi nanoparticles [104, 105], and Al nanodisks [106]. CBPs emerge due to nonlocal effects caused by the spatial correlation of the induced charge density, which prevent the accumulation of the induced charge density and create propagating longitudinal pressure waves [107–109], and are therefore not captured by local dielectric response approaches.

However, these effects can be parametrically accounted for within hydrodynamic models of the charge density response, which describe the collective motion of the electron gas in terms of both the electron density $n(\mathbf{r}, t)$ and the hydrodynamical velocity $\mathbf{v}_{\mathrm{h}}(\mathbf{r}, t)$, enabling us to take into account the pressure of the electron gas. In general, within a linearized hydrodynamic model the collective motion of the electrons in an homogeneous medium with static density n_0 (in the absence of excitations) is governed by two expressions. The first is the continuity equation [58]

$$\frac{\partial}{\partial t}n(\mathbf{r},t)+n_0\nabla\cdot\mathbf{v}_\mathrm{h}(\mathbf{r},t)=0, \tag{1.32}$$

which ensures charge conservation, and the second is the relation [58]

$$n_0(\frac{\partial}{\partial t}+\gamma_\mathrm{h})\mathbf{v}_\mathrm{h}(\mathbf{r},t)=-n_0\frac{e}{m_\mathrm{e}}\mathbf{E}(\mathbf{r},t)-\beta_\mathrm{h}^2\nabla n(\mathbf{r},t), \tag{1.33}$$

where m_e is the electron mass, γ_h is a damping parameter, and $\beta_\mathrm{h}=\sqrt{3/5}v_F$ is the compressibility parameter, with $v_F=\pi\sqrt{3n_0}$ the Fermi velocity of the electrons. These models have been used to study CBPs in MNPs under both light and electron beam excitation [57, 58, 110], and in Chapter 4 we show an application of this approach to understand the symmetries of CBPs by computing the response of a spherical Na NP of hard boundaries. The linearized hydrodynamic model is applied in such case, as described in more detail in Appendix B. On the other hand, quantum *ab initio* approaches naturally include nonlocal effects, which makes them particularly suitable for describing this type of plasmonic excitations. In Chapter 4, we analyze the excitation of CBPs in small Na MNPs within both of these frameworks.

1.3 Excitations in molecules

Although we have only discussed the interaction of light with collective electronic excitations in metallic nanoparticles so far, electromagnetic fields can also couple to other types of matter excitations. In fact, the interaction of light with interband transitions in molecules and small nanoparticles plays a key role in many applications of nanophotonics. The small number of electrons of these systems means that their energy is quantized, and therefore their light emission and absorption properties are quantum in nature. As a consequence, molecules, together with other systems possessing discrete energy levels such as quantum dots and small metallic nanoparticles, are called quantum emitters (QEs). In Figs. 1.7a and 1.7b, we plot the electronic density of states (DOS) of an organic benzene molecule and a small Al_{13} cluster, respectively, which evidence the discrete nature of their electronic energy levels. In this section, we briefly describe the two main mechanisms governing the emission of light by such molecules and other QEs.

1.3.1 Electronic transitions

Quantum emitters are characterized by the existence of a finite number of electronic energy levels, which can be either occupied or unoccupied. By the action of an incident electromagnetic field, it is possible to promote an electron in an occupied state to an unoccupied one, followed by fast relaxation to the lowest excited states, and emission of a photon when the system relaxes back to its ground state in a

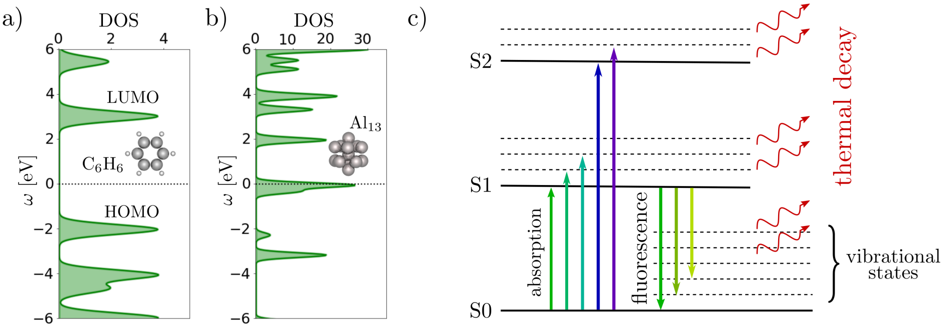

Figure 1.7: (a) Electronic density of states (DOS) of a benzene molecule as calculated with the *ab initio* SIESTA code [111]. The black dotted line marks the Fermi level. (b) DOS of an Al_{13} cluster. (c) Diagram of energy levels in a canonical molecule. The electronic energy levels are represented by solid lines, and the energies of the vibrational excitations as dashed lines. Arrows pointing upwards indicate absorption of an incident photon, and arrows pointing downwards indicate fluorescence. Non-radiative or thermal decay is indicated by wavy lines.

phenomenon known as fluorescence. Alternatively, the excited state can also relax by non-radiative thermal decay, in which case the excess energy is dissipated to the environment as heat. Since the promotion of an electron to an electronic excited state is extremely favored when the energy of the incident light matches the one of the excitation, this interaction has a markedly resonant character. In many cases, this allows us to model the excitation of a molecule by its lowest energy electronic transition, the one connecting the highest occupied molecular orbital (HOMO) and the lowest unoccupied molecular orbital (LUMO), which for organic molecules usually lays in the visible energy range.

Therefore, a typical approximation in nanophotonics is to treat the optical response of a QE as a two-level system. Within quantum mechanics, one can compute analytically the evolution in time of the population of each energy level for a two-level system excited by a harmonic electric field. Assuming that the interaction between the emitter and the incident light is weak, and that the decay rate of the emitter's excited state (represented by the damping term γ_{ex}) is small, the polarizability of a molecular QE is given by a Lorentzian function [62]

$$\alpha_{\text{QE}}(\omega) = \frac{2|\mu_t|^2}{\hbar} \frac{\omega_{\text{ex}}}{\omega_{\text{ex}}^2 - \omega^2 - i\omega\gamma_{\text{ex}}}, \tag{1.34}$$

where $\hbar$ is the reduced Planck constant, $\hbar\omega_{\text{ex}}$ is the resonance energy of the molecular excitonic transition, and μ_t is the electronic transition dipole moment of the emitter.

1.3.2 Vibrational transitions

On top of the electronic energy levels, molecules also sustain vibrational energy levels associated with the oscillations of their constituent atoms, with wavelengths typically in the infrared range. Within the Born–Oppenheimer approximation (see Section 2.1), the electronic and atomic wavefunctions can be separated, so that the corresponding electronic and vibrational energy levels can be superimposed as depicted in Fig. 1.7c, with the discrete set of electronic energy levels of molecules becoming a quasi-continuum of vibronic levels in practice. The presence of the vibrational energy levels has important consequences in the emission and absorption properties of molecules. Since it is possible to excite vibrational transitions, the absorption spectra of molecules will show several peaks in the infrared range, corresponding to the different vibrationally excited states. This allows for identifying and characterizing molecules with infrared spectroscopy [112]. Another widely used vibrational spectroscopy technique is Raman spectroscopy [113], which will be discussed is Section 1.5.

Additionally, vibrational energy levels also impact the optical emission and absorption properties of molecules. Besides from decaying to the vibrational ground state of the electronic many-particle ground state S0 (zero-phonon line), the electronic first-excited state S1 can also decay to any of the S0 vibronic states (Stokes lines), and later relax non-radiatively to the ground state. Therefore, the emission spectrum will consist on a sum of Lorentzians corresponding to the different decay pathways, though the line broadening due to dephasing makes observing these transitions separately difficult at room temperature. The probability associated to each decay process is given by the Frank–Condon factors [114], which are the overlap integrals of the respective S0 vibrational state wavefunctions with the S1 vibrational ground-state wavefunction. As a consequence, the emission spectrum of molecules is usually red-shifted with respect to their absorption spectrum, which is known as the Stokes shift [115].

1.4 Coupling between plasmons and molecular excitations

The properties of a quantum emitter can be modified in the presence of the strong electromagnetic fields generated in the proximity of a plasmonic nanocavity, as depicted in Figs. 1.8a and 1.8b. Due to electromagnetic interaction, the plasmonic modes of the nanocavity couple to the electronic excitations of the emitter, usually known as excitons [116]. In the strong-coupling regime, this is, when the strength of the coupling exceeds the losses of both the cavity mode and the exciton, this interaction gives rise to hybrid light–matter states so-called plasmon–exciton polaritons, with inseparable light and matter properties [28], as schematically depicted in Fig. 1.8b. These hybrid states show new and tunable energy levels and can thus be used to modify the chemical properties of matter [29, 30], which has led to interesting applications in photochemistry [31–33], single-photon emission

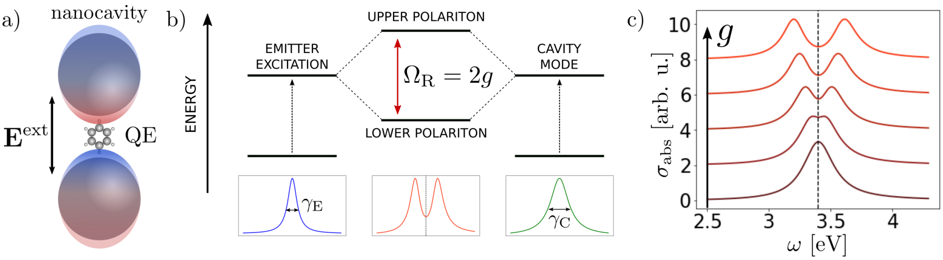

Figure 1.8: a) Sketch of a quantum emitter inside an optical nanocavity. b) Sketch of the energy level splitting in strong coupling. The modes of an emitter and a cavity with damping rates γ_{ex} and γ_{pl}, couple forming two hybrid states, so-called polaritons. The energy splitting between the hybrid states is proportional to the coupling strength g, related to the Rabi splitting as $\Omega = 2g$, and comparable to the losses of the original states. b) Absorption spectrum of a molecule coupled to a plasmonic mode, characterized as two coupled harmonic oscillators according to Eq. (1.37) for increasing coupling strength values.

[34], electroluminiscence [35], and exciton transport [36], among others. Due to the extreme field enhancement and localization associated to plasmonic nanocavities, these are a key configuration in the race for achieving the plasmon–exciton strong-coupling regime [117–119]. This phenomenon will be the main focus of Chapter 3, where we study how the geometry of a metallic nanocavity affects the strength of the coupling with a molecule placed in it.

One simple way of phenomenologically modeling the coupled system is to describe the excited states of both the emitter and the plasmonic nanocavity as two harmonic oscillators [120, 121] with resonance frequencies $\omega_{\mathrm{ex}}, \omega_{\mathrm{pl}}$, intrinsic decay rates $\gamma_{\mathrm{ex}}, \gamma_{\mathrm{pl}}$ and oscillator strengths $\alpha^0_{\mathrm{ex}}, \alpha^0_{\mathrm{pl}}$, respectively. These oscillators then couple together through the electric near-field, with a coupling strength dependent on the position of the emitter inside the cavity [122]

$$g(\mathbf{r}) = \mu_t \, \frac{|\mathbf{E}^{\mathrm{ind}}|(\mathbf{r})}{\hbar \, \max(|\mathbf{E}^{\mathrm{ind}}|(\mathbf{r}))} \sqrt{\frac{\hbar\omega_{\mathrm{pl}}}{2\varepsilon_0 V_{\mathrm{e}}}}, \tag{1.35}$$

where $\mathbf{E}^{\mathrm{ind}}(\mathbf{r})$ is the electric field induced inside the cavity, V_{e} is the effective volume of the optical mode, defined as

$$V_{\mathrm{e}} = \frac{\int |\mathbf{E}^{\mathrm{ind}}|^2(\mathbf{r}) dV}{\max\ (|\mathbf{E}^{\mathrm{ind}}|(\mathbf{r}))^2}, \tag{1.36}$$

where the integral runs over the volume of the cavity, and μ_t is the transition dipole moment of the emitter. Considering that the excitation of the emitter is dominated by the near-field generated by the cavity, and that $\alpha^0_{\mathrm{ex}} \ll \alpha^0_{\mathrm{pl}}$, the polarizability of the coupled system in the frequency domain, $\alpha_{\mathrm{hyb}}(\omega)$, can be approximated as

[120, 121]:

$$\alpha_{\text{hyb}}(\omega) \approx \alpha_{\text{pl}}^{0} \frac{\omega_{\text{ex}}^2 - \omega^2 - i\omega\gamma_{\text{ex}}}{(\omega_{\text{pl}}^2 - \omega^2 - i\omega\gamma_{\text{pl}})(\omega_{\text{ex}}^2 - \omega^2 - i\omega\gamma_{\text{ex}}) - 4g^2\omega^2}. \tag{1.37}$$

In Fig. 1.8c, we plot the absorption spectrum $\sigma_{\text{abs}}(\omega)$ of such as system, characterized as two coupled harmonic oscillators for increasing values of the coupling strength g. As it can be observed, for small g values the spectrum is indistinguishable from the spectrum of the bare cavity, whereas for larger g values two distinct modes emerge, corresponding to an upper and lower polariton whose energy splitting increases with g. By fitting the theoretical or experimental polarizability of a system to the approximated result in Eq. (1.37), one can estimate the value of the coupling strength g for the system. This allows for identifying whether the system is in the strong-coupling regime by applying one of the several criteria defining this regime [28]. In this thesis, we will use the criterion:

$$g > |\gamma_{\text{ex}} + \gamma_{\text{pl}}|/4 \tag{1.38}$$

as the threshold for strong coupling. Though the coupled harmonic oscillator model is quite limited, as it does not take into account the effect of higher-order cavity modes or the spatial extension of the emitter, it is very useful for the interpretation of results, providing valuable physical insights, and is therefore widely used for characterizing plasmon–exciton coupling in different nanosystems [121, 123–125]. We will adopt this model to interpret our *ab initio* results in Chapter 3, for instance.

1.5 Surface-Enhanced Raman Spectroscopy

We describe here one of the most widespread molecular spectroscopy techniques, Raman spectroscopy, which allows for identifying molecules and materials via the inelastic excitation of vibrational modes, setting a unique vibrational fingerprint map. In the 1920s, C. V. Raman demonstrated the inelastic scattering process by which molecules can be excited to virtual states by absorbing an incident photon, and then relax back emitting photons of different energy, as sketched in Fig. 1.9a. Since then, Raman spectroscopy has been successfully applied to fields as diverse as nanotechnology [126], pharmaceutics and medicine [127, 128], archaeology [129], chemistry [130], and many others [131].

Figures 1.9a and 1.9b display a sketch of the Raman scattering process. An incident photon of energy $h\nu_i$ excites a molecule from its vibrational ground state with energy E_0 to a virtual state. Usually, this leads to an elastic scattering process in which the virtual state decays back into the ground state, emitting a photon of the same energy $h\nu_i$, which is known as Rayleigh scattering. In some cases, however, the virtual state may decay into an excited vibrational state with energy $E_0 + h\nu_n$ instead, where the index n denotes the vibrational state of energy ν_n, which results in the emitted photon having a smaller energy $h(\nu_i - \nu_n)$. This process is known as Stokes (S) scattering. The inverse process, in which a molecule initially in a

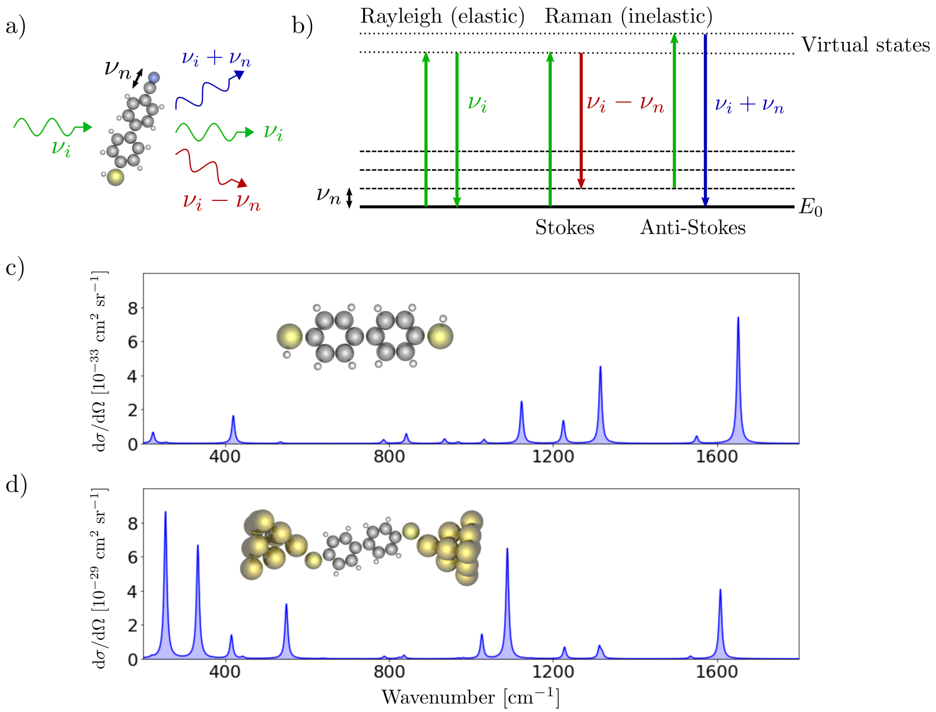

Figure 1.9: a) Schematics of light scattering by a molecule possessing a vibrational state with energy $h\nu_n$. After absorbing a photon with energy $h\nu_i$, the molecule can emit another photon with the same energy (Rayleigh scattering), a red-shifted photon with energy $h(\nu_i - \nu_n)$ (Stokes Raman scattering), or a blue-shifted photon with energy $h(\nu_i + \nu_n)$ (anti-Stokes Raman scattering). b) Diagram of the energy levels involved in the Rayleigh (left), Raman Stokes (center), and Raman anti-Stokes (right) scattering processes. c) Raman spectrum of a bare biphenyl-4,4'-dithiol (BPDT) molecule, obtained with the Gaussian16 [132] code by R. Álvarez-Boto [133]. The geometry of the molecule is displayed in the inset. d) Raman spectrum of a BPDT molecule sandwiched between two Au_{10} clusters [133], as displayed in the inset. Notice that the signal is enhanced by a factor of almost 10^4 with respect to c), and that the relative intensity of the modes changes.

vibrational excited state with energy $E_0 + h\nu_n$ is excited to a virtual state, later to decay to the ground state emitting a photon of energy $h(\nu_i + \nu_n)$, is known as anti-Stokes (aS) scattering. Since anti-Stokes scattering requires the molecule to already be in an excited state, it cannot happen at zero temperature, where there is no population of vibrational states, and even at room temperature Stokes scattering is usually dominant. The anti-Stokes scattering, however, provides very valuable information, as it allows for deducing molecular temperatures by measuring the Raman signal for several peaks and taking the anti-Stokes to Stokes ratio [134]:

$$\rho_n^{aS/S} = \frac{d\sigma_n^{aS}/d\Omega}{d\sigma_n^{S}/d\Omega} = \left(\frac{\nu_i + \nu_n}{\nu_i - \nu_n}\right)^4 e^{-\frac{h\nu_n}{k_B T}}, \tag{1.39}$$

where $\mathrm{d}\sigma_n^{(a)S}/\mathrm{d}\Omega$ is the (anti-)Stokes differential scattering cross-section of vibrational mode n, k_B is the Boltzmann constant, and T is the temperature.

When a molecule is illuminated by a monochromatic light source, the scattered light can also show emission at extra wavelengths in addition to the incident one, with each of the new wavelengths corresponding to a Raman scattering process of a different vibrational mode. Thus, the resulting spectrum contains information regarding the vibrational modes of the molecule, and can be considered as a vibrational fingerprint which allows for precisely identifying molecules. Furthermore, if one knows the energy of common chemical bonds and functional groups as they appear in the Raman spectrum, it is also possible to reconstruct the chemical structure of an unknown molecule [135].

Even though Raman spectroscopy has the advantages of being quantitatively precise, non-disruptive and label-free [136], its applications are limited by the low efficiency of Raman processes, as typical Raman cross-section values (this is, the area over which the incident photons are effectively converted into emitted Raman photons) are in the 10^{-11}–10^{-15} nm^2 range [3]. One way to overcome this drawback is by using the field enhancement provided by plasmonic nanostructures, acting on the molecules. Since the intensity of the Raman process scales with the 4th power of the local field at the position of the molecule [3], placing the molecule at hot-spots created by plasmonic nanoparticles dramatically increases the Raman signal by factors up to 10^8 or even larger, which allows for detection of even single molecules [37, 38]. This technique, so-called Surface-Enhanced Raman Spectroscopy (SERS), has grown steadily since its discovery in 1974 [137], driven by a myriad of promising applications in biomedicine [40, 138, 139], environmental monitoring [39, 140, 141], and other fields, and enabling the design of nanoarchitectures tailored for enhancing the Raman signal in specific situations [142–145]. On top of the electromagnetic enhancement driven by the electromagnetic field, a chemical enhancement factor is also present when molecules are bound to metallic surfaces. The chemical enhancement contribution is often hard to separate from the electromagnetic one, particularly for small clusters [133]. As an example of how even small MNPs can dramatically enhance chemically and electromagnetically the Raman signal, we plot in Figs. 1.9c and 1.9d the differential Raman cross sections for a bare biphenyl–4,4'–dithiol molecule and for the same molecule sandwiched between two Au_{10} clusters, which shows an enhancement factor of almost 10^4. Chapter 5 of this thesis is focused on vibrational spectroscopy of self-assembled monolayers (SAMs) on metallic surfaces, one of the most popular SERS configurations, with the aim of evaluating the effect of inter-molecule interactions in the Raman signal.

1.6 Electron Energy-Loss Spectroscopy

This thesis explores collective excitations and molecular driven by light as well as by fast electrons. Indeed, one way to overcome the limits of imaging resolution imposed by light diffraction consists in using fast electrons as probes instead of light, as the effective de Broglie wavelength of these fast electrons is small. Since E.

Ruska and M. Knoll designed the first transmission electron microscope in 1931 [146], enabling an improvement of the resolution by a factor of 1000 as compared to optical microscopes, technological improvements have allowed for developing electron microscopy devices capable of producing tightly focused electron beams and generating precise images by raster scanning a sample. This is possible by using scattered electrons originated from the interaction of the electrons with the sample, or by using the transmitted electrons themselves, collected using a series of detectors and correlated with the well-controlled position of the electron beam. Thanks to aberration correction techniques [147, 148], it is possible for state-of-the-art scanning transmission electron microscopes to resolve single atoms and even achieve sub-Å resolution [46, 149].

When electrons pass through a sample, they interact with its constituent atoms via electromagnetic forces, losing some energy and/or momentum in the process [Fig. 1.10a]. As a result, they can be scattered elastically, due to interaction with the atomic nuclei, or inelastically, when the beam electrons interact with the electrons in the sample activating single-electron or collective excitations [150]. Thus, the spectrum of electron energy-loss (EEL) probability contains information about matter excitations on a very broad energy range, from vibrational modes at the meV range [151] to outer electronic transitions and nanoparticle plasmons at the few eVs range [152, 153], and even to core losses caused by the excitation of electrons in the inner atomic shells at hundreds or thousands of eVs [154, 155]. Since in the 50s and 60s Electron Energy-Loss Spectroscopy (EELS) experiments with broad electron beams led to the identification of bulk plasmons [156] and SPPs [157], technical advancements have greatly improved the capability of EELS enabling spatial resolutions in the sub-Å range [46, 47] and sub-eV energy sensitivity [48, 49]. This has opened the door for great advancements in materials science and nanoscience, allowing for material characterization [149, 158], vibrational spectroscopy with nanometric resolution of phonons [159–161] or non-destructive identification of biomaterials [162, 163]. EELS is also widely used for analyzing single nanoparticles of sizes under 10 nm [53–55, 164, 165].

Fast electrons offer additional advantages that make them an excellent tool for studying plasmonic nanoparticles. Since electrons traveling through vacuum are sources of evanescent electromagnetic radiation, they are capable of directly exciting SPPs on metal–vacuum interfaces [166]. Furthermore, some of the plasmonic modes supported by MNPs, the so-called "dark" plasmons, not easily accessible with conventional light spectroscopy, can be excited by the evanescent fields generated by an electron beam [50, 51]. In fact, electron beams can excite different resonances according to their trajectory, as observed in Fig. 1.10b, where we plot the EEL probability spectra of a sodium spherical nanoparticle with radius $a = 2$ nm, for both central (in blue) and aloof (in red) electron trajectories at 100 keV. We model the nanoparticle's response with the same Drude dielectric function as in Fig. 1.3. Similarly to the optical absorption spectrum plotted in Fig. 1.3c, the aloof trajectory spectrum shows a resonance at $\omega \sim 3.4$ eV, which corresponds to the dipolar ($\ell = 1$) LSPP. The central trajectory spectrum, however, shows a significantly blue-shifted peak corresponding to the quadrupolar ($\ell = 2$) LSPP.

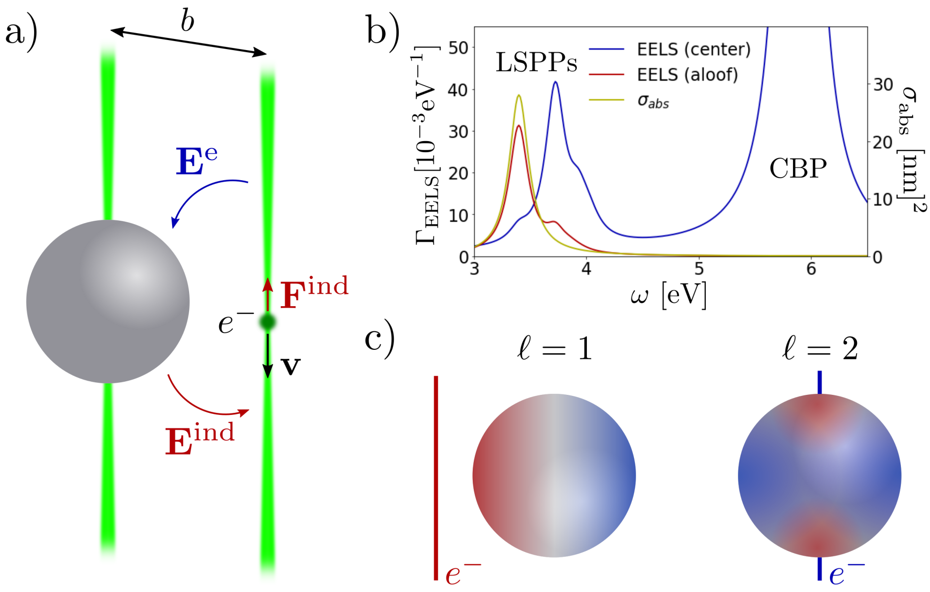

Figure 1.10: a) Sketch of an electron beam interacting with a MNP. The electric field generated by the electron $\mathbf{E}^{\mathrm{e}}$ acts on the nanoparticle, inducing a field $\mathbf{E}^{\mathrm{ind}}$ acting back on the electron and exerting a stopping force $\mathrm{F}^{\mathrm{ind}}$. b) EEL probability spectra for a sodium spherical nanoparticle with radius $a = 2$ nm, for impact parameters $b = 0$ nm (center, in blue) and $b = 3$ nm (aloof, in red). The spectra were computed with the MNPBEM [88] software, using a beam of electrons with 100 keV kinetic energy and modeling the nanoparticle's response as a Drude metal using the same parameters as in Fig. 1.3c. For comparison, we also show the optical absorption cross section $\sigma_{\mathrm{abs}}(\omega)$ in yellow. c) Sketches of the induced charge density distributions at the nanoparticle surface for the dipolar ($\ell = 1$) and quadrupolar ($\ell = 2$) LSPPs. The electron beam trajectories exciting each mode are depicted with the corresponding colors as used for the spectra in b).

Thus, electrons traveling outside and far away from the nanoparticle behave as plane-waves, exciting modes with dipolar character, whereas electrons transversing the nanoparticle may excite resonances with a different symmetry. Though there are ways to access these modes in optical spectroscopy too, such as changing the polarization of the light probe [167] or exploiting retardation effects emerging in large nanoparticles [168], fast electrons remain one of the most efficient ways to characterize the near-field of metallic nanoparticles. Additionally, fast electrons with penetrating trajectories can also excite CBPs in metallic nanoparticles, whose coupling with light is usually negligible [52, 57, 169]. This can be appreciated in Fig. 1.10b, where these modes appear in the high-energy part of the EEL spectrum for the central electron beam trajectory, but not for the aloof one.

The electrons in the beam may be approximated as point-like charges moving in vacuum with a constant velocity $\mathbf{v}$, which act on the nanoparticle inducing charge oscillations and currents generating an induced electromagnetic field acting back on the probing electron. Within the framework of classical electrodynamics, the induced fields exert a Lorentz force on the electron, $\mathrm{F}^{\mathrm{ind}}$, as sketched in Fig. 1.10a, causing the electron to lose some of its initial energy. The total energy loss can then be evaluated by integrating this force along the electron trajectory. Since probing electrons are usually highly energetic, we can neglect the component of the force perpendicular to the trajectory, which results in the following expression for the energy loss experienced by the electron [157]:

$$\mathrm{W} = e \int_{-\infty}^{\infty} \mathbf{v} \cdot \mathbf{E}^{\mathrm{ind}}[\mathbf{r_e}(t); t] \; dt, \tag{1.40}$$

where $\mathbf{r_e}(t)$ is the position of the probing electron, and $\mathbf{E}^{\mathrm{ind}}[\mathbf{r_e}(t); t]$ is the induced field. After taking the Fourier transform of the induced field, we obtain the expression for the total energy loss in the frequency domain:

$$\mathrm{W} = \int_{0}^{\infty} \hbar\omega \; \Gamma_{\mathrm{EELS}}(\omega) \; d\omega, \tag{1.41}$$

where $\Gamma_{\mathrm{EELS}}(\omega)$ is the energy loss probability per energy unit, interpreted as the probability for the probing electron to lose an amount of energy $\hbar\omega$ [170]:

$$\Gamma_{\mathrm{EELS}}(\omega) = \frac{e}{\pi\hbar\omega} \int_{-\infty}^{\infty} \mathrm{Re}\{\mathbf{v} \cdot \mathbf{E}^{\mathrm{ind}}[\mathbf{r_e}(t); t] e^{-i\omega t}\} \; dt. \tag{1.42}$$

The energy loss probability for an electron traveling through an infinite bulk metal can be computed classically by inserting the electric field induced by the electron in Eq. (1.42). In the nonretarded limit, and in the local approximation, the energy loss probability is proportional to $\mathrm{Im}\{-\frac{1}{\varepsilon(\omega)}\}$ [170]. Considering a Drude-like dielectric function to describe the response of the sample material [Eq. (1.14)], the energy-loss probability becomes:

$$\Gamma_{\mathrm{EELS}}(\omega) \propto \frac{2\gamma_{\mathrm{p}}\omega\omega_{\mathrm{p}}^2}{(\omega_{\mathrm{p}}^2 - \omega^2)^2 + 4\omega^2\gamma_{\mathrm{p}}^2}, \tag{1.43}$$

which corresponds to a Lorentzian peak at the plasma frequency ω_{p}. Thus pronounced energy losses at the plasma frequency are expected for electrons traveling through a metal, as depicted in Fig. 1.10b for a sodium nanoparticle. In the presence of boundaries, such as in the case of finite nanoparticles, the bulk energy loss probability must be corrected due to the emergence of the *begrenzung* or boundary-effect [157, 171], and surface losses appear as the excitation of surface modes becomes possible [172]. The potential of EELS as a spectroscopy technique is showcased in Chapter 4, where we analyze the complex plasmonic response of sodium nanoparticles excited by penetrating and aloof electron beams within the atomistic *ab initio* framework.

CHAPTER 2

THEORETICAL METHODS

In the previous chapter, we described the interaction between light and nanostructures within the classical electrodynamics framework, which is usually accurate enough when the characteristic dimensions of the studied systems are relatively large. However, the advances in fabrication technologies have enabled the continuous miniaturization of nanophotonic devices, reaching even the single-molecule limit [9]. When the characteristic dimensions of the system are in the order of a few nanometers, the wave nature of the electrons leads to the emergence of quantum phenomena such as nonlocal effects and tunneling, which require a proper quantum-mechanical description of the optical response. In principle, this requires solving the many-electron Schrödinger equation, but this rapidly becomes computationally unfeasible for systems with more than a few electrons. Therefore, alternative formalisms are required to tackle such a complex problem. In this chapter, we outline the quantum methodologies we employed throughout this thesis for studying the response of the considered nanostructures.

We focus on one of the most extended quantum mechanical frameworks, the density-functional theory (DFT), which simplifies the many-body electronic problem by deriving all the relevant ground-state quantities from the ground-state electronic density instead of from the many-electron wavefunction. Furthermore, its time-dependent extension also allows for computing the response of the system to an external perturbation potential, such as that due to an incident electromagnetic plane wave or an electron beam. Since, in principle, this theoretical framework allows for modeling a system of arbitrary chemical composition with no empirical input, it is usually deemed as *ab initio*. The use of *ab initio* methods to describe the optical response of metals and molecules at the nanoscale is the main focus of this chapter. We start by explaining the fundamentals of DFT and the self-consistent method used to compute the ground-state electron density in Section 2.1. In Section

2.2, we then present the linear-response time-dependent density-functional theory (TDDFT) formalism, and in particular the method implemented in the Python Numerical Atomic Orbitals (PyNAO) code [98], which we use in Chapters 3 and 4 to compute the optical and EEL spectra of plasmonic systems. In Section 2.3, we extend the quantum formalism to a periodic infinite system, in which valence electrons can interact with the lattice vibrations or phonons. We then introduce the methodology employed for computing the Raman spectra of self-assembled monolayers in Chapter 5, which treats the electron–phonon and electron–light interactions within perturbation theory.

Though *ab initio* methods allow for precisely computing the energies of metallic nanoparticles and molecules in individual configurations, finding the ground-state configuration of complex nanostructures requires minimizing their potential energy surface (PES). In some cases, this can be a very complicated problem, especially when there are many degrees of freedom involved, such as for molecular adsorbates on a metallic surface. Since the computational cost of obtaining the DFT energies is still considerable, extensively sampling the PES sometimes becomes unfeasible. This has led to the proposal of efficient structure optimization schemes like the building-block based Bayesian optimization procedure implemented in the Bayesian Optimization Structure Search (BOSS) [173] code, which we use in Chapter 5 for finding the ground-state configuration of self-assembled monolayers (SAMs). In Section 2.4 we give an overview of the Bayesian optimization formalism on which BOSS is based, together with a short example to illustrate the use of BOSS in a simple physical problem.

2.1 Fundamentals of Density Functional Theory

In this section, we introduce the quantum-mechanical DFT framework for efficiently computing the ground-state properties of a many-electron system. All the equations presented in this section and in Section 2.2 are written in atomic units ($\hbar = m_e = e = 4\pi\varepsilon_0 = 1$, see Appendix A).

2.1.1 The Born–Oppenheimer approximation

Within quantum mechanics, a system composed of M nuclei at positions $\mathbf{R}_I$ ($I = 1, \ldots, \mathrm{M}$) and N electrons at positions $\mathbf{r}_i$ ($i = 1, \ldots, \mathrm{N}$) can be described by its wavefunction $\psi(\mathbf{r}_1, \mathbf{r}_2, \ldots, \mathbf{r}_\mathrm{N}, \mathbf{R}_1, \mathbf{R}_2, \ldots, \mathbf{R}_\mathrm{M}; t)$, which represents the “probability amplitude” of finding the system in the configuration $(\mathbf{r}_1, \mathbf{r}_2, \ldots, \mathbf{r}_\mathrm{N}, \mathbf{R}_1, \mathbf{R}_2, \ldots, \mathbf{R}_\mathrm{M})$ at time t. If there are no external time-dependent perturbations, the wavefunction can be factorized into a time-dependent phase and a time-independent probability amplitude $\psi(\mathbf{r}_1, \mathbf{r}_2, \ldots, \mathbf{r}_\mathrm{N}, \mathbf{R}_1, \mathbf{R}_2, \ldots, \mathbf{R}_\mathrm{M})$ obeying the eigenvalue equation [174]

$$\hat{H}\psi = E\psi, \tag{2.1}$$

where E denotes the system eigenenergy, and $\hat{H}$ is the Schrödinger Hamiltonian operator, which reads

$$\begin{aligned}\hat{H} = &-\sum_i \frac{\nabla_i^2}{2} - \sum_I \frac{\nabla_I^2}{2M_I} + \frac{1}{2}\sum_i \sum_{j\neq i} \frac{1}{|\mathbf{r}_i - \mathbf{r}_j|} \\ &-\sum_i \sum_I \frac{Z_I}{|\mathbf{r}_i - \mathbf{R}_I|} + \frac{1}{2}\sum_I \sum_{J\neq I} \frac{Z_I Z_J}{|\mathbf{R}_I - \mathbf{R}_J|},\end{aligned} \tag{2.2}$$

with the capital indices running over the M nuclei and the small ones over the N electrons, and Z_I and M_I are the atomic number and mass of nucleus I, respectively. The first and second terms in the Hamiltonian in Eq. (2.2) stand for the kinetic energies of electrons and nuclei, respectively, and the following terms correspond to the Coulomb interactions between all pairs of bodies. Unfortunately, the complexity of diagonalizing the multi-dimensional wavefunction in Eq. (2.1) grows exponentially with the number of particles, turning the problem numerically unfeasible, and requiring the use of approximations.

A typical starting approximation, which was first devised by M. Born and B. Oppenheimer [175], is to separate the electronic and nuclear variables, taking advantage of the atomic nuclei being at least three orders of magnitude heavier than the electrons. Due to the larger masses of the nuclei, $M_I \gg m_e$, the time scale of their dynamics is much longer, which allows us to treat the nuclei as point-like particles according to classical mechanics, and consider their effect as an external potential $V_{\text{ext}}(\mathbf{r}_i)$ for the electrons. The electronic wavefunction $\psi(\mathbf{r}_1, \mathbf{r}_2, \ldots, \mathbf{r}_{\text{N}})$ then obeys the Schrödinger Eq. (2.1) with the Hamiltonian

$$\hat{H} = \sum_i^{\text{N}} \left(-\frac{\nabla_i^2}{2} + \frac{1}{2}\sum_{j\neq i}^{\text{N}} \frac{1}{|\mathbf{r}_i - \mathbf{r}_j|} + V_{\text{ext}}(\mathbf{r}_i) \right). \tag{2.3}$$

However, the computation of the electronic wavefunction still remains a daunting challenge due to the presence of the electron–electron interaction term, and further approximations are required in order to make the numerical solution of Eq. (2.3) affordable.

2.1.2 Hohenberg–Kohn theorem and Kohn–Sham equations

The DFT framework offers a way of avoiding the exponential scaling of the N-electron problem by describing the system in terms of the 3-dimensional electron density $n(\mathbf{r})$, which is defined from the wavefunction as:

$$n(\mathbf{r}) = \text{N} \int d\mathbf{r}_2 \int d\mathbf{r}_3 \ldots \int d\mathbf{r}_{\text{N}} |\psi(\mathbf{r}, \mathbf{r}_2, \ldots, \mathbf{r}_{\text{N}})|^2, \tag{2.4}$$

normalized to the number of electrons in the system N. This is made possible by the Hohenberg–Kohn theorem [176] drawing a one-to-one correspondence between the external potential $V_{\text{ext}}(\mathbf{r})$ perturbing an electronic system and its ground-state electron density (up to an arbitrary additive constant). The external potential in turn completely determines the Hamiltonian and thus all the ground-state properties of the many-electron system, such as its ground-state energy. Therefore, all ground-state properties are functionals of the electron density, even the ground-state energy itself, which can be expressed as:

$$E[n] = F[n] + \int d\mathbf{r}\ V_{\text{ext}}(\mathbf{r})\ n(\mathbf{r}), \tag{2.5}$$

where the second term accounts for the interaction between the electrons and the external potential, and $F[n]$ is an universal functional of the density, which accounts for all the interactions between electrons and their kinetic energy. If the universal functional were known, it would be possible to compute the ground-state energy E_0 by minimizing $E[n]$ with respect to the electron density $n(\mathbf{r})$, according to the variational principle. Thus, by allowing us to deal with the electron density as a fundamental quantity instead of with the many-body wavefunction, the Hohenberg–Kohn theorem radically alters the nature of the problem. Unfortunately, while the above formalism is in principle exact, there is no general known expression for the universal functional $F[n]$, and DFT becomes an approximation in practice.

Kohn and Sham [177] further pushed the efficiency of this framework by introducing an auxiliary system of noninteracting electrons with identical density $n(\mathbf{r})$ and postulating that the universal functional $F[n]$ can be decomposed into separate functionals:

$$F[n] = T_{\text{s}}[\phi] + E_{\text{H}}[n] + E_{\text{xc}}[n]. \tag{2.6}$$

The first term represents the kinetic energy of an auxiliary system of noninteracting electrons with density $n(\mathbf{r})$, and the second term is the Hartree energy functional accounting for the classical electrostatic repulsion

$$E_{\text{H}}[n] = \frac{1}{2} \iint d\mathbf{r}\ d\mathbf{r}'\ \frac{n(\mathbf{r})\ n(\mathbf{r}')}{|\mathbf{r} - \mathbf{r}'|}. \tag{2.7}$$

The third term is the exchange–correlation energy functional encompassing all the remaining many-body interactions (such as the Pauli repulsion). The introduction of this auxiliary system allows us to reformulate the variational property of $F[n]$ as a minimization with respect the single-particle Kohn–Sham (KS) wavefunctions $\phi_i(\mathbf{r})$, which form a set of orthonormal orbitals. Conveniently, the kinetic energy of the noninteracting system is directly defined as a functional of the occupied KS wavefunctions:

$$T_{\text{s}}[\phi] = \sum_{i \in occ} \int d\mathbf{r}\ \phi_i^*(\mathbf{r})\ \hat{T}\ \phi_i(\mathbf{r}), \tag{2.8}$$

where $\hat{T} = -\frac{1}{2}\nabla^2$ is the kinetic energy operator, and the density can also be expressed in terms of the occupied wavefunctions $\phi_i(\mathbf{r})$ as

$$n(\mathbf{r}) = \sum_{i \in occ} |\phi_i(\mathbf{r})|^2. \tag{2.9}$$

Introducing these expressions into Eq. (2.5) we obtain a redefinition of the total energy as a functional of the KS orbitals:

$$E[\boldsymbol{\phi}] = \sum_{i=1}^{N} \int d\mathbf{r}\ \phi_i^*(\mathbf{r}) \left(-\frac{1}{2}\nabla^2 + V_{\text{ext}}(\mathbf{r}) \right) \phi_i(\mathbf{r}) +\ E_{\text{xc}}[n]\ +\ E_{\text{H}}[n]. \tag{2.10}$$

By minimizing this total energy functional using the variational principle [178] we arrive at the Kohn–Sham equations

$$\left(-\frac{1}{2}\nabla^2 + V_{\text{ext}}(\mathbf{r}) + \frac{\delta E_{\text{H}}[n]}{\delta n(\mathbf{r})} + \frac{\delta E_{\text{xc}}[n]}{\delta n(\mathbf{r})} \right) \phi_i(\mathbf{r}) = \epsilon_i \phi_i(\mathbf{r}) \tag{2.11a}$$

$$\hat{H}_{\text{KS}}(\mathbf{r})\phi_i(\mathbf{r}) = \epsilon_i \phi_i(\mathbf{r}). \tag{2.11b}$$

where $\phi_i(\mathbf{r})$ and ϵ_i are the single-particle Kohn–Sham wavefunctions and eigenenergies respectively. This means that the ground-state density $n(\mathbf{r})$ of a system of interacting electrons can be computed by solving the Schrödinger equation for an auxiliary system of noninteracting electrons described by the effective Hamiltonian

$$\hat{H}_{\text{KS}}(\mathbf{r}) = \hat{T} + V_{\text{eff}}(\mathbf{r}), \tag{2.12}$$

where the effective potential experienced by the independent electrons $V_{\text{eff}}(\mathbf{r})$ is

$$V_{\text{eff}}(\mathbf{r}) = V_{\text{ext}}(\mathbf{r}) + V_{\text{H}}(\mathbf{r}) + V_{\text{xc}}(\mathbf{r}) = V_{\text{ext}}(\mathbf{r}) + V_{\text{Hxc}}(\mathbf{r}). \tag{2.13}$$

The terms in the expression account for the external potential, the Hartree potential due to the electron–electron Coulomb interaction in the single-electron picture,

$$V_{\text{H}}(\mathbf{r}) = \int d\mathbf{r}'\ \frac{n(\mathbf{r}')}{|\mathbf{r} - \mathbf{r}'|}, \tag{2.14}$$

and the exchange–correlation potential defined as the functional derivative of the exchange–correlation energy

$$V_{\text{xc}}(\mathbf{r}) = \frac{\delta E_{\text{xc}}[n]}{\delta n(\mathbf{r})}, \tag{2.15}$$

which accounts for the interactions present in the many-body system but not in the noninteracting auxiliary system.

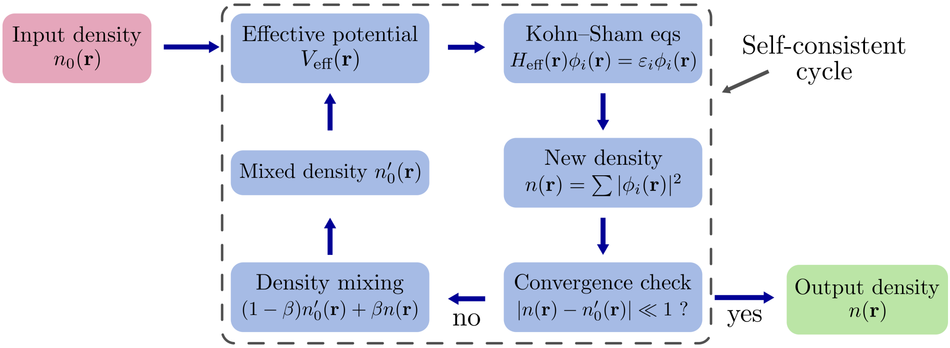

Figure 2.1: Schematic representation of the self-consistent DFT loop to obtain the ground-state density $n(\mathbf{r})$ of a system. Starting from an initial guess for the ground-state density $n_0(\mathbf{r})$, we compute the effective potential $V_{\text{eff}}(\mathbf{r})$ in Eq. (2.13). We then insert this potential into the KS equations Eq. (2.11b), which return a ground-state density $n(\mathbf{r})$. Then we compare this density to the one used for computing $V_{\text{eff}}(\mathbf{r})$. If they are similar enough to satisfy our convergence criteria, the process finishes and we can use $n(\mathbf{r})$ to derive the ground-state properties. Otherwise, we mix them and restart the loop, until convergence is reached.

2.1.3 Solving the Kohn–Sham equations

Since the potential $V_{\text{eff}}(\mathbf{r})$ depends on the occupied orbitals $\phi_i(\mathbf{r})$ through the density, the KS equations must be solved self-consistently by following the cycle depicted in Fig. 2.1. We start with an initial guess for the density $n_0(\mathbf{r})$, which we use to construct the effective potential $V_{\text{eff}}(\mathbf{r})$ and solve Eq. (2.11b) to get the KS eigenenergies ϵ_i and eigenfunctions ϕ_i, and from them the new value for the density $n(\mathbf{r})$. Then, if the new density is not similar enough to the old one to satisfy our convergence criteria, we restart the loop with a mixed density $n_0'(\mathbf{r})$. This process should be repeated until convergence is reached.

Notice that, according to the presented Kohn–Sham formalism, the ground-state density $n(\mathbf{r})$ of the KS system of N noninteracting electrons defined by the effective Hamiltonian $\hat{H}_{\text{KS}}$ is identical to the exact ground-state density of the physical system of N interacting electrons. However, this is not true in practice because the exchange–correlation energy E_{xc} cannot be determined exactly. Therefore, one of the main dilemmas when using DFT is the choice of the exchange–correlation functional, as there is a myriad of different options in the literature, some with more general applicability and others designed for specific systems [179]. Throughout this thesis, we have followed three different approximations. The first one is the local-density approximation (LDA) [180], which assumes that the local exchange–correlation energy density $\mathcal{E}_{\text{xc}}$ of a system with charge density $n(\mathbf{r})$ is that of an homogeneous electron gas with $n = n(\mathbf{r})$. For systems with an inhomogeneous electron density, it is better to use the generalized gradient approximation (GGA) [181, 182], which also takes into account the local gradient of the electronic density. Finally, for systems with significant long-range dispersive interactions between atoms that are not chemically bonded one must add a dispersion correction term to the GGA correlation energy, as is done by van der Waals functionals [183]. In Appendix C we provide a more detailed discussion of these three different approaches.

In addition to the exchange–correlation potential, there are some other choices required in DFT calculations. One of the most important is the selection of a basis set for the numerical representation of the KS orbitals, as several radically different approaches are possible, each with its own advantages and disadvantages. In this thesis, we use two different types of basis sets: localized atomic orbitals, used for computing the response of finite systems in Chapters 3 and 4, and plane-waves, used for the calculations with extended surfaces in Chapter 5. Both of these basis set types are briefly discussed in Appendix D. Another major concern is the treatment of the tightly-bound core electrons, which are chemically inert. Since their only effect in practice is screening the nuclear potential, it is possible to ignore their dynamics and reproduce their effect with an effective potential, greatly increasing the computational efficiency. In Appendix E, we discuss the two implementations used in this thesis: the pseudopotential method [184] and the projector-augmented wave (PAW) method [185].

The computation of the ground-state properties for the systems presented in this thesis was performed with two open-source DFT codes: SIESTA [111, 186] (Spanish Initiative for Electronic Simulations with Thousands of Atoms) and GPAW [187, 188] (Grid-based Projector-Augmented Wave). We used SIESTA for the calculations in Chapters 3 and 4, and GPAW for the results in Chapter 5.

2.2 Linear-response time-dependent Density Functional Theory

The DFT framework, which in principle only allows for the computation of physical properties related to the ground state of a system of N interacting electrons, can be extended to deal with the response of the system to an external perturbation. In analogy to the Hohenberg–Kohn theorem, the Runge–Gross theorem [189] states that there is a correspondence between the external time-dependent potential $V_{\text{ext}}(\mathbf{r};t)$ acting on a system of interacting electrons and the time-dependent density $n(\mathbf{r};t)$. We may thus define an auxiliary system of noninteracting electrons with the same time-dependent density as our real system, computed from the time-dependent Kohn–Sham wavefunctions $\phi_i(\mathbf{r};t)$ as

$$n(\mathbf{r};t) = \sum_{i=1}^{\mathrm{N}} |\phi_i(\mathbf{r};t)|^2, \tag{2.16}$$

with the single-particle wavefunctions satisfying the time-dependent Kohn–Sham equations

$$i\frac{\partial\phi_i(\mathbf{r};t)}{\partial t} = \left[-\frac{\nabla^2}{2} + V_{\text{eff}}[n](\mathbf{r};t)\right]\phi_i(\mathbf{r};t). \tag{2.17}$$

The time-dependent effective potential $V_{\text{eff}}[n](\mathbf{r};t)$ is unique and is defined as

$$\begin{aligned} V_{\text{eff}}[n](\mathbf{r};t) =& V_{\text{ext}}[n](\mathbf{r};t) + V_{\text{H}}[n](\mathbf{r};t) + V_{\text{xc}}[n](\mathbf{r};t) \\ =& V_{\text{ext}}[n](\mathbf{r};t) + V_{\text{Hxc}}[n](\mathbf{r};t), \end{aligned} \tag{2.18}$$

where the time-dependent Hartree potential is given by:

$$V_{\text{H}}(\mathbf{r};t) = \int d\mathbf{r}' \, \frac{n(\mathbf{r}';t)}{|\mathbf{r}-\mathbf{r}'|}. \tag{2.19}$$

Though in principle the time-dependent exchange–correlation potential $V_{\text{xc}}(\mathbf{r};t)$ depends on the evolution of the time-dependent density $n(\mathbf{r};t)$, most applications of this theory use the adiabatic approximation, which assumes that the xc energy only depends on the instantaneous density [190]. This scheme may be further simplified by treating the time-dependent part of the external potential $\delta V_{\text{ext}}(\mathbf{r};t)$ as a weak perturbation, i.e.:

$$V_{\text{ext}}(\mathbf{r};t) = \tilde{V}_{\text{ext}}(\mathbf{r}) + \delta V_{\text{ext}}(\mathbf{r};t). \tag{2.20}$$

Since our aim is to compute the spectroscopical properties of the system, the external potentials will be caused by probes, such as an electromagnetic plane-wave or an electron beam, whereas the time-independent potential will be the one generated by the ions, the same as for the ground-state calculation.

In the linear-response approximation, the response of the system to a weak time-dependent perturbation potential $\delta V_{\text{ext}}(\mathbf{r};t)$ is characterized by the induced density

$$\delta n(\mathbf{r};t) = \int dt' \int d\mathbf{r}' \; \chi(\mathbf{r},\mathbf{r}';t-t') \; \delta V_{\text{ext}}(\mathbf{r}';t'), \tag{2.21}$$

where $\chi(\mathbf{r},\mathbf{r}';t)$ is the nonlocal response function, which tells us how the density at point $\mathbf{r}$ and time t is affected by an external potential at point $\mathbf{r}'$ and time t'. By performing the Fourier transform of the above expression, one obtains the induced density in frequency domain

$$\delta n(\mathbf{r};\omega) = \int d\mathbf{r}' \; \chi(\mathbf{r},\mathbf{r}';\omega) \; \delta V_{\text{ext}}(\mathbf{r}';\omega). \tag{2.22}$$

The induced density for the KS system of noninteracting electrons is given by the equivalent expression

$$\delta n(\mathbf{r};\omega) = \int d\mathbf{r}' \; \chi_0(\mathbf{r},\mathbf{r}';\omega) \; \delta V_{\text{eff}}(\mathbf{r}';\omega), \tag{2.23}$$

where $\delta V_{\text{eff}}(\mathbf{r}';\omega) = \delta V_{\text{ext}}(\mathbf{r}';\omega) + \delta V_{\text{Hxc}}(\mathbf{r}';\omega)$ is the addition of the external perturbation and the variation of the KS Hartree and exchange–correlation potentials. Though there is no known expression for the response function of an interacting system χ, the noninteracting response function χ_0 can be explicitly expressed via products of KS eigenstates $\phi_n(\mathbf{r})$ in the well-known Lehmann representation [191]:

$$\chi_0(\mathbf{r},\mathbf{r}';\omega) = \sum_{n,m} (f_n - f_m)\, \frac{\phi_n^*(\mathbf{r})\phi_m(\mathbf{r})\ \phi_m^*(\mathbf{r}')\phi_n(\mathbf{r}')}{\omega - (\epsilon_m - \epsilon_n) + i\eta}, \tag{2.24}$$

where ϵ_n and f_n are their corresponding eigenenergies and occupation terms, and η is an artificial Lorentzian spectral broadening phenomenologically accounting for the lifetime of the electronic excited states. Thus, χ_0 is completely determined by the ground-state KS wavefunctions and eigenenergies.

From Eqs. (2.22) and (2.23) it also follows that the interacting (noninteracting) response function is the functional derivative of the induced density with respect to the external (effective) potential [191]

$$\chi(\mathbf{r},\mathbf{r}';\omega) = \frac{\delta n(\mathbf{r};\omega)}{\delta V_{\text{ext}}(\mathbf{r}';\omega)},\ \chi_0(\mathbf{r},\mathbf{r}';\omega) = \frac{\delta n(\mathbf{r};\omega)}{\delta V_{\text{eff}}(\mathbf{r}';\omega)}. \tag{2.25}$$

Moreover, the variational derivative of $\delta V_{\text{eff}}(\mathbf{r}',\omega)$ with respect to $\delta n(\mathbf{r};\omega)$ can be computed as:

$$\frac{\delta V_{\text{eff}}(\mathbf{r}';\omega)}{\delta n(\mathbf{r};\omega)} = \frac{\delta V_{\text{ext}}(\mathbf{r}';\omega)}{\delta n(\mathbf{r};\omega)} + \frac{\delta V_{\text{Hxc}}(\mathbf{r}';\omega)}{\delta n(\mathbf{r};\omega)}. \tag{2.26}$$

Combining both results and introducing the Hartree–exchange–correlation kernel

$$K_{\text{Hxc}}(\mathbf{r},\mathbf{r}') = \frac{\delta V_{\text{Hxc}}(\mathbf{r}';\omega)}{\delta n(\mathbf{r};\omega)}, \tag{2.27}$$

which is frequency-independent in the adiabatic approximation [191], we can obtain the Dyson-like Petersilka-Gossman-Gross equation [192]

$$\begin{aligned} \chi(\mathbf{r},\mathbf{r}';\omega) &= \chi_0(\mathbf{r},\mathbf{r}';\omega) \\ &\quad + \int d\mathbf{r}_1 \int d\mathbf{r}_2\ \chi_0(\mathbf{r},\mathbf{r}_1;\omega)\ K_{\text{Hxc}}(\mathbf{r}_1,\mathbf{r}_2)\ \chi(\mathbf{r}_2,\mathbf{r}';\omega). \end{aligned} \tag{2.28}$$

Multiplying both sides by a factor $\delta V_{\text{ext}}(\mathbf{r}';\omega)$ and integrating in $\mathbf{r}'$ one obtains

$$\begin{aligned} &\int d\mathbf{r}'\ \chi(\mathbf{r},\mathbf{r}';\omega)\ \delta V_{\text{ext}}(\mathbf{r}';\omega) = \int d\mathbf{r}'\ \chi_0(\mathbf{r},\mathbf{r}';\omega)\ \delta V_{\text{ext}}(\mathbf{r}';\omega) \\ &+ \int d\mathbf{r}_1 \int d\mathbf{r}_2\ \chi_0(\mathbf{r},\mathbf{r}_1;\omega)\ K_{\text{Hxc}}(\mathbf{r}_1,\mathbf{r}_2) \int d\mathbf{r}'\ \chi(\mathbf{r}_2,\mathbf{r}';\omega)\ \delta V_{\text{ext}}(\mathbf{r}';\omega), \end{aligned} \tag{2.29}$$

which using Eqs. (2.22) and (2.23) gives the following equation for the induced density

$$\begin{aligned}\delta n(\mathbf{r};\omega) = &\int d\mathbf{r}'\ \chi_0(\mathbf{r},\mathbf{r}';\omega)\ \delta V_{\text{ext}}(\mathbf{r}';\omega) \\ &+ \int d\mathbf{r}_1 \int d\mathbf{r}_2\ \chi_0(\mathbf{r},\mathbf{r}_1;\omega)\ K_{\text{Hxc}}(\mathbf{r}_1,\mathbf{r}_2)\ \delta n(\mathbf{r}_2;\omega),\end{aligned} \tag{2.30}$$

which can be recast as:

$$\begin{aligned}&\int d\mathbf{r}'\ \chi_0(\mathbf{r},\mathbf{r}';\omega)\ \delta V_{\text{ext}}(\mathbf{r}';\omega) = \\ &\qquad \int d\mathbf{r}_2 \left[\delta(\mathbf{r}-\mathbf{r}_2) - \int d\mathbf{r}_1\ \chi_0(\mathbf{r},\mathbf{r}_1;\omega)\ K_{\text{Hxc}}(\mathbf{r}_1,\mathbf{r}_2)\right] \delta n(\mathbf{r}_2;\omega),\end{aligned} \tag{2.31}$$

or alternatively

$$\begin{aligned}&\int d\mathbf{r}'\ \chi_0(\mathbf{r},\mathbf{r}';\omega)\ \delta V_{\text{ext}}(\mathbf{r}';\omega) = \\ &\qquad \int d\mathbf{r}_2 \left[\delta(\mathbf{r}-\mathbf{r}_2) - \int d\mathbf{r}_1\ \chi_0(\mathbf{r},\mathbf{r}_1;\omega)\ K_{\text{Hxc}}(\mathbf{r}_1,\mathbf{r}_2)\right] \\ &\qquad \times \int d\mathbf{r}'\ \chi_0(\mathbf{r}_2,\mathbf{r}';\omega)\ \delta V_{\text{eff}}(\mathbf{r}';\omega).\end{aligned} \tag{2.32}$$

Finally, this equation is further simplified by dividing both sides of the equation by the noninteracting response χ_0

$$\begin{aligned}&\int d\mathbf{r}'\ \delta V_{\text{ext}}(\mathbf{r}';\omega) = \\ &\qquad \iiint d\mathbf{r}_1\ d\mathbf{r}_2\ d\mathbf{r}' \left[1 - K_{\text{Hxc}}(\mathbf{r}_1,\mathbf{r}_2)\ \chi_0(\mathbf{r}_2,\mathbf{r}';\omega)\right] \delta V_{\text{eff}}(\mathbf{r}';\omega),\end{aligned} \tag{2.33}$$

The above equation is the one solved by the open-source code PyNAO [98] (Python Numerical Atomic Orbitals) developed by P. Koval, M. Barbry, and D. Sánchez-Portal, which we have used for the computation of the linear response of the nanostructures studied in this thesis. The code implements an efficient iterative algorithm to solve this alternative form of Eq. (2.28), which is described in detail in M. Barbry's thesis [20]. It uses the LCAO method (see Appendix D), in which the KS orbitals are expanded in a basis set of numerical atomic orbitals, defined by the product of a radial function with spherical harmonics and localized at the atomic sites, and products of the atomic orbitals are used to expand the response functions. This approach has been proven to be a very efficient tool to compute the response of metallic clusters containing up to several hundreds of atoms, both under light illumination [22, 23, 27, 193] and electron beam [194] excitation. In the following subsections, we briefly describe the implementation of linear-response TDDFT within the LCAO formalism and summarize how the optical and EEL probability spectra are computed.

2.2.1 LCAO implementation of the linear-response formalism

In the LCAO formalism (see Appendix D), the Kohn–Sham wavefunctions are expanded in a basis set of atomic orbitals f^a as [20]:

$$\phi_n(\mathbf{r}) = X_a^n \; f^a(\mathbf{r} - \mathbf{R}_a), \tag{2.34}$$

where we have used Einstein's summation convention over repeated indices. The f^a are a set of atomic orbitals centered at the atomic nuclei positions $\mathbf{R}_a$, which can be decomposed as the product of a radial function and real spherical harmonics

$$f^a(\mathbf{r}) = f^a(r) Y_{l,m}(\mathbf{\Omega}), \tag{2.35}$$

and X_a^n are the expansion coefficients obtained by solving the Kohn–Sham equations self-consistently.

One of the main challenges of working within this formalism is dealing with the products of atomic orbitals $f^a(\mathbf{r})f^b(\mathbf{r})$ that appear when inserting the LCAO ansatz Eq. (2.34) into Eq. (2.24). These quantities are linearly dependent and therefore they do not form a suitable basis set. In order to efficiently expand the response functions, the PyNAO code uses a basis set of dominant product functions $F^\mu(\mathbf{r})$, defined as [98, 195, 196]:

$$f^a(\mathbf{r}) f^b(\mathbf{r}) = V_\mu^{ab} F^\mu(\mathbf{r}), \tag{2.36}$$

where the index μ runs over all pairs of atoms. The product vertex coefficients V_μ^{ab} relate the original products $f^a(\mathbf{r})f^b(\mathbf{r})$ to the new basis of dominant products $F^\mu(\mathbf{r})$. The $F^\mu(\mathbf{r})$ are constructed by diagonalizing a Coulomb metric in the basis of original products, individually for each pair of atoms, and are themselves linear combinations of the original products. The basis of dominant products can also be expressed in terms of atom-centered products only, this is, products of atomic orbitals centered at the same atom, which is more convenient for some computational steps. The response function of the free-electron system can then be expressed in the new basis as

$$\chi_0(\mathbf{r}, \mathbf{r}'; \omega) = F^\mu(\mathbf{r}) \; \chi^0_{\mu\nu}(\omega) \; F^\nu(\mathbf{r}'), \tag{2.37}$$

where the matrix form of the response function $\chi^0_{\mu\nu}(\omega)$ is obtained from Eq. (2.24):

$$\chi^0_{\mu\nu}(\omega) = (f_n - f_m) \; \frac{(X_a^n V_\mu^{ab} X_b^m) \; (X_c^m V_\nu^{cd} X_d^n)}{\omega - (\epsilon_m - \epsilon_n) + i\eta}. \tag{2.38}$$

The equation solved by the code is the matrix form of Eq. (2.33):

$$\left[\delta_{\mu\nu} - K^{\mu\mu'}_{\mathrm{Hxc}} \; \chi^0_{\mu'\nu}(\omega)\right] \delta V^\nu_{\mathrm{eff}}(\omega) = \delta V^\mu_{\mathrm{ext}}(\omega), \tag{2.39}$$

using the matrix forms of the interaction kernel and the potentials defined as

$$K_{\mathrm{Hxc}}^{\mu\nu} = \int d\mathbf{r}\ d\mathbf{r}'\ F^{\mu}(\mathbf{r})\ K_{\mathrm{Hxc}}(\mathbf{r},\mathbf{r}')\ F^{\nu}(\mathbf{r}'), \tag{2.40}$$

$$\delta V_{\mathrm{ext}}^{\mu}(\omega) = \int d\mathbf{r}\ F^{\mu}(\mathbf{r})\ \delta V_{\mathrm{ext}}(\mathbf{r};\omega), \tag{2.41}$$

$$\delta V_{\mathrm{eff}}^{\mu}(\omega) = \int d\mathbf{r}\ F^{\mu}(\mathbf{r})\ \delta V_{\mathrm{eff}}(\mathbf{r};\omega). \tag{2.42}$$

2.2.2 Computation of optical spectra

The optical spectrum describes the response of a system illuminated by light as a function of its wavelength or frequency. The external electric field corresponding to an incident monochromatic electromagnetic plane wave is, in the frequency domain, $\delta\mathbf{E}_{\mathrm{ext}}(\mathbf{r};\omega) = \mathbf{E}_0^{\omega} e^{i\mathbf{kr}}$. If the dimension of the excited system is much smaller than the incident light wavelength, $\lambda = 2\pi/k = 2\pi c/\omega$, one can safely use the nonretarded approximation (see Section 1.1) and neglect the spatial variation of the external field, in which case the external perturbation potential is accurately described as $\delta V_{\mathrm{ext}} = \mathbf{E}_0 \cdot \mathbf{r}$. According to Eq. (2.22), such a potential will induce a variation in the electron density

$$\delta n(\mathbf{r};\omega) = \int d\mathbf{r}'\ \chi(\mathbf{r},\mathbf{r}';\omega)\ \mathbf{E_0}\cdot\mathbf{r}'. \tag{2.43}$$

From the induced density distribution $\delta n(\mathbf{r};\omega)$ we can compute the induced dipole moment along the j direction as:

$$p_j^{\mathrm{ind}}(\omega) = -\int d\mathbf{r}\ r_j\ \delta n(\mathbf{r};\omega). \tag{2.44}$$

The optical polarizability tensor of the system $\hat{\boldsymbol{\alpha}}(\omega)$ describing its optical response relates the external field to the induced dipole moment,

$$\mathbf{p}^{\mathrm{ind}}(\omega) = \hat{\boldsymbol{\alpha}}(\omega)\ \mathbf{E_0}. \tag{2.45}$$

By combining the last three equations, one can relate the components of the polarizability tensor to the induced density as:

$$\alpha_{ij}(\omega) = \int d\mathbf{r}\ d\mathbf{r}'\ r_i\ \chi(\mathbf{r},\mathbf{r}';\omega)\ r_j' \tag{2.46}$$

$$= -\int d\mathbf{r}\ r_i\ \delta n_j(\mathbf{r};\omega), \tag{2.47}$$

where $\delta n_j(\mathbf{r};\omega)$ is the density response to a unitary external perturbation $\delta V_{\mathrm{ext}} = r_j$. Thus to obtain all the components of the polarizability tensor one must first compute the response to external fields with $E_0 = 1$ a.u. and polarized along each of the three Cartesian axes. This is done by solving Eq. (2.39) for an external potential of the form

$$\delta V^{\mu}_{\mathrm{ext}}(\omega) = \int d\mathbf{r}\ F^{\mu}(\mathbf{r})\ r_j \tag{2.48}$$

in order to obtain the corresponding effective potential, from which the induced density can be computed as

$$\delta n_j(\mathbf{r};\omega) = F^{\mu}(\mathbf{r})\ \delta n^{j}_{\mu} = F^{\mu}(\mathbf{r})\ \chi^{0}_{\mu\nu}(\omega)\ \delta V^{\nu}_{\mathrm{eff}}(\omega). \tag{2.49}$$

If the excited nanoparticles are small enough to safely neglect the contribution of the scattering, as for the ones studied in this thesis, one can also extract the absorption cross section $\sigma_{\mathrm{abs}}(\omega)$ from the trace of the imaginary part of the polarizability using Eq. (1.31), which in atomic units reads:

$$\sigma_{\mathrm{abs}}(\omega) = \frac{4\pi\omega}{3c}\ \mathrm{Tr}[\mathrm{Im}\{\hat{\boldsymbol{\alpha}}(\omega)\}]. \tag{2.50}$$

Finally, the induced electric field in the frequency domain $\mathbf{E}^{\mathrm{ind}}(\mathbf{r};\omega)$ can be directly computed from the induced density as the Coulomb integral

$$\mathbf{E}^{\mathrm{ind}}(\mathbf{r};\omega) = -\int d\mathbf{r}'\ \frac{\mathbf{r}-\mathbf{r}'}{|\mathbf{r}-\mathbf{r}'|^{3}}\ \delta n(\mathbf{r}';\omega). \tag{2.51}$$

2.2.3 Computation of electron energy-loss spectra

The same scheme used for the optical spectra can also be applied to computing the density induced by other external perturbations, such as the fast electron beams used in STEM-EELS. The kinetic energies of typical TEM electron beams, which are in the range of tens or hundreds of keV, are much larger than the energies involved in the excitation of valence electrons, and the interaction time of such external electrons with the nanoparticles is too short to significantly change their velocity. Therefore, the probe electrons are usually modeled as point charges with uniform speed. The linear-response approximation is also valid, provided that the current density of the incoming electrons is small [166].

The electron energy-loss probability Γ_{EELS} was introduced as a function of the field acting back on the probe electron $\mathbf{E}^{\mathrm{ind}}(\mathbf{r_e}(t);t)$ in Eq. (1.42). Due to the small size of the studied nanoparticles, retardation effects can be safely ignored, and it is assumed that the induced field is given by the electrostatic Coulomb law as in Eq. (2.51). By inserting the field generated by a moving point charge into Eq. (1.42) one can reach, after some algebra, the following expression for the electron energy-loss probability as a function of the external potential and the induced charge density [20]:

$$\Gamma_{\mathrm{EELS}}(\omega) = \frac{1}{\pi}\mathrm{Im}\left[\int d\mathbf{r}\ \delta V^{*}_{\mathrm{ext}}(\mathbf{r};\omega)\ \delta n(\mathbf{r};\omega)\right]. \tag{2.52}$$

The induced density $\delta n(\mathbf{r};\omega)$ is computed in terms of the product functions $F^{\mu}(\mathbf{r})$ as in Eq. (2.49). Therefore, one first needs to solve Eq. (2.39) for the perturbing potential generated by a moving electron (external probe)

$$\delta V^{\mu}_{\text{ext}}(\omega) = \frac{1}{2\pi}\int dt\; e^{i\omega t}\int d\mathbf{r}\;\frac{F^{\mu}(\mathbf{r})}{|\mathbf{r}-\mathbf{R}^{\mu}_{\text{elec}}(t)|}, \tag{2.53}$$

where $\mathbf{R}^{\mu}_{\text{elec}}(t) = \mathbf{R}_0 + \mathbf{v}_{\text{e}}t - \mathbf{R}^{\mu}$, with $\mathbf{R}^{\mu}$ the positions of the atomic nuclei at which the product basis functions $F^{\mu}(\mathbf{r})$ are centered, and $\mathbf{R}_0$ and $\mathbf{v}_{\text{e}}$ the probe electron position and velocity, respectively. The external potential components $\delta V^{\mu}_{\text{ext}}(\omega)$ are computed in the time domain using the Laplace expansion of the Coulomb interaction [8], and then one performs the Fourier transform in order to obtain the components in frequency domain. Finally, the electron energy-loss probability is computed as follows in the basis of product functions:

$$\Gamma_{\text{EELS}}(\omega) = \frac{1}{\pi}\text{Im}\left[\delta V^{\mu *}_{\text{ext}}(\omega)\;\delta n^{\mu}(\omega)\right]. \tag{2.54}$$

2.3 Computation of Raman spectra in periodic systems

In this section, we summarize the methodology employed for computing the Raman spectra of periodic systems. We start by summarily introducing the main peculiarities of periodic systems, as well as the concepts of phonons and electron–phonon interactions. We finish with a description of the methodology implemented in the GPAW code [188], following its original description by Taghizadeh et al. [197].

2.3.1 Periodic systems

A periodic system, such as an extended solid, is composed of infinite repetitions of its primitive unit cell defined by the primitive lattice vectors $(\mathbf{a_1}, \mathbf{a_2}, \mathbf{a_3})$, forming a Bravais lattice. As a consequence, the effective potential experienced by the noninteracting KS electrons is inherently periodic:

$$V_{\text{eff}}(\mathbf{r}) = V_{\text{eff}}(\mathbf{r}+\mathbf{T}), \tag{2.55}$$

where $\mathbf{T} = n_1\mathbf{a_1} + n_2\mathbf{a_2} + n_3\mathbf{a_3}$ is any vector belonging to the Bravais lattice. As stated by Bloch's theorem [65], this means that the eigenstates of the KS Hamiltonian in a periodic system can be decomposed into the following products of functions:

$$\phi(\mathbf{r}) = e^{i\mathbf{k}\cdot\mathbf{r}}u(\mathbf{r}), \tag{2.56}$$

where $e^{i\mathbf{k}\cdot\mathbf{r}}$ is a plane wave part and $u(\mathbf{r}) = u(\mathbf{r}+\mathbf{T})$ shares the periodicity of the lattice. Another consequence of Bloch's theorem is that the eigenvalues $\epsilon_{n\mathbf{k}}$ and eigenstates $\phi_{n\mathbf{k}}(\mathbf{r})$, identified with the band index n and the wavevector $\mathbf{k}$, are periodic with respect to the reciprocal lattice vectors $\mathbf{G} = m_1\mathbf{b_1} + m_2\mathbf{b_2} + m_3\mathbf{b_3}$:

$$\epsilon_{n\mathbf{k}+\mathbf{G}} = \epsilon_{n\mathbf{k}}, \;\; \phi_{n\mathbf{k}+\mathbf{G}}(\mathbf{r}) = \phi_{n\mathbf{k}}(\mathbf{r}), \tag{2.57}$$

where the primitive vectors of the reciprocal lattice are defined from the primitive vectors as

$$\mathbf{b_1} = \frac{2\pi}{V}\mathbf{a_2} \times \mathbf{a_3}, \;\; \mathbf{b_2} = \frac{2\pi}{V}\mathbf{a_3} \times \mathbf{a_1}, \;\; \mathbf{b_3} = \frac{2\pi}{V}\mathbf{a_1} \times \mathbf{a_2}, \tag{2.58}$$

with V the volume of the primitive unit cell. Therefore, computing the eigenvalues and wavefunctions for wavevectors within the first Brillouin zone, this is, the primitive cell in reciprocal space, is enough to determine the entire electronic structure of the material. Moreover, the symmetries of the system allow for further reducing the subset of required wavevectors to those within the irreducible Brillouin zone. As a reference, in Figs. 2.2a and 2.2b we represent the Bravais lattice of a 2-dimensional graphene monolayer and its first Brillouin zone, respectively.

A basis set of plane waves (see Appendix D) is particularly convenient when dealing with periodic systems, as the matrix elements of the effective KS Hamiltonian take the form:

$$\langle \mathbf{k}+\mathbf{G}|\hat{H}_{\text{KS}}|\mathbf{k}+\mathbf{G}'\rangle = \frac{1}{2}|\mathbf{k}+\mathbf{G}|^2\delta_{\mathbf{G},\mathbf{G}'} + V_{\text{eff}}(\mathbf{G}-\mathbf{G}'). \tag{2.59}$$

The first term on the right hand side of the equation represents the kinetic energy, and the second term the Fourier transform of the KS effective potential. The kinetic energy term is conveniently diagonal, whereas the potential energy term is block-diagonal, with each block characterized by a specific momentum $\mathbf{k}$, as it only couples plane waves whose wavevectors differ by a reciprocal lattice vector $\mathbf{G}$. This allows us to diagonalize each block independently by solving the KS Hamiltonian at every allowed $\mathbf{k}$-point within the first Brillouin zone. Though in principle one should use all allowed $\mathbf{k}$-points, this is computationally unfeasible, and in practice only a finite grid of $\mathbf{k}$-points is used, usually defined by the Monkhorst-Pack algorithm [198].

We can also make the transition to the second quantization formalism by regarding the KS Hamiltonian as an effective one-body operator and using the standard prescription, which leads to the following “electronic” Hamiltonian [199]:

$$\hat{H}_e = \sum_{n\mathbf{k}} \epsilon_{n\mathbf{k}}\hat{c}^\dagger_{n\mathbf{k}}\hat{c}_{n\mathbf{k}}, \tag{2.60}$$

where $\epsilon_{n\mathbf{k}}$ denotes the eigenenergy of the single-particle electronic state $|n\mathbf{k}\rangle$ with momentum $\mathbf{k}$ and band index n, and $\hat{c}^\dagger(\hat{c})$ are the associated fermionic creation (annihilation) operators.

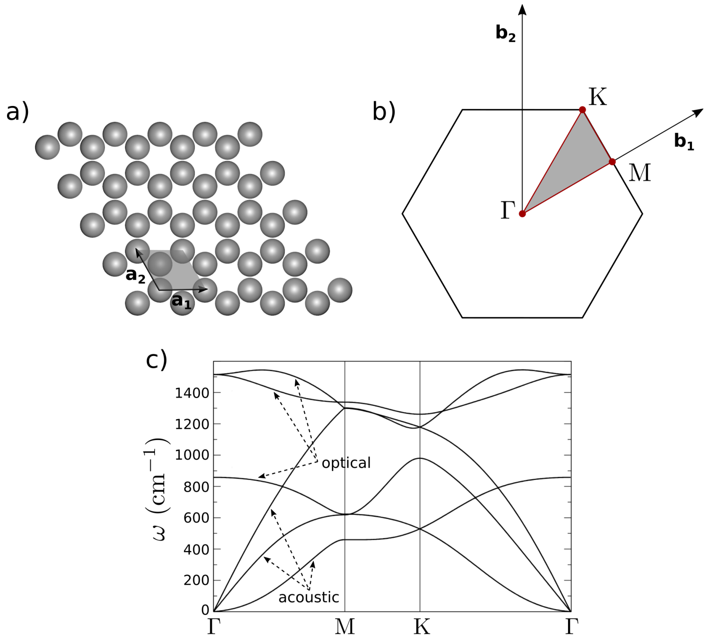

Figure 2.2: a) Bravais lattice of a 2-dimensional graphene monolayer, where the arrows represent unit cell vectors $\{\mathbf{a_1}, \mathbf{a_2}\}$, and the shadowed area represents the unit cell. b) Sketch of the first Brillouin zone of the graphene monolayer, where we depict the unit vectors of the reciprocal lattice $\{\mathbf{b_1},\ \mathbf{b_2}\}$ and the high symmetry points $\{\Gamma, \mathrm{M}, \mathrm{K}\}$. The shadowed area is the irreducible Brillouin zone. c) Phonon dispersion relation of the graphene monolayer along the path outlined in b), taken from Ref. [200].

2.3.2 Phonons and the electron–phonon interaction

An extended system supports collective oscillations of the ions in the lattice, known as phonons. Two types of phonons exist, characterized by markedly different dispersion relations. On the one hand, acoustic phonons correspond to coherent movements of the lattice ions, in which the neighboring atoms oscillate almost on-phase, and exhibit a linear relation between frequency and wavevector, with their frequencies tending to zero at the long wavelength limit ($\mathbf{q} = 0$, also known as the Γ point in the Brillouin zone). On the other hand, optical phonons correspond to an out-of-phase motion of neighboring ions, and are characterized by nonzero frequencies at the Γ point, and a mostly flat dispersion relation. Some of the latter can indirectly couple to an incident electromagnetic field, and are therefore accessible through Raman spectroscopy (see Section 1.5). As a reference, in Fig. 2.2c we plot the phonon dispersion relation of a graphene monolayer along the path outlined in Fig. 2.2b, taken from Ref. [200], in which acoustic and optical phonons are clearly distinguishable.

Up to this point, we have been working within the Born–Oppenheimer approximation, neglecting the dynamical coupling between the electrons and the lattice ions. However, this coupling plays a fundamental role in many physical phenomena, and one must often go beyond the Born–Oppenheimer approximation in order to adequately address them. The first step to account for electron–phonon interactions is introducing the ionic Hamiltonian, associated with the energies of the lattice vibrations, which, in the harmonic approximation, is written as a summation of independent harmonic oscillators [201]

$$\hat{H}_{\nu} = \sum_{\nu\mathbf{q}} \hbar\omega_{\nu\mathbf{q}} \left(\hat{a}^{\dagger}_{\nu\mathbf{q}} \hat{a}_{\nu\mathbf{q}} + \frac{1}{2} \right), \tag{2.61}$$

where $\hbar\omega_{\nu\mathbf{q}}$ is the energy of normal phonon mode ν with wavevector $\mathbf{q}$, and $\hat{a}^{\dagger}(\hat{a})$ are the associated bosonic creation (annihilation) operators. In the case of $|\mathbf{q}| = 0$, there are three normal modes for which $\hbar\omega_{\nu\mathbf{q}} = 0$, corresponding to the acoustic phonon modes, which will be skipped from now on.

Now that we have introduced both the ionic and electronic Hamiltonians, the next step is to add the electron–phonon coupling term $\hat{H}_{\mathrm{e}\nu}$. The standard form of the Hamiltonian describing a coupled electron–phonon system, to the first order in the atomic displacements, is [201]:

$$\hat{H}_{\mathrm{e}} + \hat{H}_{\nu} + \hat{H}_{\mathrm{e}\nu}, \tag{2.62}$$

where $\hat{H}_{\mathrm{e}\nu}$ is the electron–phonon coupling Hamiltonian, defined as:

$$\hat{H}_{\mathrm{e}\nu} = \sum_{\substack{nm\nu \\ \mathbf{kq}}} \sqrt{\frac{\hbar}{\omega_{\nu\mathbf{q}}}} g^{\nu\mathbf{q}}_{nm\mathbf{k}} \hat{c}^{\dagger}_{n\mathbf{k}} \hat{c}_{m\mathbf{k}} \left(\hat{a}_{\nu\mathbf{q}} + \hat{a}^{\dagger}_{\nu(-\mathbf{q})} \right), \tag{2.63}$$

with $g^{\nu\mathbf{q}}_{nm\mathbf{k}} = \langle n\mathbf{k} + \mathbf{q} | \partial_{\nu\mathbf{q}} V_{\mathrm{eff}} | m\mathbf{k} \rangle$ the electron–phonon coupling matrix elements, which are computed from the partial derivatives of the Kohn–Sham effective potential in Eq. (2.13) with respect to the atomic displacements.

2.3.3 Computation of Raman spectra

As described in Section 1.5, incident electromagnetic radiation can excite an electron to a virtual state, creating a hole in its original band. This electron can then interact with the lattice phonons, exciting some of them and losing energy in the process, so that when it recombines with the hole the emitted photon has a smaller energy than the incident one, which is known as a Raman Stokes process. The order of the Raman process is given by the number of phonons involved. The major contribution to the Raman signal usually comes from first-order Raman Stokes processes, depicted in Fig. 2.3a, in which the photon scattering results in the excitation of a single phonon. Since the momentum is conserved in electron–phonon interactions and the electron and the hole must be close in momentum for the recombination to be possible, only phonons near the Γ point (zone-centered phonons) can participate in this process [202]. This restriction is relaxed for higher-order Raman processes,

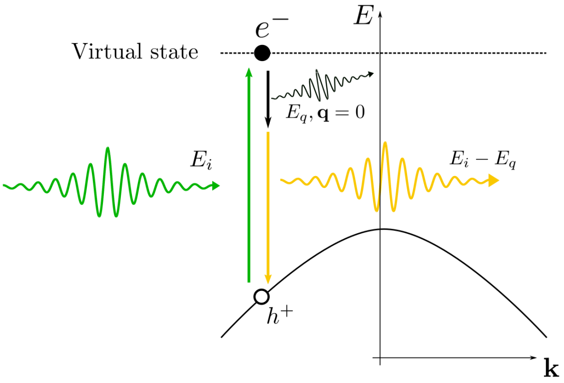

Figure 2.3: Schematic representation of a first-order Raman Stokes scattering process. An incident photon with energy E_i excites an electron to a virtual state, leaving a hole behind. The electron interacts with a phonon mode loosing some energy E_q, and later recombines with the hole emitting a photon with energy $E_i - E_q$. In order for the recombination to be possible, the electron and the hole must be close in momentum, and therefore due to momentum conservation the phonon momentum must be almost zero.

such as the second-order process, in which two phonons with opposite momentum are excited. However, in this thesis we will restrict ourselves to first-order Raman intensities, and therefore only zone-centered phonons will be considered.

In order to compute the Raman spectra, we have employed the third-order perturbation theory approach [197] as implemented in the open-source GPAW code. A system of electrons interacting both with phonons and with an incident electromagnetic field are described, in the independent-particle approximation, by a perturbative Hamiltonian of the form:

$$\hat{H}_{\mathrm{R}} = \hat{H}_0 + \hat{H}_{\mathrm{e}\gamma} + \hat{H}_{\mathrm{e}\nu}, \tag{2.64}$$

where $\hat{H}_0$ is the unperturbed Hamiltonian of the electrons and ions

$$\hat{H}_0 \equiv \hat{H}_{\mathrm{e}} + \hat{H}_{\nu}, \tag{2.65}$$

with $\hat{H}_{\mathrm{e}}$ and $\hat{H}_{\nu}$ the electronic and ionic Hamiltonians, described respectively in Eqs. (2.60) and (2.61), and $\hat{H}_{\mathrm{e}\nu}$ is the electron–phonon coupling term in Eq. (2.63). The electron–light interaction is described by $\hat{H}_{\mathrm{e}\gamma}$ in the velocity or minimal coupling gauge [203], in which the electric field is completely determined by the magnetic vector potential $\boldsymbol{\mathcal{A}}$ as $\mathbf{E} = -\partial\boldsymbol{\mathcal{A}}/\partial t$. The Hamiltonian describing this interaction is given by [204]:

$$\hat{H}_{\mathrm{e}\gamma}(t) = \frac{e}{m_{\mathrm{e}}}\boldsymbol{\mathcal{A}}(t) \cdot \sum_{nm\mathbf{k}} \mathbf{p}_{nm\mathbf{k}}\hat{c}^{\dagger}_{n\mathbf{k}}\hat{c}_{m\mathbf{k}} + \frac{e^2}{2m_{\mathrm{e}}}\boldsymbol{\mathcal{A}}(t)^2, \tag{2.66}$$

where $\mathbf{p}_{nm\mathbf{k}} = \langle n\mathbf{k}|\hat{\mathbf{p}}|m\mathbf{k}\rangle$ are the momentum matrix elements. The term in $\boldsymbol{\mathcal{A}}^2$ does not contribute to the linear Raman response, and therefore it is not taken into account from now on. This Hamiltonian neglects the Coulomb interactions between electrons and holes (excitonic effects), which only become important when the excitation energy is in resonance with the exciton energy [205].

The expression for the Raman intensity is derived by treating the electron–light and electron–phonon Hamiltonians as perturbations to $\hat{H}_0$. A general time-dependent perturbation is expressed as $\hat{H}'(t) \equiv \sum_{\omega_l} \hat{H}'(\omega_l) \exp(-\mathrm{i}\omega_l t)$, with ω_l running over positive, zero, and negative frequencies. Assuming a monochromatic illumination, the perturbative electric field can be written as:

$$\mathbf{E}(t) = E_{\mathrm{in}} \mathbf{u}_{\mathrm{in}} \exp\left(-\mathrm{i}\omega_{\mathrm{in}} t\right) + E_{\mathrm{out}} \mathbf{u}_{\mathrm{out}} \exp\left(-\mathrm{i}\omega_{\mathrm{out}} t\right) + c.\ c., \tag{2.67}$$

with $\omega_{\mathrm{in(out)}}$ being the frequencies of the input (output) electromagnetic fields, and $\mathbf{u}_{\mathrm{in(out)}}$ and $E_{\mathrm{in(out)}}$ denoting respectively their polarization vectors and amplitudes. This means that there are three distinct frequencies in our perturbation Hamiltonian: input and output light frequencies (ω_{in} and ω_{out}) from the electron–light interaction part and zero frequency from the time-independent electron–phonon coupling.

The transition probability from an initial state $|\Psi_i\rangle$ to a final state $|\Psi_f\rangle$ within third-order perturbation theory, $P^{(3)}_{i\to f}$, is computed using Fermi's golden rule as [206]

$$\begin{aligned} P^{(3)}_{i\to f} = \frac{2\pi}{\hbar} & \left| \sum_{ab} \sum_{(\omega_1\omega_2\omega_3)} \frac{\langle \Psi_i|\hat{H}'(\omega_3)|\Psi_b\rangle\langle\Psi_b|\hat{H}'(\omega_2)|\Psi_a\rangle\langle\Psi_a|\hat{H}'(\omega_1)|\Psi_f\rangle}{(E_i - E_b + \hbar\omega_3)(E_i - E_a + \hbar\omega_2 + \hbar\omega_3)} \right|^2 \\ & \times \delta(E_f - E_i - \hbar\omega), \end{aligned} \tag{2.68}$$

where $\{|\Psi_a\rangle, |\Psi_b\rangle\}$ denote all eigenstates of the unperturbed system, $\{E_a, E_b\}$ their respective energies, and ω_n (with $n = 1, 2, 3$) are the three frequencies involved in the perturbative Hamiltonian, with the constraint that the sum $\omega_1 + \omega_2 + \omega_3 = \omega$ must be held fixed. The Dirac delta ensures the energy conservation.

The eigenstates of the unperturbed Hamiltonian can be written as a convolution of the electronic and phononic states:

$$|\Psi\rangle = |\psi\rangle \otimes |m_\nu\rangle, \tag{2.69}$$

with the index ν running over phonon modes, so that $|m_\nu\rangle$ denotes a state with m phonons of frequency ω_ν, and $|\psi\rangle$ denotes a many-body electronic state. The intensity of the Stokes Raman process in the first-order approximation is proportional to the transition rate corresponding to a photon absorption followed by an emission of a single phonon and a photon. This corresponds to initial and final states

$$|\Psi_i\rangle = |0\rangle \otimes |m_\nu\rangle, \quad |\Psi_f\rangle = |0\rangle \otimes |m_\nu + 1\rangle, \tag{2.70}$$

where $|0\rangle$ is the ground state of the electronic system, so that $E_f - E_i = \hbar\omega_\nu$. We can also write the intermediate states $|\Psi_{a(b)}\rangle$ as a convolution $|\psi_{a(b)}\rangle \otimes |m_{\nu'}\rangle$. The electron–phonon perturbation $\hat{H}_{e\nu}$ is linear in the phononic operator, which means that

$$\langle\Psi_a|\hat{H}_{\mathrm{e}\nu}|\Psi_i\rangle = \langle\psi_a|\hat{H}_{\mathrm{e}\nu}|0\rangle\delta_{\nu'\nu}\delta_{m_{\nu'}(m_\nu\pm1)}. \tag{2.71}$$

with δ_{ij} the Kronecker delta. The electron–light perturbation, on the other hand, does not depend on the phononic operator, and therefore

$$\langle\Psi_a|\hat{H}_{\mathrm{e}\gamma}|\Psi_i\rangle = \langle\psi_a|\hat{H}_{\mathrm{e}\gamma}|0\rangle\delta_{\nu'\nu}\delta_{m_{\nu'}m_\nu}. \tag{2.72}$$

This means that the intermediate states only contribute to the Stokes response if their phonon state $|m_{\nu'}\rangle$ is either $|m_\nu\rangle$ or $|m_\nu \pm 1\rangle$.

For the process described above, in which a photon is absorbed in order to emit a phonon and a photon, $(\omega_1,\, \omega_2,\, \omega_3)$ are any permutation of $(\omega_{\mathrm{in}},\, -\omega_{\mathrm{out}},\, 0)$, as the frequency of the emitted light enters with a negative sign. This means that we will have six different terms contributing to the Stokes response, one for each permutation of $(\omega_{\mathrm{in}},\, -\omega_{\mathrm{out}},\, 0)$. For example, for $\omega_1 = \omega_{\mathrm{in}}$, $\omega_2 = 0$, $\omega_3 = -\omega_{\mathrm{out}}$ we have the term

$$\begin{aligned}\frac{\langle\Psi_i|\hat{H}'(\omega_3)|\Psi_b\rangle\,\langle\Psi_b|\hat{H}'(\omega_2)|\Psi_a\rangle\,\langle\Psi_a|\hat{H}'(\omega_1)|\Psi_f\rangle}{(E_i - E_b + \hbar\omega_3)(E_i - E_a + \hbar\omega_2 + \hbar\omega_3)} &\rightarrow \\ \rightarrow \frac{\langle 0|\mathbf{u}_{\mathrm{out}}\cdot\hat{\mathbf{P}}|\psi_b\rangle\,\langle\psi_b|\hat{G}_\nu|\psi_a\rangle\,\langle\psi_a|\mathbf{u}_{\mathrm{in}}\cdot\hat{\mathbf{P}}|0\rangle}{(-\hbar\omega_{\mathrm{out}} - \epsilon_b)(-\hbar\omega_{\mathrm{in}} - \epsilon_a)}&,\end{aligned} \tag{2.73}$$

where $|\psi_a(b)\rangle$ denote the intermediate electronic states, $\epsilon_{a(b)}$ denotes the energy (with respect to the electronic ground state) of the electronic state $|\psi_{a(b)}\rangle$, and the many-body electronic operators are defined as $\hat{\mathbf{P}} \equiv \sum_{nm\mathbf{k}}\mathbf{p}_{nm\mathbf{k}}\hat{c}^\dagger_{n\mathbf{k}}\hat{c}_{m\mathbf{k}}$ and $\hat{G}_\nu \equiv \sum_{nm\mathbf{k}} g^{\nu\mathbf{0}}_{nm\mathbf{k}}\hat{c}^\dagger_{n\mathbf{k}}\hat{c}_{m\mathbf{k}}$. Taking into account all frequency permutations and summing for all the possible final states (this is, all phonon modes ν) leads to the expression for the total Raman intensity:

$$I(\omega) = I_0 \sum_\nu \frac{n_\nu + 1}{\omega_\nu}|P_\nu|^2\delta(\omega - \omega_\nu), \tag{2.74}$$

where $n_\nu = [\exp(\hbar\omega_\nu/k_B T) - 1]^{-1}$ is the Bose-Einstein distribution. The factor I_0 is a constant proportional to the intensity of the incident light which also depends on the input frequency, and [207]

$$\begin{aligned}
P_\nu \equiv \sum_{ab} & \left[\frac{\langle 0|\hat{P}_{\text{in}}|\psi_b\rangle\langle\psi_b|\hat{G}_\nu|\psi_a\rangle\langle\psi_a|\hat{P}_{\text{out}}|0\rangle}{(\hbar\omega_{\text{in}}-\epsilon_b)(\hbar\omega_{\text{out}}-\epsilon_a)} + \frac{\langle 0|\hat{P}_{\text{in}}|\psi_b\rangle\langle\psi_b|\hat{P}_{\text{out}}|\psi_a\rangle\langle\psi_a|\hat{G}_\nu|0\rangle}{(\hbar\omega_{\text{in}}-\epsilon_b)(\hbar\omega_\nu-\epsilon_a)} \right. \\
& + \frac{\langle 0|\hat{P}_{\text{out}}|\psi_b\rangle\langle\psi_b|\hat{G}_\nu|\psi_a\rangle\langle\psi_a|\hat{P}_{\text{in}}|0\rangle}{(-\hbar\omega_{\text{out}}-\epsilon_b)(-\hbar\omega_{\text{in}}-\epsilon_a)} + \frac{\langle 0|\hat{P}_{\text{out}}|\psi_b\rangle\langle\psi_b|\hat{P}_{\text{in}}|\psi_a\rangle\langle\psi_a|\hat{G}_\nu|0\rangle}{(-\hbar\omega_{\text{out}}-\epsilon_b)(\hbar\omega_\nu-\epsilon_a)} \\
& \left. + \frac{\langle 0|\hat{G}_\nu|\psi_b\rangle\langle\psi_b|\hat{P}_{\text{in}}|\psi_a\rangle\langle\psi_a|\hat{P}_{\text{out}}|0\rangle}{(-\hbar\omega_\nu-\epsilon_b)(\hbar\omega_{\text{out}}-\epsilon_a)} + \frac{\langle 0|\hat{G}_\nu|\psi_b\rangle\langle\psi_b|\hat{P}_{\text{out}}|\psi_a\rangle\langle\psi_a|\hat{P}_{\text{in}}|0\rangle}{(-\hbar\omega_\nu-\epsilon_b)(-\hbar\omega_{\text{in}}-\epsilon_a)} \right],
\end{aligned} \tag{2.75}$$

where $\hat{P}_{\text{in}} = \mathbf{u}_{\text{in}} \cdot \hat{\mathbf{P}}$, $\hat{P}_{\text{out}} = \mathbf{u}_{\text{out}} \cdot \hat{\mathbf{P}}$, and the summations over a and b include only electronic states. Due to momentum conservation only phonons with $\mathbf{q} = \mathbf{0}$, at the center of the Brillouin zone, contribute to the first-order Raman signal (see Fig. 2.3a), and ω_ν stands for the zone-centered phonon frequencies $\omega_{\nu 0}$. Both operators $\hat{\mathbf{P}}$ and $\hat{G}_\nu$ are also bi-linear in the electronic operator, so, for the matrix elements not to vanish, the intermediate electronic states $|\psi_{a(b)}\rangle$ must include singly-exited states (terms in the form $\hat{c}^\dagger_{c\mathbf{k}}\hat{c}_{v\mathbf{k}}|0\rangle$, with indices c and v denoting conduction and valence bands respectively). As we are neglecting excitonic effects, each singly-excited state $|\psi_{a(b)}\rangle = \hat{c}^\dagger_{c\mathbf{k}}\hat{c}_{v\mathbf{k}}|0\rangle$ contributes individually to the response with an energy $\epsilon_{a(b)} = \epsilon_{c\mathbf{k}} - \epsilon_{v\mathbf{k}}$. At finite temperature, one should consider $|\psi_{a(b)}\rangle = f_i(1-f_j)\hat{c}^\dagger_{j\mathbf{k}}\hat{c}_{i\mathbf{k}}|0\rangle$, where $f_i = (1+\exp[(\epsilon_{i\mathbf{k}}-\mu_c)/k_B T])^{-1}$ is a Fermi-Dirac distribution with chemical potential μ_c.

We can now recast the expression for the Raman intensity in terms of single-particle variables and polarization vectors as:

$$I(\omega) = I_0 \sum_\nu \frac{n_\nu + 1}{\omega_\nu} \left| \sum_{\alpha\beta} u^\alpha_{\text{in}} R^\nu_{\alpha\beta} u^\beta_{\text{out}} \right|^2 \delta(\omega - \omega_\nu), \tag{2.76}$$

where $R^\nu_{\alpha\beta}$ denotes the Raman tensor component for phonon mode ν:

$$\begin{aligned}
R^\nu_{\alpha\beta} \equiv \sum_{ijmn\mathbf{k}} & \left[\frac{p^\alpha_{ij}(g^\nu_{jm}\delta_{in} - g^\nu_{ni}\delta_{jm})p^\beta_{mn}}{(\hbar\omega_{\text{in}}-\epsilon_{ji})(\hbar\omega_{\text{out}}-\epsilon_{mn})} + \frac{p^\alpha_{ij}(p^\beta_{jm}\delta_{in} - p^\beta_{ni}\delta_{jm})g^\nu_{mn}}{(\hbar\omega_{\text{in}}-\epsilon_{ji})(\hbar\omega_\nu-\epsilon_{mn})} \right. \\
& + \frac{p^\beta_{ij}(g^\nu_{jm}\delta_{in} - g^\nu_{ni}\delta_{jm})p^\alpha_{mn}}{(-\hbar\omega_{\text{out}}-\epsilon_{ji})(-\hbar\omega_{\text{in}}-\epsilon_{mn})} + \frac{p^\beta_{ij}(p^\alpha_{jm}\delta_{in} - p^\alpha_{ni}\delta_{jm})g^\nu_{mn}}{(-\hbar\omega_{\text{out}}-\epsilon_{ji})(\hbar\omega_\nu-\epsilon_{mn})} \\
& \left. + \frac{g^\nu_{ij}(p^\alpha_{jm}\delta_{in} - p^\alpha_{ni}\delta_{jm})p^\beta_{mn}}{(-\hbar\omega_\nu-\epsilon_{ji})(\hbar\omega_{\text{out}}-\epsilon_{mn})} + \frac{g^\nu_{ij}(p^\beta_{jm}\delta_{in} - p^\beta_{ni}\delta_{jm})p^\alpha_{mn}}{(-\hbar\omega_\nu-\epsilon_{ji})(-\hbar\omega_{\text{in}}-\epsilon_{mn})} \right] \\
& \times f_i(1-f_j)f_n(1-f_m),
\end{aligned} \tag{2.77}$$

with $\epsilon_{ij} \equiv \epsilon_{i\mathbf{k}} - \epsilon_{j\mathbf{k}}$, $p^\alpha_{ij} \equiv \langle i\mathbf{k}|\hat{p}^\alpha|j\mathbf{k}\rangle = k\delta_{ij} - \langle i\mathbf{k}|\nabla^\alpha|j\mathbf{k}\rangle$, $g^\nu_{ij} \equiv \langle i\mathbf{k}|\partial_{\nu\mathbf{0}}V_{\text{eff}}|j\mathbf{k}\rangle$,

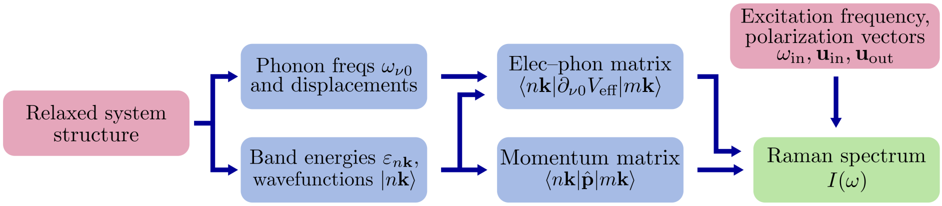

Figure 2.4: Flowchart of the GPAW method for the computation of Raman intensities of a relaxed system structure, for an incident light frequency, and input/output polarization vectors.

and (i, j, m, n) (ν) are the electron (phonon) band indices. The first term in Eq. (2.77) is known as the resonant term, as it diverges when the incident or outgoing photon frequencies are resonant with an interband transition. In practice, a small imaginary part $i\eta$ is added to the photon frequencies ω_{in} and ω_{out} to phenomenologically account for the line-shape broadening, which we have set to 100 meV in this work.

The procedure for computing these intensities within the implementation in GPAW follows the scheme depicted in Fig. 2.4. Starting from the relaxed structures, a DFT calculation is performed to obtain the ground state electronic band energies and wavefunctions. From these quantities, the momentum matrix elements p_{ij}^{α} are computed with a finite-difference scheme and stored. In parallel, the forces and potentials are computed for displaced atomic positions along the Cartesian axes. From these forces, the zone-centered phonons are computed using the finite-difference approach as described in Ref. [208] and implemented within the Atomic Simulation Environment (ASE) package [209], to which GPAW is interfaced. The electron–phonon matrix elements are then evaluated from the electronic states and phonon modes as implemented in GPAW [188]. With that aim, the displaced potentials are used to compute the gradient of the KS potential with a finite-difference scheme [210]. Next, the gradient is projected onto a set of atomic orbitals from an LCAO basis set and transformed to the real-space representation. The final electron–phonon coupling matrix is obtained by projecting the transformed matrix into the ground state wavefunctions and the phonon modes. Finally, the Raman spectrum is obtained from the momentum and electron–phonon matrix elements given an incident light frequency and input/output polarizations.

2.4 Introduction to Bayesian optimization

In this section, we introduce the procedure used in this thesis to tackle the problem of finding the minimum energy configuration of a self-assembled monolayer (SAM) on a metallic surface. In order to obtain the ground-state atomistic structure of a system one needs to minimize its potential energy surface (PES), which correlates the configurational phase-space of the system with its potential energy. Minima of the PES correspond to stable configurations, and its global minimum gives the ground-state geometry. Even though *ab initio* methods described in Section 2.1 allow for the computation of the energy of a nanostructure with a great degree of accuracy, the computational cost of extensively sampling the PES is usually unaffordable. This problem is aggravated for metal–organic environments such as SAMs [42] due to the sheer variety of possible morphologies, i.e., the many possible distributions and orientations of the molecules, which makes regular or random sampling strategies unfeasible. In this context, artificial intelligence methods such as the recently developed Bayesian Optimization Structure Search (BOSS) method [173] are very useful tools to improve sampling efficiency and accelerate structure optimization. BOSS consists on a Bayesian optimization scheme modeling the PES as a *Gaussian process* (see Subsection 2.4.1) fitted to DFT data points, which is refined by the iterative acquisition of more data points according to a smart sampling strategy, which uses a building-block approach to simplify the configurational phase space. In this section, we give an overview on Bayesian optimization, following the recent book by R. Garnett [211], and then discuss its implementation within the BOSS method employed in Chapter 5 to obtain the minimum energy configuration of SAMs.

Let us first briefly discuss the concept of optimization. Having a real-valued *objective function* f defined in some real domain X, $f : X \to \mathbb{R}$, the goal of an optimization procedure is to systematically search for the point x with the globally maximum (or minimum) function value $f(x)$. The iterative procedure can be summarized as follows. We start with an initial dataset $\mathcal{D} = (\mathbf{x}, \mathbf{y})$, consisting on a series of observed values $\mathbf{y}$ at points $\mathbf{x}$, which grows through sequential observations. At each iteration, an optimization policy inspects the available information and selects the location of the next observation. We then add the result of the new observation to the dataset and must decide if we perform another iteration or conclude the optimization process, usually by checking if some predefined termination condition is met. Thus every optimization process requires at least the following ingredients: an *observation model*, an *optimization policy*, and a *termination condition*.

Bayesian optimization is based on the Bayesian method for the statistical inference of uncertain features of a system from observations, in which all unknown quantities are treated as random variables. This allows us to encode our initial beliefs or assumptions about these quantities in their initial probability distributions, and then refine them iteratively as we acquire new information. Suppose we want to infer the value of a certain function f on point x, $\Phi = f(x)$. We first define a *prior probability distribution* (or prior) $p(\Phi \mid x)$ encoding the values we assume plausible. We then perform an observation of the function at x, with a result y, which depends not only on the objective value Φ, but also on the observation model. The distribution explaining the observed values in terms of the objective values is the *likelihood probability distribution* (likelihood) $p(y \mid x, \Phi)$. For example, if our observation model assumes a Gaussian noise, the likelihood will be a Gaussian distribution centered at y. With the new data, we may derive the

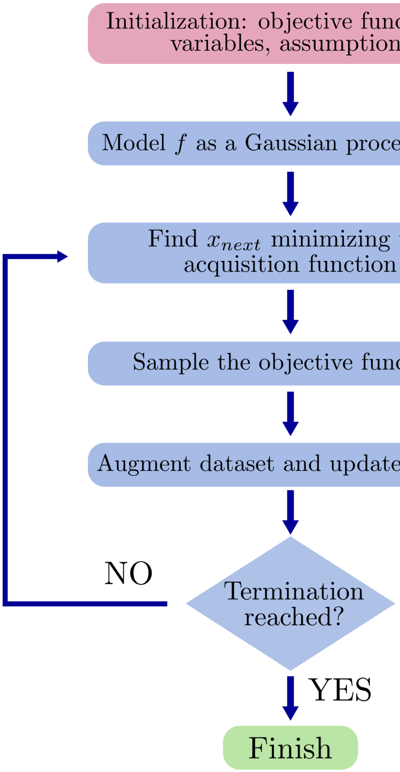

Figure 2.5: Scheme of the Bayesian optimization procedure. The unknown objective function f is modeled as a Gaussian process which encodes all our assumptions about f, such as smoothness, range or periodicity. To gather information, we sample the function at the point given by the acquisition function, and update the Gaussian process model in light of the new data. The sampling continues, governed by the acquisition function, until the convergence criteria are met.

posterior probability distribution (posterior) using Bayes' theorem [211]:

$$p(\Phi \mid x, y) = \frac{p(\Phi \mid x)\, p(y \mid x, \Phi)}{p(y \mid x)}, \tag{2.78}$$

where the denominator is just a normalization constant. Thus, the posterior is proportional to the prior weighted by the likelihood of the observed value. In the case of an exact observation, for example, the likelihood distribution is a Dirac delta distribution $p(y \mid x, \Phi) = \delta(y - \Phi)$, and then one measurement is enough to determine Φ. If that is not the case and we want to perform additional observations, we take the posterior as the new prior and continue the inductive process.

If the object of the inference is a function instead, this probabilistic belief takes the form of a *stochastic process*, this is, an infinite collection of random variables, each of which represents the value of the function at a given point of

Term	Definition
Objective function $f(x) : X \to \mathbb{R}$	Unknown function to minimize.
Gaussian process $p(f) = \mathcal{GP}(f; \mu, K)$	Stochastic process such that the marginal probability distribution for every finite subset of the random variables is a multivariate normal distribution.
Mean function $\mu(x) : X \to \mathbb{R}$	Expected function value at any point in the domain.
Covariance function $K(x, x') : X \times X \to \mathbb{R}$	Function that determines the correlation between function values in different points of the domain.
Hyperparameters	Parameters defining the space of possible surrogate models. In the special case of a GP, the hyperparameters are the parameters defining the prior mean and covariance functions.
Acquisition function $\alpha(x; \mathcal{D}) : X \to \mathbb{R}$	Function that determines the next observation point.

Table 2.1: Glossary with the most relevant terms defined in this section, listed by their order of appearance in the text.

the (multi-dimensional) domain. An intuitive way of understanding stochastic processes is as probability distributions over functions, which return functions when sampled. We start with a *prior process* $p(f)$, which will always be a Gaussian process in our case (see Subsection 2.4.1), encoding all initial assumptions, such as smoothness, range or periodicity. After gathering some data $\mathcal{D}$, we can build the *posterior process* $p(f \mid \mathcal{D})$, which incorporates both our initial assumptions and the information provided by the observations. In the practical case of minimizing a PES, this sampling is done by computing the DFT energy of the system for a given configuration. Then, if the convergence criteria are not met, we sample the objective function again at the position determined by the *acquisition function* (see Subsection 2.4.5), designed to select the optimal sampling position, and obtain the new posterior process. This loop, represented in Fig. 2.5, is repeated until convergence is reached. In the following sections, we describe in more detail the steps of this procedure.

2.4.1 Gaussian processes

Following the Bayesian approach of treating all unknown quantities as random variables, we can model the unknown objective function $f : X \to \mathbb{R}$ as a Gaussian process (GP), which is the generalization of the *Gaussian probability distribution*. The definition of a Gaussian probability distribution, together with other concepts from probability and statistics used throughout this section, is given in Appendix F. The most relevant terms defined in this section are summarized in Table 2.1. A GP is defined as a stochastic process such that the *marginal probability distribution* for every finite subset of the random variables is a *multivariate normal distribution*. Gaussian processes are defined by a *mean function* and a *covariance function*. The mean function $\mu(x) : X \to \mathbb{R}$ determines the expected function value $\Phi = f(x)$ at any point in the domain:

$$\mu(x) = \mathbb{E}[\Phi \mid x], \tag{2.79}$$

and the covariance function $K(x, x') : X \times X \to \mathbb{R}$, which must be positive semidefinite, determines how deviations from the mean are structured:

$$K(x, x') = \operatorname{cov}[\Phi, \Phi' \mid x, x']. \tag{2.80}$$

Knowing the mean and covariance functions of the process, we can compute the marginal distribution of function values $\boldsymbol{\Phi}$ for any finite set of points $\mathbf{x}$ on demand, which, by definition, will be a multivariate normal distribution:

$$p(\boldsymbol{\Phi} \mid \mathbf{x}) = \mathcal{N}(\boldsymbol{\Phi}; \boldsymbol{\mu}, \boldsymbol{\Sigma}), \tag{2.81}$$

whose mean vector $\boldsymbol{\mu}$ and Gram matrix $\boldsymbol{\Sigma}$ are determined by the mean and covariance functions:

$$\boldsymbol{\mu} = \mu(\mathbf{x}), \quad \boldsymbol{\Sigma} = K(\mathbf{x}, \mathbf{x}) = \sum_{i,j} K(x_i, x_j). \tag{2.82}$$

By extension, the marginal distribution of the function value at a single point is a univariate normal, and the pointwise variance $\sigma^2 = K(x, x)$ provides a measure of the model uncertainty at the location.

Let us now have a look at an example GP. Suppose we want to model the objective function $f(x) = \sin(x) + 1.5 \exp(-(x - 4.3)^2)$ in the domain $X = [0, 7]$. A sensible choice for the prior distribution could be a GP with mean function $\mu(x) = 0$ and the squared exponential covariance function, defined as

$$K(x, x') = \exp(-\frac{1}{2}|x - x'|^2). \tag{2.83}$$

We represent this GP, together with some functions sampled from it, in Fig. 2.6a. The shadowed region is the 95% (or 2σ) confidence interval, which stands for the uncertainty of the model at each point. Since we have not acquired any information yet, the uncertainty is the same in all X.

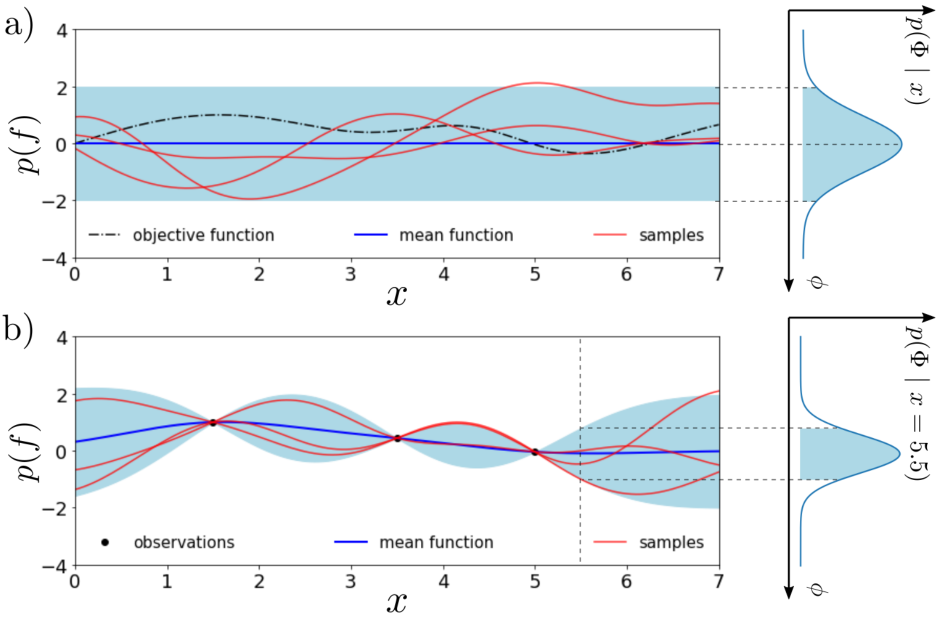

Figure 2.6: a) Representation of a GP in $X = [0, 7]$ with zero mean function (in blue) and squared exponential covariance. The shaded area represents the 95% confidence interval (this is, 2σ). The red lines depict three possible realizations of this GP, which were drawn by defining a grid of 140 equidistant points in the domain and taking random samples from their corresponding marginal distribution following Eq. (2.81). The black dashed-dotted line stands for the objective function we are trying to model with this GP, $f(x) = \sin(x) + 1.5\exp(-(x - 4.3)^2)$. The probability distribution for any function value $\Phi = f(x)$ is a Gaussian distribution with mean $\mu = \mu(x)$ and variance $\sigma^2 = K(x, x)$. b) Posterior process obtained by conditioning the GP in (a) on three exact observations of the objective function at positions $x = [1.5, 3.5, 5]$, marked with black dots. In blue, we plot the posterior mean function and the shaded region representing the 95% confidence interval, together with three exemplary realizations of the process in red. The probability distribution for any function value $\Phi = f(x)$ is still a Gaussian distribution, but now the mean $\mu = \mu_{\mathcal{D}}(x)$ and variance $\sigma^2 = K_{\mathcal{D}}(x, x)$ vary through the domain. The right side plot illustrates the probability distribution for $\Phi = f(x = 5.5)$.

Inference

In Bayesian inference, our previous assumptions about the function are updated in light of the new information. We start by initializing the surrogate GP with covariance and mean functions encoding our prior assumptions about the objective function. This prior process can then be conditioned to acquired data $\mathcal{D} = \{(\mathbf{x_i}, \mathbf{y_i}) \mid i = 1, ..., n\}$, which yields a posterior process reflecting both our prior assumptions and the information contained in the data. If the observations are exact or there is only an additive Gaussian noise, the posterior is also a GP, which allows us to continue updating the model as we perform successive observations.

It is possible to condition a Gaussian process $p(f) = \mathcal{GP}(f; \mu, K)$ on any vector of observations $\mathbf{y}$, as long as they share a joint Gaussian distribution. Such *joint distribution* is denoted as

$$p(f, \mathbf{y}) = \mathcal{GP}\left(\begin{bmatrix} f \\ \mathbf{y} \end{bmatrix}; \begin{bmatrix} \mu \\ \mathbf{m} \end{bmatrix}, \begin{bmatrix} K & \kappa^T \\ \kappa & \mathbf{C} \end{bmatrix}\right), \tag{2.84}$$

where $\mathbf{m}$ and $\mathbf{C}$ are the mean vector and Gram matrix defining the marginal probability distribution on $\mathbf{y}$

$$p(\mathbf{y}) = \mathcal{N}(\mathbf{y}; \mathbf{m}, \mathbf{C}), \tag{2.85}$$

and $\kappa(x)$ is the *cross-covariance* function between $\mathbf{y}$ and f

$$\kappa(x) = \operatorname{cov}[\mathbf{y}, \Phi \mid x]. \tag{2.86}$$

Conditioning the joint distribution on the observed data $\mathcal{D} = (\mathbf{x}, \mathbf{y})$ yields the posterior process

$$p(f \mid \mathcal{D}) = \mathcal{GP}(f; \mu_{\mathcal{D}}, K_{\mathcal{D}}), \tag{2.87}$$

where

$$\mu_{\mathcal{D}}(x) = \mu(x) + \kappa(x)^T \mathbf{C}^{-1}(\mathbf{y} - \mathbf{m}), \tag{2.88}$$

$$K_{\mathcal{D}}(x, x') = K(x, x') - \kappa(x)^T \mathbf{C}^{-1} \kappa(x'). \tag{2.89}$$

In the case of exact observations, any observation vector shares a joint Gaussian distribution with any other set of function values, which allows us to perform the conditioning procedure described above. If we observe the objective function f at some points $\mathbf{x}$, obtaining the corresponding function values $\boldsymbol{\Phi} = f(\mathbf{x})$, we can compute the posterior by conditioning the prior GP on the gathered data $\mathcal{D} = (\mathbf{x}, \boldsymbol{\Phi})$. The marginal distribution of $\boldsymbol{\Phi}$ is Gaussian:

$$p(\boldsymbol{\Phi} \mid \mathbf{x}) = \mathcal{N}(\boldsymbol{\Phi}; \boldsymbol{\mu}, \boldsymbol{\Sigma}), \tag{2.90}$$

and the cross-covariance between the observed data and any function value will be given by the covariance function:

$$\kappa(x) = \operatorname{cov}[\boldsymbol{\Phi}, \Phi \mid \mathbf{x}, x] = K(\mathbf{x}, x). \tag{2.91}$$

Thus the posterior process will be:

$$p(f \mid \mathcal{D}) = \mathcal{GP}(f; \mu_{\mathcal{D}}, K_{\mathcal{D}}), \tag{2.92}$$

with

$$\mu_{\mathcal{D}}(x) = \mu(x) + K(x, \mathbf{x})^T \boldsymbol{\Sigma}^{-1}(\boldsymbol{\Phi} - \boldsymbol{\mu}), \tag{2.93}$$

$$K_{\mathcal{D}}(x, x') = K(x, x') - K(x, \mathbf{x})^T \boldsymbol{\Sigma}^{-1} K(\mathbf{x}, x'). \tag{2.94}$$

Let us now illustrate how this conditioning procedure works using the objective function and the prior Gaussian distribution in Fig. 2.6a. Suppose that we observe the objective function at three different locations $x = [1.5, 3.5, 5]$. Then, we could update our prior GP to include this new information as described in equations (2.93) and (2.94). This leads to the posterior process represented in Fig. 2.6b, which shows how the acquired information has changed our beliefs about the objective function. As it can be seen, the posterior mean smoothly interpolates through the observed values, while the uncertainty (represented by the 95% confidence interval) quickly diminishes in their vicinity, until it vanishes at their location. At the unexplored regions, however, the posterior process remains very similar to the prior. This illustrates how GPs are an excellent way of combining our prior assumptions about the objective function with observational data. Furthermore, the conditioning procedure can also be performed in a similar way for noisy observations, as long as the probability distribution of the noise is Gaussian. We will now briefly discuss the importance of the mean and covariance functions, and how they should be dealt with in the optimization framework.

2.4.2 The mean function

As we have already defined in Eq. (2.79), the mean function of a GP gives the expected value of the objective function at any location. However, the choice of the *prior mean function* is usually not a great concern in optimization processes, because the behavior of the sample paths is mostly determined by the covariance function. In fact, the sample paths of a GP, $\mathcal{GP}(f; \mu, K)$, are equivalent to the ones of the centered process $\mathcal{GP}(f - \mu; 0, K)$ except for a pointwise shift of μ. This is, the sample paths of any GP with the same covariance function are effectively the same up to translation.

As we can see from the expressions for the posterior process in Eq. (2.93), the prior mean function only influences the posterior process through the *posterior mean function*. In regions where $K(x, \mathbf{x})$ is large, which means that function values are strongly correlated with observation values, the posterior mean will diverge from the prior mean, whereas in regions where the correlation with observations is smaller the posterior mean will be close to the prior. Therefore, the main effect of the prior mean will be to set the posterior mean for extrapolatory regions far away from the measured data. Figure 2.6b provides us with an example of this behavior: the posterior mean at the central region is determined mainly by the observations, while at the extremes it tends to the prior zero mean. For all of this, the most common choice for prior mean function is a constant, especially when we don't have any prior knowledge pointing to other options. The special case in which $\mu = 0$ is called a *centered Gaussian process*.

2.4.3 The covariance function

Most fundamental properties of sample path behavior are determined by the covariance function. It can be understood as a measure of similarity between points in the domain, because, after normalization, it gives us the correlation between function values for different points:

$$\rho = \mathrm{corr}[\Phi, \Phi' \mid x, x'] = \frac{K(x, x')}{\sqrt{K(x, x)K(x', x')}}. \tag{2.95}$$

For a covariance function to be valid it must be symmetric and positive semidefinite (this is, all eigenvalues of the Gram matrix $K(\mathbf{x}, \mathbf{x})$ must be nonnegative).

A covariance function $K(x, x')$ will be *stationary* if it only depends on the difference $x - x'$, which allows us to write it in terms of a single input. If it is combined with a constant mean, then the process itself is considered to be stationary. This means that translation does not affect the distribution of a given set of function variables, and thus finding the local behavior of a function around a given point defines its global behavior, which is a very convenient property for modeling. A covariance function depending only on the Euclidean distance $d_{\mathrm{E}} = |x - x'|$ is called *isotropic*, and will be invariant under both translation and rotation. Typical covariance functions are isotropic, such as the ones we describe next.

The Matérn family

The *Matérn family* is a widely used class of covariance functions which allows for modeling isotropic behaviors of any desired degree of smoothness. They are defined as

$$K_{M(\nu)} = \frac{1}{2^{\nu-1}\Gamma(\nu)} \left(\sqrt{2\nu} d_{\mathrm{E}}\right)^{\nu} K_{\nu}(\sqrt{2\nu} d_{\mathrm{E}}), \tag{2.96}$$

where $\Gamma(\nu)$ are Gamma functions and K_ν are modified Bessel functions of the second kind. The parameter ν is directly related to the smoothness, as sample paths from a centered GP using this covariance are k times differentiable only if $\nu > k$, and it is almost always taken to be a half-integer. The extreme cases of Matérn covariances are the exponential covariance with $\nu = 1/2$:

$$K_{M(1/2)} = \exp(-d_{\mathrm{E}}), \tag{2.97}$$

which gives sample paths that are continuous but nowhere differentiable, and the squared exponential covariance with $\nu = \infty$

$$K_{M(\infty)} = K_{\mathrm{SE}} = \exp(-\frac{1}{2} d_{\mathrm{E}}^2), \tag{2.98}$$

which produces infinitely differentiable sample paths. The squared exponential kernel is the most popular covariance function in statistics and machine learning, but infinite differentiability may be an unreasonable assumption for most physical systems. Therefore, the intermediate cases $\nu = 3/2$ and $\nu = 5/2$ (once and twice differentiable) are sometimes more appropriate. In Fig. 2.7 we show sample paths produced by these two covariances and the squared exponential covariance for centered GPs.

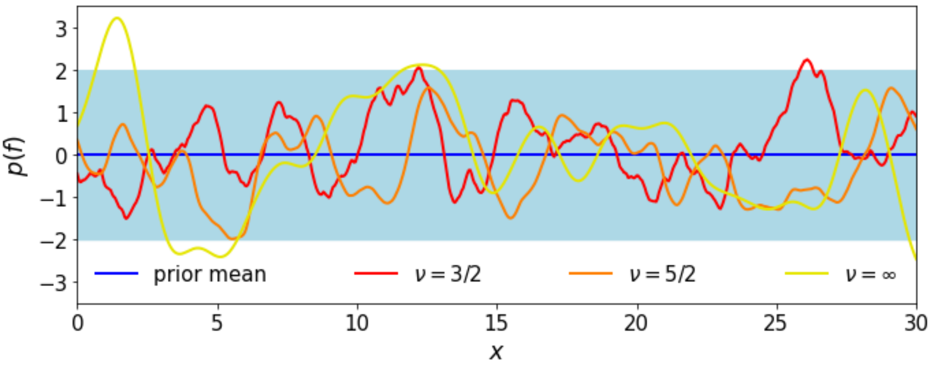

Figure 2.7: Sample paths for three different centered GPs with Matérn covariances as in Eq. (2.96) of increasing ν values, from $\nu = 3/2$ (red) to $\nu = \infty$ (yellow), illustrating the increasing smoothness with increasing ν. The blue line denotes the mean function shared by all, and the shaded region is the 95% confidence interval.

Modification of covariance functions

Even though the presented covariance functions are too rigid to be universally valid, we can achieve a great deal of flexibility by introducing modifications to these simple functions. For all the previously described functions, the pointwise variance is always equal to 1, which is just an arbitrary choice of scale. Fortunately, it is possible to easily re-scale the amplitude of the sample paths. If we have a function $f : X \to \mathbb{R}$ with covariance K, and a scaling function $a : X \to \mathbb{R}$, then the covariance function of the scaled function $a(x)f(x)$ will be

$$\operatorname{cov}[af \mid a] = a(x)K(x, x')a(x'). \tag{2.99}$$

If the scaling function is a constant $a(x) = \lambda_{\mathrm{os}}$, then the new covariance is just $\lambda_{\mathrm{os}}^2 K(x, x')$. We may then extend a base covariance function into a parametric family of covariance functions with an arbitrary scale $K'(x, x'; \lambda) = \lambda_{\mathrm{os}}^2 K(x, x')$, where λ_{os} is known as the *output scale*. The influence of the output scale in the amplitude of sample paths can be observed in Fig. 2.8a.

Another important trait of covariance functions is the characteristic length scale, which is related to how fast sample paths change. For the previous examples, it was approximately 1, which means that if two points in the domain are separated a distance $d_{\mathrm{E}} = |x - x'| \approx 1$, the correlation between their function values drops to 1/2. We can change this scale by applying the dilation $\mathbf{x} \to \mathbf{x}/l_{\mathrm{s}}$, producing a new parametric family of covariance functions

$$K'(x, x'; l_{\mathrm{s}}) = K(d_{\mathrm{E}}/l_{\mathrm{s}}). \tag{2.100}$$

For a base covariance K of unit length scale, the length scale of the dilated covariance K' is just l_{s}, so we directly call this parameter the *length scale*. As we

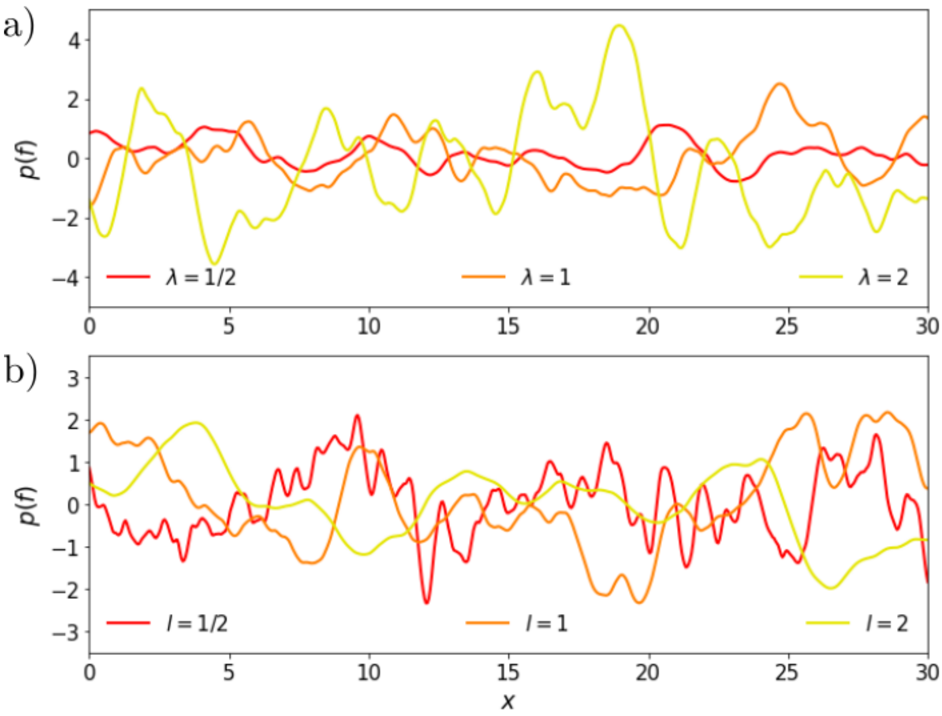

Figure 2.8: a) Sample paths for the Matérn covariance with $\nu = 5/2$ for values of the output scale $\lambda_{\text{os}} = 1/2$ (red), $\lambda_{\text{os}} = 1$ (orange), and $\lambda_{\text{os}} = 2$ (yellow). b) Sample paths for the Matérn covariance with $\nu = 5/2$ for values of the length scale $l_{\text{s}} = 1/2$ (red), $l_{\text{s}} = 1$ (orange), and $l_{\text{s}} = 2$ (yellow).

can see in Fig. 2.8b, large values of the length scale produce smooth sample paths, whereas shorter lengths create wiggly samples.

If these transformations are not enough, one can take advantage of the fact that the addition or the pointwise multiplication of two different covariance functions results in another valid covariance function, which allows us to use any polynomial combination of simple covariances to model complex function behaviors. Furthermore, it is also possible to apply nonlinear transformations to the domain in order to impose some structure. The simplest example is to map the domain into a periodic function, for example $x \to r\cos(x)$, and redefine one of the previous covariance functions in that space, which yields a perfect correlation between points separated by any multiple of the period $2\pi r$.

2.4.4 Model assessment

While the flexibility of GPs allows for modeling functions with a wide range of different behaviors, it also gives rise to a nontrivial question: how do we select a model that is appropriate for our objective function? As we showed in the previous subsection, we could use any mean function for our GP model, and the covariance function can be made arbitrarily complex. Usually, the situation is even further complicated due to the lack of prior information about the shape of the objective function or the nature of the observation model.

Fortunately, we can postpone this decision until we have acquired some data, as it is then possible to assess which models are more compatible with these data. To do so, we first have to define a space of models to be considered, which in the case of GPs will consist in parametric mean and covariance functions, and an observation model. The parameters of these model components (as could be, for example, the length scales of the covariance function) will be known as *hyperparameters*. We can then treat these hyperparameters as random variables to be inferred, and assess the adequacy of the models in the space of models by performing Bayesian inference over the hyperparameters from the observed data.

Let's consider the following simple space of candidate models:

- Observation model: additive homoskedastic (this is, the variance is the same in all the domain) Gaussian noise with variance σ_n^2.
- Mean function: Constant zero mean function.
- Covariance function: Matérn covariance function ($\nu = 5/2$) with unknown output and length scales $\lambda_{\mathrm{os}}, l_{\mathrm{s}}$:

$$K(x, x'; \lambda_{\mathrm{os}}, l_{\mathrm{s}}) = \lambda_{\mathrm{os}}^2 K_{M(5/2)}(d_{\mathrm{E}}/l_{\mathrm{s}}) \tag{2.101}$$

This defines a model space with three hyperparameters $\boldsymbol{\Theta} = [\sigma_n, \lambda_{\mathrm{os}}, l_{\mathrm{s}}]$. We denote such a model space as

$$p(f \mid \boldsymbol{\Theta}) = \mathcal{GP}\left(f; \mu(x, \boldsymbol{\Theta}), K(x, x'; \boldsymbol{\Theta})\right) = \mathcal{GP}\left(f; 0, K(x, x'; \boldsymbol{\Theta})\right). \tag{2.102}$$

Our initial beliefs about the plausibility of the models in this model space are encoded in the model prior distribution $p(\boldsymbol{\Theta})$. This distribution is often taken to be an uninformative constant for convenience. However, in some cases we can make informed assumptions about the nature of our objective function that can be encoded here. This is especially true for physical systems, for which the order of magnitude of lenghtscales and amplitudes can usually be estimated.

After we have performed some observations $\mathcal{D} = (\mathbf{x}, \mathbf{y})$, the posterior distribution over the proposed models can be obtained via Bayes' theorem:

$$p(\boldsymbol{\Theta} \mid \mathcal{D}) \propto p(\boldsymbol{\Theta})\; p(\mathbf{y} \mid \mathbf{x}, \boldsymbol{\Theta}). \tag{2.103}$$

The term $p(\mathbf{y} \mid \mathbf{x}, \boldsymbol{\Theta})$ determines how consistent a given model is with the data, and is known as the *model evidence*. The most straightforward way of model selection is to choose the hyperparameters maximizing the posterior model distribution $p(\boldsymbol{\Theta} \mid \mathcal{D})$, which, in the case of uninformative priors, reduces to a maximization of the model evidence $p(\mathbf{y} \mid \mathbf{x}, \boldsymbol{\Theta})$. This can be understood as selecting the model which better explains the acquired data. Conveniently, when dealing with GP models with additive Gaussian noise the model evidence can be computed as a closed expression:

$$p(\mathbf{y} \mid \mathbf{x}, \boldsymbol{\Theta}) = \mathcal{N}(\mathbf{y}; \boldsymbol{\mu}, \boldsymbol{\Sigma} + \mathbf{N}), \tag{2.104}$$

where $\mathbf{N}$ is the covariance matrix of the observation noise (which is the zero matrix for exact observations), and $\boldsymbol{\mu}$ and $\boldsymbol{\Sigma}$ are the prior mean and covariance of the latent objective function values $\boldsymbol{\Phi}$ (see Eq. (2.82)).

2.4.5 The acquisition function

At the core of an optimization procedure lays the optimization policy, whose role is to analyze the already gathered data and take the crucial decision of where to make the next observation. This is usually done by defining an *acquisition function* $\alpha : X \to \mathbb{R}$, which assigns a score to every point in the domain, reflecting our preferences over locations for the next observation. These functions are usually designed with the goal of selecting locations that would return the most useful information, this is, that would maximize some *utility* $u(\mathcal{D})$. However, there are many valid ways to define this utility, and therefore a wide array of possible acquisition functions. Thus, before even beginning the optimization process, we must set our preferences regarding the acquisition of new data.

Usually, most optimization policies are of the *one-step lookahead* type, this is, they only consider the increase in utility that the next measure will provide. Though it is possible to design policies taking into account all remaining observations until the end of the optimization process, the cost of these computations increases exponentially. Since one-step lookahead policies are good enough for most cases, we will stick to this type of policies.

Regardless of how they are designed, all acquisition functions must address the dilemma between *exploitation*, which means sampling where the objective function is expected to be high, and *exploration*, which means sampling where the uncertainty is high. An acquisition function that is too exploitative could get bogged down around the local minima that are already known, while an excess of exploration may slow down the optimization by sampling at less relevant locations.

Expected improvement

A typical example of acquisition function is the *expected improvement*, a one-step lookahead acquisition function which selects the observation location maximizing the simple reward utility

$$u(\mathcal{D}) = \min\, \mu_{\mathcal{D}}(\mathbf{x}), \tag{2.105}$$

this is, the minimum value of the posterior mean at the observation locations. In the case of exact observations, the utility of a dataset is just the minimal observed value

$$u(\mathcal{D}) = \Phi^* = \min\, (\boldsymbol{\Phi}), \tag{2.106}$$

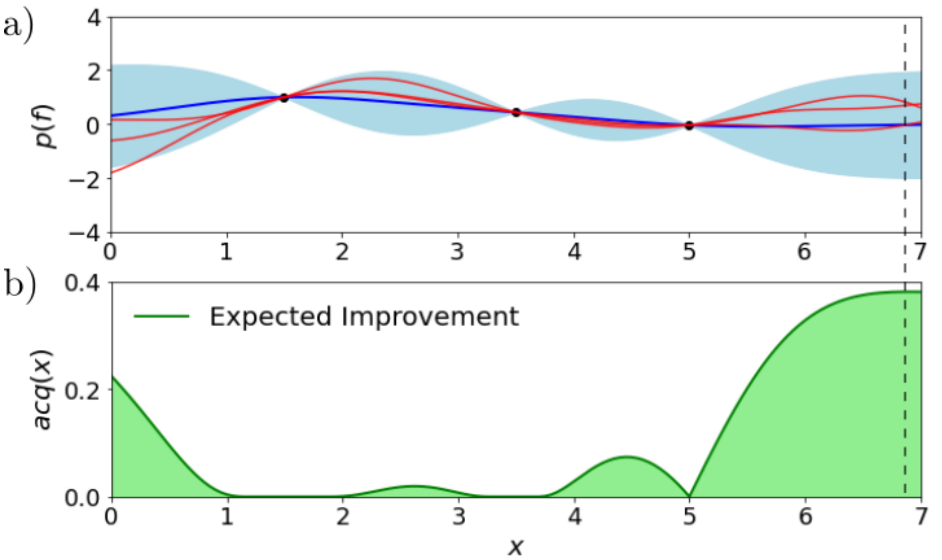

Figure 2.9: a) Gaussian process in Fig. 2.6b. b) Expected improvement acquisition function following Eq. (2.108), computed for the Gaussian process in a). The dashed line at $x \simeq 7$ marks the maximum of the acquisition function, which is the recommended next observation location.

and the change in utility by adding a new measure (x, Φ) to the dataset is just

$$u(\mathcal{D}') = \min(\Phi^*, \Phi). \tag{2.107}$$

From this utility we can derive the expected improvement acquisition function for any point in X, given a current dataset $\mathcal{D}$

$$\alpha_{\mathrm{EI}}(x; \mathcal{D}) = \int d\Phi \, \max(\Phi^* - \Phi, 0) \; p(\Phi \mid x, D), \tag{2.108}$$

where $p(\Phi \mid x, D)$ is the probability of a measure at x returning value Φ, given the available data $\mathcal{D}$. By definition, this probability distribution will be a Gaussian centered at the prior mean value $\mu(x)$, and with variance $K(x, x)$. Notice that, although we have defined this acquisition function for a minimization problem, an equivalent function for a maximization problem can be straightforwardly obtained just by changing the utility to $u'(\mathcal{D}) = \max\, \mu_{\mathcal{D}}(\mathbf{x})$.

As an example, we show in Fig. 2.9b the expected improvement computed for the GP in Fig. 2.6, which we also reproduce in Fig. 2.9a as a reference. It vanishes at the locations of the previous observations, as it is impossible to improve the simple reward by measuring there, and increases at the high uncertainty regions. However, uncertainty is not the only aspect shaping the acquisition function, as it can be seen by examining the two highest uncertainty regions: the left and right extremes of the domain. In both cases the high uncertainty means that there is some probability of a measure returning a value smaller than any of the available observations, and thus the expected improvement is not zero, but the mean function takes smaller values in the right extreme. Therefore, it will be more likely to improve the current minimum by measuring there, which translates into higher values for the acquisition function. The dashed line marks the location maximizing the expected improvement, and it will thus be the next sampling location recommended by this acquisition function.

Lower confidence bound

Throughout this thesis, we have used the *exploration-modified lower confidence bound* (eLCB) acquisition function, defined as [212]

$$\alpha_{\mathrm{eLCB}}(x) = -\mu(x) + \kappa_t \sigma(x), \tag{2.109}$$

where t denotes the optimization step, and $\kappa_t = 2\log[t^{d/2+2}\pi^2/(3\epsilon_{\mathrm{ac}})]$, with ϵ_{ac} being a small constant. This acquisition function yields a good compromise between exploitation, as the first term favors sampling in regions where the expected value is small, and exploration, as the second term encourages sampling in high uncertainty regions. The trade-off between both is governed by κ_t, which increases with the optimization step to encourage exploration and avoid getting bogged down on local minima.

Cost Functions

Sometimes, it can be useful to modify the acquisition functions to include criteria that cannot be easily expressed with the information provided by the prior process. For example, it could happen that measurements at different points or regions of the domain X have different associated costs. In this case, it may be helpful to penalize observations with a high cost in order to improve the speed of the optimization process. However, this difference in cost cannot be taken into account by acquisition functions defined directly from the prior process, and we must resort to other techniques. A convenient way of doing it is by modifying the acquisition function by adding a cost function modeling this behavior. We discuss a particular case of cost function in Chapter 5, in which a specific cost function is used in order to avoid sampling unphysical system configurations.

2.4.6 Bayesian Optimization Structure Search (BOSS)

To search for the minima of the PES in Chapter 5 we have used the Bayesian Optimization Structure Search (BOSS) code [173], which is designed for inferring the structure of metal–organic interfaces. It models the PES as a surrogate Gaussian process (see subsection 2.4.1) fitted to data sampled iteratively with DFT energy calculations. The sampling is governed by an acquisition function (see Subsection 2.4.5) efficiently searching for the global energy minimum. To reduce the dimensionality of the configurational phase space, the system is divided into rigid 'building blocks' chosen according to chemical rules. For our calculations, we selected a zero prior mean, the squared exponential kernel (or the standard periodic kernel [213] for periodic variables), and the eLCB acquisition function. The details about the configurational space and the steps carried for the PES optimization are explained in Chapter 5.

Using BOSS

Let us briefly illustrate how a BOSS search works with a simple physical example. Assume we have a CO_2 molecule, whose linear geometry is displayed in Fig. 2.10a, and that we do not know the optimal C–O bond length ℓ_{CO}, which is the one minimizing the energy of the system E. Although the function f relating ℓ_{CO} an E is also unknown, we can "observe" it by computing the DFT energy for a given bond length, and therefore we can use BOSS to search for the global minimum of f. For this purpose, we first need to define the search space, this is, the range of ℓ_{CO} values to be considered, which we set as the interval between 0.5 Å and 1.5 Å. Then we must choose the initial specifications of the surrogate model, which will be a GP with zero mean and the squared exponential kernel. In order to initialize the model hyperparameters, a rough estimation of the range of function values is also required. Finally, we need to select an acquisition function, which will be eLCB in this case.

After introducing all these initial data, we are ready to start the optimization procedure. Since we know little about the objective function f initially, the algorithm first realizes some observations at predetermined equidistant points, without taking the output into account. The number of initial observations can be fixed by the user, and we set it to two for this example. In Fig. 2.10b, we depict the posterior surrogate GP model after these two observations. The acquired data points are represented as red circles, the posterior mean function μ as a blue line, and the posterior uncertainty as a shaded gray region. The position of the predicted global minimum x_{min}, this is, the point with the minimum mean function value, is marked by a vertical red line. When the initial data points have been acquired, the next observation location x_{next}, marked by a green dashed line, is determined by the acquisition function. In Fig. 2.10c, we depict the posterior surrogate GP model after one additional observation is made. We then let the process continue for some more acquisitions until we reach the situation depicted in Fig. 2.10d, in which the global minimum position is already clearly determined, after a total of seven acquisitions. Here we can see the competing principles of exploration and exploitation at play. The first is represented by the acquisitions at the domain edges, as well as by the recommended next acquisition location, which is in a region with the largest current uncertainty, but where a low-energy value is highly unlikely. The second is represented by the small cluster of observations close to the global minimum, which allowed to fine-tune its position.

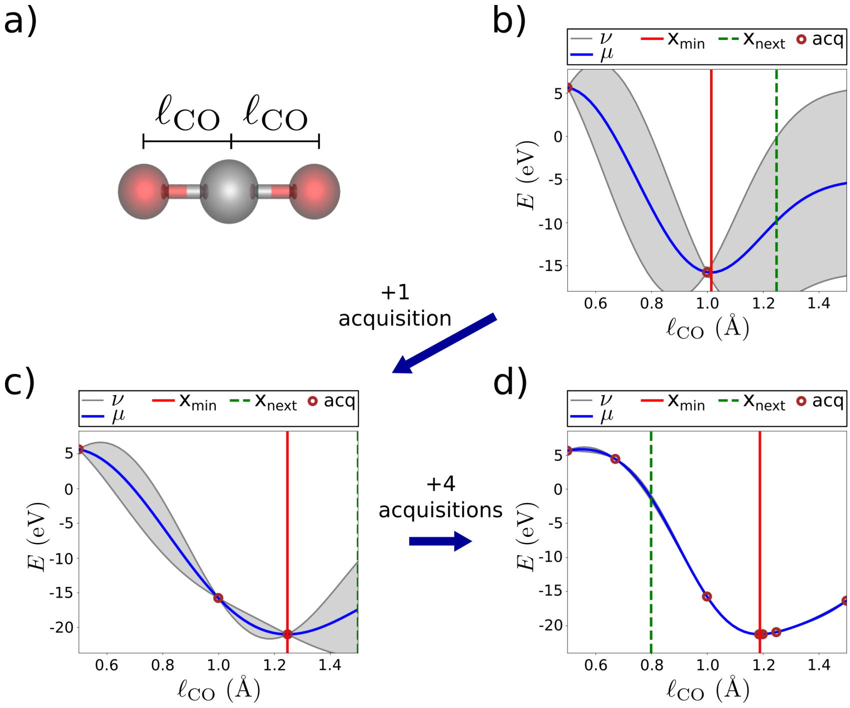

Figure 2.10: a) Illustration of the CO_2 molecule with bond length ℓ_{CO}. Oxygen atoms are depicted in red, and the carbon atom in gray. b) Posterior GP after the two initial acquisitions, which are marked as red circles. The posterior mean function μ and the variance ν are represented in blue and gray, respectively. The vertical red line indicates the estimated position of the global minimum x_{min}, whereas the vertical dashed green line indicates the next observation location x_{next}. c) Posterior GP after a total of three acquisitions. d) Posterior GP after a total of seven acquisitions.

2.5 Summary

In this chapter, we have reviewed the methodologies employed in this thesis for the computational simulation of the optical response of nanostructures. We have provided a brief overview of the DFT method used for computing the ground-state density and the derived properties in Section 2.1, followed by the description of the linear-response TDDFT formalism for obtaining the excitation properties of the studied systems in Section 2.2. Then we have focused on the LCAO method implemented by the PyNAO code for computing the response of nanostructures as probed by both light and electron beams used in Chapters 3 and 4. Thereafter, in Section 2.3, we have described the method for obtaining the first-order Raman intensity from electron–phonon interactions used in the SERS study of self-assembled monolayers in Chapter 5. Finally, in Section 2.4 we have provided an overview on Bayesian optimization and described the Bayesian

Optimization Structure Search method, which we employ in Chapter 5 to search for stable configurations of organic molecules adsorbed on a gold substrate in order to obtain their Raman spectrum.

CHAPTER 3

INFLUENCE OF ATOMISTIC FEATURES IN PLASMON–EXCITON COUPLING

As described in Chapter 1, plasmonic nanocavities allow for an extreme localization of the induced electric field at optical frequencies [82]. When a quantum emitter, such as an organic molecule, is placed inside such a cavity, its electronic transitions (i. e., excitons) can couple to the electromagnetic modes of the plasmonic cavity, which in the strong-coupling regime leads to the formation of hybrid light–matter states so-called polaritons [28, 30] as related in Section 1.4. Under certain conditions, the emergence of these new modes allows for tuning the optical properties of the emitter. In the last years, this has led to the proposal of many applications in fields such as photochemistry [31–33], single-photon emission [34], electroluminiscence [35], and exciton transport [36, 214], among others.

The optical response of molecules coupled to metallic nanoparticles (MNPs) is often described within the classical electrodynamics framework introduced in Chapter 1 [215], in which the electronic transitions of the molecules are approximated as point dipoles, and the optical response of plasmonic cavities is described within the dielectric formalism. Nevertheless, the extreme electromagnetic field localization induced by nanoscale plasmonic cavities may result in the generation of a local inhomogeneous field experienced by the molecule. In such a situation, the widely used model of a point-dipole subjected to a specific homogeneous field would fail to correctly capture the plasmon–exciton interaction [216, 217]. Moreover, the classical description of the cavity is not able to address quantum phenomena arising at narrow gaps, such as the spill in/out of the induced charge density at the interfaces [60, 218–220], or charge transfer between the

MNPs and the molecule [10, 221] (see Section 1.2.5). Although comprehensively accounting for all these phenomena within a single framework remains challenging, the shortcomings of classical methods have lead to the development of a wide variety of semiclassical and quantum approaches to describe plasmon–exciton coupling in the last years [222–224].

The aforementioned effects can be addressed with the use of quantum many-body frameworks [27, 225], which offer suitable tools to describe molecule–MNPs coupled systems in subnanometric cavities, when the system is small enough as to be computationally affordable. Different approaches have been successfully implemented within time-dependent density functional theory (TDDFT) to describe quantum phenomena occurring in hybrid molecule–MNP systems, such as charge transfer [226–228], or chemical enhancement in surface-enhanced Raman scattering [41, 229]. Recent theoretical works have also reliably reproduced the strong-coupling regime between metallic clusters and molecules by first-principles modeling [24, 25, 230], and calculations with simplified jellium models have also suggested that the molecule–MNPs coupling can be significantly perturbed by quantum effects arising at sub-nanometric distances, such as the hybridization between the atomic orbitals of the molecule and the electronic wavefunctions of the metal [231]. Furthermore, atomistic TDDFT methods naturally account for geometrical features of the hybrid system, which have significant influence in the detailed optical response in extreme nano- and pico-cavities [27, 225, 232].

In this chapter, we analyze the optical response of a coupled molecule–MNP dimer system from an atomistic ab initio perspective within the linear-response TDDFT framework, implemented in the PyNAO code [98] (see Section 2.2), which uses a basis set of numerical atomic orbitals and norm-conserving pseudopotentials. This computational tool offers a fully quantum description of the optical response of a nanosystem incorporating all the aforementioned quantum phenomena, while accounting for its atomistic features. We start by describing the optical response of bare silver clusters and dimers in Section 3.1 for reference. Then, in Section 3.2 we focus our analysis on the optical response of a molecule–MNP dimer system, which for dimer gaps smaller than 2 nanometers strongly depends on the specific atomistic features of the nanocavity. Indeed, as we show in Section 3.3, the atomistic morphology of the cavity at these extreme dimensions significantly affects the coupling strength, and the molecule–MNPs coupling can be quenched for certain atomistic configurations of the cavity due to the electronic coupling between molecular and metallic orbitals. Finally, in Section 3.4 we explore the emergence of charge-transfer modes, and show that this process is also determined by the atomistic configuration of the cavity.

3.1 Optical response of silver clusters and dimers

We have focused our study on atomistic silver MNPs, one of the most widely used metals in nanophotonics, thanks to its sharp plasmonic resonance at visible frequencies and to its reduced chemical activity. We model them as an icosahedral

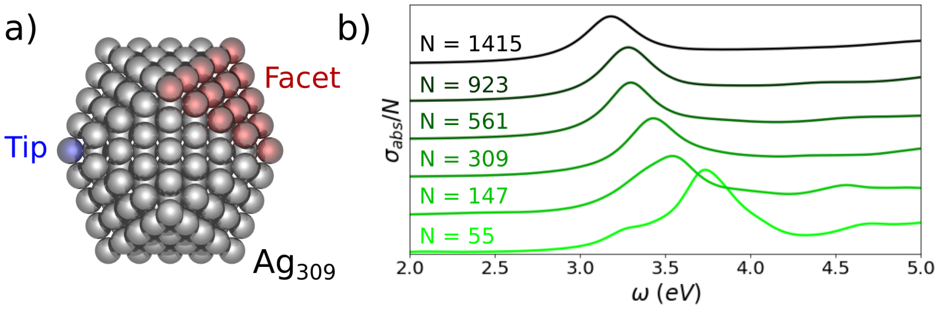

Figure 3.1: a) Atomistic structure of an Ag_{309} icosahedral cluster. The main geometrical features are highlighted: in blue, the atom defining one of the cluster tips, and in red, the atoms defining one of its facets. b) Normalized absorption spectra of silver icosahedral clusters with increasing number of atoms N.

body, which is a very stable configuration for small metallic clusters [233, 234]. To obtain their exact geometries, we first optimized the lattice constant of ideal icosahedral clusters by computing the ground-state energy with *ab initio* DFT as a function of the lattice constant, and searching for the minimum in the curve. After identifying the optimal lattice constant, we used it to build perfect icosahedral clusters of varying sizes, which we then relaxed until the residual atomic forces were smaller than 0.02 eV/Å. In Fig. 3.1a, we show the Ag_{309} cluster as an example of such a geometry. The nanoparticle displays clearly defined geometrical features, such as tips and facets, highlighted in the figure in blue and red, respectively. All the DFT ground-state calculations were performed using the SIESTA code [111] and the GGA exchange–correlation functional developed by Wu and Cohen [182] (see Appendix C), which has been shown to correctly reproduce the experimental lattice constant and bulk modulus of silver [235]. We used a double-ζ polarized basis set of numerical atomic orbitals (see Appendix D) and norm-conserving pseudopotentials to effectively describe the core electrons (see Appendix E). On top of incorporating all the previously mentioned quantum effects, an additional advantage of this methodology is that it allows us to straightforwardly describe the semicore 4d electrons of silver, which have a critical effect on the size dispersion of the LSP resonance frequency [53, 236, 237]. These electrons are removed from the pseudopotential and treated as valence electrons.

We then use the KS orbitals and energies obtained from the ground-state calculations to compute the absorption spectra of the MNPs within linear-response TDDFT as implemented in the PyNAO code [98] (see Section 2.2). In Fig. 3.1b, we plot the resulting absorption spectra for a series of silver icosahedral clusters of varying sizes, normalized with respect to the number of atoms. The spectra are dominated by the dipolar LSP (see Section 1.2.4), whose resonance energy lies in the range from ∼3.7 eV for the smallest cluster Ag_{55}, to ∼3.2 eV for the largest one, Ag_{1415}. This inverse relation between cluster size and LSP resonance energy agrees with experimental results for silver and other noble metals [53], and is caused by the quantum size effect together with thw background polarizability of the 4d electrons [20].

By placing two of these icosahedral clusters together in close proximity, we can create a more efficient optical cavity resonator. Due to the atomistic nature of the nanoparticles, the morphology of the cavity can be modified by changing the orientation of the MNPs, which has an important effect on the induced field [22]. In this thesis, we have studied two different cavity configurations: the tip-to-tip configuration, depicted in Fig. 3.2a, in which the dimer axis passes through the nanoparticle tips, and the facet-to-facet configuration, depicted in Fig. 3.2b, in which the cavity is formed by the facets of the opposing nanoparticles. In Figs. 3.2c and 3.2d, we plot the calculated absorption spectra in the 3–4 eV spectral range of these dimers under illumination with a plane-wave polarized along the dimer axis as a function of the gap size D. This gap size is defined as the minimal distance between atoms from the two different clusters. The spectra are dominated by the Bonding Dipolar Plasmon resonance (BDP, see Section 1.2.5). For large D values, this resonance appears at around 3.4 eV, matching the LSP resonance energy of the single Ag_{309} nanoparticle, and starts to red-shift as the gap closes, with the red-shift being more pronounced in the facet-to-facet case. The identification of the BDP mode is confirmed by the induced charge density plots in Figs. 3.2e and 3.2f, which reveal a dipolar pattern of the induced charge density at the surface of each MNP, characteristic of BDP excitations, as depicted in Fig. 1.4 for a dimer of sodium spheres. As we will describe in detail in the next section, these induced charge densities can be understood as snapshots of the real-time induced charge density, which means that these dipoles will be oscillating in time, with a phase delay of $\pi/2$ with respect to the oscillations of the incident field. In these plots one can also appreciate the clear dipolar distributions of the induced charge density around the individual atomic sites, which are a signature of the atomistic response associated with the localized 4d orbitals of silver.

When an emitter is placed in the plasmonic cavity of a dimer, a hybrid molecule–MNP system is formed. In this work, we consider a porphine molecule as the emitter. This molecule has a family of derivative compounds, known as porphyrins, which have multiple applications in photochemistry [238, 239]. Its atomistic structure is depicted in Fig. 3.3a. In Fig. 3.3b, we plot the absorption spectrum of the isolated molecule, together with the dimer spectra for both gap configurations and a gap size $D = 1.5$ nm. Notice that the molecular transition at 3.4 eV matches the plasmonic resonance of the dimer, which allows for a very efficient electromagnetic molecule–MNPs coupling. In the insets of Fig. 3.3b, we also display the isosurfaces of the imaginary part of the induced charge density of both dimer BDPs and of the molecular resonance. The latter displays a noticeable dipolar character, similar to that of the individual nanoparticles, which shows that this resonance corresponds to the electronic dipolar transition of the molecule.

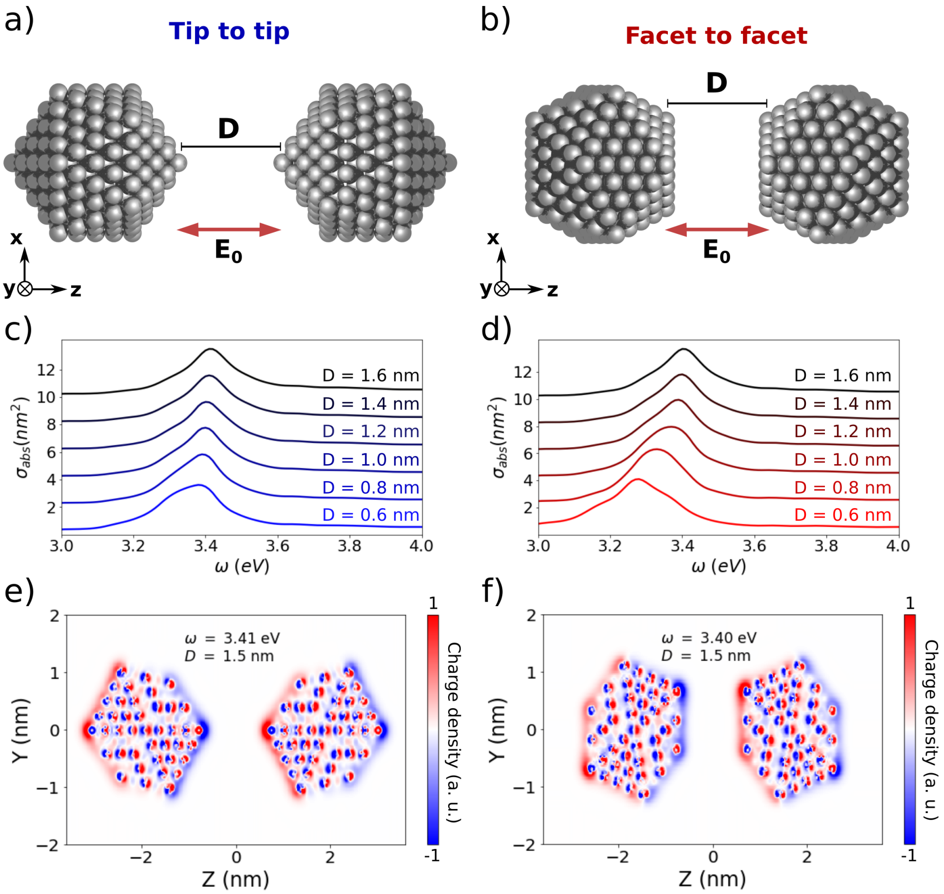

Figure 3.2: a) Atomistic structure of a dimer of Ag_{309} icosahedral clusters in the tip-to-tip configuration, with a gap size D and incident electric field $\mathbf{E_0}$ polarized along the dimer axis direction (z axis). b) Atomistic structure of a dimer of Ag_{309} icosahedral clusters in the facet-to-facet configuration. c) Absorption spectra for the tip-to-tip dimer configuration for varying D values. d) Absorption spectra for the facet-to-facet dimer configuration for varying D values. (e) Snapshot of the induced charge density for the bare tip-to-tip silver dimer with separation distance D=1.5 nm, at resonance (ω=3.41 eV). (f) Snapshot of the induced charge density for the bare facet-to-facet silver dimer with separation distance D=1.5 nm, at resonance (ω=3.40 eV).

3.2 Optical response of hybrid molecule–dimer systems

After analyzing the optical response of the isolated constituents, we study the effect of the optoelectronic coupling on the optical response of the molecule–MNPs hybrid system, which is depicted in Fig. 3.4a (3.4b) for the tip-to-tip (facet-to-facet)

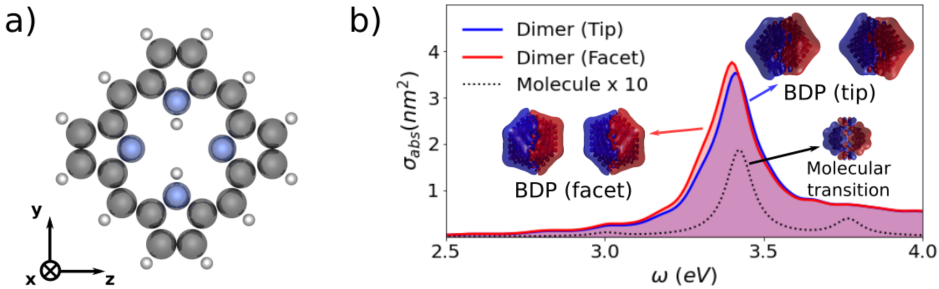

Figure 3.3: (a) Atomistic structure of the porphine molecule. Hydrogen atoms are depicted in white, Carbon atoms in gray, and Nitrogen atoms in blue. (b) Comparison of the absorption spectrum of a porphine molecule (black dotted line) with the absorption spectra of Ag_{309} dimers (D=1.5 nm) in the tip-to-tip (blue) and facet-to-facet (red) configurations. The molecular transition at 3.4 eV overlaps with the bonding dipole plasmon (BDP) modes of the dimers. The insets represent the isosurfaces of the imaginary part of the induced charge density at the resonance frequencies of the molecular transition and the BDP modes, respectively.

configuration. We first focus on the tip-to-tip configuration, in order to describe the general behavior of the system, and later study the influence of the cavity morphology on the coupling, by comparing these results with those obtained in a facet-to-facet configuration. Figure 3.4c shows its absorption spectra for values of the gap size ranging from D=1.4 nm (bottom) to D=1.8 nm (top). Two well separated peaks, so-called polaritons, are distinguishable in all the spectra, which is a characteristic of strongly coupled systems. We notice that the lower polariton (LP) resonance, marked with yellow dots, is red-shifted with respect to the resonances of the bare dimer and the molecule, displayed in Fig. 3.3b, whereas the upper polariton (UP) resonance, marked with green dots, is blue-shifted. However, the splitting of the LP and UP peaks depends greatly on the electromagnetic field acting on the dipole moment of the molecule, and this field is directly related to the gap size. Therefore, the polaritonic splitting also depends on the gap size: for small values of D (large field enhancement), both polaritons are clearly distinguished, but they merge gradually when the value of D is increased (smaller field enhancement). This behavior indicates that the strength of the coupling between the molecular and plasmonic resonances decreases when increasing the gap size, following the decay of the induced field inside the cavity. In Fig. 3.4d, we plot isosurfaces of the imaginary part of the induced charge density for the D=1.4 nm polaritons, which are labeled as A and B in the corresponding spectrum. These isosurfaces show clear dipolar patterns for the induced charge density on each of the constituents of the system, for both the lower (A) and upper (B) polaritons. Notice that, as for the modes of the isolated constituents, these dipoles oscillate in time. However, as can be observed in Fig. 3.4d, there is a key difference between the lower and upper polaritons: in the first case, the induced charge density oscillations in the molecule and in the nanoparticles are in-phase, whereas in the second case these oscillations are out-of-phase. Such a behavior is consistent with previous results for

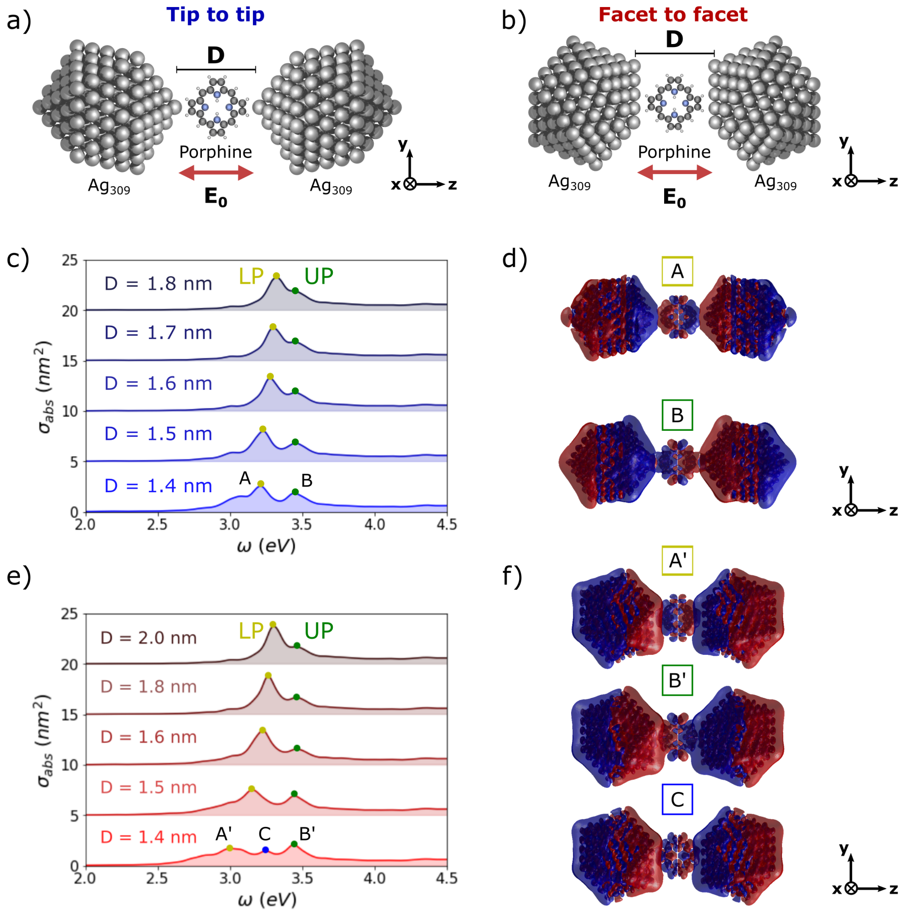

Figure 3.4: (a-b) Representation of the canonical system under study in the tip-to-tip (a) and facet-to-facet (b) configurations. A porphine molecule is placed in the middle of the cavity formed by two silver icosahedral nanoparticles of 309 atoms each, and the system is excited by light polarized along the dimer axis direction (z axis). A gap size D=1.5 nm is considered in both figures. (c) Optical absorption spectra of the hybrid molecule–MNPs system in the tip-to-tip configuration for different gap sizes D. Spectra on the top correspond to large D values, and spectra on the bottom to smaller D values. Yellow and green dots mark the LP and UP resonances, respectively. (d) Isosurfaces of the imaginary part of the induced charge density for the LP (A, yellow) and UP (B, green) resonances in the D=1.4 nm geometry. (e) Optical absorption spectra of the hybrid molecule–MNPs system in the facet-to-facet configuration for different gap sizes D. Spectra on the top correspond to large D values, and spectra on the bottom to small D values. Yellow and green dots mark the lower and upper polariton resonances, respectively, and the resonance emerging between them for D = 1.4 nm is marked in blue. (f) Isosurfaces of induced imaginary charge density for the LP (A', yellow) and UP (B', green) resonances in the D=1.4 nm geometry, and for the new resonance emerging between them (C, blue).

similar hybrid molecule–MNPs systems [24], and can be used as a criterion for the existence of coupling.

The distribution of the induced electric field inside a nanocavity is strongly influenced by its morphology, specially by atomistic features such as tips, edges, or facets [22]. To illustrate the dependence of the coupling between the dimer and the molecule on the atomistic details, we have repeated the previous tip-to-tip calculations for the facet-to-facet configuration of the MNPs displayed in Fig. 3.4b. We have found in this case that, for the smallest value of the gap size considered in this work, D=1.4 nm, the expected two-peak profile breaks up, with a third peak emerging between the LP and the UP resonances. This pattern can be observed in Fig. 3.4e, which shows the absorption spectra for the facet-to-facet configuration as a function of the gap size D. Figure 3.4f displays the isosurfaces of the induced charge density calculated for the three peaks in the absorption spectra. The peak at 3.0 eV (A') shows a pattern of in-phase oscillations similar to the LP resonance in Fig. 3.4d, whereas in the one at 3.45 eV (B'), molecule and MNPs are nearly out-of-phase, as for the UP resonance in Fig. 3.4d. For the resonance at 3.25 eV (C), visual inspection is not enough to identify the phase difference, and this needs to be computed numerically from the induced charge densities (see Section 3.2.1).

The emergence of this third peak between the LP and UP resonances in the facet-to-facet configuration is attributed to the hybridization between the electronic states of the molecule and of the MNPs [231, 240, 241], which provides an additional decay channel for the molecular excitation, decreasing its lifetime and causing a quenching of the signature of the molecular excitation in the absorption spectrum. Nevertheless, our calculations show that the double-peak structure in the absorption spectrum is recovered in the facet-to-facet configuration for larger D values (see Fig. 3.4e), with decreasing mode splitting for increasing gap size due to the smaller field enhancement, as in the tip-to-tip case.

3.2.1 Computation of the phase difference

To support the previous visual analysis of the induced charge densities and get further insight into the nature of the hybrid polaritonic modes, we have computed the phase difference between the induced charge density oscillations in the molecule and in the nanoparticles for the different modes, from the real and imaginary parts of the induced charge densities. In the linear-response formalism, the time-dependent evolution of the charge induced by an external monochromatic field of angular frequency ω_0 $\mathbf{E} = \mathbf{E_0} \cos(\omega_0 t)$ is given by the expression [20]

$$\delta n(\mathbf{r}; t, \omega_0) = \delta n_{\mathrm{Re}}(\mathbf{r}; \omega_0) \cos(\omega_0 t) + \delta n_{\mathrm{Im}}(\mathbf{r}; \omega_0) \sin(\omega_0 t), \tag{3.1}$$

where $\delta n_{\mathrm{Re}}(\mathbf{r}; \omega_0)$ and $\delta n_{\mathrm{Im}}(\mathbf{r}; \omega_0)$ are respectively the real and imaginary parts of the induced charge density in the frequency domain. This means that the real-time induced density oscillates between the real (at $\omega_0 t = 0, \pi$) and imaginary (at $\omega_0 t = \pm\frac{\pi}{2}$) induced densities in the frequency domain. We illustrate this by plotting in in Figs. 3.5a and 3.5b the real-time induced charge densities for the

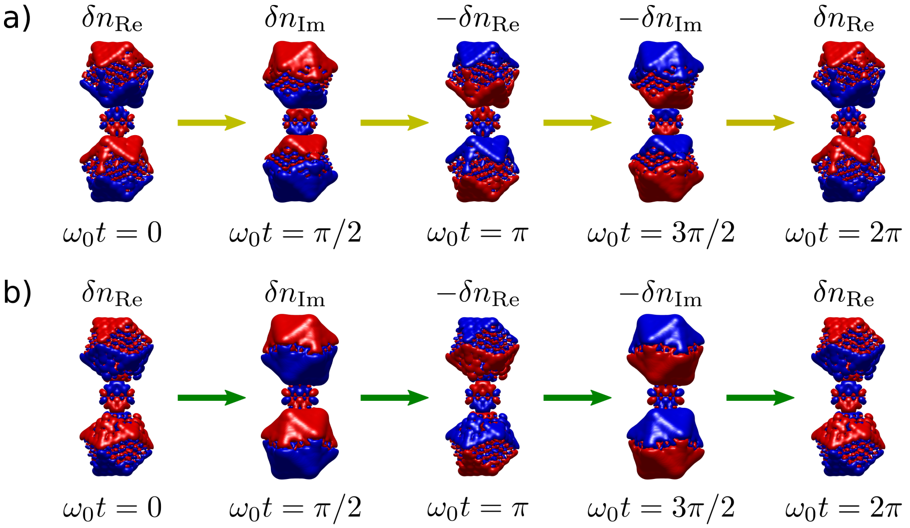

Figure 3.5: Real-time evolution of the induced charge density as described in Eq. (3.1). The real-time induced density oscillates between the frequency-space real and imaginary induced densities. a) Induced densities for the D = 1.5 nm facet-to-facet hybrid system at the excitation energy of the LP mode ($\omega_0 = 3.15$ eV). b) Induced densities for the same system at the excitation energy of the UP mode ($\omega_0 = 3.44$ eV).

D = 1.5 nm facet-to-facet hybrid system at the LP and UP excitation energies, respectively.

Therefore, the z-component of the induced dipole moment also presents an oscillatory behavior, given by

$$\begin{aligned} p_z(t,\omega_0) &= \int d\mathbf{r}\ \delta n(\mathbf{r};t,\omega_0)\ z \\ &= \cos(\omega_0 t) \int d\mathbf{r}\ \delta n_{\mathrm{Re}}(\mathbf{r};\omega_0)\ z + \sin(\omega_0 t) \int d\mathbf{r}\ \delta n_{\mathrm{Im}}(\mathbf{r};\omega_0)\ z \\ &= \cos(\omega_0 t)\ p_z^{\mathrm{Re}}(\omega_0) + \sin(\omega_0 t)\ p_z^{\mathrm{Im}}(\omega_0), \end{aligned}$$

where $p_z^{\mathrm{Re}}(\omega_0)$ and $p_z^{\mathrm{Im}}(\omega_0)$ are the parts of the z-component of the induced dipole moment in the frequency domain derived from the real and imaginary induced charge densities, respectively. From the previous equation, it follows that the real-time dipole moment is maximum when

$$\tan(\omega_0 t) = \frac{p_z^{\mathrm{Im}}(\omega_0)}{p_z^{\mathrm{Re}}(\omega_0)}. \tag{3.2}$$

For systems with a single sharp resonance, as in the case of our isolated constituents, the real part of the polarizability usually vanishes at the resonance frequency, and thus the dipole moment of the system oscillates with a phase difference of $\pi/2$ with respect to the incident field. However, this is not true anymore for more complex systems with several resonances, such as the molecule–MNPs hybrid system studied here, for which the real part of the response is not negligible.

When there are several constituents in the system, it is also possible to define their individual dipole moments, which may oscillate with different phases. Therefore, we have computed the phase difference in the oscillations between the molecule and the MNPs from the induced charge densities. We first define the induced dipoles for the constituents of our system:

$$p_{z,j}(t,\omega_0) = \int_j d\mathbf{r}\ \delta n(\mathbf{r};t,\omega_0)\ z, \tag{3.3}$$

where j stands for the molecule or the MNPs, and the integral over j means an integration only in the spatial region of the corresponding constituent. Then we define the phase of each constituent as

$$\theta_j = \arctan \frac{p^{\mathrm{Im}}_{z,j}(\omega_0)}{p^{\mathrm{Re}}_{z,j}(\omega_0)}, \tag{3.4}$$

which corresponds to the value $\omega_0 t$ at which the induced dipole moment of the constituent is maximum. Then, the phase difference is computed as

$$\delta\theta = |\theta_{\mathrm{mol}} - \theta_{\mathrm{MNP}}|. \tag{3.5}$$

The value of $\delta\theta$ is situated in the interval between 0, which corresponds to the molecule and the MNPs oscillating in-phase, and π, which corresponds to the molecule and the MNPs oscillating with opposite phases.

In Fig. 3.6a (3.6b), we show the phase difference in the oscillations between the dipoles induced at the MNPs and at the molecule in the tip-to-tip (facet-to-facet) configuration, computed using the methodology described above. The values of this phase difference for each mode are displayed as a function of the gap distance D. We focus our attention first on the tip-to-tip case, and we can observe that, in the LP, the MNPs and the molecule oscillate almost in phase, and this behavior is maintained for the whole range of analyzed gap sizes. In the UP, in contrast, the phase difference shows that, for the smallest gap size geometry, the induced dipoles in the molecule and in the MNPs oscillate in anti-phase, which is consistent with the induced charge density depicted in Fig. 3.4b. However, the phase difference decreases to less than $\pi/2$ as the gap size increases, which is interpreted as an additional evidence of the diminishing coupling strength. In the facet-to-facet configuration, the LP and UP resonances show a similar behavior, with almost on-phase oscillations at the LP frequency and close to anti-phase oscillations at the UP one. The main difference is the emergence of a new resonance for the D = 1.4 nm case (labeled as C in Fig. 3.4e), for which the phase difference in the oscillations (marked as MR in Fig. 3.6b) is close to $\pi/2$, which means that the

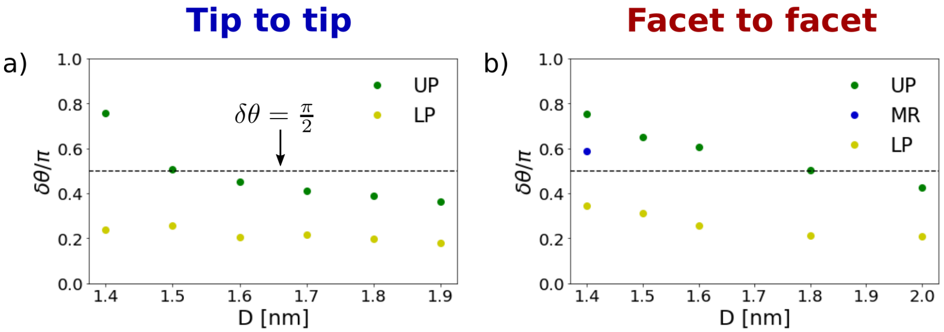

Figure 3.6: (a) Phase difference between the dipoles induced at the MNPs and at the molecule for both the LP (yellow) and UP (green) resonances in the tip-to-tip configuration, as a function of the gap size D. (b) Phase difference between the dipoles induced at the MNPs and at the molecule for both the LP (yellow) and UP (green) resonances in the facet-to-facet configuration, as a function of the gap size D. The single blue dot marks the phase difference for the resonance emerging between LP and UP for the closest gap (MR).

induced dipole moment in the molecule has its maximum value when it is zero in the MNP, and vice versa.

3.3 Influence of the cavity configuration on the coupling strength

A coupled molecule–MNPs system is considered to be in the strong-coupling regime when the splitting of the emerging hybrid modes is larger than the losses of the system. To identify the strong-coupling regime, we will use the criterion presented in Eq. (1.38) of Section 1.4, which defines the threshold for the coupling strength g as $g > |\gamma_{\mathrm{ex}} + \gamma_{\mathrm{pl}}|/4$, where γ_{ex} and γ_{pl} are the intrinsic damping rates of the excitonic emitter and the plasmonic cavity, respectively. In our case, we obtain the values of $\gamma_{\mathrm{ex}} = 0.107$ eV and $\gamma_{\mathrm{pl}} = 0.191$ eV by fitting the absorption spectra of the isolated constituents to Lorentzian functions, as described in Eq. (1.34). We notice that the plasmonic losses vary slightly for the different dimer configurations considered, so we take the largest of them. Following this criterion, the value of g for the molecule–MNPs system is then estimated by fitting the absorption spectra of the hybrid system to a coupled-oscillator model [Eq. (1.37)]. Figure 3.7 shows the values of the coupling strength g obtained for different gap sizes and for the two configurations of the MNPs considered in this work, ranging between 0.07 (large D) eV and 0.14 eV (small D). The strong-coupling condition, marked by the dotted black line in Fig. 3.7, is fulfilled for the whole range of considered gap sizes. The D=1.4 nm case for the facet-to-facet configuration is omitted, because its absorption spectrum does not show the characteristic two-peak behavior.

As we can see, the facet-to-facet configuration consistently outperforms the

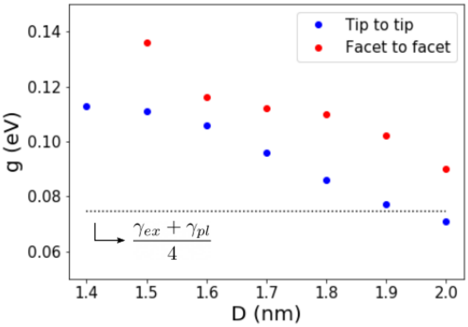

Figure 3.7: Values of the coupling strength g for both the tip-to-tip and facet-to-facet configurations as a function of the gap size D, computed by fitting the TDDFT absorption spectra to a coupled-oscillator model [(1.37)] . The dotted line represents the threshold for strong coupling according to Eq. (1.38). γ_{ex} and γ_{pl} are the excitonic and plasmonic losses respectively.

tip-to-tip configuration, with a mean difference in coupling strength larger than 20%, confirming the influence of atomic features in setting up the plasmon–exciton interaction in the dimer cavity. This difference in the coupling strength is caused by the dissimilarity of the spatial distributions of the induced electric field at the cavity of each configuration, as illustrated in Figs. 3.8a and 3.8b, which show the normalized induced electric field $|\mathbf{E}^{\mathrm{ind}}|/|\mathbf{E}_0|$ for the bare dimer BDPs in the tip-to-tip and facet-to-facet configurations, respectively, directly obtained from the induced densities plotted in Fig. 3.2 using Eq. (2.51). In the tip-to-tip case, the induced field is strongly localized around the vertices of the MNPs due to the atomistic lightning rod effect [22], whereas in the facet-to-facet case the field is more homogeneously distributed inside the cavity, enabling a more efficient coupling with the molecule. The final coupling strength is thus a consequence of the field enhancement associated to the particular atomistic structure of the gap, which determines its inhomogeneity and extension.

To further confirm this statement, we use estimations of the coupling strength from the induced fields and the molecular dipole, in which the strength of the light–matter coupling for an emitter located at position $\mathbf{r}$ in the presence of an optical cavity mode is determined by Eq. (1.35). To do so, we first need the transition dipole moment of the isolated porphine molecule μ_t, which is obtained by describing the polarizability spectrum of the isolated molecule shown in Fig. 3.3b through Eq. (1.34). In this way, we obtain a value of $\mu_t = 8.35$ Debye for the transition dipole moment of the porphine molecule. We then use Eq. (1.35) to estimate the coupling strength of the hybrid molecule–MNPs system, approximating the porphine molecule as a point dipole placed at the center of the gap and using the induced fields computed for the bare dimers. The values of the coupling strength obtained in this way are shown in Fig. 3.9, marked with crosses, together with the effective values of g extracted from the coupled harmonic oscillators model applied to the absorption spectra, marked with solid dots. Although this simple approximation

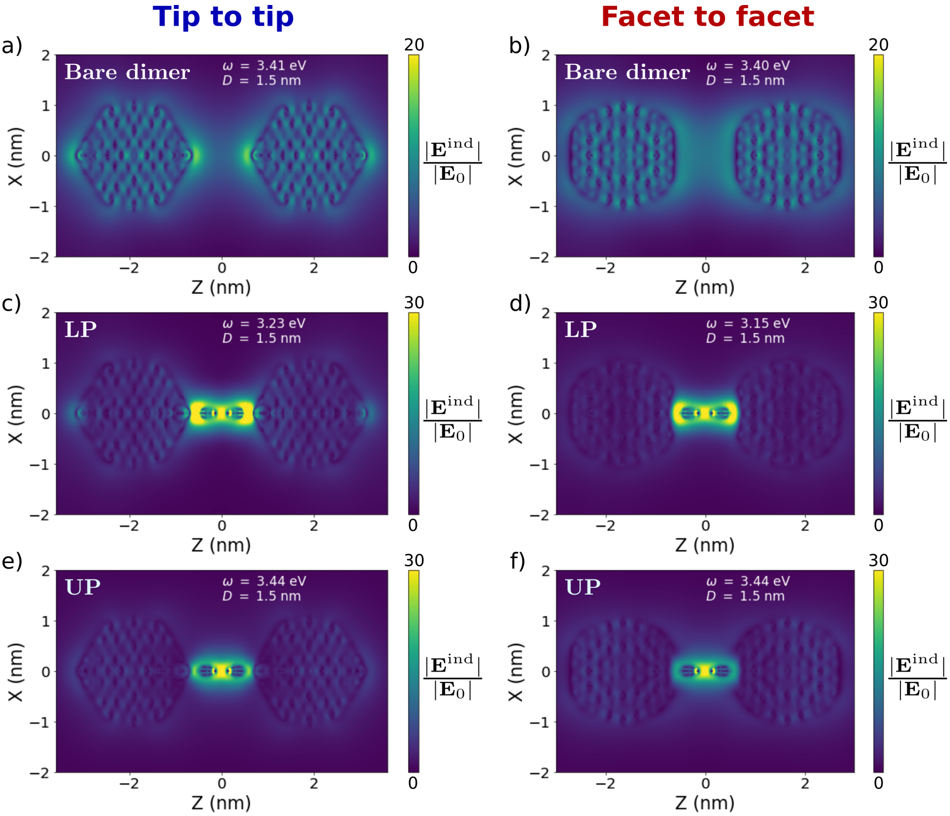

Figure 3.8: (a-b) Electric field enhancement at the BDP resonance on the XZ plane for a bare nanoparticle dimer with gap size D=1.5 nm for the tip-to-tip (a) and facet-to-facet (b) configurations. (c-d) Electric field enhancement on the XZ plane for the LP resonance of the tip-to-tip (c) and facet-to-facet (d) hybrid geometries (with molecule) with gap size D=1.5 nm. (e-f) Electric field enhancement on the XZ plane for the UP resonance of the tip-to-tip (e) and facet-to-facet (f) hybrid geometries (with molecule) with gap size D=1.5 nm.

results in coupling strengths that are significantly larger than the values obtained from the coupled harmonic oscillator model, it correctly predicts stronger coupling in the facet-to-facet configuration than in the tip-to-tip configuration, and confirms our hypothesis of a more homogeneous and extended field distribution in the facet-to-facet configuration enabling a stronger coupling.

There are several possible reasons for the quantitative discrepancy in the coupling strength values obtained within the two aforementioned approximations. Since the size of the molecule is relatively large compared to the gap size, the point-dipole approximation is not well justified, and the spatial extension of the molecule should be considered. Typically, this is done by substituting in Eq. (1.35) the values of field and dipole in a point by the integral of the induced field weighted

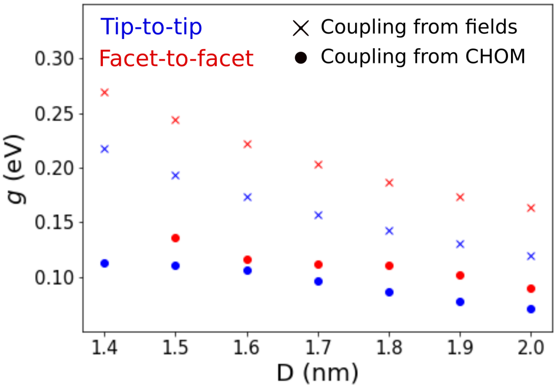

Figure 3.9: Comparison of the coupling strengths, g, estimated from the induced fields at the cavity using Eq. (1.35) (crosses) and the coupling strengths from a coupled harmonic oscillator model (CHOM) applied to the absorption spectra (dots), for both the tip-to-tip (blue) and facet-to-facet (red) configurations.

by the normalized molecular electronic transition density [216]. Regrettably, within the TDDFT approach implemented in this thesis we do not have access to the electronic transition density. Therefore, we have limited ourselves to estimate this effect by applying an averaged value of the induced field on the electronic transition dipole:

$$g = \frac{\mu_t}{\hbar \ \max(|\mathbf{E}^{\mathrm{ind}}|(\mathbf{r}))} \sqrt{\frac{\hbar\omega_{\mathrm{pl}}}{2\varepsilon_0 V_{\mathrm{e}}}} \int d\mathbf{r} \ |\mathbf{E}^{\mathrm{ind}}|(\mathbf{r}), \tag{3.6}$$

where the average is done by considering the fields over the spatial extent of the molecule. However, we have found that this does not significantly change the estimated coupling strength values. Another aspect which might contribute to the discrepancy between the results of the two models could be the different treatment of the screening in both methods. The *ab initio* calculations naturally account for molecular screening, whereas the approximate average field approach does not. In the classical formalism, screening can be considered by introducing a factor $1/\epsilon_{\mathrm{scr}}$ in Eq. (1.35), with $\epsilon_{\mathrm{scr}} = (2\epsilon_0 + \epsilon_{\mathrm{e}})/(3\epsilon_0)$, where ϵ_{e} is the permittivity of the emitter [122]. Although this permittivity is not well defined in the atomistic formalism, we can estimate it by adjusting the screening factor so that the coupling strengths from the induced fields formalism match the ones from the atomistic spectra, which returns an estimated value of $\epsilon_{\mathrm{e}} \approx 3$.

In addition to the bare dimer BDPs, the induced fields for the hybrid system's LP and UP modes also differ in some key aspects. In Fig. 3.8 we compare the enhancement of the electric field for the bare nanoparticle dimer at the BDP resonance and for the molecule–MNPs system at both the LP and the UP resonances, for both the tip-to-tip and facet-to-facet configurations. As observed in Figs. 3.8c and 3.8d, the induced field in the LP is distributed along the entire cavity, and specially in the volume between the molecule and the MNPs, whereas the induced field in the UP, shown in Figs. 3.8e and 3.8f, appears to be concentrated around the center of the molecule. A similar behavior has already been predicted in calculations with tetracene molecules and Mg nanoparticle dimers [25]. In both cases, the distribution of the field is drastically modified with respect to the BDP of the bare nanoparticle dimer displayed in Figs. 3.8a and 3.8b. In spite of the quantitative differences in the values of the coupling strength described previously, the general qualitative properties of the induced field distributions of each polariton do not seem to be greatly influenced by the configuration of the cavity.

3.4 Charge-transfer plasmons

Following the analysis of the optical response of the molecule–MNPs system and the nature of the characteristic resonances, we put now our focus on the low-energy range of the spectra. In Fig. 3.10a, we show the absorption spectra of the hybrid system zoomed at the spectral range between 0 eV and 1 eV, in both the tip-to-tip (blue) and the facet-to-facet (red) configurations for D=1.4 nm, together with the bare dimer (green) and the isolated molecule (dotted black) spectra. As observed, the cavity morphology plays a key role in the optical response at low energies. The isolated constituents do not exhibit any resonances in this frequency range, and the same occurs for the hybrid system in the tip-to-tip configuration. However, in the facet-to-facet configuration, several new peaks emerge at low energies. To get deeper insight into these low-energy resonances, we plot the corresponding induced charge densities in Fig. 3.10b. The two main resonances, labeled D and E, display clear monopolar patterns on the surface of the MNPs, meaning that the individual MNPs posses nonzero net induced charges of opposite signs. As described in Section 1.2.5, this is a signature of the flow of charge from one cluster to the other through the molecular junction, which suggests their identification as charge-transfer plasmon (CTP) modes [94]. Since both modes are CTPs, the corresponding isosurfaces of induced charge density look very similar.

Shift of the molecular energy levels

In order to confirm the identification of these modes as CTPs, we make use of the well known fact that for a molecule placed between two MNPs, the existence of molecular states close to the Fermi level of the MNPs triggers the electron conductivity of the system, which makes the intensity of CTP resonances very sensitive to the relative position of these molecular energy levels [227]. In practice, the relative position of these levels can be shifted by applying an external potential, as in single-molecule resonant tunneling experiments [13]. In the present atomistic ab initio framework, it is possible to shift these energy levels in a controlled way by introducing a background potential localized around the atomic sites of the molecule. This shifting is performed using a feature initially implemented in SIESTA for the *ab initio* computation of the U parameter within the LDA+U framework, following the formalism in refs. [242] and [243]. Such feature allows us to apply an

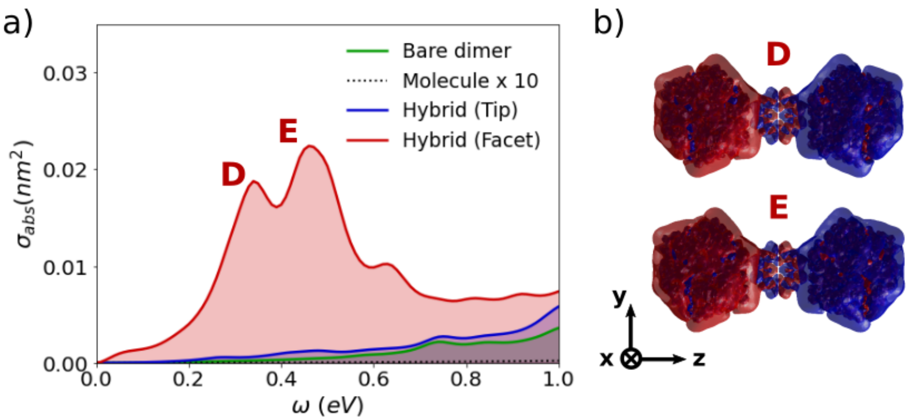

Figure 3.10: (a) Low-energy range of the absorption spectrum for the bare dimer (green), the isolated porphine molecule (dotted black), and the hybrid system of both the tip-to-tip (blue) and facet-to-facet (red) configurations, with D=1.4 nm. The emerging modes for the facet-to-facet configuration at 0.34 eV and 0.45 eV are marked as D and E, respectively. (b) Snapshots of the induced charge densities at the resonances D and E appearing for the facet-to-facet geometry.

energy shift to the electronic levels of the system according to their projections onto a specific subset of atomic orbitals. Thus, the total energy of the system becomes

$$E_{\text{shift}}[n(\mathbf{r})] = E_{\text{DFT}}[n(\mathbf{r})] + \sum_{I,m} \Delta^I_m n^I_{mm} \ , \tag{3.7}$$

where n^I_{mm} is the occupation of the orbital m of the atom I and Δ^I_m is the local potential shift applied to that orbital. The occupations are computed according to the expression

$$n^I_{mm'} = \sum_\nu f_\nu \langle \phi_\nu | P^I_{mm'} | \phi_\nu \rangle, \tag{3.8}$$

with ϕ_ν and f_ν standing, respectively, for the Kohn–Sham orbitals and their occupation for quantum number ν. The $P^I_{mm'}$ are localized projectors used to compute the local populations

$$P^I_{mm'} = |\varphi^I_m\rangle\langle\varphi^I_{m'}|. \tag{3.9}$$

In SIESTA the projector functions φ^I_m are defined using two possible methods: either as numerical atomic orbitals similar to those used as a basis set, or as exact solutions to the pseudoatomic problem with a radial cutoff r_c applied using a Fermi function. The cutoff radius r_c is chosen to prevent a large overlap between projectors in neighboring atoms. This second method is the default in SIESTA, and is the one used in our calculations.

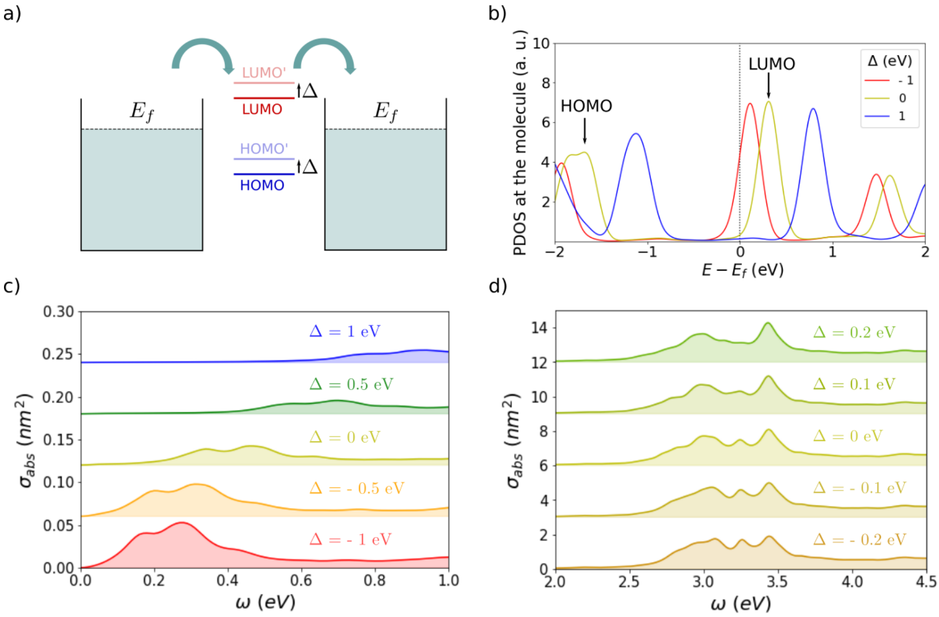

Figure 3.11: (a) Sketch illustrating the shifting of molecular energy levels. (b) Projected density of electronic states (PDOS) of the molecule around the Fermi level for different values of the energy shift Δ. The dotted black line stands for the Fermi level of the MNPs, and the HOMO and the LUMO are indicated for the $\Delta = 0$ case. (c) Absorption spectra of the system at CTP energies for different values of the energy shift Δ ranging from -1 eV (bottom) to 1 eV (top). (d) Absorption spectra of the system at higher energies for values of the energy shift ranging from -0.2 eV (bottom) to 0.2 eV (top).

The expression of the energy in Eq. (3.7) corresponds to a modified Hamiltonian

$$\hat{H}_{\text{shift}} = \hat{H}_{\text{KS}} + \sum_{I,m} \Delta^I_m |\varphi^I_m\rangle\langle\varphi^I_m|. \tag{3.10}$$

To simulate an homogeneous shifting of the molecular energy levels, we set the shifting parameter for all the orbitals of the molecule to the same value Δ, i.e., $\Delta^I_m = \Delta$ if atom I belongs to the molecule and $\Delta^I_m = 0$ otherwise. This shift is maintained during the self-consistent calculation and gives rise to a corresponding shift on the Kohn–Sham eigenstates of the hybrid system that are localized at the molecule.

Taking advantage of this methodology, we analyze the effect of a controlled shift of the molecular energy levels on the optical absorption of the system, as depicted in Fig. 3.11a. Since we are interested in the charge-transfer regime, all the calculations in this subsection are performed for the D=1.4 nm case in the facet-to-facet configuration. In Fig. 3.11b, we show the projected electronic density of states (PDOS) at the molecule for different values of the energy shift Δ, choosing the Fermi level of the MNPs as the zero-energy reference. For $\Delta = 0$ eV (i.e., when no shift is introduced), the highest occupied molecular orbital (HOMO) and the lowest unoccupied molecular orbital (LUMO) are localized around -1.6 eV and 0.4 eV, respectively. We analyze the energetics of the LUMO in the molecule, as it holds the main role in charge transport. As can be observed in the figure, negative Δ values shift the LUMO closer to the Fermi level of the MNPs, whereas for positive Δ values, the opposite occurs: the LUMO shifts to higher energies, increasing its energy separation with respect to the Fermi level.

Note that the shiftings do not exactly correspond to the introduced value of Δ, for which there are several possible explanations. Although the states labeled as the molecular HOMO and LUMO are concentrated around the molecule, as shown by the PDOS, they are in fact Kohn–Sham eigenstates of the whole system, and as such they will also be partially spread through the rest of the system. Moreover, the projector functions φ_m^I determining if a given state is localized at the molecule are obtained from the isolated neutral atom solutions, which is a radically different chemical environment from the one analyzed here, with covalent bonds between molecular atoms and a significant hybridization between the cluster and molecular states. Additionally, since the potential energy shifts are included in the self-consistent calculations, their presence itself should modify the spatial distribution of the KS eigenstates. Nevertheless, this does not change the general behavior: negative Δ values shift the LUMO closer to the Fermi level of the MNPs, whereas for positive Δ values, the opposite occurs.

In Fig. 3.11c, we compare the low-energy part of the absorption spectra for the range of Δ values presented in Fig. 3.11b, with the negative values at the bottom and the positive ones at the top. As a result of lowering the LUMO energy and bringing it closer to the Fermi energy, the intensity of the CTP resonances is significantly strengthened for negative Δ values. In contrast, shifting the LUMO away from the Fermi level, thus impairing the charge transfer, leads to a weakening of the CTP modes in the absorption spectrum. Together with this variation of the intensity of the CTP modes, the shift of the molecular levels also results in a displacement of the CTP resonances. This behavior confirms the identification of these modes as CTPs, and evidences the versatility of the *ab initio* TDDFT approach employed for this work to assess the nature of complex microscopic transport processes at optical frequencies. Additionally, Fig. 3.11c clearly shows that the CTP modes are red-shifted for negative Δ values, and blue-shifted for positive values. As described above, this is explained by the change in the energy gap between the LUMO and the Fermi level of the MNPs, which increases for positive Δ values and decreases for negative ones. It is also interesting to look at the influence of the molecular energy level shift Δ on the higher-energy part of the absorption spectrum, which we show in Fig. 3.11d. Positive values of Δ as small as 0.2 eV remove the middle resonance (labeled as C in Fig. 3.4a), while negative Δ values increase the height of this peak, which suggests a connection with the charge transfer through the molecule. The other spectral features related to the LP and the UP are not affected by the shifting of the molecular energy levels, which identifies the role of the molecule as a continuous conductive block in such resonances.

3.5 Summary

In this chapter, we have analyzed the optical response of a porphine molecule coupled to an Ag_{309} dimer within an ab initio atomistic linear-response TDDFT framework. We have started by describing the optical response of bare icosahedral silver clusters and dimers in Section 3.1, as well as that of the isolated porphine molecule. In Section 3.2, we then focused on the response of the hybrid molecule–MNPs system. Our results showed the splitting of the plasmonic resonance of the dimer into two clearly distinct polaritons, which is supported by an analysis of the induced charge densities. This confirms that the system is at the strong-coupling regime for gap sizes smaller than 2 nm. A comparison of the coupling strength g values in Section 3.3 for the different gap geometries has shown that the atomistic configuration has a significant effect on the coupling strength We showed that the more homogeneous induced fields of the facet-to-facet configuration result in larger g values. In Section 3.4, we focused in the low-energy range of the optical response for different dimer configurations, proving that atomistic features also have a crucial influence on the emergence of charge-transfer plasmons, which, for our system, only appear in the facet-to-facet configuration. We also performed an analysis of the CTP modes emerging at low frequencies, and showed that their intensity and spectral position can be tuned by shifting the position of the molecular energy levels with respect to the Fermi level of the MNPs, which provides valuable insights into the mechanism behind charge-transfer phenomena. In general, this work stresses the importance of the effects caused by atomistic details in the response of molecule-MNPs coupled systems. Additionally, these results demonstrate the suitability of the employed TDDFT method for addressing the coupling between molecules and MNPs, while simultaneously accounting for the influence of the atomistic configuration and quantum effects arising at narrow gaps. The results presented in this chapter thus further consolidate atomistic *ab initio* methods as a feasible tool to describe the most extreme cases of quantum emitter–nanocavity interactions.

CHAPTER 4

PLASMONIC RESPONSE OF SMALL METALLIC NANOPARTICLES AS PROBED BY FAST PENETRATING ELECTRONS

The technical advances in electron microscopy produced in the last decades have led to an improvement of spatial resolution [46, 47] and energy sensitivity [49], thus enabling the characterization of single nanoparticles (NPs) of sizes under 10 nm by the analysis their electron energy-loss (EEL) spectra. For such tiny metallic NPs, a series of effects caused by the quantum nature of the electron gas emerge, and their influence in the excitation of collective oscillations localized at the NP surface has received much attention in the literature [53, 54, 244]. In this context, quantum *ab initio* methods have demonstrated to be an efficient theoretical tool to investigate the sensitivity of valence Electron Energy-Loss Spectroscopy (EELS, see Section 1.6) to the atomistic structure of small metallic NPs [194]. In this chapter, we demonstrate the ability of such *ab initio* methods to comprehensively describe the complex plasmonic response of metallic NPs.

Localized surface plasmons (LSPs) have been recently studied within the framework of atomistic *ab initio* calculations [194]. Therefore, we will focus our analysis on confined bulk plasmons (CBPs), which are longitudinal collective oscillations of the electron density confined within the volume of a nanostructure (Section 1.2,). Unlike LSPs, CBPs are not typically detected using standard optical spectroscopy techniques, due to their inefficient coupling with light [52, 57, 169] and, as a result, they have received limited attention in the literature over the years. Nevertheless, recent research has proposed exploiting bulk plasmon excitations in various applications, including the precise measurement of local temperature at the nanoscale [245–247]. In addition to LSPs, which have received most attention, CBPs are effectively excited by swift electron beams that penetrate the sample and longitudinally perturb the electron cloud in it, as demonstrated across a variety of structures and materials, including thin Mg films [101], Ge nanorods [103], Bi nanowires [102], Bi nanoparticles [104, 105], and Al nanodisks [106].

Although the dispersion relation of CBPs in small NPs and other nanostructures has been theoretically explored [52, 57, 58, 165], a complete picture of the physical mechanisms that drive their excitation by penetrating electron beams in small nanoparticles has remained elusive. Moreover, the limitations of the more widespread local approaches [248] emerge when the nanoparticles size approaches the few-nanometer scale, as these frameworks do not describe effects linked to the atomistic structure [232, 249], quantum confinement [250], nonlocal dynamical screening [14–16], and variations of the electron density at the surface [97, 220, 251], all of them significantly influencing the plasmonic response. In this context, further theoretical insights are required to understand the impact of these effects on CBPs.

In this chapter, we explore the full plasmonic response of icosahedral Na NPs of approximate radius in the range $a = 1$–2.5 nm, as excited by 100 keV penetrating electron beams, using the atomistic TDDFT framework described in Sections 2.1 and 2.2. In Fig. 4.1a we show a sketch of an electron beam interacting with an atomistic icosahedral sodium nanoparticle, defining the impact parameter b as the minimum distance between its trajectory and the nanoparticle center. Sodium is particularly suited for this study because its electrodynamical response is primarily governed by conduction electrons, and is therefore an excellent free-electron metal prototype, which clearly reveals the aforementioned quantum phenomena. Moreover, the free-electron character of sodium enables the comparison of the atomistic TDDFT results with those of alternative jellium TDDFT and hydrodynamic approaches also employed here and briefly introduced in the next section, allowing us to perform a comprehensive analysis of quantum and nonlocal effects. We will be using atomic units ($\hbar = e = m_e = 1$) throughout this chapter.

In order to illustrate the general properties of the EEL spectra which are the focus of this chapter, Fig. 4.1b shows the calculated atomistic TDDFT spectra of sodium nanoparticles of icosahedral shape [252] and different sizes, ranging from $a \approx 1$ nm (147 atoms) to $a \approx 2.5$ nm (2057 atoms) for a central penetrating electron trajectory. Notice that for the smallest nanoparticle considered, the spectrum is dominated by several peaks due to single electron–hole excitations ([253, 254], see Section 1.3). However, as the particle size increases, three different types of modes emerge at distinct excitation energies: localized surface plasmons (LSPs), confined bulk plasmons (CBPs), and Bennett or multipole plasmons (MPs). The lowest-energy peak (~ 3.1 eV) corresponds to a LSP, as evidenced by the induced charge density shown in the inset, in which the induced charge density is concentrated at the nanoparticle surface. The excitation of LSPs and its dependence on the nanoparticle geometry is briefly discussed in Section 4.3. At higher energies (~ 5.2 eV) another set of peaks emerges (see the corresponding induced charge density in the inset). These are identified as Bennett plasmons [255], which are also known

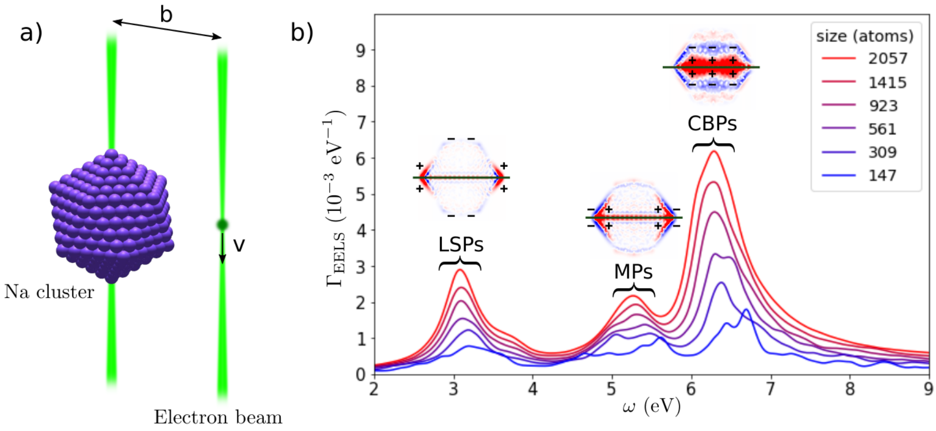

Figure 4.1: (a) Sketch of an electron beam traveling with impact parameter b and velocity $\mathbf{v}$, interacting with an icosahedral Na nanoparticle. (b) EEL probability spectra calculated with atomistic *ab-initio* TDDFT for 100 keV electrons probing icosahedral sodium nanoparticles. The different colors correspond to spectra of central electron trajectories (b=0 nm) through NPs of different size (number of atoms), ranging from $a \approx 1$ nm (147 atoms) to $a \approx 2.5$ nm (2057 atoms). The three main peaks labeled in the spectra correspond to localized surface plasmons (LSPs), Bennett or multipole plasmons (MPs), and confined bulk plasmons (CPBs). The insets display a schematics of the electron beam incidence and 2D plots of the cross-sectional views of the induced charge density distribution of the LSP, MP, and CBP resonances for the Na_{2057} NP. The red and blue colors in the induced charge densities refer to positive and negative values, respectively.

as multipole plasmons [256, 257] (MPs). The emergence of these modes deserves further attention, and we analyze them in greater detail is Section 4.3. The most prominent peaks (~ 6.3 eV) in the EEL spectra shown in Fig. 4.1b are those close to the plasma frequency ω_{p} of Na, and correspond to charge density oscillations confined within the volume of the NP, so-called CBPs [194] (see Section 1.2), as demonstrated by the induced charge density displayed in the inset. They are composed of a series of satellite peaks and shoulders, evidencing the complex nature of the CBP excitations. The characterization of these bulk modes is the main focus of this chapter. To this end, we will support the *ab initio* calculations with a linearized hydrodynamic model (HDM) in Section 4.3. We focus on the analysis of a Na_{561} ($a \approx 1.6$ nm) nanoparticle, for which the isolated electron–hole excitation peaks have already transitioned into well-defined collective excitations.

4.1 Modeling the EEL probability spectra of small MNPs

Even though the focus of this chapter is theoretically analyzing the plasmonic response of small MNPs through the EEL probability spectra obtained within atomistic TDDFT, we have also used auxiliary calculations for a reference spherical

MNP to facilitate the interpretation of the results. In this section we provide a brief reminder of the atomistic TDDFT method, as well as of both the HDM and the jellium TDDFT method employed in the reference calculations.

4.1.1 Atomistic TDDFT model

The clusters that we have used for this study are sodium clusters with icosahedral shape, like the silver clusters in Chapter 3. As we did in that case, in order to obtain their exact geometries we optimized the inter-atomic separation of ideal icosahedral clusters by computing with atomistic DFT the ground-state energy of the clusters as a function of the lattice constant, and then searching for the minimum energy. Since the effect of an additional unconstrained geometry relaxation in the resulting EEL spectra is found to be negligible, we limit our analysis to non-relaxed, perfectly icosahedral geometries. All the DFT ground-state calculations were performed using the SIESTA code [111] with the GGA exchange–correlation functional developed by Perdew, Burke, and Ernzerhof [181] (see Appendix C). We used norm-conserving pseudopotentials to effectively describe the core electrons (see Appendix E) and a DZP basis set of numerical atomic orbitals (see Appendix D) generated using an energy shift of 10 meV ([258], see Appendix D). We then use the KS orbitals and energies obtained from the ground-state calculations to compute their corresponding absorption spectra within linear-response TDDFT as implemented in the PyNAO code [98] and explained in Section 2.2.

While *ab initio* atomistic TDDFT offers a state-of-the-art parameter-free platform for calculating the EEL spectra in small NPs [194], the interpretation of the results is challenging due to the overlapping of different resonances, particularly at CBP energies. In order to shed light and guide the characterization of the modal composition of CBP resonances, we also compute the electron energy-loss probability $\Gamma_{\mathrm{EELS}}(\omega)$ for a reference spherical Na nanoparticle of the same size, using two additional models accounting for nonlocal effects, a hydrodynamic model and a jellium TDDFT model.

4.1.2 Hydrodynamic Model

As a first reference, we obtain the optical response of the NP within an analytical HDM [59, 259], which describes the NP as a compressible electron gas with Wigner–Seitz radius $r_{\mathrm{s}} = 3.93\ a_0$ (a_0 is the Bohr radius, see Appendix A) and plasma frequency $\omega_{\mathrm{p}} \approx 6.05$ eV, confined within a sphere of hard boundaries with vanishing current at the boundary, preventing the electron spill-out. The electron gas dynamics are obtained by solving the Helmholtz equation inside the NP under the aforementioned boundary conditions. In order to do so, the induced charge density is expanded in terms of spherical harmonics $Y_\ell^m(\Omega)$, which allows us to obtain analytical expressions for the radial components of the induced charge density in terms of spherical Bessel functions. This leads to a set of resonances labeled as (ℓ, n), where ℓ is related to the angular distribution of the electron density of the corresponding mode, and n is the number of nodes of the radial oscillations [58].

Notice that the azimuthal number m is degenerate and, for noncentral trajectories, multiple modes with different m's can be excited simultaneously. A more detailed account of the HDM is provided in Appendix B. The HDM calculations presented in this chapter were developed by M. Urbieta and E. Ogando in the Theory of Nanophotonics group.

4.1.3 Jellium TDDFT model

We support our atomistic and HDM results with the EEL probability computed for an analogous spherical nanoparticle within the TDDFT formalism and the jellium model of free-electron metals [19, 60], in which the external potential of the lattice ions is modeled as a uniform positive background charge with density

$$n_+(\mathbf{r}) = \begin{cases} n & \text{inside the metal} \\ 0 & \text{outside the metal} \end{cases}, \tag{4.1}$$

where $n = 3/(4\pi r_\mathrm{s})$ is the average homogeneous electron density of sodium, with $r_\mathrm{s} = 3.93\, a_0$ its Wigner–Seitz radius. Conduction electrons are treated as interacting particles confined within a finite spherical potential well in the TDDFT formalism, and their response to a penetrating electron beam is then computed with a wave-packet propagation method developed by A. G. Borisov [260]. This formalism allows for describing variations of the induced charge density near the NP's surface associated with a finite potential barrier at the metal–vacuum interface, an effect that the hard-boundary HDM cannot capture [219]. Thus, the simplified quantum description of the jellium electron gas excludes features captured by the atomistic TDDFT model related to the precise atomistic structure and to the non-spherical shape of the NP, while still accurately accounting for nonlocal effects in the dynamics of conduction electrons that the HDM seeks to address. The jellium TDDFT calculations presented in this chapter were computed by A. Babaze with the methodology implemented by A. G. Borisov in previous work [61, 261], which is restricted to axial electron trajectories.

In order to address the adequacy of the HDM in describing the excitation of CBPs, in Figs. 4.2a and 4.2b we compare the $\Gamma_\mathrm{EELS}(\omega)$ as computed within the two models for a reference spherical Na NP of radius $a = 2.13$ nm, in the CBP spectral range, highlighting the contribution of each angular momentum l component. As can be appreciated, the hard-boundary nature of the HDM leads to a systematic blue-shift of LSPs, with the presence of artificial resonance features close to the bulk plasma frequency ω_p. In addition, there are several differences in the induced charge density at the surface. By comparing the insets in Figs. 4.2a and 4.2b, it can be observed that, while the HDM induced density is cut sharp at the boundary, the jellium one presents a significant spill-out along the electron path, and a spill-in in regions far from it. However, despite these limitations, the HDM properly accounts for the general description of the nonlocal plasmonic response in the volume of the NP. Both the HDM and the jellium TDDFT model consistently predict that CBP resonances are formed by several volume modes with different angular momenta l,

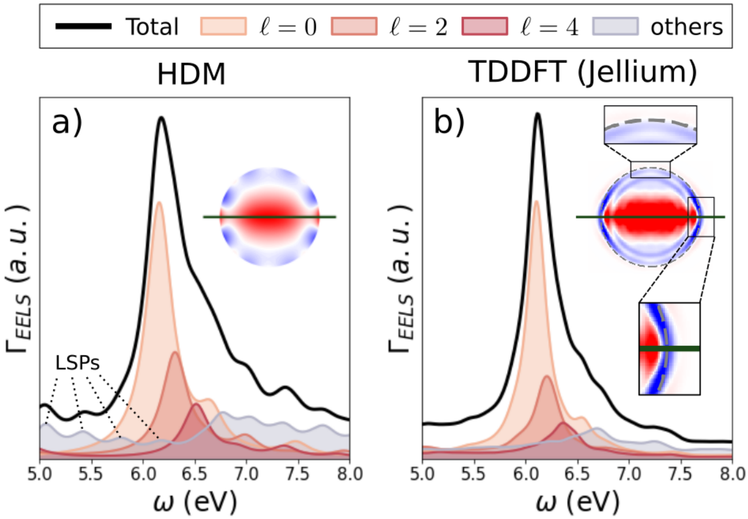

Figure 4.2: EEL spectra for 100 keV electrons passing through the center of a spherical Na nanoparticle calculated with two different approaches. (a) HDM results for a reference spherical Na NP of radius $a = 2.13$ nm. The contributions of the main ℓ components are distinguished with different colors. The 2D cross-sectional view of the induced charge density at the main CBP resonance energy is displayed in the inset (red for positive charge and blue for negative charge). (b) TDDFT results within the jellium model for a reference spherical Na NP containing 1074 conduction electrons. The inset shows the 2D induced charge density cross-sectional view computed within the jellium model at the main CBP resonance energy. The dashed line represents the boundary of the background positive charge density of the jellium sphere. The magnified insets outline the spill-out of the electron cloud at the surface around the electron path and far from it.

which proves the utility of the HDM in identifying the CBPs excited in small NPs by using analytical expressions and minimal computational resources.

4.2 Effect of the surface description

Before starting the analysis of the results presented in this chapter, we will briefly stress how the description of the NP surface within the atomistic TDDFT model impacts the resulting EEL probability spectra. The spill-out of the induced charge density plays a key role in the excitation of surface plasmon modes, especially in the case of Bennett plasmons, as we will describe in Section 4.5. In the atomistic TDDFT model, the spatial support of the Kohn–Sham eigenstates, and therefore of the induced charge density, is limited by the basis set used for solving the KS equations. This basis set consists on numerical atomic orbitals localized at the positions of the system atoms, whose spatial extension is determined by an energy cutoff known as the “energy shift” (see Appendix D). The smaller the energy shift, the larger the spatial extension of the atomic orbitals. In Fig. 4.3a, we plot the

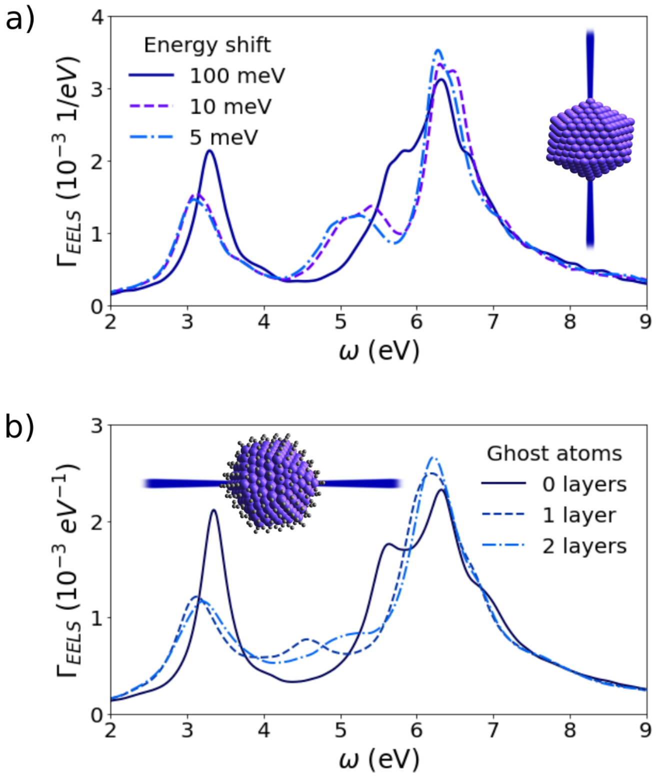

Figure 4.3: (a) EEL probability spectrum of a 100 keV electron passing through an icosahedral Na_{561} NP in the “tip” central trajectory, for different values of the energy shift parameter controlling the spatial extension of the atomic orbitals in the basis set. In the inset, we represent the atomistic structure of the NP and the electron beam. (b) EEL probability spectrum of a 100 keV electron passing through an icosahedral-like Na_{380} NP in the “tip” central trajectory, for basis sets including zero, one and two layers of ghost atoms, respectively. The energy shift is 100 meV in the three cases. In the inset, we represent the atomistic structure of the NP and the electron beam, together with a single layer of ghost atoms, depicted in gray.

EEL probability spectrum of a 100 keV electron passing through the center of an icosahedral Na_{561} NP and two of its vertices, a trajectory we will identify as “tip” from now on, for different values of the energy shift parameter. As observed, both LSP and MP modes are significantly dependent on this parameter. LSP modes red-shift as the spatial range of the atomic orbitals increases, i. e. the energy shift decreases, while at the same time they are less intensely excited. The MPs, which for an energy shift of 100 meV are close to the bulk frequency, also red-shift considerably. This trend mostly converges for an energy shift value of 10 meV, as further reducing it to 5 meV does not qualitatively alter the spectrum.

Alternatively, one can also increase the spatial support of the induced charge density by augmenting the basis set. It is possible to introduce additional atomic orbitals centered at positions outside the nanoparticle, which are then included in the KS description but do not have associated pseudopotentials nor electrons. These new orbitals are usually identical to the ones in the original atomic positions, and are therefore referred to as “ghost atoms”. In Fig. 4.3b, we plot the EEL probability spectrum of a 100 keV electron passing through an icosahedral-like Na_{380} NP in the “tip” central trajectory, obtained with three different basis sets of atomic orbitals with an energy shift of 100 meV. The first basis set only contains orbitals centered at the positions of the 380 atoms of the cluster, whereas the second one also includes ghost atoms at the positions that would be occupied by the next layer of Na atoms, and an additional second layer of ghost atoms was inserted in the third basis set. As observed, the inclusion of these new atomic orbitals has a similar effect to increasing the spatial range of the orbitals themselves: a red-shift of both LSP and Bennett modes and a reduction in their excitation strength. This confirms the importance of appropriately describing the nanoparticle surface when analyzing the excitation of surface plasmon modes. Note that the excitation energy of the Bennett modes is especially dependent on the parameters governing the description of the nanoparticle surface, which is consistent with the differences between the atomistic and jellium model spectra observed in Section 4.5.

4.3 Excitation of LSPs

As observed in Fig. 4.1b, the EEL probability spectrum is dominated by the LSPs in the visible spectral range. Localized surface plasmons were recently addressed for similar icosahedral-like nanoparticles within the atomistic *ab initio* framework by M. Urbieta et al. [194]. To illustrate that these modes are extremely sensitive to the crystallographic effects of the NP’s geometry, we have selected three representative electron trajectories crossing the center of the nanoparticle. The first trajectory is the aforementioned “tip” trajectory, in which the electron beam crosses through two nanoparticle vertices, and is depicted in blue in Fig. 4.4a. The second one, “edge”, consists in the electron passing through two geometric edges of the NP, and is depicted in green in Fig. 4.4a. The third and last trajectory, labeled as “facet” and depicted in red in Fig. 4.4a, corresponds to electrons travelling perpendicularly to two opposite crystallographic facets of the NP.

In Fig. 4.4b, we show the atomistic TDDFT EEL spectra corresponding to each of the three electron trajectories through a Na_{561} icosahedral NP in the 2–5 eV excitation energy range, which evidence the sensitivity of the spectra to atomic-scale features. For the tip trajectory (blue), a single peak at energy ≈ 3.1 eV emerges, whereas both the edge and facet trajectories show a main peak at ≈ 3.8 eV and a shoulder at ≈ 3.1 eV. The EEL spectra are complemented in the figure by the optical absorption spectrum describing the response of the NP to incident light polarized parallel to the edge trajectory. The absorption spectrum has a prominent peak at ≈ 3.05 eV, slightly red-shifted with respect to the EELS low-energy peak, and a shoulder at ≈ 3.7 eV.

In order to understand the nature of these excitations, we explore the induced

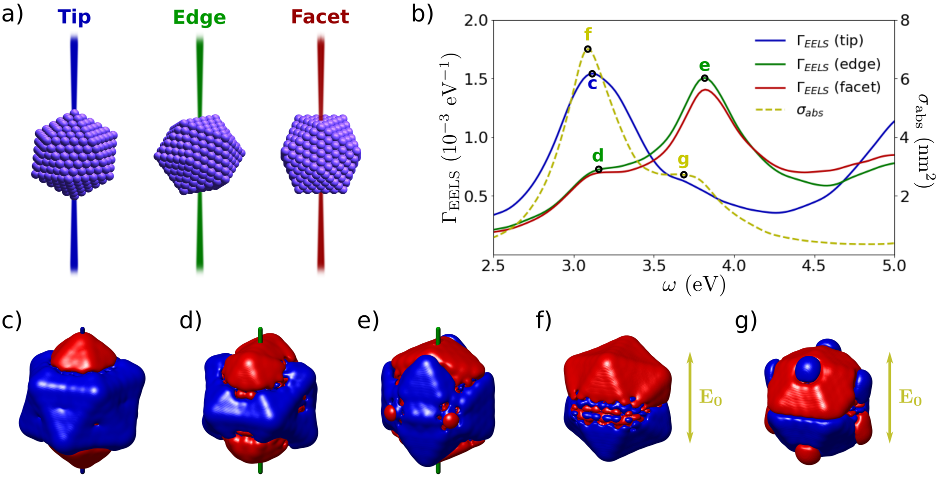

Figure 4.4: (a) Sketches of the three canonical incident electron trajectories through the center of the Na_{561} nanoparticle: a trajectory crossing through two opposite vertices (tip, in blue), a trajectory passing through two opposite edges (edge, in green), and a trajectory crossing two opposite facets (facet, in red). (b) EEL probability spectra Γ_{EELS} for the three electron trajectories depicted in (a). The absorption spectrum σ_{abs} of the same nanoparticle is depicted in yellow for incident light polarized parallel to the edge trajectory. (c–g) Induced charge density isosurfaces corresponding to the resonances marked in (b).

charge density distributions associated with each of the modes identified in Fig. 4.4b. In Figs. 4.4c–4.4g, we plot isosurfaces of their corresponding induced charge densities. As clearly observed, both the main peak in the tip EEL spectrum in Fig. 4.4c and the low-energy shoulder on the edge spectrum (Fig. 4.4d) correspond to a quadrupolar ($\ell = 2$) induced charge density distribution. In contrast, the symmetry of the induced charge density for the main LSP peak in the edge spectrum (4.4e) is more difficult to identify, with strong concentrations of induced charge at the nanoparticle vertices, and corresponds to a collection of higher-order modes. We do not display the induced densities for the facet trajectories, as they look very similar to those of the edge trajectory. As we discussed in Section 1.2, the main peak in the optical absorption spectrum (Fig. 4.4f) shows a clearly dipolar induced charge distribution, and corresponds therefore to the dipolar ($\ell = 1$) LSP. The higher-energy shoulder in Fig. 4.4g, however, displays strong induced charge concentrations at the nanoparticle vertices on top of a dipolar background. These results evidence that, even for central electron trajectories, the EEL spectrum is greatly dependent on the nanoparticle orientation, and therefore any quantitative study of the NP response should take into account the effect of crystallographic features.

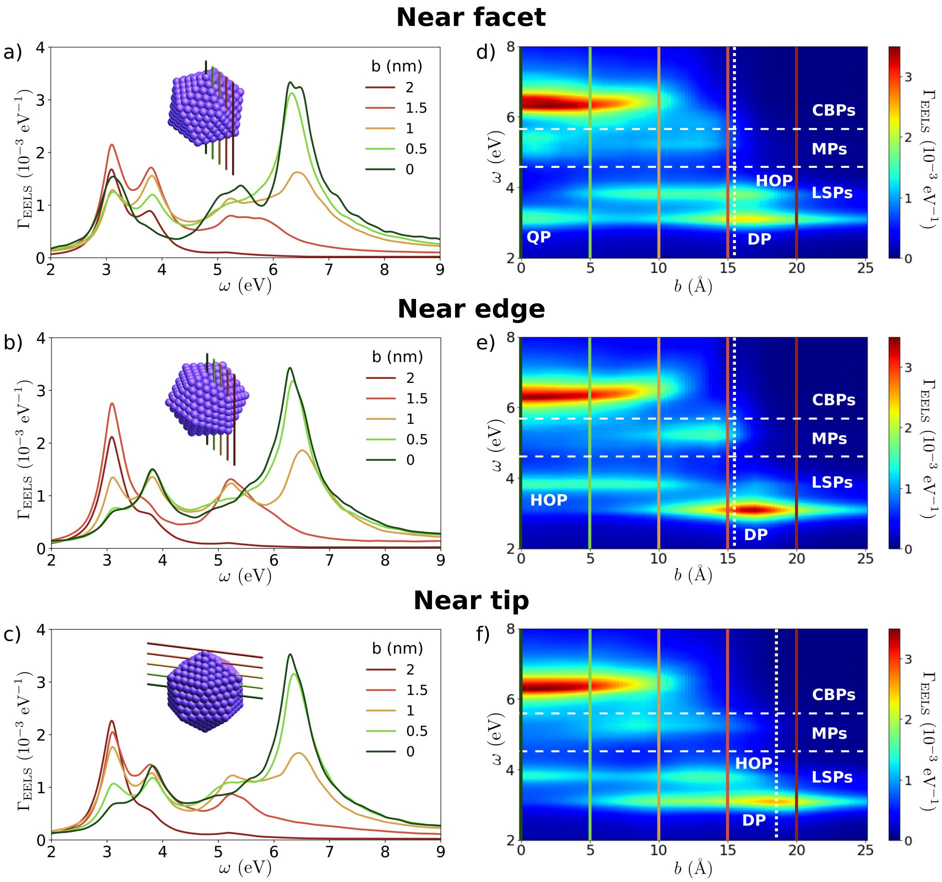

Figure 4.5: (a–c) EEL probability spectra for incident electron beams scanning a Na_{561} NP with varying impact parameter, as depicted in the insets, from $b = 0$ nm trajectories to $b = 2$ nm ones. The electron trajectory sets are labeled according to the closest surface element to the external trajectories as “Near facet”, “Near edge”, and “Near tip”. (d–e) Colormaps of the EEL probability spectra of each configuration for the range of impact parameter values $b = 0 - 2.5$ nm, corresponding to penetrating and external trajectories. The vertical solid lines mark the spectra shown in (a–c), and the vertical dotted lines mark the surface of the NP. The horizontal dashed lines separate the spectral regions of the LSP, MP, and CBP modes.

4.3.1 Impact parameter dependence

Although we have only considered central trajectories so far, typical EELS experiments in STEM are usually performed while scanning the nanoparticles, and therefore involve trajectories with varying impact parameters. As we mentioned in Section 1.6, external trajectories far from the nanoparticle surface act similarly to an homogeneous electromagnetic field probe, exciting the dipolar LSP mode. For the icosahedral, sphere-like particles considered in this study, the excitation energy of the dipolar LSP is not very dependent on the relative orientation of the NP [27, 262]. However, as the electron beam gets closer to the surface of the NP, the intensity of higher order modes increases, and thus the plasmonic response shows a dependence on the impact parameter. In order to discuss this dependence, in Figs. 4.5a–4.5c we plot the EEL probability spectra for representative trajectories as displayed in the insets. We include the central trajectory spectra in Fig. 4.4b and show $\Gamma_{\rm EELS}$ for increasing impact parameters. We also depict 2D colormaps of the EEL spectra within the whole $b = 0 - 2.5$ nm impact parameter range in Figs. 4.5d–4.5f, with the representative spectra from Figs. 4.5a–4.5c highlighted in their corresponding colors.

The spectra for external trajectories ($b \gtrsim 2$ nm) are dominated by LSPs, and bulk modes are not efficiently excited. In particular, when the trajectories are far from the NP surface, the main excitation is the dipolar ($\ell = 1$) LSP at around ~ 3.1 eV, as for light illumination. As the impact parameter decreases, the intensity of higher-energy surface modes increases. For grazing trajectories, a peak at $\omega \sim 3.8$ eV emerges, corresponding to higher-order LSPs, labeled as HOPs, such as the ones excited for the edge and facet central trajectories. Notice that the NP orientation plays a key role in determining whether these higher-order modes are excited, as it is observed when comparing Figs. 4.5d and 4.5e. In the first case, labeled as “Near facet”, grazing trajectories ($b \sim 2$ nm) efficiently excite HOP modes, but then their intensity decreases when the beam is moved towards the NP center, disappearing for central trajectories. The opposite happens in the second case, labeled as “Near edge”, as higher-order modes are not visible for grazing trajectories, but then their intensity gradually increases and becomes maximum when $b = 0$ nm. On top of this, the footprint of the dipolar LSP, labeled as DP, gradually vanishes for penetrating trajectories, as the lack of azimuthal symmetry of this mode prevents its excitation by electron beams traveling close to the nanoparticle center. The dipolar mode is instead substituted by the quadrupolar mode, labeled as QP, which dominates the low-energy region of the spectrum for “Near facet” central trajectories.

In addition to LSPs, the spectra in Figs. 4.5a–4.5c also clearly illustrate the emergence of modes that will be discussed next in this chapter. When the electrons approach the NP surface, another set of surface resonances are excited at higher energies, as observed for the $b = 1.5$ nm spectra. The new peaks correspond to Bennett or multipole plasmons (MPs), which will be discussed in detail in Section 4.5. Furthermore, a band of CBPs emerges above the plasma frequency for penetrating trajectories. Their intensity is very sensitive to the impact parameter, and increases gradually as the impact parameter decreases. In contrast to the LSPs and the MPs, whose excitation depends greatly on the orientation of the electron beam, the excitation of CBPs is only affected by the impact parameter, and is not sensitive to the particular orientation of the electron trajectory with respect to the NP. Therefore, we focus our study in the next sections on the tip electron beam trajectories, for which the identification of the separate CBP modes in the spectrum is slightly easier.

4.4 Excitation of CBPs

In order to characterize the complex CBP modal structure observed in the atomistic TDDFT EEL probability spectra, we complement the atomistic Γ_{EELS} results with calculations for an analogous spherical Na NP described within the hydrodynamic model as in Section 4.1.2. Based on our previous conclusion that the excitation of CBPs is not very sensitive to the orientation of the electron beam, in this section we focus on the tip electron beam trajectories. Figure 4.6 compares the atomistic TDDFT (panel a) and HDM (panel b) Γ_{EELS} calculations for increasing impact parameters b of the electron beam trajectory. For the central trajectory ($b = 0$), multiple CBP peaks are identified and labeled as CBP_j, with $j = \{1, 2, 3\}$ in Fig. 4.6a (bottom spectrum). By comparing these spectra with the corresponding HDM results in Fig. 4.6b (bottom spectrum), it is possible to draw a correspondence between the CBP peaks of the atomistic TDDFT and the well-defined spectral modes of the HDM. As discussed in Section 4.1.2, these modes are labeled as (ℓ, n), where ℓ is related to the angular distribution of the electron density, and n is the number of nodes in the radial direction. Notice that for the axial trajectory, $b = 0$, only even ℓ-numbers contribute [259] to the EEL probability, as only modes with the adequate azimuthal symmetry can be significantly excited in this case. According to this analogy between atomistic TDDFT and HDM results, the main peak CBP_1 at 6.30 eV corresponds to the $(\ell, n) = (0, 1)$ mode, while the subsequent peak CBP_2 at 6.48 eV corresponds to the $(2, 1)$ mode, and CBP_3 at 7.10 eV to the $(4, 1)$ mode. The excellent matching between the atomistic TDDFT and HDM results is further demonstrated through the visualization of the isosurfaces of the induced charge densities and their cross-sectional views along different planes in Figs. 4.7a–4.7b, supporting the consistent relationship between CBP peaks and specific (ℓ, n) modes.

The similarity between the atomistic TDDFT induced densities and their HDM counterparts is easily detected by visual inspection. For example, both the CBP_1 and the $(0, 1)$ mode display a concentration of positive charge inside the nanoparticle volume, surrounded by a layer of negative charge at the surface. However, in the atomistic case there is an additional thin layer of positive charge, which is not present in the HDM case. This discrepancy is caused by the different descriptions of the nanoparticle surface used by each model: the atomistic TDDFT model allows for the spill-out of the NP charge, whereas the HDM assumes a hard boundary and does not allow the spill-out. Even though this may cause small differences in the induced charges at the surface, these can be safely neglected when analyzing the bulk modes. A similar correspondence is observed for the induced charge density patterns of the atomistic CBP_2, CBP_3 and the HDM $(2, 1)$, $(4, 1)$ modes, respectively. Therefore, the direct comparison of the atomistic induced charge densities with the HDM ones nicely supports the previous identification of the CBP excitations in the atomistic spectrum.

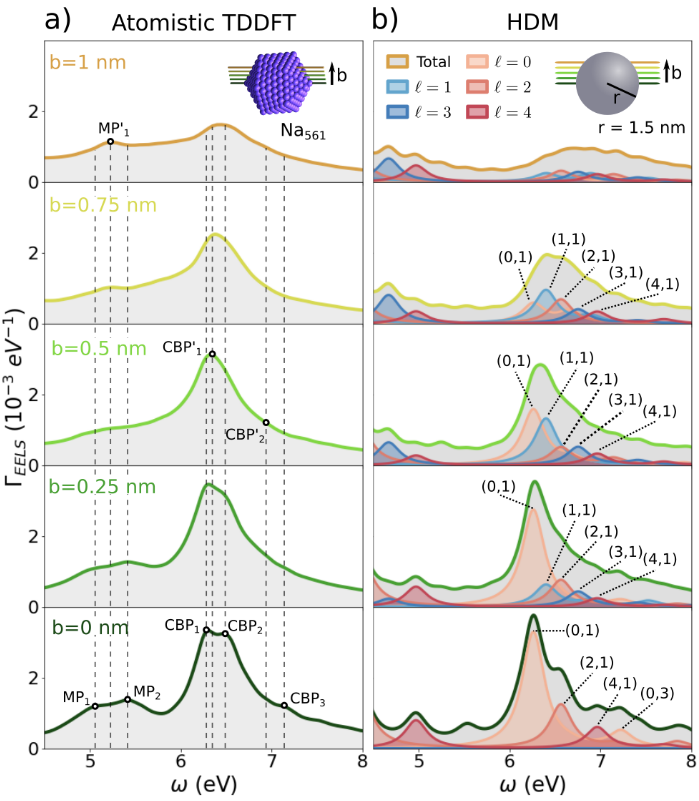

Figure 4.6: High-energy range of the EEL spectra for 100 keV electron trajectories, as calculated with (a) the atomistic TDDFT formalism and (b) the HDM through (a) an icosahedral Na$_{561}$ NP and (b) a reference spherical Na NP ($a = 1.5$ nm), for different electron trajectories characterized by their impact parameters b, as sketched in the insets. Impact parameter increases from panels on the bottom to panels on the top. The different modes are labeled as CBP$_j$ and CBP'$_j$ (confined bulk plasmons), and MP$_j$ and MP'$_j$ (Bennett or multipole plasmons). The contribution of the (ℓ, n) modes in the HDM spectra are displayed separately, using different colors to distinguish even (red) and odd (blue) angular momentum ℓ contributions.

4.4.1 Impact parameter dependence

As described in Section 1.6, in STEM-EELS experiments the electron probe scans the target, varying its impact parameter. Therefore, in order to generalize our study, we extend our analysis to noncentral beam trajectories ($b \neq 0$), which cause significant changes in the spectral shape of Γ_{EELS}, as observed in Fig. 4.6. First, the overall contribution of the CBP modes to the Γ_{EELS} spectrum decreases with increasing b, as the incident electrons' path inside the NP is shorter. Second, the resonance profile of the EEL probability spectrum changes, in concordance with the loss of rotational symmetry of the induced charge density (C_5 rotation around a vertex–vertex axis for the atomistic icosahedral nanoparticles and azimuthal

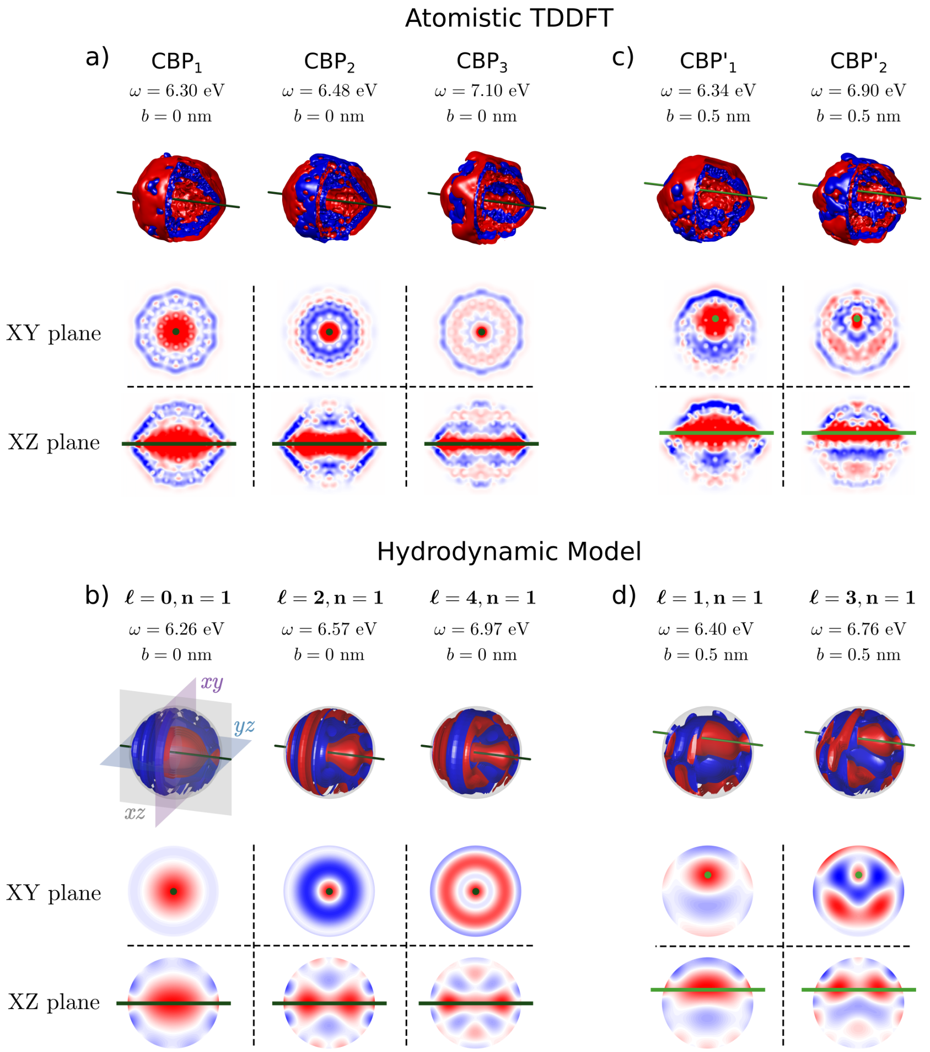

Figure 4.7: Induced charge densities for the CBP resonances excited by a central electron beam ($b = 0$ nm) through (a) a Na$_{561}$ NP, calculated with atomistic TDDFT, and (b) a reference spherical sodium NP ($a = 1.5$ nm), calculated with the HDM. The 3D images depict isosurfaces of the induced charge density for each of the modes identified in Figs. 4.6a and 4.6b (with a quarter of the NP removed), whereas the 2D plots show cross-sectional views of the induced density along the X–Y and X–Z planes. Each of the HDM modes in (b) is labeled with its corresponding ℓ and n numbers. Note that, while the main contributions at these energies correspond to the labeled modes, there are also contributions from other overlapping modes, and thus the induced densities do not strictly follow the symmetry associated to the (ℓ, n) mode. (c) Same as in panel (a) but for impact parameter $b = 0.5$ nm. (d) Same as in panel (b) but for impact parameter $b = 0.5$ nm.

symmetry for the spherical ones), as observed in Figs. 4.7c and 4.7d. The main spectral changes observed are the blue-shift of the main overall CBP peak and the smoothening of the higher-energy peaks, which become less prominent. We label the new peaks emerging for noncentral electron trajectories, corresponding to a sum of contributions of several multipolar resonances, as CBP'$_1$ and CBP'$_2$.

The observed trends are understood by examining the corresponding HDM spectra, which reveal that the shifts are driven by the excitation of odd-ℓ modes, which are forbidden for central trajectories due to symmetry constraints [259]. As a result of the rotational symmetry breaking when the electron trajectory departs from the center of the NP, the main peak blue-shifts as the $(0,1)$ mode is gradually surpassed in intensity by the $(1,1)$ mode emerging at a slightly higher energy. Simultaneously, the excitation of odd-ℓ CBP modes intercalated between the even-ℓ ones smoothens the high-energy tail of the EEL probability spectra, which explains the difficulty to identify the separate modes in the atomistic TDDFT results. The spatial characterization of odd-ℓ CBP modes, activated by the symmetry breaking of noncentral trajectories, is more clearly illustrated in Figs. 4.7c and 4.7d, where the isosurfaces of the induced charge densities for the main spectral peaks are displayed for nonaxial electron trajectories. The excellent matching of the atomistic TDDFT and HDM patterns is evident by comparing panels c) (modes CBP'$_1$ and CBP'$_2$) and d) (HDM modes $(1,1)$ and $(3,1)$) for nonaxial $b = 0.5$ nm trajectory.

4.5 Excitation of Bennett Plasmons

We now examine the spectral features emerging between the LSP and CBP modes in the atomistic TDDFT Γ_{EELS} spectra, labeled as MP$_1$, MP$_2$, and MP'$_1$ in Fig. 4.6a, which can be identified as Bennett plasmons [255]. These resonances are characterized by an induced dipole moment formed by induced charge densities of opposite sign across the nanoparticle boundary, and are therefore localized at the metal surface [218, 263]. This particular pattern of induced charge distribution can be observed in Fig. 4.8, where we plot induced charge density isosurfaces and their cuts along the XY and XZ planes for the three aforementioned MPs. The induced dipole moment at the nanoparticle surface is especially visible in the XZ plane cuts along the electron path for central trajectories, and in the XY plane cuts for the MP$_2$ and MP'$_1$ peaks. Furthermore, it is possible to associate an angular momentum number ℓ to each of these induced charge density distributions, according to their corresponding symmetries. By direct inspection we can conclude that MP$_1$, MP'$_1$, and MP$_2$ correspond respectively to the $\ell = 0$, $\ell = 1$, and $\ell = 2$ modes, thus matching the order of their excitation energies. Additionally, in Fig. 4.8b we also depict the induced density for the MP emerging in the $b = 1.5$ nm "Near edge" spectra in Figs. 4.5b and 4.5e, which looks very similar to MP'$_1$.

With the aim of further exploring the nature of these modes and their differences with the LSP and CBP modes described previously, we introduce the *accumulated charge ratio*, $R_q(r)$. This function measures the ratio of the total (atomistic TDDFT) induced charge, in absolute value, contained within a spherical shell of radius r, as

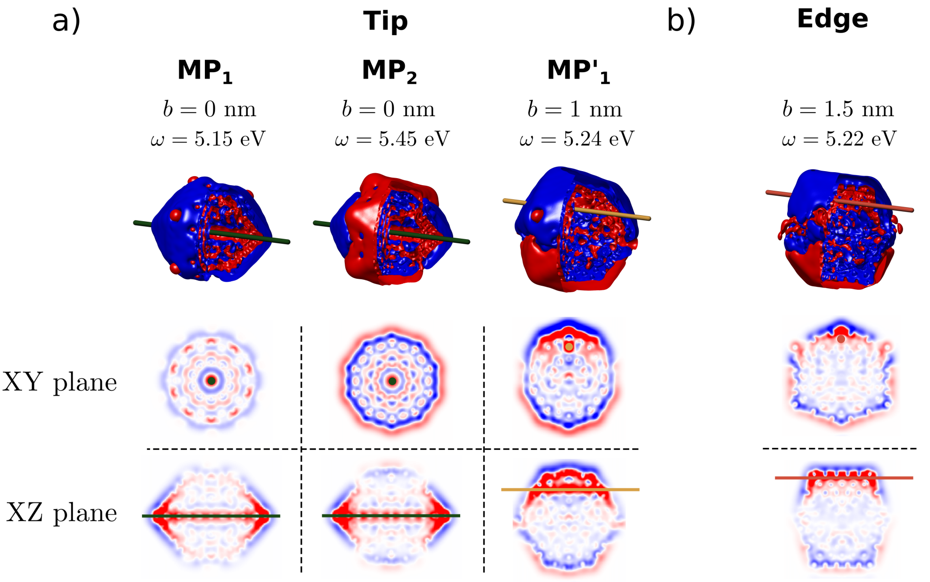

Figure 4.8: (a) Induced charge densities of the modes identified as MPs (or Bennett plasmons) in Fig. 4.6a, computed with the atomistic TDDFT model. The 3D images depict isosurfaces of the induced charge density for each of the modes (with a quarter of the NP removed), whereas the 2D plots show cross-sectional views of the induced density along the XY and XZ planes. (b) Same as in (a) but for the MP emerging for grazing trajectories in the "Near edge" electron beam trajectory, visible in Figs. 4.5b and 4.5e.

depicted in the inset in Fig. 4.9a:

$$R_q(r,\omega) = \frac{\int_0^r r'^2 |\delta n(r',\phi,\theta,\omega)| \sin\theta \; dr' \; d\phi \; d\theta}{\int_0^{r_{\max}} r'^2 |\delta n(r',\phi,\theta,\omega)| \sin\theta \; dr' \; d\phi \; d\theta}, \tag{4.2}$$

where $\delta n(r',\phi,\theta,\omega)$ is the induced charge density in spherical coordinates (r',ϕ,θ) at excitation energy ω.

Figure 4.9(a) shows the calculated $R_q(r,\omega)$ as a function of r, for all the volume and surface modes studied throughout this work, for the Na_{561} nanoparticle and the "tip" central electron trajectory as in Fig. 4.6a. The dashed black line corresponds to a homogeneous spherical charge distribution, i.e, $R_q(r,\omega) = r^3/r^3_{\max}$, plotted for reference. From the comparison, it is clear that the induced charge of the CBP modes (blue lines) is accumulated inside the volume of the NP, while the LSP mode (yellow line) exhibits an induced density distribution shifted towards the surface. Importantly, the Bennett plasmons MP_1 and MP_2 (green lines) exhibit a behavior similar to the LSP, with a slightly larger penetration into the NP, thus confirming their surface nature. These trends are better appreciated in Fig. 4.9b, where we plot the difference between the $R_q(r,\omega)$ associated with each mode and

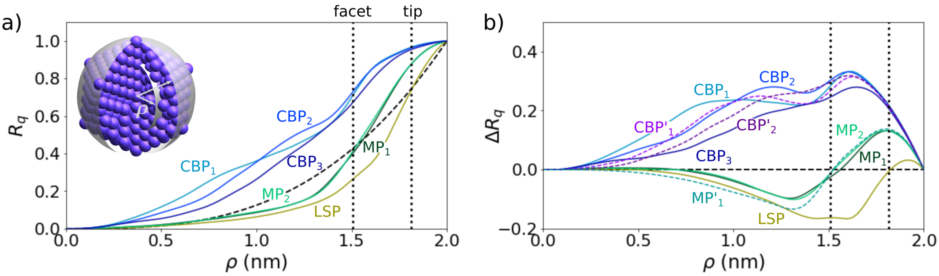

Figure 4.9: (a) Accumulated charge ratio $R_q(r,\omega)$ for various modes excited by an electron beam with $b = 0$ for the Na$_{561}$ nanoparticle, as identified in Fig. 4.6a. The results corresponding to the quadrupolar LSP mode are represented by a yellow line, Bennett or MP modes by green lines, and CBP modes by blue lines, with the homogeneous charge density reference depicted as a dashed-black line. The inset depicts the spherical shells used for the computation of $R_q(r,\omega)$. The vertical dotted lines indicate the limits of the interval of r values associated to the atomic positions of the atoms in the outermost layer, 1.51 nm $< r <$ 1.81 nm. The lower limit corresponds to atoms in the NP's facet, and the upper limit to atoms in the vertices of the NP. (b) Difference between $R_q(r,\omega)$ and the homogeneous charge density reference, $\Delta R_q(r,\omega)$. In addition to the modes in (a), CBP modes excited by a $b = 0.5$ nm electron beam trajectory are also included in dashed purple.

the homogeneous charge density reference, $\Delta R_q(r,\omega)$. We have also included the modes emerging in the case of noncentral trajectories in the spectra of Fig. 4.6a, in order to show that their induced charge distributions are consistent with those of the central trajectory.

In order to complement our understanding from the atomistic TDDFT results, we have computed the EEL probability spectrum of an analogous spherical Na NP within the *ab initio* jellium framework described in Subsection 4.1.3. Although the peaks associated with Bennett plasmons do not appear as prominently as in the atomistic case, one can distinguish several peaks between the LSP and CBP regions when Γ_{EELS} is plotted in a logarithmic scale, as we do in Fig. 4.10a. In addition to the well-defined LSP and CBPs, three broadened excitations are visible in this plot, appearing as maxima in the contributions of the different angular momentum components ℓ to the spectrum, labeled as MP$_i$, with $i = 1, 2, 3$. In Fig. 4.10b we plot the corresponding induced charge densities at their excitation energies, together with the one associated to the quadrupolar LSP for reference. As it can be observed, the induced charge densities for the jellium MP$_1$ and MP$_2$ match quite closely their atomistic counterparts, shown in Fig. 4.8a. The jellium MP$_1$, which shows an induced charge distribution similar to that of the atomistic MP$_1$, corresponds to a peak in the jellium $\ell = 0$ angular momentum contribution, whereas the jellium MP$_2$, which shows an induced charge distribution similar to that of the atomistic MP$_2$, corresponds to a peak in the jellium $\ell = 2$ angular momentum contribution. This supports our previous identification of the MP$_1$ and MP$_2$ as $\ell = 0$ and $\ell = 2$ Bennett modes. Additionally, we can also identify a maximum in the $\ell = 4$ contribution, labeled as MP$_3$, which does not have an atomistic equivalent.

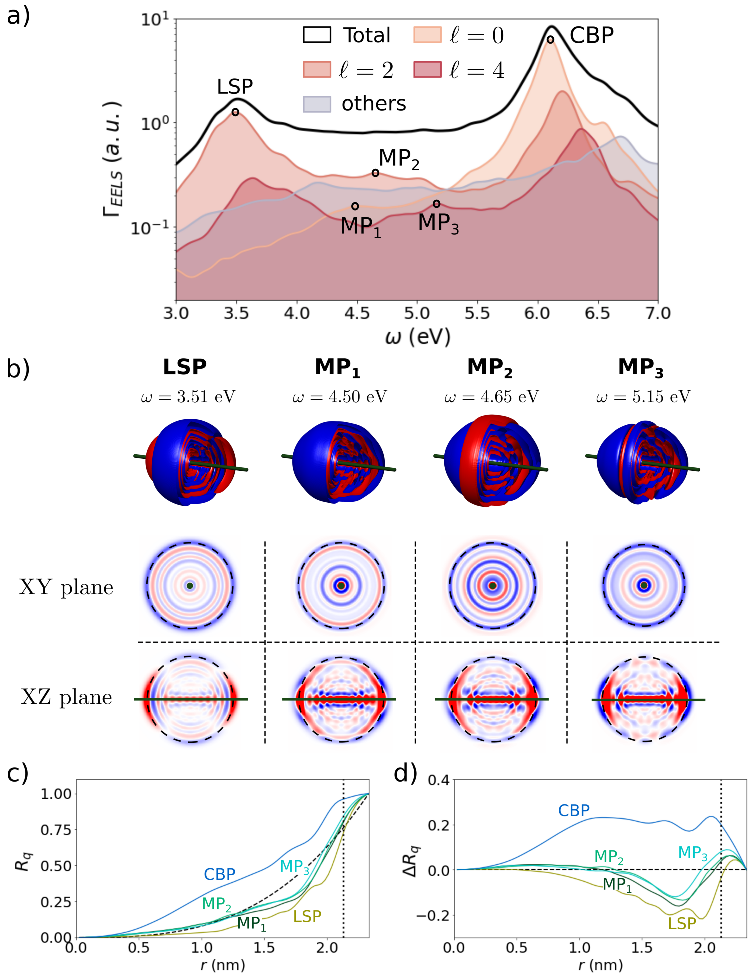

Figure 4.10: (a) EEL probability spectra in logarithmic scale for 100 keV electron trajectories, as calculated with the jellium TDDFT formalism (see Subsection 4.1.3) through a spherical Na NP with 1074 conduction electrons ($a = 2.13$ nm). The different peaks are labeled as LSP (localized surface plasmon), MP$_j$ (Bennett or multipole plasmons), and CBP (confined bulk plasmon). The contribution of the different angular momentum ℓ components to Γ_{EELS} are displayed separately. (b) Induced charge densities obtained with jellium TDDFT for the peaks identified in panel a and associated with surface modes, displaying both 3D isosurfaces (with one quarter removed) and cross-sectional views along the XY and XZ planes. The dashed lines represent the boundaries of the background positive charge density in the jellium calculations. (c) Accumulated charge ratio $R_q(r)$ for various modes identified in panel a. The results corresponding to the LSP mode are shown by a yellow line, Bennett or MP modes by green lines, and the CBP mode by a blue line, with the homogeneous charge density reference depicted in dashed black. The vertical dotted line indicates the boundaries of the jellium positive charge background. (d) Difference between $R_q(r)$ and the homogeneous charge density, $\Delta R_q(r)$, for the same modes as in panel c.

Unfortunately, our implementation of the jellium methodology does not allow for increasing the impact parameter, and a comparison with the odd-ℓ MPs excited for noncentral trajectories within the atomistic model is therefore not possible.

The analogy between the atomistic and jellium TDDFT results is further reinforced by the results in Figs. 4.10c and 4.10d, which show the accumulated charge ratios for all the excitations identified in Fig. 4.10a. As one can appreciate, the radial distributions of the jellium induced charge densities nicely match their atomistic counterparts displayed in Fig. 4.9. Thus, the excitation of Bennett plasmons in small nanoparticles by penetrating electron beams is robustly demonstrated, regardless of the specific quantum framework adopted to describe the electronic structure of the metal. Furthermore, our results also suggest the excitation of several Bennett plasmons with different angular distribution, depending on the electron path and the energy of the excitation. However, quantitative details such as the MP excitation energies depend on the specific description of the metal surface, as evidenced by the significant differences between the excitation energies in our atomistic and jellium results. Such quantitative differences, however, are to be expected, as we already discussed in Section 4.2 that the excitation energies of MP modes are very sensitive to the details of the description of the surface.

4.6 Summary

In this chapter, we have characterized the full plasmonic response of sodium nanoparticles by analyzing the EEL probability for penetrating electron beam trajectories within the atomistic TDDFT framework described in Sections 2.1 and 2.2. We have complemented the atomistic TDDFT results with Γ_{EELS} calculations with two auxiliary models described in Section 4.1, a hydrodynamic model (HDM) and a jellium TDDFT model. This is followed by a brief discussion on the sensitivity of the surface plasmon modes to the details of the description of the surface within the atomistic TDDFT model in Section 4.2. In Section 4.3, we have provided an overview of the excitation of localized surface plasmon (LSP) modes at optical frequencies and its dependence on the nanoparticle geometry. Next, in Section 4.4, we have placed our focus on the analysis of confined bulk plasmons (CBPs), which appear in the atomistic spectra as a series of satellite peaks and shoulders above the plasma frequency. With the help of analytic expressions of the EEL probability derived from the HDM, we have identified well-defined CBP modes that contribute to the peaks in the EEL spectra, and analyzed the effect of the impact parameter of the electron trajectory on their excitation. Finally, in Section 4.5 we have shown that electron beams penetrating the sample can efficiently excite Bennett plasmons localized at the surface, and appearing in the spectra between the LSP and CBP resonance energies. Notably, these modes are not described by the HDM model due to the impossibility of of classical non-local descriptions to capture the diffuse nature of the electron density at the NPs surface. The overall good qualitative, and even quantitative, agreement between theoretical models which include nonlocality in the response of the nanoparticles at different levels underscores the robustness of the studied phenomena in small sodium nanoparticles. Furthermore, our study serves to interpret the experimentally observed blue-shift of the bulk peak in Bi nanoparticles [105] and Al disks [106] with increasing impact parameters, and to provide a deeper understanding of the behavior of CBPs in metallic nanostructures. The conceptual characterization of CBPs and Bennett plasmons as performed here will allow for a more exhaustive analysis and technological exploitation of plasmonic features in valence EELS of metal nanoparticles.

CHAPTER

5

AB INITIO CALCULATION OF RAMAN SPECTRA OF ORGANIC SELF-ASSEMBLED MONOLAYERS ON METALLIC SURFACES

Self-assembled monolayers (SAMs) play a central role in modern surface chemistry and nanotechnology, owing to their wide range of applications in areas such as nanoelectronics [264–266], sensing [267–269], and catalysis [270–272]. Despite this versatility, several scientific and technological challenges remain unsolved. One of the most significant difficulties lies on determining the geometrical structure of monolayers of adsorbed aromatic molecules, due to the vast number of possible configurations. Although experimental techniques like scanning tunneling microscopy (STM) or X-ray spectroscopy [273, 274] can provide valuable insights into the coverage density and the monolayer thickness, accurately resolving molecular tilt angles and the twist of the aromatic backbone often requires more sophisticated procedures, such as near-edge X-ray absorption fine-structure (NEXAFS) analysis [275, 276] or Kelvin probe force microscopy [277]. In this context, theoretical calculations based on DFT have proven their usefulness, as they complement experimental data and allow for evaluating the suitability of proposed stable structures [278–280]. However, a comprehensive theoretical exploration of the vast configuration space is generally impractical, particularly for tightly packed assemblies where long-range dispersive interactions between molecules become relevant, which has stimulated the demand of efficient search methodologies.

One of the most established techniques for studying such interfaces is Surface-Enhanced Raman Spectroscopy (SERS, see Section 1.5), with recent studies emphasizing its potential for high-resolution molecular imaging or even revealing single-atom dynamics within SAMs [281, 282]. Although SAMs typically exhibit tightly packed molecular arrangements such as the (2×2) hexagonal patterns observed in experimental preparations of 1,1'-biphenyl-4-thiol monolayers on Au(111) [274], most theoretical atomistic descriptions of SERS for SAM systems rely on simplified finite models of the periodic structure [44, 45, 133]. As a result, these models often fail to fully capture the intermolecular interactions essential in the formation of this kind of systems. Furthermore, accounting for the complete periodic structure is crucial when dealing with collective Raman effects arising from the coupling of molecular infrared dipoles across the monolayer [283–285].

In this chapter, we study the structure of SAMs formed by 4'-cyanobiphenyl-4-thiol molecules ($C_{13}H_9NS$, thereafter referred to as CN-BPT) on an Au(111) surface, along with their Raman spectra, using a fully periodic *ab initio* approach. This methodology naturally accounts for all inter-molecule interactions and collective effects to address the final SERS fingerprint of the whole assembly. We start with a brief overview of SAMs in Section 5.1, including an explanation of the notation used to describe overlayer periodicities. In Section 5.2, we introduce a methodology for obtaining stable SAM configurations based on Bayesian optimization techniques outlined in Section 2.4, which are employed here to minimize the adsorption energy landscape of the CN-BPT monolayer system onto the metallic surface. Section 5.3 presents a detailed analysis of the Raman spectra of this SAM corresponding to the five lowest-energy configurations within its (2×2) periodic arrangement, as obtained using the perturbation theory approach described in Section 2.3. In Section 5.4, we then compare the Raman spectra of CN-BPT SAMS for varying surface coverage densities in order to analyze the emergence of collective vibrational effects. Next, in Section 5.5 we consider the possibility of surface reconstruction by introducing an alternative adatom-mediated geometry and examine its influence on the resulting Raman spectrum. Finally, Section 5.6 evaluates the relative importance of the aforementioned factors in accurately modeling the Raman response of SAMs and outlines potential directions for future research based on the findings in this chapter.

5.1 Self-assembled monolayers

Self-assembled monolayers (SAMs) are among the most ubiquitous nanostructures in surface science. They consist of periodic assemblies of organic molecules spontaneously adsorbed onto solid surfaces and organized into crystalline arrangements [286]. For the adsorption process to be energetically favorable, the molecules must contain a chemical functional group with strong affinity for the metallic surface, commonly referred to as *ligand* or *headgroup*. The portion of the adsorbed molecule that constitutes the outer surface of the film is known as the *tailgroup*, and it plays a key role in defining the surface properties of the SAM, such as the wettability. Connecting the headgroup and the tailgroup is the *spacer* —also known as *backbone*— as illustrated in Fig. 5.1.

One of the key advantages of SAMs is their ease of fabrication. In many cases,

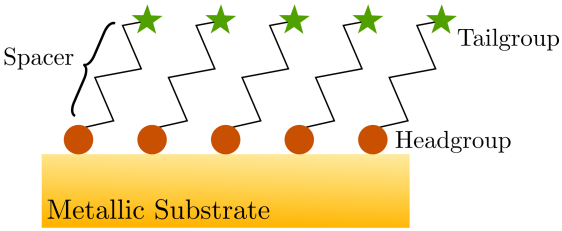

Figure 5.1: Sketch of a typical SAM. The molecules are "chemisorbed" onto the metallic substrate via a headgroup with strong affinity for the surface, commonly a thiol group in the case of noble metals. The tailgroup constitutes the outer surface of the film, while the spacer links the headgroup and the tailgroup.

the molecules can be deposited directly from solution under ambient conditions or, alternatively, from physical vapor under ultra-high vacuum. Another major strength lies on their remarkable versatility: the properties of SAMs can be finely tuned by modifying the tailgroup or altering the molecular arrangement. Furthermore, it is also possible to build SAMs on top of nanostructures of any shape and size, and not only on top of flat surfaces. These characteristics make SAMs an essential component in nanotechnology, where they are employed for material protection [287], stabilization and functionalization of nanostructures [288, 289], and as building blocks in complex nanodevices, such as sensors [268] and molecular motors [290]. Additionally, SAMs play a crucial role in the field of SERS, enabling the attachment of SERS-active probe molecules to metallic surfaces and nanoparticles [143, 291], or their integration into nanocavities [292].

The most commonly employed headgroup in SAM formation is the thiol (–SH) functional group, which exhibits high affinity for noble metal surfaces [293] and enables the formation of well-defined structures with a wide range of chemical properties. In particular, the ordered adsorption of alkanethiolates —organic alkane chains (C_nH_{2n+2}) bounded to a thiol group— and thioaromatic compounds —molecules featuring a backbone of phenyl rings— has been extensively studied on gold [294, 295], silver [294, 296], and copper [294] substrates. In this chapter, we focus on the specific case of CN-BPT molecules adsorbed on an Au(111) surface. It is well known that the formation of strong covalent bonds between the S atom in the thiol group and the Au atoms of the surface can lead to a significant reconstruction of the substrate. In some cases, this may result in the displacement of Au atoms into the overlayer and the formation of adatom-mediated structures [297, 298]. Although an example of such a structure will be considered in Section 5.5, the rest of the discussion in this chapter will be limited to conventional SAM structures for the sake of clarity and focus.

The formation of ordered molecular layers on metallic surfaces is governed by two competing effects which determine the crystalline structure of the monolayer. The first effect is the interaction between the substrate and the adsorbate. Due to the variation in adsorption energies at different coordinated surface sites, this interaction induces a lateral ("horizontal") corrugation of the potential energy surface (PES) that reflects the periodicity of the substrate. Consequently, this interaction plays a dominant role in determining the preferred adsorption sites for individual molecules. The second effect arises from the inter-molecule interactions, which are primarily governed by van der Waals forces between the aromatic backbones. These interactions play a crucial role in determining the packing density and the orientation of the adsorbed molecules. The confluence of surface–adsorbate and intermolecular forces gives rise to a very complex PES, making the precise prediction and characterization of the exact configuration of SAM structures particularly challenging. A variety of experimental techniques are available to probe SAM structures, including scanning probe microscopy techniques such as atomic force microscopy or scanning tunneling microscopy, diffraction techniques like X-ray or electron diffraction, and spectroscopic approaches such as Raman spectroscopy or X-ray absorption spectroscopy. On the theoretical side, DFT remains the primary tool for studying SAMs, offering accurate predictions of structural and electronic properties, provided that the long-range dispersive interactions are adequately treated. Nevertheless, identifying the most stable SAM configurations exclusively using theoretical methods is often challenging due to the intricate nature of the PESs associated with these systems.

Overlayer periodicity

The adsorbed molecules, or adsorbates, arrange themselves on the surface in an ordered manner, forming well-defined overlayer structures. These structures can adopt a wide variety of configurations depending on factors such as the nature of the adsorbate and the surface coverage density. To classify and describe the resulting structures accurately, it is essential to establish clear and objective criteria. The most effective way to proceed is by describing the overlayer in relation to the underlying substrate structure. This first requires identifying the surface unit cell, which is defined by the primitive lattice vectors $\mathbf{a}_1$ and $\mathbf{a}_2$, as illustrated in Fig. 5.2. Next, the same procedure must be applied to the overlayer unit cell, defined by the vectors $\mathbf{a}'_1$ and $\mathbf{a}'_2$, which should ideally be chosen parallel to the substrate unit cell vectors. Using Wood's notation of surface crystallography [299], the overlayer structure is described as:

$$(|\mathbf{a}'_1|/|\mathbf{a}_1|\ R\theta_1 \times |\mathbf{a}'_2|/|\mathbf{a}_2|\ R\theta_2)\,, \tag{5.1}$$

where θ_1 and θ_2 are the angles between $\mathbf{a}_1$ and $\mathbf{a}'_1$, and between $\mathbf{a}_2$ and $\mathbf{a}'_2$, respectively. The label R before the angular values indicates that the overlayer vectors are rotated with respect to the substrate ones. These angles only need to be included if they are nonzero. Figure 5.2 illustrates three different overlayer structures on an Au(111) surface, along with their corresponding label using Wood's notation. This notation is particularly well-suited for describing simple overlayer structures which maintain the symmetry of the underlying substrate, but it is less effective for complex overlayer structures, where matrix notation is more convenient

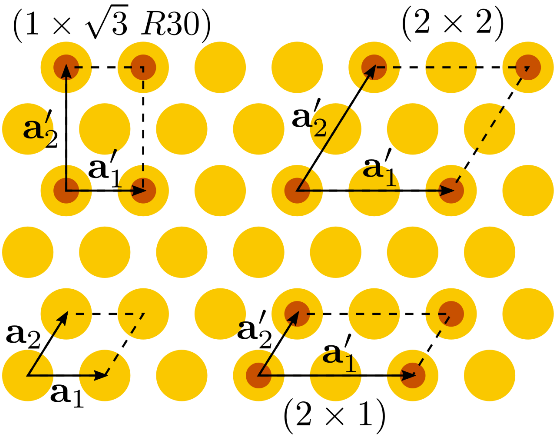

Figure 5.2: Schematic illustration of the periodicity of an adsorbed overlayer. Yellow circles represent gold atoms arranged in the characteristic hexagonal lattice of the Au(111) surface, whereas red circles represent the adsorbate. The primitive lattice vectors of the substrate, $\mathbf{a}_1$ and $\mathbf{a}_2$, are represented at the bottom left, together with the substrate primitive unit cell. Three overlayer lattices with varying coverage densities are also depicted, each with its own set of overlayer lattice vectors $\{\mathbf{a}'_1, \mathbf{a}'_2\}$, unit cells, and corresponding Wood's notation labels.

[300]. Since we will be focusing exclusively on simple overlayer structures in this chapter, we will stick to Wood's notation.

5.2 Bayesian optimization of CN-BPT SAMs

In this section, we address the problem of determining the optimal configuration of a SAM of CN-BPT molecules on an Au(111) surface, using the Bayesian optimization methodology implemented in the BOSS code (see Section 2.4). This will serve as an exemplary case which will show the possibilities of this methodology to determine SAM configurations. We assume that the molecules are densely packed in a hexagonal (2×2) arrangement, consistent with experimental observations of 1,1'-biphenyl-4-thiol SAMs on Au(111) [274]. The PES of the system is modeled as a surrogate Gaussian process, which is iteratively fitted to data sampled with DFT energy calculations. This approach yields a set of candidate structures corresponding to local minima of the PES, which are then subsequently relaxed using conventional optimization methods in order to identify the true ground-state configuration and the lowest-energy minima.

5.2.1 Computational details

We employed the BOSS code ([173], see Section 2.4) to search for the minima of the adsorption energy function, E_{ads}, defined as:

$$E_{\mathrm{ads}} = E_{\mathrm{SAM}} - E_{\mathrm{mol}} - E_{\mathrm{slab}}, \tag{5.2}$$

where E_{mol}, E_{slab}, and E_{SAM} correspond to the energies of the isolated molecule, the clean gold slab, and the hybrid SAM system, respectively. For the periodic systems, all the energies are computed per unit cell. The adsorption energy function was modeled using a surrogate Gaussian process with a constant prior mean function and a squared exponential correlation kernel (a standard periodic kernel was used for periodic variables). This surrogate Gaussian process model is iteratively refined by fitting to E_{ads} values computed with DFT for points (specific configurations) of the configuration space, as guided by the eLCB acquisition function.

The DFT energy calculations were carried out with the open-source GPAW code [187], which uses the PAW method for effectively describing the core electrons (see Appendix E). The combined substrate + adsorbate system was modeled with the periodic atomistic structure shown in Fig. 5.3a. The calculations employed the optPBE-vdW exchange–correlation functional incorporating long-range dispersive interactions [301] (see Appendix C), along with a plane-wave basis set with an energy cutoff of 400 eV (see Appendix D). To build those structures, we first optimized the lattice constant of bulk Au, and then used it to build a 3-layer periodic Au slab, allowing the atoms in the outermost layer to relax with conventional structure optimization. The CN-BPT molecule was then added as an adsorbate, after having been fully relaxed in isolation. The configurational phase space for the Bayesian optimization searched with BOSS was defined by the parameters governing the adsorption position and the molecular orientation.

The Rama spectra presented later in this chapter were computed using the methodology outlined in Section 2.3, as implemented in the open-source GPAW package [188], for incident unpolarized light with a wavelength of 500 nm and at room temperature. All calculations were performed with the optPBE-vdW exchange–correlation functional [301]. First, the system's eigenfunctions and eigenenergies were obtained from converged LCAO ground-state calculations using a double-ζ polarized basis set (see Appendix D). A real-space grid spacing of 0.2 Å was used to represent the wavefunctions and Kohn-Sham potentials, and the Brillouin zone sampling was performed with a Monkhorst-Pack k-mesh of 20 Å^{-1}. Since our 2D system possesses a net surface dipole, we applied a dipole layer correction in order to compensate the artificial electric field arising from the periodic boundary conditions of the supercell [302]. The displaced forces and potentials —used to compute the Γ-point phonon modes and the electron–phonon coupling matrix elements— were obtained using a plane-wave basis set with an energy cutoff of 700 eV and a Monkhorst-Pack k-mesh density of 12 Å^{-1}. As described in Section 2.3, phonon modes and electron–phonon coupling matrix elements were computed within a finite-difference scheme. To account for the phonon mode broadening in the Raman spectra, a Gaussian smearing with a standard deviation of 5 cm^{-1} was applied. All Raman spectra presented in this chapter are normalized, as consistent with the standard practice in the literature.

5.2.2 Translational search

Even with the most efficient optimization algorithms, the computational cost of identifying the minima of a multi-dimensional function increases exponentially with the number of dimensions. To mitigate this, we separate the configurational search space into two distinct groups of parameters: the translational parameters determining the adsorption position, and the rotational parameters, which define the orientation of the molecule. We begin by searching for the optimal adsorption site, i.e., the energetically most favorable position for the thiol headgroup. This is done by displacing the rigid CN-BPT molecule horizontally and vertically above the Au(111) surface, maintaining it in an upright orientation. This procedure is illustrated in Fig. 5.3b, which shows a scheme of the molecule adsorbed on the gold surface and highlights the relevant variables: the vertical displacement of the molecule, z, and the in-plane displacements along the unit cell vectors $\{\mathbf{a}'_1, \mathbf{a}'_2\}$. The search space is horizontally constrained to the shaded area, which coincides with the substrate unit cell depicted in Fig. 5.2, and vertically to the 1 nm $< z <$ 3 nm interval. Given the periodic nature of the in-plane displacements, these are modeled with the standard periodic kernel, while the (non-periodic) vertical displacement is described using the squared exponential kernel.

Figure 5.3c presents the surrogate Gaussian process model after convergence is achieved, which occurs after around 50 iterations. The model identifies the optimal adsorption position as $\{\mathrm{a}'_1 = 1.00\ \text{Å}, \mathrm{a}'_2 = 1.03\ \text{Å}, z = 2.03\ \text{Å}\}$, corresponding to the high-symmetry FCC adsorption site of the Au(111) substrate. This position is marked with a blue cross in Fig. 5.3b. The 2D plot in Fig. 5.3c shows a cut of the Gaussian process mean function —which represents the predicted adsorption energy— at the $z = 2.03$ Å plane. The predicted optimal adsorption location, x_{min}, is marked with a red star. The blue triangle indicates the next sampling point proposed by the acquisition function, while pink rings represent the projection of all previously sampled configurations onto the $z = 2.03$ Å plane. The size of each ring reflects the recency of the corresponding acquisition, with larger rings indicating later iterations. The positions of the substrate gold atoms are visible as bright local maxima at the corners of the unit cell. In addition to the predicted global minimum near the FCC adsorption site, the model also identifies a secondary local minimum near the HCP adsorption site, marked with a green cross in Fig. 5.3b. This secondary minimum is energetically very close to the FCC one, reflecting the nearly equivalent adsorption environments. The only difference between these two adsorption sites lies on the arrangement of the gold atoms in the subsurface layers. In the HCP site, a gold atom is located directly beneath the adsorption site in the second layer, whereas in the FCC site, there is no atom in the second layer directly below, but one is present in the third layer. Given the minimal energetic difference and the structural similarity between these two high-symmetry sites, we will consider both as ideal adsorption positions in this work.

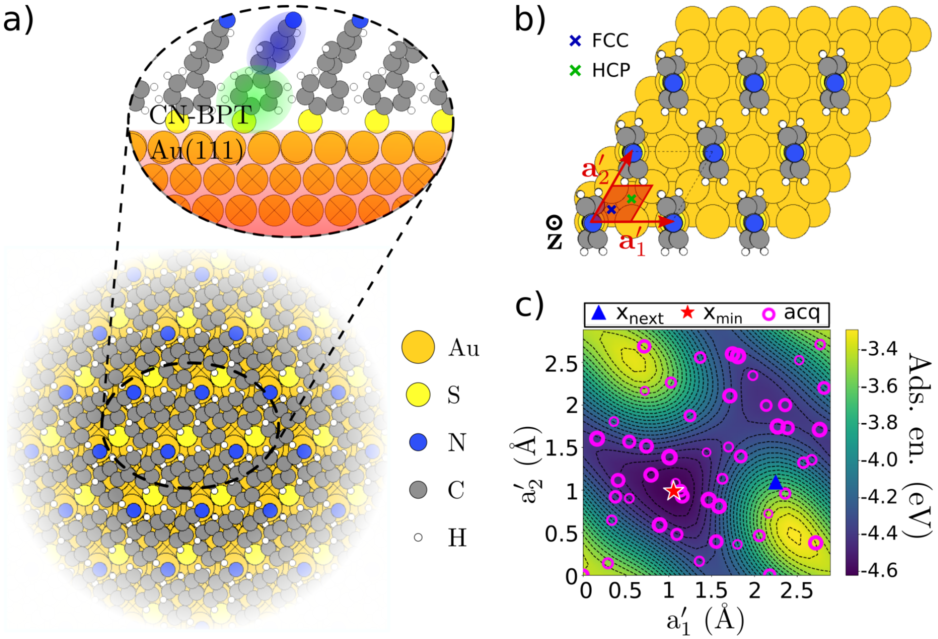

Figure 5.3: (a) Representation of a self-assembled monolayer (SAM) of CN-BPT molecules on an Au(111) surface. The structural building blocks considered during the BOSS optimization process are highlighted in different colors. (b) Schematic illustration of the BOSS search for the optimal adsorption position, with the translational variables $\{a_1', a_2', z\}$ indicated. The FCC and HCP high-symmetry adsorption sites are marked with a blue cross and a green cross, respectively. (c) Two-dimensional slice of the predicted adsorption energy surface at $z = 2.03$ Å, obtained after 50 BOSS iterations (sample acquisitions). The plot shows the mean of the surrogate Gaussian process. Sampled locations are marked with purple rings (with size indicating iteration order), the predicted global minimum location is marked with a red star, and the next suggested sampling point is shown as a blue triangle.

5.2.3 Rotational search

Once the optimal adsorption positions have been identified, the next step in the structure search process consists in determining the optimal orientation of the molecule. To this end, we define a set of rotation angles that leverage the symmetries of the system, as illustrated in Fig. 5.4a, where the sulfur atom is taken as the origin. The periodic variable α denotes a rotation of the molecule around the z axis. The variable β corresponds to the tilt angle of the molecule, and is inherently non-periodic. For closely-packed structures, experimental studies involving similar molecules typically report tilt angles in the range of 20° to 50°, with flat-lying configurations only observed for more sparse surface coverages [273–277]. Accordingly, we discard flat-lying configurations and restrict our search to the interval between 0° and 60°, which also helps avoiding geometries with overlapping building blocks. The periodic variable γ_1 corresponds to a rotation of the whole molecule around its principal axis, defined as the line connecting the S and N atoms. Finally, the variable γ_2 describes the relative orientation of the phenyl rings, and corresponds to the rotation of the lower phenyl ring around the molecular axis. We set the value of $\gamma_2 = 0°$ so that it corresponds to the relaxed geometry of the isolated molecule, in which the phenyl rings exhibit a relative twist angle of approximately 32°.

Exploring the configurational space of densely packed SAMs poses a significant challenge, as non-physical configurations, such as those with overlapping molecules, introduce substantial irregularities in the PES, resulting in a highly rugged landscape. This not only complicates the optimization procedure, but also increases the likelihood of triggering exploitation acquisitions around suboptimal local minima. Furthermore, the coexistence of regions where the PES is smooth with other regions where the PES oscillates rapidly hampers the convergence of the model hyperparameters. To address these issues, we employ a series of heuristic strategies aimed at improving the robustness and efficiency of the optimization process.

Damping

The first of the strategies to make the optimization process more efficient involves damping the high-energy regions of the PES in order to reduce the spread of adsorption energy values. This is achieved by modifying the objective function: specifically, we replace the adsorption energy by its logarithm in regions where is positive —that is, where the total energy of the SAM exceeds the sum of the energies of the isolated molecule and the substrate. Accordingly, we minimize the modified adsorption energy, $E'_{\text{ads}}(\mathbf{x})$ defined as:

$$E'_{\text{ads}}(\mathbf{x}) = \begin{cases} E_{\text{ads}}(\mathbf{x}) & \text{if } E_{\text{ads}}(\mathbf{x}) < 0, \\ \log\left[E_{\text{ads}}(\mathbf{x}) + 1\right] & \text{if } E_{\text{ads}}(\mathbf{x}) > 0, \end{cases} \tag{5.3}$$

where $\mathbf{x}$ stands for the points of the search space. This transformation leads to a smoother PES with a reduced range of energy variation, which facilitates the optimization of the model hyperparameters. This approximation is justified by the fact that regions with positive adsorption energy correspond to energetically unfavorable configurations for which the adsorption of the molecule is not thermodynamically preferred. As such, they lie far from the relevant local minima and are not interesting for our purposes. By deprioritizing these regions, we improve the efficiency of the optimization process without compromising the accuracy of the physically relevant results.

Symmetries

It is also crucial to exploit the symmetries inherent to the system as much as possible, as it allows for reducing the size of the search space while enabling the use of more efficient periodic kernels, thereby directly enhancing the speed of the optimization process. Thanks to the three-fold rotational symmetry associated with

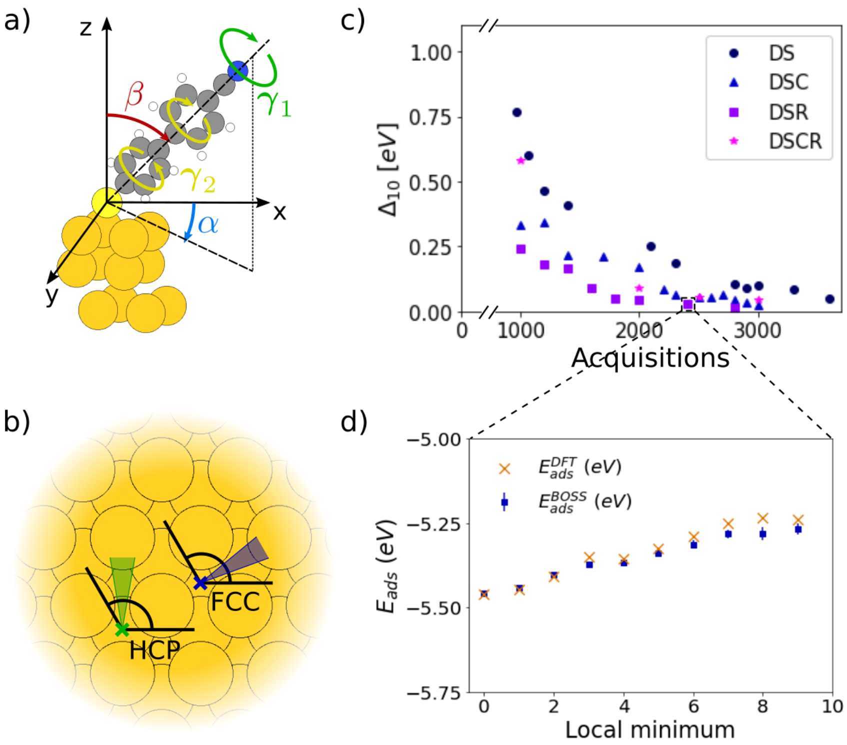

Figure 5.4: (a) Schematic representation of the rotation angles used as variables in the BOSS rotational search. The rotation around the z-axis, α, is shown in blue, the tilt angle, β, in red, the rotation of the molecule around its own axis, γ_1, in green, and the twist angle, γ_2, in yellow. (b) Projection of the α rotational search space onto the Au(111) substrate for both FCC and HCP adsorption sites. The predicted minima identified by BOSS are concentrated within the shadowed regions (see also Fig. 5.6a). (c) Convergence behavior of the BOSS rotational search. The convergence parameter Δ_{10} [Eq. (5.5)] is plotted as a function of the number of acquisitions for four different search strategies using various acceleration techniques. Dark blue dots correspond to the search process using only energy damping [Eq. (5.3)] and symmetry exploitation, labeled as DS. Blue triangles, labeled as DSC, correspond to the use of the cost function [Eq. (5.4)] with $d_{\text{cut}} = 1.25$ Å, in addition to the aforementioned damping and symmetries. Purple squares, labeled as DSR, include a restriction on the γ_2 search space along with the damping and symmetry use. Pink stars, labeled as DSCR, correspond to a search that combines the application of all the mentioned techniques. (d) Adsorption energies for the ten lowest-energy configurations found in the DSR search after 2400 acquisitions. Blue squares indicate the adsorption energies and uncertainty estimates predicted by BOSS, while orange crosses represent the corresponding values computed via exact DFT calculations.

both the FCC and HCP adsorption sites, the search domain for the angle α can be confined to the interval between 0° and 120°. Additionally, the molecule's 2-fold rotational symmetry also allows for restricting the search ranges for the angles γ_1 and γ_2 to the interval between $-90°$ and $90°$.

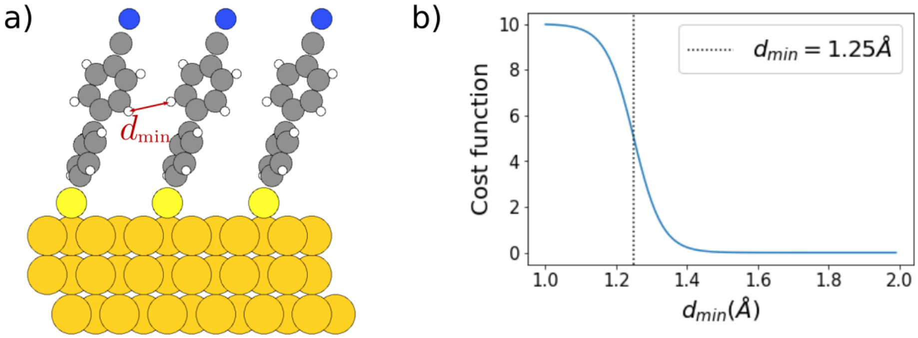

Figure 5.5: (a) Schematic representation of the minimum inter-molecular distance, $d_{\min}$, for a given configuration. (b) Plot of the cost function defined in Eq. (5.4) as a function of $d_{\min}$. The cost function is incorporated into the acquisition function during the optimization procedure, and penalizes sampling configurations where $d_{\min}$ falls below a threshold value of 1.25 Å.

Cost function

In order to avoid sampling in uninteresting or non-physical regions of the configuration space, we have employed a cost function approach. As introduced in Section 2.4.5, cost functions are user-defined ad-hoc functions that modify acquisition functions. By integrating them into the optimization loop, one can control the sampling locations and steer the search process towards physically meaningful regions. Since sampling non-physical configurations, such as the ones with overlapping molecules or molecule–surface superposition, leads to a highly oscillatory PES and difficults the search process, we have implemented a cost function, f_{cost}, which penalizes acquisitions associated with such non-physical geometries:

$$f_{\text{cost}}(d_{\min}) = \frac{\text{A}_{\text{cost}}}{1 + \exp(s\ (d_{\min} - d_{\text{cut}}))}. \tag{5.4}$$

Here $d_{\min}$ denotes the minimum distance between atoms of different molecules or between the molecule and the surface —whichever is smaller. The parameter d_{cut} defines the cutoff distance below which a contact is considered to occur. The scaling factor A_{cost} determines the magnitude of the penalty, while s controls the steepness between the penalized and non-penalized regions. In our BOSS searches, when incorporating this cost function, we have used the following parameter values: $d_{\text{cut}} = 1.25$ Å, $\text{A}_{\text{cost}} = 10$ eV, and $s = 25$ Å^{-1}, which yield the smooth cost function plotted in Fig. 5.5b.

Spatial restrictions

In certain cases, prior knowledge of the system allows us to restrict the search to a reduced, more relevant, region of the configuration space, rather than exploring the full domain. For instance, as previously mentioned, there is enough experimental evidence indicating that flat-lying molecular configurations are not viable at the surface coverage density considered in this study [274]. Therefore, we have restricted the tilt angle β to a maximum value of 60° in all search processes. Similarly, one can also constraint the twist angle γ_2, as experimental observations suggest that it closely resembles the value found in the gas-phase configuration [275]. However, such restrictions should be applied with caution, particularly when they transform a periodic variable into a non-periodic one, since non-periodic variables require increased sampling density near the boundaries of the search space. To mitigate this issue, we introduce an artificial energy penalty at the edges of the search region. This penalty discourages sampling in those areas, thereby improving the efficiency and stability of the optimization process.

Convergence

Throughout the optimization process, the surrogate model, defined by the mean and covariance functions of the Gaussian process, remains fully accessible. The mean function acts as a model of the PES, assigning an estimated adsorption energy value to each possible SAM configuration, and the pointwise variance serves as an estimation of the model's error. In order to identify the candidate geometries for stable adsorption geometries, we apply a classical gradient descent minimization procedure to the known Gaussian process mean function. This returns a set of local minimum configurations along with their corresponding predicted adsorption energies. The convergence of the model can then be assessed by comparing these predicted energies to reference values obtained from DFT calculations for the same structures. In order to quantify the convergence of the optimization process, we compute the convergence parameter Δ_N, which measures the average deviation between the BOSS predicted adsorption energies and their corresponding DFT values for the first N minima:

$$\Delta_N = \frac{1}{N}\sum_{n=1}^{N} |E^{\mathrm{BOSS}}_{\mathrm{ads},n} - E^{\mathrm{DFT}}_{\mathrm{ads},n}|. \tag{5.5}$$

Here the sum extends to the first N minima, and $E^{\mathrm{BOSS}}_{\mathrm{ads},n}$ and $E^{\mathrm{DFT}}_{\mathrm{ads},n}$ stand for the adsorption energies corresponding to minimum n as predicted by BOSS and computed with DFT, respectively.

In Fig. 5.4c, the convergence behavior of four different optimization strategies is illustrated through the evolution of the convergence parameter Δ_{10}. In Fig. 5.4d we display the predicted adsorption energies from BOSS, $E^{\mathrm{BOSS}}_{\mathrm{ads},n}$, alongside the corresponding DFT-calculated values, $E^{\mathrm{DFT}}_{\mathrm{ads},n}$, used to compute one of the Δ_{10} evaluations. The dark blue dots correspond to a search process incorporating only the energy dampening [Eq. (5.3)] and symmetry exploitation strategies, labeled as DS. The blue triangles, labeled as DSC, correspond to a search that additionally incorporates the cost function [Eq. (5.4)] with a cutoff distance $d_{\mathrm{cut}} = 1.25$ Å built upon the aforementioned DS strategy. As can be observed, the introduction of the cost function significantly enhances the convergence speed of the optimization process, allowing the global minima to be reliably identified after approximately 2000 iterations. The purple squares (DSR) denote a search process in which the γ_2 variable is constrained in addition to using dampening and symmetries. Both the cost function and the restriction of γ_2 yield a remarkable improvement in convergence speed, with the twisting-restricted process slightly outperforming the cost function alone in terms of speed. Note that both the DSC and DSR searches converge to the same global minimum, characterized by the parameter values $\{\alpha \approx 27°, \beta \approx 46°, \gamma_1 \approx -5°, \gamma_2 \approx 7°\}$. This convergence towards the same configuration provides strong evidence for the robustness and reliability of the surrogate model's predictions.

Finally, we also performed a BOSS search combining simultaneously all the aforementioned techniques, labeled as DSCR, which is represented by pink stars. Surprisingly, this combined strategy does not lead to a cumulative improvement in convergence speed. Instead, its performance aligns closely with that of the cost-function only (DSC) process, suggesting less effective returns when stacking multiple acceleration techniques.

In principle, one could use the pointwise variance of the surrogate model — representing the uncertainty at each location in the configuration space— as a direct indicator of convergence. However, we have found this approach to be unreliable. This can be observed in Fig. 5.4d, where the actual adsorption energies computed with DFT, marked with orange crosses, fall outside the predicted confidence intervals, illustrated by the blue error bars. Therefore, we devise the Δ_N convergence parameter as a more reliable indicator of the model convergence, although ideally it should be complemented by additional criteria, such as the stability of the predicted global minimum and the consistency of the model hyperparameters over the final stages of the search. In practice, we have considered an optimization process to be converged when two conditions are met: the value of Δ_{10} drops below approximately 0.05 eV, and the predicted global minimum is stable, i.e., its location remains unchanged over the final iterations. Once these conditions are met, the optimization is stopped and one can move to the analysis of the BOSS predictions. It is worth noting that higher-energy local minima typically lie in less thoroughly explored regions of the configuration space, and therefore their predicted energies tend to carry larger errors, as evidenced in Fig. 5.4d. This means that a Δ_{10} value of 0.05 eV indicates that the actual errors in the energies of the lowest-energy configurations are generally much smaller.

5.2.4 Analysis of the resulting stable configurations

Since the local minima are computed through a gradient descent procedure requiring multiple restarts, it is common for this process to return several instances of the same configuration. Therefore, the first step in analyzing the results is to filter out these duplicates, which yields a list of unique, well-defined local minima. Each of these minima corresponds to a set of rotational variable values defining a stable SAM configuration, as predicted by the surrogate model. Although, in principle,

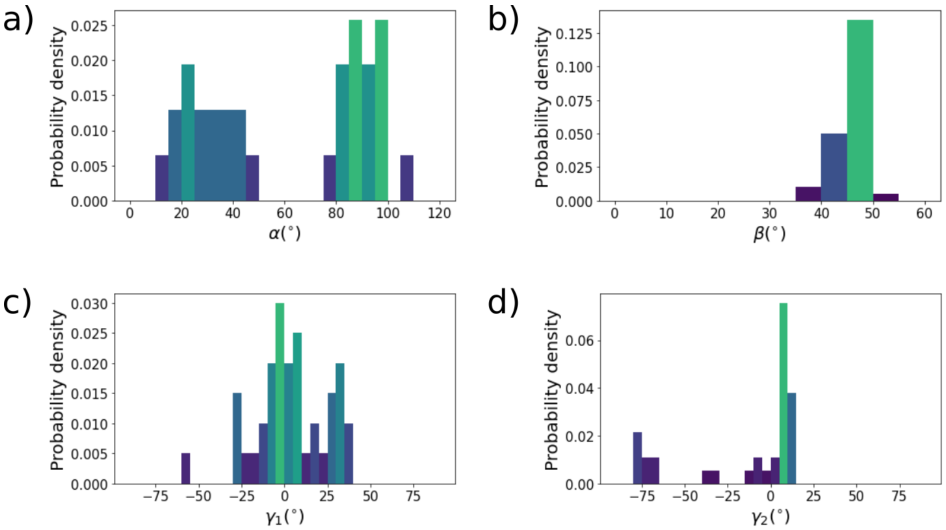

Figure 5.6: Histograms showing the probability density distributions of the rotational variables used to describe the monolayer configurations. The bars represent the probability density of the angle falling in the corresponding 5° interval. Panels (a–d) give the probability densities of the angles α, β, γ_1, and γ_2, respectively.

the geometry of the SAM should be given by the global minimum, analyzing the trends followed by the local minima provides additional insight. This analysis can help to identify systematic features of the PES and mitigate the effects of possible prediction errors from the surrogate model.

Figure 5.6 presents the probability density distributions for the four rotational variables, taking into account the ten lowest-energy local minima obtained for both FCC and HCP adsorption sites, and from both DSC and DSR BOSS search strategies. This yields a dataset of 40 configurations in total. As shown in Fig. 5.6a, the α values are clustered into two distinct groups, centered around approximately 30° and 90°. This reflects nicely the honeycomb symmetry of the Au(111) substrate. These preferred orientations suggest that SAM configurations where the molecular axis projects into the hollow regions between the nearby gold atoms are energetically favored (see Fig. 5.4b). In contrast, the β values are clearly concentrated between 40° and 50°, as illustrated in Fig. 5.6b. This range can be considered as an estimation of the molecular tilting angle in the physical system. Note that these values are only slightly higher than those obtained from NEXAFS experiments for SAMs composed of similar molecules [275], though this discrepancy may be attributed to differences in surface coverage. The tendency is less clear for the γ_1 angle, which represents a rotation of the molecule around its axis, as seen in Fig. 5.6c. However, large values are discouraged, since they increase the likelihood of steric clashes between the lower phenyl and the gold substrate. Finally, the histogram for γ_2, shown in Fig. 5.6d, reveals that the favored molecular twist in the SAM environment increases by 5° to 10°, as compared to that of the isolated molecule ($\approx 32°$), which fits the experimental estimates derived from NEXAFS studies [275], suggesting a moderate conformational adjustment driven by intermolecular and substrate interactions within the SAM.

Relaxation

The final step in the process of obtaining the optimal SAM configuration involves relaxing the geometries of the local minima identified by BOSS. For the sake of simplicity, and in order to avoid duplicated entries, from now on we will only consider the local minima of the DSR search process, which was the fastest to converge. During the relaxation the positions of gold and sulfur atoms, which remained fixed during the rotational optimization, are also allowed to move. This relaxation leads to a significant reduction in the adsorption energies of the local minima, as illustrated in Figures 5.7a and 5.7b. These figures compare the DFT energies of the BOSS-predicted minima before (blue) and after (red) relaxation, for both FCC (a) and HCP (b) adsorption sites. The magnitude of the adsorption energy reduction varies significantly among configurations, and it should not be overlooked, as in some cases it can alter the relative stability ranking of the local minima. For instance, the second FCC minima predicted by BOSS exhibits a much smaller energy decrease than the neighboring minima, as shown in Figure 5.7a, suggesting that it is no longer a good candidate for a stable geometry following relaxation.

This different behavior can be rationalized by examining Fig. 5.7c, which depicts the relationship between the energy decrease during relaxation, δE, and the displacement of the sulfur atom from the initial adsorption site. Visual inspection reveals a clear correlation, which is quantitatively confirmed by the computed correlation coefficient $\rho = 0.79$ (see Appendix F). In some cases, the molecule remains close to the original adsorption site, resulting in minimal changes of the adsorption energy. In contrast, in other cases the molecule undergoes significant drift, moving closer to "bridge" adsorption positions, which causes a larger drop in energy. Upon inspection of the energies of the relaxed minima, we find that several configurations exhibit energies that are quite close. In particular, the difference between the adsorption energies of the first 5 lowest-energy minima and the global minimum falls within the range of thermal fluctuations expected at room temperature, which are given by approximately $k_B T \sim 25$ meV. Therefore, our calculations suggest that multiple alternative SAM configurations may coexist under experimental conditions, and we should consider these low-energy local minima in the subsequent analysis of the Raman spectra. Figures 5.7d–h present the unit cell geometries of these 5 minima. The relevant information regarding these configurations, including the adsorption sites, rotational variables, and BOSS-predicted and DFT-computed adsorption energies, are summarized in Table 5.1.

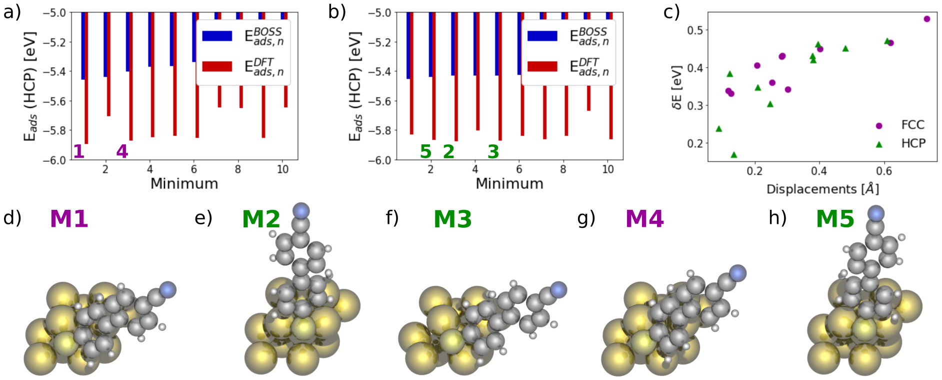

Figure 5.7: Bar plots of the BOSS-predicted adsorption energies for the first ten local minima at the FCC (a) and HCP (b) adsorption sites (blue), alongside their corresponding energies after geometric relaxation (red). (c) Correlation plot between the displacement of the S atom during relaxation and the total energy decrease resulting from relaxation δE. Panels (d)–(h) illustrate the unit cell geometries of the five most stable minima after relaxation, labeled in order of increasing adsorption energy.

Minimum	Site	$\alpha(°)$	$\beta(°)$	$\gamma_1(°)$	$\gamma_2(°)$	$\mathrm{E}^{\mathrm{BOSS}}_{\mathrm{ads},n}$ (eV)	$\mathrm{E}^{\mathrm{DFT,rel}}_{\mathrm{ads},n}$ (eV)
M1	FCC	27.1	46.2	-4.9	7.3	-5.458	-5.895
M2	HCP	91.7	47.5	3.2	-72.6	-5.430	-5.875
M3	HCP	23.9	46.6	-1.5	5.5	-5.429	-5.871
M4	FCC	38.1	46.1	-10.6	5.3	-5.403	-5.870
M5	HCP	84.0	47.3	-6.1	9.8	-5.440	-5.866

Table 5.1: Summary of the five lowest-energy minima identified in Fig. 5.7. From left to right, the table lists the label assigned to each minimum, its original adsorption site, the rotational variable values and adsorption energies predicted by the BOSS search, and the DFT adsorption energies obtained after relaxation.

5.3 Computation of Raman spectra of stable SAM configurations

After determining the most energetically stable configurations for the (2×2) SAM of CN-BPT molecules on an Au(111) surface, we proceed to analyze their Raman spectra, computed following the methodology described in Section 5.2.1. Figure 5.8 displays the spectra corresponding the five configurations introduced in Fig. 5.7, arranged in ascending order of adsorption energy. The overall shape of the computed spectra closely resembles experimental Raman spectra reported for SAMs of the same molecule [282]. Key features include a distinct peak near 2250 cm^{-1},

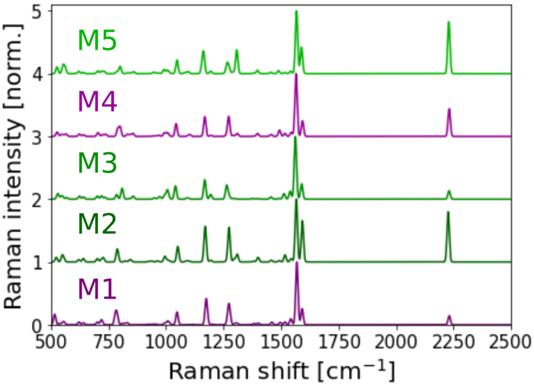

Figure 5.8: Raman spectra calculated for the five lowest-energy SAM configurations of the CN-BPT SAM on Au(111) in Fig. 5.7. Spectra corresponding to FCC adsorption sites are shown in purple, whereas those from HCP sites are shown in green.

two prominent peaks in the range from 1550 cm^{-1} to 1600 cm^{-1}, and a series of minor peaks at lower frequencies. The largest-energy peak is assigned to the C–N stretching vibrational mode, which corresponds to mode 62 of the isolated CN-BPT molecule, as illustrated in Fig. G.1. The other two major peaks in the mid-frequency region correspond to antisymmetric and symmetric stretching modes of the phenyl rings, analogous to vibrational modes 61 and 60 of the isolated molecule, respectively.

Although all five spectra exhibit very similar main features, the relative intensities of the Raman peaks vary significantly. For three of the five minima (M1, M3, M4), the phenyl ring stretching modes dominate the spectrum, whereas for the other two minima (M2, M5) the C–N stretching mode matches them in intensity. This observation suggests that the relative weight of the different Raman modes, and therefore the overall spectral profile, are strongly correlated with the geometrical configuration of the SAM. In order to verify this hypothesis, it is necessary to define a quantitative figure of merit of similarity between the geometries of the different SAM configurations. One straightforward approach is to consider only the values of the rotational angles $\theta = \{\alpha, \beta, \gamma_1, \gamma_2\}$ obtained in the BOSS search, and to define a metric of distance between two configurations i, j as the average absolute difference of their corresponding angles:

$$d_{ij}^{\theta} = \frac{1}{4} \sum_{l}^{4} |\theta_l^i - \theta_l^j|, \tag{5.6}$$

where θ_l^i denotes the value of the l-th rotational angle in SAM configuration i. However, this distance alone does not capture differences arising from varying adsorption sites or molecular rearrangements induced by relaxation. Therefore it must be complemented with an alternative metric. We define this complementary spatial distance as the mean absolute difference between the atomic positions of the molecule:

$$d_{ij}^{s} = \frac{1}{N}\sum_{n=1}^{N} |\mathbf{x}_n^i - \mathbf{x}_n^j|, \tag{5.7}$$

where the sum runs over the N atoms of the molecule. By combining these two measures, we construct a normalized distance that accounts for rotational and positional differences. For each pair of SAM configurations ij, the normalized distance is defined as:

$$d_{ij}^{\text{norm}} = \begin{cases} \frac{d_{ij}^{s}}{\max(\hat{\mathbf{d}}^{s})} + \frac{d_{ij}^{\theta}}{\max(\hat{\mathbf{d}}^{\theta})} & \text{if } i \geq j \\ 0 & \text{if } i < j \end{cases}, \tag{5.8}$$

where $\max(\hat{\mathbf{d}}^{s})$ and $\max(\hat{\mathbf{d}}^{\theta})$ denote maximum values of the spatial and angular distances across all configuration pairs, respectively, i.e., the largest entry in the respective matrix. This normalization ensures that elements d_{ij}^{norm} of the resulting matrix are constrained within the interval (0–2). Since the distance matrix is symmetric by construction, for simplicity the elements below the diagonal are set to zero.

In Fig. 5.9a, we show the normalized distance matrix for the five most stable configurations. The values clearly indicate that these configurations can be separated into two distinct groups, G1={M1, M3, M4} and G2={M2, M5}, with the intra-group distances significantly smaller than the inter-group ones. This grouping aligns nicely with the qualitative differences observed in the Raman spectra shown in Fig. 5.8, as discussed above. Such classification can be further supported by quantitatively evaluating the differences between the Raman spectra. This can be done by computing the Euclidean distances between each pair of spectra $I_i(\omega)$ and $I_j(\omega)$, defined as

$$\delta I_{ij} = \left[\int_0^{\infty} d\omega \; |I_i(\omega) - I_j(\omega)|^2\right]^{1/2}, \tag{5.9}$$

where each individual spectrum has been normalized so that its total area equals unity. Figure 5.9b depicts the matrix of Euclidean distances δI_{ij}, constructed analogously to the normalized distance matrix in Fig. 5.9a. A comparison of these matrices reveals a clear correlation between geometrical distance and spectral similarity. This relationship is further explored in Fig. 5.9c, where we plot the normalized geometrical distances against the Euclidean spectral distances for each pair of configurations. Visual inspection alone reveals a strong correlation, quantitatively confirmed by a correlation coefficient of $\rho = 0.75$. Moreover, the configuration pairs are divided into intra-group and inter-group pairs, using the previously defined classification $G_1 = \{\text{M1, M3, M4}\}$ and $G_2 = \{\text{M2, M5}\}$, represented with blue and red crosses, respectively. The consistently smaller distances for intra-group configuration pairs as compared to inter-group ones confirms the initial visual classification and allows for simplifying the original set

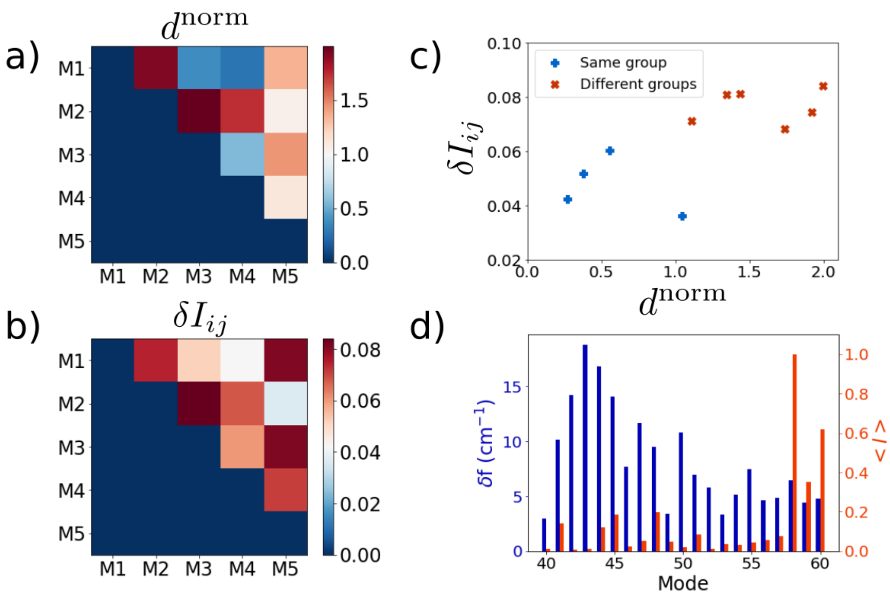

Figure 5.9: a) Normalized distance matrix computed for all possible SAM configuration pairs, as defined in Eq. (5.8). The color of element [i,j] indicates the similarity between SAM configurations i and j. b) Representation of the matrix of Euclidean distances of the Raman spectra computed for all possible SAM configuration pairs. c) Correlation between geometrical and spectral distances. Each cross corresponds to a certain pair of SAM configurations: blue crosses represent intra-group pairs, i.e., similar configurations, and red crosses denote inter-group ones (more distinct configurations). d) Bar plots showing the mode frequency shifts when varying the SAM configuration (blue), alongside the average normalized Raman intensity of each vibrational mode within the 1000 cm^{-1} – 2500 cm^{-1} range.

of 5 configurations into two representative groups, symbolized by the lowest-energy configuration M1 and the second-lowest one M2, respectively.

Finally, we examine the dependence of the SAM phonon frequencies on the configuration, for a subsequent analysis of collective effects. The blue bars in Fig. 5.9d show the shift of the resonance frequencies of the vibrational modes within the 1000 cm^{-1} – 2500 cm^{-1} range across the configurations represented in Fig. 5.8. For reference, the average Raman intensities of these vibrational modes are shown as red bars. Most values of the frequency shift lie between 5 cm^{-1} and 10 cm^{-1}, as it is the case for the most prominent modes (58, 59, 60). Although these shifts are modest, and the main importance of adequately modeling SAM configurations lies on the relative Raman intensities, such frequency shifts may become relevant when a larger degree of precision of phonon energies is required, such as when analyzing collective Raman effects, which will be addressed in the following section.

5.4 Raman spectrum dependence on the coverage density and emergence of collective effects

When two molecules with vibrational modes characterized by strong infrared transition dipoles are placed in close proximity, dipole–dipole coupling between these modes occurs. This coupling leads to the emergence of two new vibrational modes: one corresponding to in-phase vibrations, and the other one to antiphase vibrations. As a result of this interaction, the resonance frequencies of these collective modes are shifted with respect to the original uncoupled molecular vibrations. In extended periodic molecular assemblies, such as SAMs, this coupling leads to the formation of a vibrational band structure, a continuum of phonon modes representing collective vibrations across the molecular lattice. Among these modes, the zone-centered phonon mode plays a key role, as it corresponds to the collective on-phase vibration of the SAM's molecules and is the primary contributor to the Raman signal. As pointed out, the frequency of the zone-centered phonon is shifted with respect to the vibrational frequency of the isolated molecule, resulting in a systematic displacement of the corresponding Raman peaks. Importantly, the magnitude of this shift depends strongly on the molecular coverage density within the SAM. Closer packing leads to stronger dipole–dipole interactions and therefore larger shifts. As a result, the spectral position of SERS peaks, especially those corresponding to modes with large infrared dipole moments, is not solely determined by the local molecular structure, but also by the collective vibrational coupling mediated by the SAM lattice. This phenomenon is commonly referred to as "collective effects" in Raman spectroscopy.

One effective approach to capture these collective effects in dense molecular assemblies is to model the molecules as a 2D lattice of coupled point dipoles. According to Ref. [285], the frequency shift of the vibrational mode n predicted by a 2D dipole lattice model scales as

$$\Delta\nu_n \propto \frac{p_n^2}{r_\mathrm{d}^3}, \tag{5.10}$$

where p_n is the infrared (IR) transition dipole moment associated with the vibrational mode n, and r_d is the dipole–dipole separation distance. The IR transition dipole moment is related to the IR intensity, $I_{IR,n}$ (in units of D^2 $\mathrm{Å}^{-2}$ amu^{-1}), and to the mode frequency ν_n as:

$$p_n = \sqrt{\frac{\hbar I_{IR,n}}{4\pi\nu_n}}. \tag{5.11}$$

The separation r_d is related to the coverage density of the SAM configurations, defined as dens $= N_{mol}/A$, with A the area of the unit cell and N_{mol} the number of molecules in the unit cell, respectively, and since the molecules form a 2D lattice:

$$r_\mathrm{d} \propto \mathrm{dens}^{-1/2}. \tag{5.12}$$

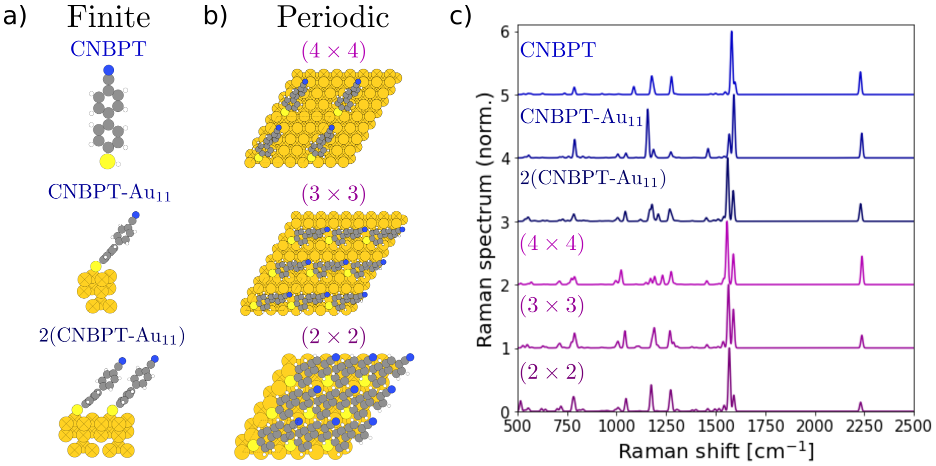

Figure 5.10: a) Atomistic representations of finite configurations modeling the CN-BPT SAM on Au(111). From top to bottom: isolated CN-BPT molecule, CN-BPT molecule attached to an Au$_{11}$ cluster, and two CN-BPT molecules attached to an Au$_{22}$ cluster. b) Sketch of the optimized periodic SAM configurations at different surface coverage densities. From top to bottom: SAM with (4×4) coverage, SAM with (3×3) coverage, and SAM with (2×2) coverage. c) Raman spectra of all the systems shown in a) and b). Blue spectra correspond to finite systems, while purple spectra represent periodic SAMs.

Moreover, the dipole moment p_n is independent of the coverage density, and by substituting Eqs. (5.11) and (5.12) into Eq. (5.10), we obtain the scaling of the frequency shift with the coverage density:

$$\Delta\nu_n \propto \mathrm{dens}^{-3/2}. \tag{5.13}$$

This result indicates that modes with strong IR character experience larger shifts in the Raman peak positions as the SAM becomes denser.

In this section, we analyze the influence of collective effects on the Raman spectra of CN-BPT SAMs on an Au(111) substrate by studying configurations with varying molecular coverage densities. To this end, we first generate energetically stable SAM configurations for different coverage densities using the methodology described in Section 5.2. Figure 5.10b displays the optimized configurations for two reduced coverage densities, corresponding to overlayer periodicities (4×4) and (3×3). These configurations serve as lower-density counterparts to the previously studied (2×2) SAM. For a comprehensive analysis of collective effects, it is also critical to consider the spectrum of the isolated CN-BPT molecule, for comparison. To simulate the effect of the Au(111) surface, in this case, we attach the molecule to a cluster of 11 gold atoms arranged to mimic the local geometry of the SAM unit cell, as illustrated in Fig. 5.10a. In addition to the single-molecule system, we also consider an analogous finite system with two molecules. The Raman spectra corresponding to all the aforementioned configurations are plotted in Fig. 5.10c.

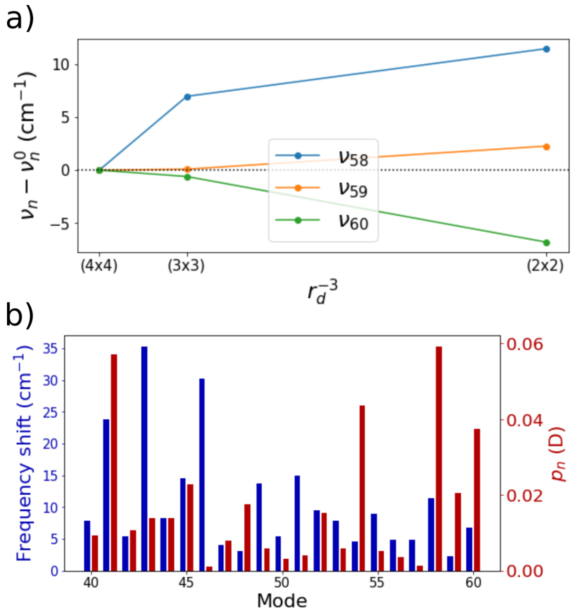

Figure 5.11: a) Energies of the main Raman-active vibrational modes for SAMs with varying coverage densities as a function of r_d^{-3}, using the frequency of the modes for the (4×4) configuration as a reference. b) Bar plot showing the absolute frequency shifts (blue) of all vibrational modes within the 1000 cm^{-1} – 2500 cm^{-1} range, together with the corresponding infrared dipole moments (red) computed for the isolated CN-BPT molecule.

As can be appreciated, the overall shape of the Raman spectrum remains quite consistent. The only exception is the case of the single molecule attached to an Au$_{11}$ cluster, for which the relative intensities of the phenyl ring stretching modes 58 and 59 are inverted, and a prominent peak at ≈ 1200 cm^{-1} appears. The molecule–cluster spectrum will be further discussed in Section 5.6. Additionally, although it cannot be easily appreciated in the figure, the frequencies of the vibrational modes shift due to the previously described collective effects, which will be analyzed in detail in the following paragraphs.

The frequency shifts induced by collective effects are illustrated in Fig. 5.11a, where we plot the excitation frequencies of the main Raman-active vibrational modes as a function of r_d^{-3} for varying coverage densities, using the (4×4) mode frequency as a reference. As one can observe, the magnitude of the frequency shift varies significantly across vibrational modes. For example, the C-N stretching mode frequency ν_{60} exhibits a red-shift of around 7 cm^{-1}, whereas the phenyl ring stretching mode frequencies ν_{59} and ν_{58} show blue-shifts of roughly 2 cm^{-1} and 11 cm^{-1}, respectively.

At first glance, it may seem reasonable to attribute the frequency shifts observed above solely to collective effects. However, as shown in the previous section (see

Fig. 5.9d), changes in the molecular orientation can also induce frequency shifts of similar magnitude, indicating that further analysis is required. If the observed shifts were due to collective effects, their magnitude should scale with the square of the infrared dipole moment of the corresponding mode, as predicted by Eq. (5.10). To assess this, we complemented our analysis by computing the IR dipole moments for the vibrational modes of the isolated CN-BPT molecule. In Fig. 5.11b we plot these dipole moments, together with the absolute frequency shifts of the corresponding vibrational modes observed in the SAM configuration as a function of the coverage density. Notably, for the key vibrational modes $(58-60)$, the data align well with the expectations: modes with larger p_n exhibit larger absolute frequency shifts, indicating a strong correlation between both factors and supporting their attribution to collective effects. However, this correlation breaks down for the less Raman-active modes. Some of these modes display unexpectedly large shifts despite having weak IR dipole moments. This behavior suggests that factors other than collective effects can play a significant role in the spectral shift. Indeed, as shown in the previous section, the excitation frequencies of several modes are very sensitive to the molecular configuration of the SAM, even at constant coverage density, providing a reasonable explanation for the shifts observed here.

Although the results presented in this section are constrained by the limited number of studied configurations, efforts are currently underway to extend the analysis to (3×2) and (4×2) coverages. These additional configurations will improve the reliability of the observed trends in frequency shifts. Moreover, it should be possible to disentangle the effects of the coverage density from those of the molecular orientation by studying mixed SAMs, as commonly done in experimental studies [285]. For instance, one could combine our CN-BPT molecules with biphenyl-4-thiol molecules. Since BPT is structurally similar to CN-BPT, differing only in the absence of the terminal CN group, mixed SAMs of varying CN-BPT/BPT ratios could be modeled just by adapting the pure SAM configuration that has already been computed. This approach would allow for a direct investigation of collective effects, thereby isolating their contribution from that of orientation or local environment.

5.5 Influence of adatom-mediated surface reconstruction on the Raman spectrum

As discussed in Section 5.1, the strong affinity between the substrate Au atoms and the thiol headgroup often results in significant reconstruction of the original substrate. Although in the previous study we accounted for this by allowing full relaxation of the outermost Au atoms, we did not consider the formation of adatom-mediated geometries via the displacement of substrate atoms into the overlayer to form Au-S-Au bridges. Such behavior has been experimentally observed in several thiolate SAMs [293] and is known to play a critical role in determining spectroscopic properties. In the context of SERS, adatom configurations have been termed as picocavities [44, 303]. These configurations require unit cells containing at least

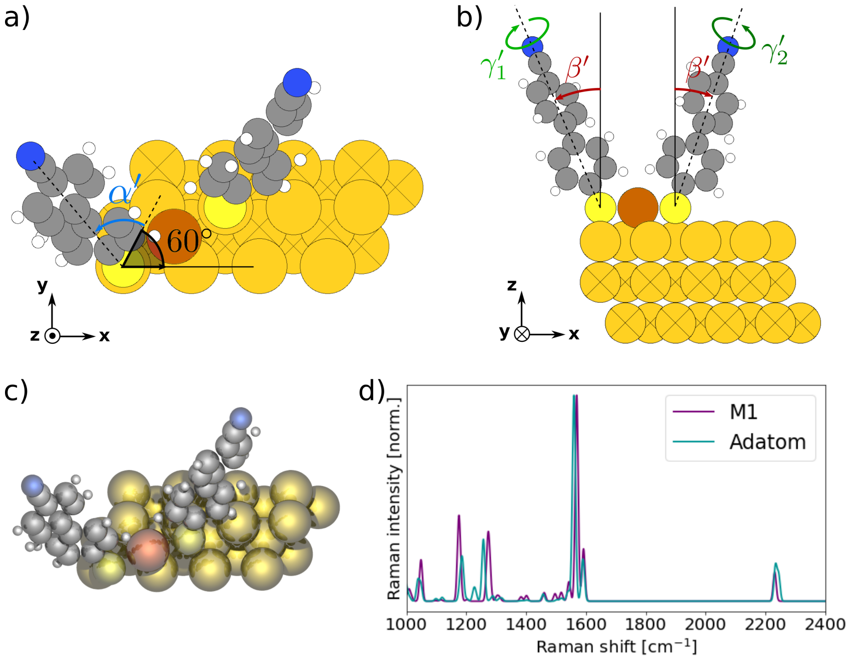

Figure 5.12: Top (a) and side (b) views of the adatom-mediated geometry, with the rotational search variables outlined. The Au adatom is highlighted in orange to emphasize its position relative to the molecule. c) Representation of the global minimum adatom-mediated configuration after relaxation, as shown from a top view. d) Comparison of the normalized Raman spectra computed for the (2×2) global minimum configuration (purple) and for the optimized adatom-mediated configuration shown in (c) (blue).

two molecules to accurately capture the symmetry-breaking and bonding motifs introduced by the presence of the adatom, such as the one depicted in Figs. 5.12a and 5.12b, based on the structures proposed in Refs. [279, 304]. This increases the number of geometrical degrees of freedom and therefore complicates the search for the optimal structure.

Nevertheless, in order to further explore the configurational landscape of adatom-mediated SAMs, we have performed a limited BOSS rotational search for finding suitable configurations with the same surface coverage density as the conventional (2×2) SAM. Figures 5.12a and 5.12b show the rotational variables used in the search. First, we fixed the projection of the molecular axis of the rightmost molecule onto the horizontal plane, and defined the variable α' as the relative angle between the projections of the two molecular axes. Then, we defined the tilt angle β', which we kept the same for both molecules. Finally, we defined the variables γ'_1 and γ'_2, which correspond to rotations around the respective molecular axes. The optimization process resulted in a global minimum at the values $\{\alpha' = 70.0°, \beta' = 33.3°, \gamma'_1 = -16.2°, \gamma'_2 = 49.2°\}$, which correspond to the geometry depicted in Figs. 5.12a and 5.12b. The main difference with the conventional (2×2) SAM is that the tilting is significantly smaller for this adatom-mediated structure. Although this search does not consider all available degrees of freedom, as we are ignoring the molecular twist and the rotation of one molecule around the z axis, it provides a reasonably comprehensive sampling of the relevant orientations. This serves to demonstrate the versatility of the BOSS optimization method. We then relax the BOSS global minimum, which results in the structure depicted in Fig. 5.12c. As it occurred for the conventional SAMs, this procedure causes a displacement of the S atoms towards the "bridge" adsorption positions, but the molecular orientations remain mostly unchanged.

Finally, we have computed the Raman spectrum for the optimized adatom-mediated SAM structure, which is shown in Fig. 5.12d. As can be observed, including an Au adatom does have some qualitative effects on the overall spectral profile of the SAM. The relative intensities of the main Raman active modes changes, with the relative intensities of the C-N stretching mode 60 and of the phenyl ring stretching mode 59 increasing significantly. One can also observe small but non-negligible shifts in the frequencies of key vibrational modes. The magnitude of these shifts is quantified in Table 5.2, where the mode-wise changes with respect to the conventional (2×2) SAM configuration are detailed. Furthermore, the spectrum for the adatom-mediated geometry also presents a small splitting of some vibrational modes, including the signature mode 58 and some of the vibrational modes appearing below 1400 cm^{-1}.

5.6 Conclusions and outlook

After having computed the Raman spectra for a variety of configurations and models of a CN-BPT SAM on Au(111) surfaces throughout this chapter, we can summarize how different modeling choices affect the computed Raman spectra. Table 5.2 presents the frequency variations $\Delta\nu_n$ for the main vibrational modes analyzed along with the mode-averaged value $\langle\Delta\nu\rangle$, across the different SAM models explored.

- The "Geometry" row shows the maximum frequency shifts observed among the five different local minima of the (2×2) SAM configurations examined in Section 5.3.
- The "Coverage" row quantifies frequency shifts arising from changes in SAM coverage density, reflecting collective effects as analyzed in Section 5.4.
- The "Periodicity" row presents frequencies from a finite cluster model, as depicted in Fig. 5.10a, where a molecule is attached to an Au cluster, constructed by replicating the unit cell of the periodic (2×2) SAM global minimum and allowing further relaxation, and compares them to the periodic (2×2) SAM global minimum frequencies.

	$\Delta\nu_{58}$ (cm^{-1})	$\Delta\nu_{59}$ (cm^{-1})	$\Delta\nu_{60}$ (cm^{-1})	$\langle\Delta\nu\rangle$ (cm^{-1})	Δ_I
Geometry (Section 5.3)	4.00	5.83	3.12	4.32	0.070
Coverage (Section 5.4)	8.54	2.38	6.80	5.90	0.098
Periodicity (Section 5.4)	0.40	0.38	5.82	2.20	0.105
Adatom (Section 5.5)	2.43	2.07	11.32	5.27	0.062

Table 5.2: Summary of how the differences in modeling the SAM modify the Raman spectra. The metrics used are the maximal variations in the vibrational mode frequencies $\Delta\nu_n$ and the maximal Euclidean distances between Raman spectra Δ_I as defined in Eq. (5.9). Below each row label, we specify the section where the corresponding spectra can be found.

- The “Adatom” row compares vibrational frequency shifts between the (2×2) global minimum SAM and the adatom-mediated geometry discussed in Section 5.5.

In order to complement the previous frequency analysis with information about the relative Raman intensities, the maximum Euclidean distances between Raman spectra $\Delta_I = \max_{ij}(\delta I_{ij})$ are also displayed.

From the results obtained, one can conclude that the largest spectral variations originate from the coverage density and the presence of adatoms. The magnitude of the frequency shifts depends significantly on the vibrational mode, although this is to be expected in the case of collective effects as these are supposed to depend on the mode-specific infrared transition dipole moments. Notably, adatom-mediated geometries strongly influence the isolated C-N stretching mode, used as a benchmark in many studies, highlighting the importance of considering such configurations. Nevertheless, molecular orientation changes between stable local minima induce frequency shifts on the order of approximately 5 cm^{-1} for all relevant modes. Interestingly, transitioning from periodic to finite cluster geometries does not seem to have a very large impact in the vibrational frequencies, likely because the finite model was generated by simple replication of the unit cell of the periodic (2×2) SAM without a full geometry optimization. This suggests that the effect of inter-molecule interactions is more relevant during the geometry optimization steps rather than in the calculation of the phonon modes directly. However, periodicity can significantly affect relative Raman intensities, as the Δ_I values related to this property are comparable to those of the other studied properties. This result concurs with the differences between the relative Raman intensities of the periodic systems and the molecule–cluster one that can be observed in Fig. 5.10c.

Finally, the methodology developed here for molecular monolayers can be readily extended to more complex nanocavity configurations such a nanoparticle-on-mirror systems or molecular junctions, which provide even greater Raman signal enhancements and are therefore of wide interest. Incorporating an additional gold slab above the molecules, however, significantly complicates the structure optimization process by introducing new variables, such as the gap size and the relative position of the top layer atoms. This represents an exciting direction for future work, although it remains unexplored in the present study.

5.7 Summary

In this chapter, we have investigated the structure and Raman spectra of 4'-cyanobiphenyl-4-thiol (CN-BPT) self-assembled monolayers (SAMs) on an Au(111) surface within a fully periodic *ab initio* approach that inherently includes all inter-molecule interactions and collective effects. Section 5.1 introduced the topic of SAMs and the notation for overlayer periodicities. In Section 5.2, we detailed our methodology for obtaining stable SAM configurations, based on using the Bayesian optimization techniques introduced in Section 2.4 for minimizing the adsorption energy of the system. We then applied this methodology to the aforementioned SAM of CN-BPT molecules with a (2×2) coverage in two steps: first, we determined the favored adsorption sites by minimizing the adsorption energy with respect to the translations of the molecule, and then we obtained the most stable molecular orientations by optimizing a set of rotational variables. The identification of the lowest-energy configurations was completed by relaxing the candidate structures and ranking them according to their relaxed adsorption energies.

This optimization step was followed by an analysis of the Raman spectra corresponding to the five lowest-energy configurations presented in Section 5.3. These spectra were obtained within the perturbation theory approach outlined in Section 2.3. Subsequently, in Section 5.4 we compared the Raman spectra of SAMs composed of the same CN-BPT molecule at varying surface coverage densities, in order to analyze the frequency shifts in vibrational modes arising from the coupling of their infrared transition dipoles. In Section 5.5 we considered the possibility of Au(111) surface reconstruction by introducing an alternative adatom-mediated geometry, relevant in experimental situations. Finally, Section 5.6 evaluated the importance of accurately modeling the SAM by examining the variations in the Raman spectra across the different models discussed in the previous sections. Altogether, these results constitute a significant advancement in the *ab initio* modeling of periodic organic assemblies and their vibrational spectroscopic properties.

CONCLUSIONS

In this thesis, we have investigated light–matter interactions at the nanoscale with the use of a fully *ab initio* atomistic framework. We have focused on the study of three canonical configurations, namely, molecule–gap antenna configurations, small metallic clusters, and self-assembled monolayers on metallic surfaces. Each configuration has been respectively explored through the analysis of the signal from absorption optical spectroscopy (molecule–gap antennae), electron energy-loss spectroscopy (metallic clusters), and surface-enhanced Raman spectroscopy (self-assembled monolayers). The *ab initio* methodology has allowed us to connect aspects of the microscopic scale of these configurations with the overall spectral signals obtained for each case. The application of time-dependent density-functional theory (TDDFT) methods in the *ab initio* calculations has been shown to accurately capture relevant atomic scale effects of light–matter interactions at the nano- and pico-scale.

Below, we summarize the main findings and conclusions obtained in this thesis:

- Chapter 1 summarizes the fundamentals of light–matter interactions at the nanoscale. It is focused on the classical electromagnetic description of plasmonic resonances in spherical metallic nanoparticles and dimers, as well as on optical excitations in molecules and hybrid metal–molecule systems. In addition to optical spectroscopy, we also introduce the two other spectroscopy techniques used throughout this thesis: electron energy-loss spectroscopy (EELS), and surface-enhanced Raman spectroscopy (SERS).

- Chapter 2 outlines the theoretical framework of atomistic TDDFT, which is used to model the interaction of the studied systems with light and electron beams. Additionally, we introduce the method for computing the Raman spectra of periodic systems, based on perturbation theory. We also present a Bayesian Optimization procedure designed for obtaining the minimum energy configurations of nanoscale systems, such as molecular adsorbates on metallic surfaces.

- Chapter 3 examines the optical response of a hybrid system composed of a porphine molecule sandwiched by two silver nanoparticles in the facet-to-facet and tip-to-tip configurations. We focus on the influence of the atomistic features on the electromagnetic coupling strength and on the emergence of quantum phenomena such as charge transfer and electronic coupling through the molecular junction. Our results show the splitting of the plasmonic resonance of the dimer into two clearly distinct polaritons as a result of the electromagnetic coupling. By fitting the optical absorption spectra to a coupled harmonic oscillator model, we find that the nanoparticles' facet-to-facet configuration leads to a significantly larger coupling strength, g, for most of the studied gap sizes. However, for the smallest gaps, the polaritonic two-peak structure is disturbed by the emergence of an additional resonance, which we attribute to the hybridization between the electronic orbitals in the molecule and the metal. The atomistic configuration also determines the emergence of charge-transfer plasmons at lower frequencies, which are only observed in the facet-to-facet configuration. Overall, this study highlights the importance of considering the atomistic morphology when dealing with extreme cases of interaction in plasmonic nanocavities.

- Chapter 4 explores the full plasmonic response of sodium nanoparticles as probed by penetrating high-energy electron beams. Electron energy-loss (EEL) probability spectra computed with atomistic TDDFT reveal that, in addition to localized surface plasmons excited at optical frequencies, penetrating electrons can also excite high-energy surface modes, and confined bulk plasmons (CBPs) above the plasma frequency. With the help of analytic expressions for the EEL probability derived from an auxiliary hydrodynamic model, we identify the well-defined CBP modes that contribute to the peaks in the EEL spectra, and analyze the effect of the impact parameter of the electron trajectory on their excitation. The implementation of auxiliary calculations within a jellium TDDFT model helps us to identify the higher-order surface resonances excited as Bennett or multipole plasmons. This study provides a deeper understanding of the behavior of CBPs and Bennett plasmons. The overall good qualitative —and even quantitative— agreement between theoretical models which include nonlocality in the response of the nanoparticles at different levels underscores the robustness of the description of the symmetries of the bulk modes excited in small sodium nanoparticles. Our conceptual characterization also provides insight into the experimentally observed blue-shifts of the bulk plasmon peak identified in several nanostructures, and lays the groundwork for a more exhaustive analysis and exploitation of plasmonic features in valence EELS of metallic nanoparticles.

- Chapter 5 introduces a fully *ab initio* methodology for computing the Raman spectrum of a self-assembled monolayer of aromatic thiolate molecules on an Au(111) surface, naturally accounting for inter-molecule interactions and collective effects. After minimization of the potential energy surface of the system using a Bayesian optimization method and analyzing the obtained local energy minima, we identify the most suitable monolayer configurations after relaxation. By comparing the Raman spectra of the self-assembled monolayers, we analyze the importance of accurately modeling the atomistic

> structure and the interaction between the molecules. We extend this study by applying the same method of analysis to monolayers with different coverage densities. By doing so, we observe the emergence of collective Raman effects and study the frequency shifts of the molecular vibrational modes. Finally, we explore an alternative optimized adatom-mediated configuration, which allows us to investigate how the reconstruction of the Au surface may impact the resulting spectra. Overall, the presented methodology allows for an accurate modeling of the monolayer structure while naturally incorporating inter-molecule interactions, paving the way for more precise simulations of densely-packed molecular assemblies.

We believe that the research presented in this thesis further consolidates the role of atomistic *ab initio* methods as a fundamental tool for understanding the response of plasmonic nanostructures and their interaction with organic molecules. This methodology allows for addressing atomic-scale effects in optical spectroscopy, as well as for providing deeper insights into the significance of quantum many-body effects in optical, electron, and Raman spectroscopies. In addition, our results raise new challenges that could be addressed using the methodologies presented here. For instance, the comprehensive description of the plasmonic response of sodium nanoparticles in Chapter 4 paves the way for similar studies on other materials with more direct technological applications, such as noble metals, or for investigating the influence of the nanoparticle's environment, such as an embedding medium or a molecular coating. These aspects could, in principle, be explored within the same framework, which naturally incorporates *d*-electron shells and molecular environments. Furthermore, the methodology proposed in Chapter 5 for computing the Raman spectrum of molecular adsorbates could be readily extended to nano- and picocavity configurations that are at the forefront of SERS research.

Appendices

Appendix A

Atomic units

The Hartree atomic units (au), which are frequently used in this thesis, consider the following fundamental physical constants as unity by definition:

- electron mass m_e,
- elementary charge e,
- Bohr radius a_0,
- Reduced Planck's constant $\hbar = h/2\pi$,
- Coulomb's constant $1/(4\pi\epsilon_0)$.

The equivalence between Hartree atomic units and the International System of Units (SI) of the main physical quantities is given in Table A.1.

Quantity	Hartree atomic units	SI units
Mass	m_e	$9.1094 \cdot 10^{-31}$ kg
Charge	e	$1.6022 \cdot 10^{-19}$ C
Length	a_0	$5.2918 \cdot 10^{-11}$ m
Energy	$E_h = \hbar^2/(m_e a_0^2)$	$4.3597 \cdot 10^{-18}$ J
Electric dipole moment	ea_0	$8.4784 \cdot 10^{11}$ C · m
Electric field	$E_h/(ea_0)$	$5.1422 \cdot 10^{11}$ V/m

Table A.1: Equivalence between Hartree atomic units and SI units of the main physical quantities.

Appendix B

Electron energy-loss probability in the Hydrodynamic Model

In this appendix, we describe in greater detail the hydrodynamic model employed for the calculations of the EEL probability in Chapter 4. The following discussion is adapted from Refs. [59, 259]. The general dynamics equation of an inhomogeneous electron gas under the influence of an external charge probe is given by [59]:

$$\begin{aligned}&\widetilde{\beta}^2(\mathbf{r})\nabla^2\delta n(\mathbf{r},\omega)+[(\omega+i\gamma_{\rm h})\omega-\widetilde{\omega}_{\rm p}^2(\mathbf{r})]\delta n(\mathbf{r},\omega)\\&+\frac{1}{4\pi}\nabla\widetilde{\omega}_{\rm p}^2(\mathbf{r})\cdot\nabla\int d\mathbf{r}'\frac{\delta n(\mathbf{r}',\omega)}{|\mathbf{r}'-\mathbf{r}|}+\nabla\widetilde{\beta}^2\cdot\nabla\delta n(\mathbf{r},\omega)\\&=\widetilde{\omega}_{\rm p}^2(\mathbf{r})n^{\rm e}(\mathbf{r},\omega)-\frac{1}{4\pi}\nabla\widetilde{\omega}_{\rm p}^2(\mathbf{r})\cdot\nabla\int d\mathbf{r}'\frac{n^{\rm e}(\mathbf{r}',\omega)}{|\mathbf{r}'-\mathbf{r}|},\end{aligned} \tag{B.1}$$

where $\delta n(\mathbf{r},\omega)$ is the induced charge density of the electron gas, the function $\widetilde{\beta}(\mathbf{r})$ is the local compressibility of the electron gas that stands for the local dispersion at position $\mathbf{r}$, the function $\widetilde{\omega}_{\rm p}^2(\mathbf{r})=4\pi n(\mathbf{r})$ stands for the frequency of the local plasmon at $\mathbf{r}$, $\gamma_{\rm h}$ is a constant damping term, and $n^{\rm e}(\mathbf{r},\omega)$ is the external probe charge density. For an electron probe traveling parallel to the z-axis, in spherical coordinates and in frequency domain, $n^{\rm e}(\mathbf{r},\omega)$ can be expressed as:

$$n^{\rm e}(\mathbf{r},\omega)=-\frac{e}{v}\frac{\delta(r\sin\theta-b)\delta(\varphi)}{r\sin\theta}e^{i\omega r\cos\theta/v}, \tag{B.2}$$

where v is the speed of the probe electron, and b is the impact parameter, this is, the distance between the z-axis and the beam trajectory.

The equation can be considerably simplified if we consider a homogeneous electron gas inside a metallic sphere of radius a, with constant density (in the absence of perturbations) $n(\mathbf{r})=n=3/4\pi r_s^3$ for $r<a$, where r_s is the Wigner-Seitz radius. In this case, the plasma frequency is also constant: $\widetilde{\omega}_{\rm p}(\mathbf{r})=\omega_{\rm p}=\sqrt{4\pi n}$ for $r<a$ and $\widetilde{\omega}_{\rm p}(\mathbf{r})=0$ for $r>a$, and the dispersion of the medium is described by a constant compressibility parameter $\widetilde{\beta}(\mathbf{r}) = \beta_\mathrm{h} = \sqrt{3/5}v_\mathrm{F}$ for $r < a$, where $v_\mathrm{F} = (3\pi^2 n)^{1/2}$ is the Fermi velocity of the electron gas. With these assumptions, the equation of the electron gas dynamics reduces to the Helmholtz equation inside the nanoparticle [59]:

$$[\nabla^2 + \mu_\mathrm{h}^2(\omega)]\delta n(\mathbf{r},\omega) = \frac{\omega_\mathrm{p}^2}{\beta_\mathrm{h}^2} n^\mathrm{e}(\mathbf{r},\omega), \tag{B.3}$$

where μ_h is an ω-dependent parameter defined as:

$$\mu_\mathrm{h}^2(\omega) = \frac{1}{\beta_\mathrm{h}^2}\Big[\omega(\omega + i\gamma_\mathrm{h}) - \omega_\mathrm{p}^2\Big]. \tag{B.4}$$

At the interface ($r = a$), the solutions to Eq. (B.3) must satisfy the hydrodynamic boundary condition of zero electron current normal to the surface, expressed as:

$$\begin{aligned} -\frac{1}{4\pi}\omega_\mathrm{p}^2 \frac{\partial}{\partial r}\int d\mathbf{r}' \frac{\delta n(\mathbf{r}',\omega)}{|\mathbf{r}'-\mathbf{r}|} - \beta_\mathrm{h}^2 \frac{\partial}{\partial r}\delta n(\mathbf{r},\omega) = \\ = \frac{1}{4\pi}\omega_\mathrm{p}^2 \frac{\partial}{\partial r}\int d\mathbf{r}' \frac{n^\mathrm{e}(\mathbf{r}',\omega)}{|\mathbf{r}'-\mathbf{r}|}. \end{aligned} \tag{B.5}$$

Taking advantage of the spherical symmetry of the probed particle, we can expand the charge densities, $n^\mathrm{e}(\mathbf{r},\omega)$ and $\delta n(\mathbf{r},\omega)$, in terms of spherical harmonics $Y_\ell^m(\Omega)$. This allows for obtaining analytical expressions for the radial components of the induced charge density $\delta n_{\ell m}(r,\omega)$ in terms of the spherical Bessel functions of the first and second kind, $j_\ell(x)$ and $y_\ell(x)$, respectively. The induced electric potential can then be directly computed by integrating the induced density over the volume of the NP:

$$\begin{aligned} \phi^\mathrm{ind}(\mathbf{r},\omega) &= \int_V d\mathbf{r}' \frac{\delta n(\mathbf{r}',\omega)}{|\mathbf{r}'-\mathbf{r}|} = \sum_{\ell=0}^{\infty}\sum_{m=-l}^{\ell} Y_\ell^m(\Omega)\phi_{\ell m}^\mathrm{ind}(r,\omega) \\ &= \sum_{\ell=0}^{\infty}\sum_{m=-\ell}^{\ell} Y_\ell^m(\Omega)\frac{4\pi}{2\ell+1}\int_0^a dr' r'^2 \frac{r_<^\ell}{r_>^{\ell+1}}\delta n_{\ell m}(r',\omega), \end{aligned} \tag{B.6}$$

where $r_< = \min(r,r')$ and $r_> = \max(r,r')$. The electron energy loss probability can then be computed from the induced potential as:

$$\Gamma_\mathrm{EELS}(\omega) = \frac{1}{\pi v}\int_{-\infty}^{\infty} dz' \mathrm{Im}\Big\{-\phi^\mathrm{ind}(\mathbf{r}',\omega)e^{-i\omega z'/v}\Big\}. \tag{B.7}$$

The resulting integral can be separated into three terms [259]:

$$\begin{aligned}\Gamma(\omega) = \frac{4a\omega_{\rm p}^2}{\pi v^2}\sum_{\ell=0}^{\infty}\sum_{m=0}^{\ell}(-1)^{\ell+m}(2-\delta_{m0})\frac{(\ell-m)!}{(\ell+m)!}\\ \times \,\mathrm{Im}\{\Gamma_{\ell m}^{\rm bulk}+\Gamma_{\ell m}^{\rm Begr}+\Gamma_{\ell m}^{\rm ext}\}.\end{aligned} \tag{B.8}$$

Here the $\Gamma_{\ell m}^{\rm bulk}$ term is related to the bulk losses in an unbound medium:

$$\begin{aligned}\Gamma_{\ell m}^{\rm bulk} =& \frac{2}{a\mu_{\rm h}^2}\beta_{\rm h}^2\int_0^{\sqrt{a^2-b^2}} dz\frac{1}{r^{\ell+1}}P_\ell^m\left(\frac{z}{r}\right)g_{\ell m}\left(\frac{\omega z}{v}\right)\\ &\times\int_0^z dz' r'^{\ell}P_\ell^m\left(\frac{z'}{r'}\right)g_{\ell m}\left(\frac{\omega z'}{v}\right),\end{aligned} \tag{B.9}$$

where $P_\ell^m(x)$ is the associated Legendre polynomial of degree ℓ and order m and

$$g_{\ell m}(x) = \begin{cases}\cos(x) & \text{if } \ell+m \text{ is even,}\\ i\,\sin(x) & \text{if } \ell+m \text{ is odd.}\end{cases} \tag{B.10}$$

These losses are reduced by the Begrenzung term $\Gamma_{\ell m}^{\rm Begr}$ that accounts for the presence of a boundary [157]. This term can be further separated in two terms:

$$\Gamma_{\ell m}^{\rm Begr} = \Gamma_{\ell m}^{\rm Begr,i}+\Gamma_{\ell m}^{\rm Begr,o}. \tag{B.11}$$

The first (inner) term $\Gamma_{\ell m}^{\rm Begr,i}$ corresponds to the path of the electron probe inside the NP both when perturbing the electron cloud and when suffering the energy loss:

$$\begin{aligned}\Gamma_{\ell m}^{\rm Begr,i} =& \frac{\ell+1}{M_\ell}\left(1+\frac{\omega_{\rm p}^2}{\mu_{\rm h}^2\beta_{\rm h}^2}\right)\mathcal{I}_{\ell m}(b,a)\left[\frac{j_{\ell-1}(\mu_{\rm h}a)}{2\ell+1}\mathcal{I}_{\ell m}(b,a)-\frac{2}{a^2\mu_{\rm h}^2}\mathcal{J}_{\ell m}(b,a)\right]\\ &-\frac{2\ell+1}{a\beta_{\rm h}^2\mu_{\rm h}^3}\left[\frac{N_\ell}{M_\ell}[\mathcal{J}_{\ell m}(b,a)]^2-\right.\\ &\left.2\mu_{\rm h}\int_0^{\sqrt{a^2-b^2}} dz\; y_\ell(\mu_{\rm h}r)P_\ell^m\left(\frac{z}{r}\right)g_{\ell m}\left(\frac{\omega z}{v}\right)\mathcal{J}_{\ell m}(b,r)\right],\end{aligned} \tag{B.12}$$

where

$$N_\ell = \omega_{\rm p}^2\frac{\ell+1}{2\ell+1}y_{\ell+1}(\mu_{\rm h}a)-\beta_{\rm h}^2\mu_{\rm h}^2y_\ell'(\mu_{\rm h}a), \tag{B.13}$$

$$M_\ell = \omega_{\rm p}^2\frac{\ell+1}{2\ell+1}j_{\ell+1}(\mu_{\rm h}a)-\beta_{\rm h}^2\mu_{\rm h}^2j_\ell'(\mu_{\rm h}a), \tag{B.14}$$

and

$$\mathcal{I}_{\ell m}(r_1, r_2) = \int_{r_1}^{r_2} dr \; \frac{r^\ell}{a^{\ell+1}} \frac{\Pi_{\ell m}(r)}{\sqrt{1 - b^2/r^2}}, \tag{B.15}$$

$$\mathcal{J}_{\ell m}(r_1, r_2) = \int_{r_1}^{r_2} dr \; \mu_\mathrm{h} j_\ell(\mu_\mathrm{h} r) \frac{\Pi_{\ell m}(r)}{\sqrt{1 - b^2/r^2}}, \tag{B.16}$$

with

$$\Pi_{\ell m}(r) = g_{\ell m} \left(\frac{\omega}{v} \sqrt{r^2 - b^2} \right) P_\ell^m \left(\sqrt{1 - \frac{b^2}{r^2}} \right). \tag{B.17}$$

The second (outer) term $\Gamma_{\ell m}^{\mathrm{Begr,o}}$ is related to the path of the electron probe outside the NP when perturbing the electron cloud and inside the NP when suffering the energy loss, and vice versa:

$$\Gamma_{\ell m}^{\mathrm{Begr,o}} = -\frac{2\ell}{M_\ell} \mathcal{O}_{\ell m}(a, \infty) \left[\frac{j_{\ell-1}(\mu_\mathrm{h} a)}{2\ell + 1} \mathcal{I}_{\ell m}(b, a) - \frac{1}{a^2 \mu_\mathrm{h}^2} \mathcal{J}_{\ell m}(b, a) \right], \tag{B.18}$$

where

$$\mathcal{O}_{\ell m}(r_1, r_2) = \int_{r_1}^{r_2} dr \; \frac{a^\ell}{r^{\ell+1}} \frac{\Pi_{\ell m}(r)}{\sqrt{1 - b^2/r^2}}. \tag{B.19}$$

The term $\Gamma_{\ell m}^{\mathrm{ext}}$ contains the contribution from the losses by the part of the electron trajectory lying externally to the NP (both when inducing the plasmons and when suffering the energy loss):

$$\Gamma_{\ell m}^{\mathrm{ext}} = \frac{\ell j_{\ell+1}(\mu_\mathrm{h} a)}{(2\ell + 1) M_\ell} [\mathcal{O}_{\ell m}(a, \infty)]^2, \tag{B.20}$$

whose main contribution is associated to LSPs.

One can also obtain the eigenmodes of the system by solving Eq. (B.3) in the absence of excitation sources ($n^\mathrm{e}(\mathbf{r}, \omega) = 0$) and applying the boundary conditions at the interface [Eq. (B.5)]. This leads to the following mode condition:

$$\omega_\mathrm{p}^2 \frac{\ell + 1}{2\ell + 1} j_{\ell+1}(\mu_\mathrm{h} a) - \beta_\mathrm{h}^2 \mu_\mathrm{h}^2 j_\ell'(\mu_\mathrm{h} a) = 0, \tag{B.21}$$

which gives multiple eigenenergies $\omega_{\ell n}$ for each ℓ polar term, where $n = 0, 1, 2, 3, \ldots$ is the number of nodes in the radial component of the eigenmode. Since the azimuthal number m is degenerated, we will characterize these modes by the (ℓ, n) tuples.

In Figure B.1a, we show the isosurfaces of the charge densities corresponding to the lowest order eigenmodes ($\ell = 0 - 3$, $n = 0 - 3$, $m = \ell$). As observed, the $n = 0$ modes are confined to the nanoparticle surface, and represent the LSPs, with the exception of the ($\ell = 0, n = 0$) mode, which does not conserve the charge and is therefore unphysical. The $n > 0$ solutions present charge densities distributed through all the nanoparticle volume, and correspond to the confined

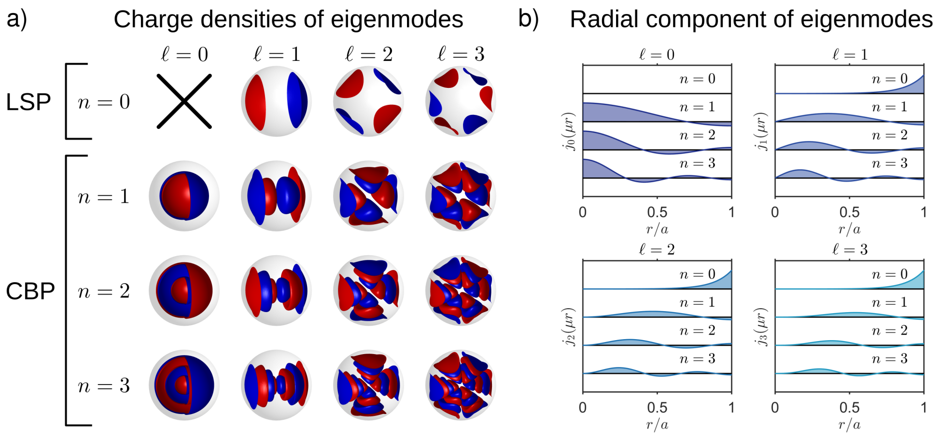

Figure B.1: (a) 3D charge density isosurfaces associated to the lowest order eigenmodes of the oscillations of an homogeneous electron gas in a spherical particle within the HDM ($\ell = 0 - 3$, $n = 0 - 3$, $m = \ell$). The spherical nanoparticle is outlined in gray. (b) Radial component of the induced charge density distribution associated to the HDM eigenmodes displayed in (a). All results depicted in this figure were provided by M. Urbieta.

bulk plasmons (CBPs). The difference between LSP and CBP modes can be clearly appreciated in Figure B.1b, where we plot the radial component of the charge densities associated with the different modes. LSPs ($n = 0$) show an exponential decay of the associated charge density from the surface into the NP, while the CBPS ($n > 0$) show oscillations of the charge density with n nodes inside the NP.

Appendix C

Exchange–correlation functionals

Even though DFT would be an exact theory according to the Kohn-Sham formalism presented in Section 2.1, this does not occur in practice because the exchange–correlation energy E_{xc} cannot be determined exactly. Different approximations have been proposed to calculate E_{xc}, which can have a drastic effect on the results obtained, and thus the choice of the exchange–correlation functional is an essential consideration when using DFT. Here we present the different approaches that have been followed throughout this thesis. The simplest one is the local-density approximation (LDA), which assumes that the functional only depends on the local electronic density. This is used by PyNAO for computing the optical and EEL spectra in the linear-response regime. The generalized gradient approximation (GGA), which is used for computing the ground state of metallic clusters, also takes into account the gradient of the electronic density. On top of this, van der Waals functionals also incorporate long-range dispersive interactions between non-bonded atoms, and they are used for calculations involving a metal–organic molecule interface in Chapter 5. These approximations are briefly described in the next sections, following the standard literature.

The local-density approximation (LDA)

The simplest functional for E_{xc} is given by the local-density approximation (LDA), which considers the local exchange–correlation energy density $\mathcal{E}_{\mathrm{xc}}$ of a system with charge density $n(\mathbf{r})$ as that of a homogeneous electron gas with $n = n(\mathbf{r})$ [177]:

$$E_{\mathrm{xc}}^{\mathrm{LDA}}[n(\mathbf{r})] = \int d\mathbf{r}\; n(\mathbf{r})\mathcal{E}_{\mathrm{xc}}(n(\mathbf{r})). \tag{C.1}$$

The exchange–correlation energy density can be decomposed into the exchange and correlation components:

$$\mathcal{E}_{\mathrm{xc}}(n(\mathbf{r})) = \mathcal{E}_{\mathrm{x}}(n(\mathbf{r})) + \mathcal{E}_{\mathrm{c}}(n(\mathbf{r})). \tag{C.2}$$

The exchange part can be computed analytically in the well-known Slater approximation [305]:

$$\mathcal{E}_{\mathrm{x}}(n(\mathbf{r})) = -\frac{3}{4}\left(\frac{3}{\pi}\right)^{1/3} e^2 n(\mathbf{r})^{1/3}. \tag{C.3}$$

Although there is no exact analytical expression for the LDA correlation energy density, it can be computed numerically with Monte Carlo methods. Using these numerical results, several parametrized functions $\mathcal{E}_{\mathrm{c}}(r_s)$ have been developed, where $r_s = (\frac{3}{4\pi n})^{1/3}$ is the Wigner–Seitz radius. The default expression in SIESTA and the one used in this work for computing the linear-response of the systems in Chapters 3 and 4 with PyNAO is the form developed by Perdew and Zunger [180], based on quantum Monte Carlo calculations by Ceperley and Alder [306].

In principle, this local approximation is only justified if the electronic density varies smoothly in space. Nevertheless, it has been used with remarkable success even for systems that do not fulfill such requirement. This is partially caused by a cancellation of errors between the typically overestimated correlation energy and the usually underestimated exchange energy.

The generalized gradient approximation (GGA)

The semi-local generalized gradient approximation (GGA) also takes into account the local gradient of the electronic density:

$$E_{\mathrm{xc}}^{\mathrm{GGA}}[n(\mathbf{r})] = \int d\mathbf{r}\; f(n(\mathbf{r}), \nabla n(\mathbf{r})), \tag{C.4}$$

which allows for a better simulation of systems with inhomogeneous electronic density. As we did in the previous section, one can separate the GGA energy into the exchange and correlation parts. The correlation contribution is usually much smaller than the exchange one, and is equal to the LDA correlation in the slowly varying density limit ($|\nabla n| \to 0$), while it vanishes in the rapidly varying limit. The exchange contribution is usually expressed as a multiplication of the local uniform energy density by an enhancement factor depending on the dimensionless reduced density gradient $s_{\mathrm{g}} = |\nabla n|/k_{\mathrm{F}} n$, where $k_{\mathrm{F}} = (3\pi^2 n)^{1/3}$ is the Fermi wavevector:

$$\mathcal{E}_{\mathrm{x}}^{\mathrm{GGA}}(n, s_{\mathrm{g}}) = \mathcal{E}_{\mathrm{x}}^{\mathrm{LDA}}(n) F_{\mathrm{x}}(s_{\mathrm{g}}). \tag{C.5}$$

One of the most commonly used GGA functionals is the one created by Perdew, Burke and Ernzerhof, known as PBE [181], which assumes an exchange enhancement factor that takes the form

$$F_{\mathrm{x}}(s_{\mathrm{g}}) = 1 + \kappa_{\mathrm{g}} - \frac{\kappa_{\mathrm{g}}}{1 + x_{\mathrm{g}}/\kappa_{\mathrm{g}}}, \tag{C.6}$$

with $\kappa_{\mathrm{g}} = 0.804$ and $x_{\mathrm{g}} = \mu_{\mathrm{g}} s^2$, with $\mu_{\mathrm{g}} = 0.21951$. We have used this functional for computing the ground states of Na clusters in Chapter 4 with SIESTA. In addition to PBE, in this work we have also used the variant functional developed by Wu and Cohen [182] for computing the ground states of the Ag clusters and those of the hybrid molecule–MNPs systems in Chapter 4. This functional uses the alternative ansatz

$$x_{\mathrm{g}} = \frac{10}{81} s_{\mathrm{g}}^2 + \left(\mu_{\mathrm{g}} - \frac{10}{81} \right) s_{\mathrm{g}}^2 \exp(-s_{\mathrm{g}}^2) + \ln(1 + c_{\mathrm{g}} s_{\mathrm{g}}^2), \tag{C.7}$$

with $c_{\mathrm{g}} = 0.00793$. Note that both of the described exchange enhancement factors tend to 1 in the slowly varying density limit ($s_{\mathrm{g}} \to 0$).

Van der Waals functionals

The aforementioned approaches are local or semi-local in nature, and therefore fail to take into account the long-range dispersive interactions between non-bonded atoms, which play a fundamental role in determining the properties of systems with many interacting molecules, such as liquids, molecular crystals or self-assembled monolayers. In order to deal with these forces within the DFT framework, one can use van der Waals functionals which add a dispersion correction term, $E_{\mathrm{c}}^{\mathrm{nl}}[n]$, to the usual correlation energy [183]:

$$E_{\mathrm{c}}[n] = E_{\mathrm{c}}^{0}[n] + E_{\mathrm{c}}^{\mathrm{nl}}[n]. \tag{C.8}$$

There are two general methods for computing the non-local dispersion terms. The simplest one is by performing a summation over all atomic pairs {A,B}:

$$E_{\mathrm{c}}^{\mathrm{nl}} = -\sum_{A<B} \sum_{n=6,8,10\ldots} f_n^{\mathrm{dmp}}(R_{\mathrm{AB}}) \frac{C_n^{\mathrm{AB}}}{R_{\mathrm{AB}}^n}, \tag{C.9}$$

where R_{AB} is the inter-atomic distance, and the C_n^{AB} terms are the dispersion coefficients for the atomic pair, which depend on the atomic species of the pair, and are computed empirically. The factor f_n^{dmp} is a damping function avoiding divergences at small distances

$$f_n^{\mathrm{dmp}}(R_{\mathrm{AB}}) = \frac{s_n}{1 + \exp^{-d_{\mathrm{d}}(\frac{R_{\mathrm{AB}}}{R_{0\mathrm{AB}}} - 1)}}, \tag{C.10}$$

where s_n is a global scaling parameter, $R_{0\mathrm{AB}}$ is the sum of the van der Waals radii of atoms A and B, and the value of d_{d} determines the steepness of the damping function.

The more general form of a non-local dispersion correction takes the form [307]:

$$E_{\mathrm{c}}^{\mathrm{nl}} = \frac{1}{2} \int d\mathbf{r}\; d\mathbf{r}'\; n(\mathbf{r}) \xi(\mathbf{r}, \mathbf{r}') n(\mathbf{r}'), \tag{C.11}$$

where $\xi(\mathbf{r}, \mathbf{r}')$ is a general function depending on the separation $|\mathbf{r} - \mathbf{r}'|$, as well as on the density and its gradient. This is the method followed for the construction of the optPBE-vdW functional [301], which is used for the self-assembled monolayer calculations in Chapter 5.

Appendix D

Basis sets for solving the Kohn–Sham equations

In order to solve the KS equations introduced in Section 2.1 [Eq. (2.11b)] numerically, the eigenorbitals ϕ_i must be expanded on some basis set of functions $\{\varphi_\alpha\}$

$$\phi_i(\mathbf{r}) = \sum_\alpha C_{i\alpha}\varphi_\alpha(\mathbf{r}). \tag{D.1}$$

By inserting this expansion into the KS equations, one obtains the following matrix equation

$$\sum_\alpha H_{\beta\alpha}C_{i\alpha} = \varepsilon_i \sum_\alpha S_{\beta\alpha}C_{i\alpha}, \tag{D.2}$$

where $H_{\beta\alpha} = \langle\varphi_\beta|\hat{H}_{\mathrm{KS}}|\varphi_\alpha\rangle$ are the matrix elements of the effective KS Hamiltonian, and $S_{\beta\alpha} = \langle\varphi_\beta|\varphi_\alpha\rangle$ are the elements of the overlap matrix. Thus, to obtain the KS eigenorbitals and eigenvalues one must diagonalize an $M \times M$ matrix, where M is the number of functions in the basis set. It is easy to see how the computational costs of solving the KS equations are directly related to the choice of the basis set, as the computational cost of solving the eigenvalue problem scales as M^3. In order to expand the ground-state density of a system with N electrons at least $N/2$ orbitals are required, and thus solving the KS equations conventionally scales as N^3. On top of that, the overlap matrix should ideally be diagonal or at least sparse.

Through the years, many different kinds of basis sets have been proposed, each of which has its own advantages and pitfalls. In this appendix we give a short overview on the two types of basis sets used for the calculations presented in this thesis.

Plane-wave basis

Taking advantage of Bloch's theorem for solids [65], which prescribes that the wave functions in periodic systems are composed of a phase factor and a periodic part, we could expand the KS orbitals as a sum of plane waves [308]

$$\phi_{i,\mathbf{k}}(\mathbf{r}) = e^{i\mathbf{k}\cdot\mathbf{r}} \sum_{\mathbf{G}} C_{i,\mathbf{k}}(\mathbf{G}) e^{i\mathbf{G}\cdot\mathbf{r}}, \tag{D.3}$$

where $\mathbf{k}$ is a vector in the Brillouin zone, and $\mathbf{G}$ are the reciprocal lattice vectors. This allows us to define a basis set of plane waves $\varphi_{\mathbf{G}}(\mathbf{r})$

$$\phi_{i,\mathbf{k}}(\mathbf{r}) = \sum_{\mathbf{G}} C_{i,\mathbf{k}}(\mathbf{G}) \varphi_{\mathbf{G}}(\mathbf{r}), \quad \varphi_{\mathbf{G}}(\mathbf{r}) = e^{i(\mathbf{k}+\mathbf{G})\cdot\mathbf{r}}. \tag{D.4}$$

Although a complete basis set requires the use of infinite plane waves, this is impossible to implement in practice. Fortunately, the contribution of plane waves with large kinetic energies is usually very small, which allows for truncating the basis set with a cutoff energy E_{cut}, such that only plane waves with energies smaller than this cutoff are included in the expansion:

$$\frac{1}{2}|\mathbf{k}+\mathbf{G}|^2 \leq E_{\text{cut}}. \tag{D.5}$$

Plane waves have the advantage of being a conceptually simple and intuitive basis set. The computation of their derivatives and integrals is straightforward, they allow for systematic convergence with respect to the cutoff energy, and they are orthonormal by definition. Furthermore, the matrix elements of the Hamiltonian are quite easy to compute in such a basis set, as the kinetic energy operator is diagonal, and the matrix elements of the effective potential are just Fourier transforms of the same potential. All of these qualities have made plane wave functions one of the most popular choices for basis sets.

However, plane wave calculations can be expensive, as the number of basis functions required to achieve convergence may be quite large, especially for tight-bound orbitals such as the *d* orbitals in silver. Furthermore, this basis is not well-suited for order-N methods, as these methods require locality [309] and plane-waves extend over the whole system, which hampers their scalability for larger systems.

Localized basis sets

Though conventionally solving the eigenvalue equation, Eq. (D.4), scales as N^3, it is possible to improve this scaling thanks to the principle of "nearsightedness", which states that electrons are shielded from changes in the external potential far from their position [310]. Order-N methods exploit this property to achieve linear scaling with the electron number [311], which generally requires the use of some kind of localized functions for expanding the KS wavefunctions, such as spherical waves [312], "blip" functions [313] or real-space grids [314].

Among the different options to implement localized basis sets, atomic orbitals offer significant advantages because of their efficiency (as it is possible to achieve good accuracies with few basis functions) and straightforward physical interpretation. This has led to the emergence of different types of basis sets of atomic orbitals, such as Gaussian orbitals [315] or Slater-type orbitals [316]. In this thesis, we have used a basis set of numerical atomic orbitals (NAO) as implemented in the popular order-N SIESTA method [111], which are the product of radial functions and real-valued spherical harmonics:

$$\varphi_{In\ell m}(\mathbf{r}) = R_{I\ell n}(|\mathbf{r} - \mathbf{R}_I|)Y_{\ell m}(\hat{r}_I), \tag{D.6}$$

where I denotes the atom index, n the principal quantum number, ℓ the azimuthal quantum number, and m the magnetic quantum number, and $\mathbf{R}_I$ is the position of atom I. The radial functions are obtained by numerically solving the KS equation for the isolated pseudoatoms, using the same approximations that will be used for the calculations with the complete system. The simplest basis set of this type uses a single radial function for each occupied angular momentum shell, and is known as single-ζ or SZ. To model a Si atom with valence shell $3s^2 3p^2$ the corresponding SZ basis would be composed of four functions: one s-type orbital and three p-orbitals with identical radial part and angular parts with $\ell = 1$ and $m = [-1, 0, 1]$. There are two ways to augment such a basis set. The first one is by adding more radial functions per occupied angular momentum shell, leading to the so-called multiple-ζ basis sets. The second is by adding additional angular momentum shells, which are called "polarized" orbitals. Thus, going back to the Si example, a standard double-ζ polarized (DZP) basis set, which is the one used for our SIESTA calculations, will be composed of 13 orbitals. To the original s-type orbital we add another s-type orbital with a different radial part, and three more to the original p-orbitals. On top of this, we add five more orbitals with $n = 3, \ell = 2, m = [-2, -1, 0, 1, 2]$.

When solving the radial part of the Schrödinger equation for the isolated pseudoatom exactly, the eigenfunctions only become zero at the $r \to \infty$ limit. Directly using these solutions for constructing the basis set of atomic orbitals would not be efficient, as orbitals centered at different atomic positions would always overlap, and thus constraining the spread of the radial functions becomes mandatory. One of the most extended ways for controlling the extension of the radial part of the atomic orbitals is via the *energy shift* parameter. This quantity is added to the orbital eigenenergies, causing the radial functions to vanish at a finite r value instead. The node is then taken as the cutoff radius for the orbitals, and they are not represented beyond it. As a consequence, the larger the value of the energy shift, the more localized the resulting orbital, as can be appreciated in Fig. D.1. Although more localized orbitals lead to more efficient calculations, the results of the more extended orbitals are in principle more precise, which establishes a trade off between computational cost and accuracy, and requires the performance of convergence tests so that reasonable values of the energy shift are used.

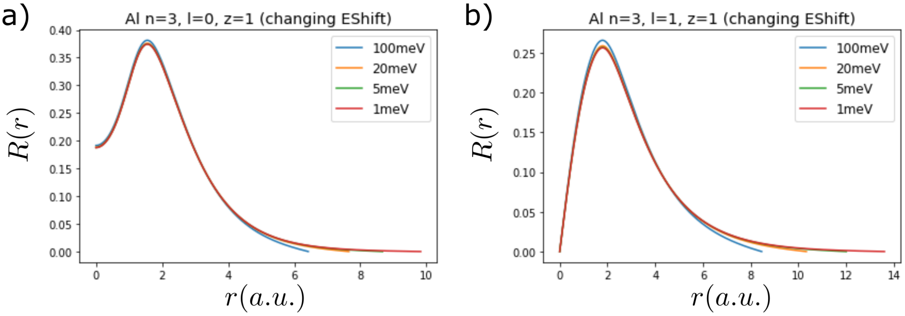

Figure D.1: (a) Radial part of the first-ζ 3s orbital of Al generated by using different values of the energy shift. (b) Same but for the first-ζ 3p orbital of Al.

Appendix E

Treatment of the core electrons

The pseudopotential method

The pseudopotential approach exploits the fundamental differences between core and valence electrons in order to improve the computational efficiency of *ab initio* simulations. Here we provide a short description of the fundamentals of pseudopotential theory following Refs. [308, 317]. Core electrons are tightly bound to the atomic nuclei, which causes their wavefunctions to be highly localized and oscillatory. It is also well known that core electrons are chemically inert, this is, they are not involved in the formation of chemical bonds, and their only effect is to screen the ion–electron potential. As a consequence of this screening, valence electrons are more free to move and interact with nearby atoms. However, due to the orthogonality constraint, the wavefunctions of valence electrons present similar oscillations close to the nuclei, even if their shape is smoother in the outer regions. These oscillations complicate the accurate description of the electronic wavefunctions, especially in the plane-wave basis case, in which a large cutoff energy would be necessary. Fortunately, if one assumes that the core electrons are not affected by chemical interactions, it is possible to simplify the problem by removing them completely from the picture and replacing the steep ion–electron potential with a smoother pseudopotential. This means that the nuclei, together with the core electrons, are considered as small perturbations of the electron gas. On top of obtaining smoother wavefunctions for valence electrons, this approach has the additional advantage of completely removing a large part of the electrons from the calculation, thereby increasing the computational efficiency. A physical justification for this approximation is that, since the core regions are already occupied, there is a strong Pauli repulsion between valence and core electrons, which almost cancels out with the partially screened nuclear attraction.

In order to construct a pseudopotential, one must first solve the all-electron Kohn–Sham equations for the corresponding isolated atom in a chosen reference electronic configuration, using the same exchange–correlation potential that will be used in the target calculation. The standard choice for the electronic configuration is the ground state of the neutral isolated atom. Since the isolated atom problem has spherical symmetry, it is possible to decouple the radial and angular parts and just solve the radial equation [308]:

$$\left[-\frac{1}{2}\frac{d^2}{dr^2}+\frac{\ell(\ell+1)}{2r^2}+V_{\text{eff}}[n^{\text{AE}}](r)\right]rR^{\text{AE}}_{n\ell}(r)=\epsilon_{n\ell}rR^{\text{AE}}_{n\ell}(r), \tag{E.1}$$

where n^{AE} is the all-electron density, $R^{\text{AE}}_{n\ell}(r)$ is the radial part of the all-electron eigenfunctions, $\epsilon_{n\ell}$ are the all-electron eigenenergies, and the effective Kohn-Sham potential for an atom with atomic number Z is given by

$$V_{\text{eff}}[n^{\text{AE}}](r)=-\frac{Z}{r}+V_{\text{Hartree}}[n^{\text{AE}}]+V_{\text{xc}}[n^{\text{AE}}]. \tag{E.2}$$

Once the all-electron wavefunctions are known, one must construct the nodeless pseudo-wavefunctions, which are parameterized inside the core region using one of the multiple available prescriptions. In order to ensure an accurate description of the valence charge density, the pseudo-wavefunction and the all-electron one must coincide beyond a cutoff radius r_c, and the matching at the boundary must be smooth. In general, there is a trade off in the choice of the cutoff radii, as smaller radii lead to pseudopotentials that are more realistic but also less smooth, and vice versa. For norm-conserving pseudopotentials, as the ones used in this work, pseudo and all-electron wavefunctions must also have the same norm and energy eigenvalues. In Fig. E.1a, we show norm-conserving pseudo and all-electron wavefunctions for the element Mo, taken from Ref. [318]. Note that both wavefunctions match for radii larger than the cutoff radius, and that the pseudo-wavefunction is much smoother for smaller radii.

Since we already know the pseudo-wavefunction, we can now obtain the pseudopotential $V^{\text{P}}_{(\text{sc})\ell}(r)$ by inverting the radial Schrödinger equation for the pseudo-wavefunction, which is always possible because the pseudo-wavefunction is nodeless. The inversion is done for the lowest-lying valence state of each angular momentum, so we can drop the principal quantum number:

$$V^{\text{P}}_{(\text{sc})\ell}(r)=\epsilon_\ell-\frac{\ell(\ell+1)}{2r^2}+\frac{1}{2rR^{\text{P}}_\ell(r)}\frac{d^2}{dr^2}[rR^{\text{P}}_\ell(r)], \tag{E.3}$$

where $R^{\text{P}}_\ell(r)$ is the radial part of the pseudo-wavefunction. In Fig. E.1b, we show the pseudopotentials obtained from the pseudo wavefunctions in Fig. E.1a, together with the potential generated by a point charge with the same charge as the nucleus screened by the core $-Z_V/r$.

The effective potential used to solve the all-electron Kohn–Sham equations was computed from the charge density of the isolated atom. Though the core electron density is impervious to the chemical environment, the valence density is extremely dependent on it. Therefore, the last step of the pseudopotential generation procedure is to unscreen (subtract) the valence part of the Hartree and

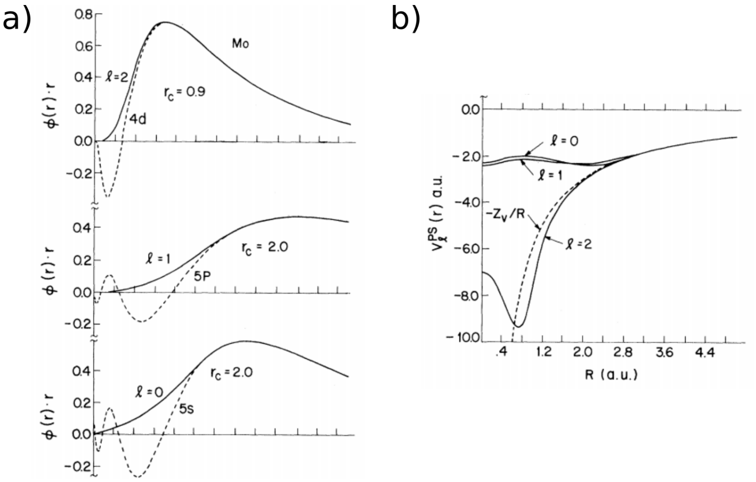

Figure E.1: Example of norm-conserving pseudopotentials and pseudo-wavefunctions for Mo, taken from Ref. [318]. a) Comparison of norm-conserving pseudo-wavefunctions (solid lines) and all-electron valence radial functions (dashed lines). b) Comparison between the pseudopotentials $V^{\mathrm{P}}_{(\mathrm{sc})\ell}(r)$ for the first three angular momentum shells (solid lines) and $-Z_V/r$ (dashed line).

exchange–correlation potentials, so that when performing the target calculation one can use the valence charge density computed for the target system to screen the nuclear potential:

$$V^{\mathrm{P}}_{\ell}(r) = V^{\mathrm{P}}_{(\mathrm{sc})\ell}(r) - V_{\mathrm{Hartree}}[n_{\mathrm{v}}] - V_{\mathrm{xc}}[n_{\mathrm{v}}], \tag{E.4}$$

where the pseudo valence density is computed from the pseudo-wavefunction as:

$$n_{\mathrm{v}}(r) = \sum_{\ell=0}^{\ell_{\max}} \sum_{m=-\ell}^{\ell} |rR^{\mathrm{P}}_{n\ell}(r)|^2. \tag{E.5}$$

The PAW method

An alternative method to deal with the rapid oscillations of the wavefunctions around the atomic nuclei is the projector-augmented wave (PAW) method [185]. Here we outline the fundamentals of the PAW method as described in Blöchl's original work and in Carsten Rostgaard's notes [319]. The PAW approach is based on the introduction of an auxiliary smooth wavefunction $|\tilde{\phi}_n\rangle$, related to the Kohn-Sham single-particle wavefunction $|\phi_n\rangle$ via a linear transformation $\hat{\mathcal{T}}$ [320]:

$$|\phi_n\rangle = \hat{\mathcal{T}}\,|\tilde{\phi}_n\rangle\,, \tag{E.6}$$

where n is a quantum state label comprising a **k** index, a band index and a spin index. We may now rewrite the Kohn-Sham equations as:

$$\hat{\mathcal{T}}^\dagger \hat{H}_{\mathrm{KS}} \hat{\mathcal{T}} \, |\tilde{\phi}_n\rangle = \epsilon_n \hat{\mathcal{T}}^\dagger \hat{\mathcal{T}} \, |\tilde{\phi}_n\rangle \, . \tag{E.7}$$

The operator $\hat{\mathcal{T}}$ must be defined in a way which ensures that the auxiliary wavefunctions are smooth. Since the valence part of the true wavefunctions is already smooth, the operator only needs to modify the parts close to atomic cores, and can therefore be separated into a sum of localized atom-centered transformations:

$$\hat{\mathcal{T}} = 1 + \sum_a \hat{\mathcal{T}}^a, \tag{E.8}$$

where the index a runs over all atoms. The localized operators $\hat{\mathcal{T}}^a$ only affect augmentation spheres centered around the atomic nuclei and defined by some cutoff radii r_c^a, which should not overlap. Inside these spheres, we can expand the true function in a set of partial waves φ_i^a, each of which has a corresponding auxiliary smooth partial wave $\tilde{\varphi}_i^a$, and we can require that:

$$|\varphi_i^a\rangle = (1 + \hat{\mathcal{T}}^a) \, |\tilde{\varphi}_i^a\rangle \;\Leftrightarrow\; \hat{\mathcal{T}}^a \, |\tilde{\varphi}_i^a\rangle = |\varphi_i^a\rangle - |\tilde{\varphi}_i^a\rangle \, . \tag{E.9}$$

This completely defines the transformation for a given φ and $\tilde{\varphi}$. From this it also follows that the partial waves and their smooth counterparts must be identical outside the augmentation sphere.

If the smooth partial waves form a complete set inside the augmentation sphere, we can expand the auxiliary smooth wavefunction as

$$|\tilde{\phi}_n\rangle = \sum_i P_{ni}^a \, |\tilde{\varphi}_i^a\rangle \;\text{ for } r < r_c^a, \tag{E.10}$$

with P_{ni}^a the coefficients of the expansion. The expansion coefficients will be the same for the alternative expansion

$$|\phi_n\rangle = \sum_i P_{ni}^a \, |\varphi_i^a\rangle \, , \;\text{ for } r < r_c^a \tag{E.11}$$

The requirement of the transformation $\hat{\mathcal{T}}^a$ being linear demands that the coefficients P_{ni}^a are linear functionals of $|\tilde{\phi}_n\rangle$, this is

$$P_{ni}^a = \langle \tilde{p}_i^a | \tilde{\phi}_n \rangle = \int d\mathbf{r} \; \tilde{p}_i^{a*}(\mathbf{r} - \mathbf{R}^a) \tilde{\phi}_n(\mathbf{r}), \tag{E.12}$$

where we introduced the functions $|\tilde{p}_i^a\rangle$ which we call smooth projector functions. Since there is no overlap between the augmentation spheres, the one-center expansion of the smooth wavefunction is identical to the smooth wavefunction inside the sphere:

$$|\varphi_n^a\rangle = \sum_i |\tilde{\varphi}_i^a\rangle \langle \tilde{p}_i^a|\tilde{\phi}_n\rangle \quad \Rightarrow \quad \sum_i |\tilde{\varphi}_i^a\rangle \langle \tilde{p}_i^a| = 1 \text{ for } r < r_c^a. \tag{E.13}$$

This completeness relationship is equivalent to the requirement that the $\tilde{p}_i^a$ should produce the correct expansion coefficients, and also implies that the projector functions should be orthonormal to the smooth partial waves inside the sphere:

$$\langle \tilde{p}_i^a|\tilde{\varphi}_j^a\rangle = \delta_{i,j} \ , \ \text{for } r < r_c^a. \tag{E.14}$$

As there are no restrictions for the projectors outside the spheres, we can define them as local functions that vanish outside of them. The most general form of the projector functions satisfying the completeness relation Eq. (E.13) was obtained by Blöchl [185]:

$$\langle \tilde{p}_i^a| = \sum_j (\{\langle f_k^a|\tilde{\varphi}_l^a\rangle\})_{ij}^{-1} \langle f_j^a| \, , \tag{E.15}$$

where $|f_j^a\rangle$ is any set of linearly independent functions. The projector functions will be localized if these functions are localized.

Inserting the completeness relation Eq. (E.13) in the definition of the localized operators $\hat{\mathcal{T}}^a$, Eq. (E.9), one observes that

$$\hat{\mathcal{T}}^a = \sum_i \hat{\mathcal{T}}^a |\tilde{\varphi}_i^a\rangle \langle \tilde{p}_i^a| = \sum_i (|\varphi_i^a\rangle - |\tilde{\varphi}_i^a\rangle) \langle \tilde{p}_i^a| \, , \tag{E.16}$$

and thus the whole operator can be written as:

$$\hat{\mathcal{T}} = 1 + \sum_a \sum_i (|\varphi_i^a\rangle - |\tilde{\varphi}_i^a\rangle) \langle \tilde{p}_i^a| \, . \tag{E.17}$$

Therefore the relationship between the all-electron KS wavefunction and the smooth auxiliary wavefunction is:

$$\phi_n(\mathbf{r}) = \tilde{\phi}_n(\mathbf{r}) + \sum_a \sum_i [\varphi_i^a(\mathbf{r}) - \tilde{\varphi}_i^a(\mathbf{r})] \langle \tilde{p}_i^a|\tilde{\phi}_n\rangle \, , \tag{E.18}$$

and thus, the transformation between the auxiliary smooth wavefunction and the real one depends on the partial waves $\varphi_i^a(\mathbf{r})$, the smooth partial waves $\tilde{\varphi}_i^a(\mathbf{r})$, and the smooth projector functions $\tilde{p}_i^a(\mathbf{r})$.

The choice of the partial wave and smooth partial wave sets is restricted by the requirement that they must be complete sets inside the augmentation spheres, so that they can be used to expand all-electron wavefunctions. Since they are only used as basis sets they can be chosen as real functions. The smooth projector functions must satisfy the completeness relation Eq. (E.13), which in turn means that they must be constructed according to Blöchl's formula, Eq. (E.15). All the remaining degrees of freedom should be used to make the expansions converge as fast and possible, and to make the smooth functions as smooth as possible.

By introducing this transformation, one manages to separate the original wavefunctions, which are smooth in some regions and oscillatory in others, into an auxiliary smooth wavefunction and localized oscillatory contributions. This separation allows for the independent treatment of the different types of waves. Furthermore, it is frequently assumed that the core states of isolated atoms are localized within the augmentation spheres, and that they are not affected by the formation of bonds. This approximation, known as the frozen core approximation, means that the KS core states are identical to the atomic core states, and therefore only valence states are included in the expansions of $|\phi_n\rangle$ and $|\tilde{\phi}_n\rangle$. Thus, one only needs to compute the smooth KS wavefunctions in order to obtain a complete description of the electron density, which greatly enhances the computational efficiency by requiring much lower energy cutoffs.

Appendix F

Relevant concepts for Bayesian optimization

In this appendix, we provide the definition of relevant concepts in statistics and Bayesian optimization appearing in Section 2.4 of this thesis, in alphabetic order.

- **Conditional probability distribution**: given a joint probability distribution on a set of random variables, the conditional probability distribution of a subset of those random variables is the probability distribution of the variables contained in the subset, contingent on the values of the other variables. Assuming a known joint distribution of two discrete random variables X and Y, $p_{X,Y}(x,y)$, the conditional distribution of the variable Y, $p_{Y|X}(y|x)$, is the joint distribution of both y and x divided by the marginal distribution of variable X:

$$p_{Y|X}(y|x) = p(Y = y|X = x) = \frac{p_{X,Y}(x,y)}{p_X(x)}. \tag{F.1}$$

- **Covariance and Correlation**: The covariance is a measure of the joint variability of two random variables. Its sign shows the tendency in the linear relationship between the variables (this is, if the two variables tend to be higher or lower at the same time, the covariance will be positive). The mathematical expression of the covariance is

$$\mathrm{cov}[X,Y] = \mathbb{E}[(X-\mathbb{E}[X])(Y-\mathbb{E}[Y])] = \mathbb{E}[XY] - \mathbb{E}[X]\mathbb{E}[Y], \tag{F.2}$$

where $\mathbb{E}$ means the expected value. If one normalizes the covariance dividing by the product of the standard deviations of the variables, it is possible to obtain the expression for the correlation

$$\rho[X,Y] = \frac{\mathrm{cov}[X,Y]}{\sigma_X \sigma_Y} = \frac{\mathbb{E}[(X-\mathbb{E}[X])(Y-\mathbb{E}[Y])]}{\sigma_X \sigma_Y}, \tag{F.3}$$

which is contained in the [-1,1] interval. An absolute correlation value of 1 indicates that there is a linear relation between both variables, and a value of 0 indicates no linear dependency.

- **Gaussian distribution**: a normal or Gaussian distribution is a type of continuous probability distribution for a real-valued random variable, x, with a probability density of the form:

  $$\mathcal{N}(x;\mu,\sigma)=\frac{1}{\sigma\sqrt{2\pi}}e^{-\frac{1}{2}\left(\frac{x-\mu}{\sigma}\right)^2}. \tag{F.4}$$

  This distribution is characterized by two scalar parameters: the mean μ, which specifies the expectation value of the distribution (it is at the same time mean, median and mode), and the variance σ^2, which serves as a scale parameter. The special case with zero mean and unit variance is called standard normal distribution.

- **Joint probability distribution**: given a set of random variables in the same probability space, their joint probability distribution is the probability distribution of all possible combinations of values for these variables:

  $$p_{X,Y}(x,y)=p(X=x \text{ and } Y=y). \tag{F.5}$$

- **Marginal probability distribution**: given a joint probability distribution on a set of random variables, the marginal probability distribution of a subset of those random variables is the probability distribution of the variables contained in the subset, without taking into account the values of the other variables. Assuming a known joint distribution of two discrete random variables X and Y, $p_{X,Y}(x,y)$, the marginal distribution of variable X, $p_X(x)$, this is, the probability distribution of X without referencing the values of Y, can be calculated by summing over all possible values of Y

  $$p_X(x)=\sum_y p_{X,Y}(x,y). \tag{F.6}$$

- **Multivariate Gaussian distribution**: it is the generalization of the one-dimensional or univariate Gaussian distribution to an arbitrary random vector $\mathbf{x}$. If the covariance matrix $\mathbf{\Sigma}$ is positive semidefinite, then the probability density exists and is expressed as:

  $$\mathcal{N}(\mathbf{x};\boldsymbol{\mu},\mathbf{\Sigma})=\frac{1}{\sqrt{|2\pi\mathbf{\Sigma}|}}e^{-\frac{1}{2}\Delta^2}, \tag{F.7}$$

  with

  $$\Delta^2=(\mathbf{x}-\boldsymbol{\mu})^T\mathbf{\Sigma}^{-1}(\mathbf{x}-\boldsymbol{\mu}). \tag{F.8}$$

The standard multivariate normal distribution is a special case for which $\boldsymbol{\mu} = \mathbf{0}$ and $\boldsymbol{\Sigma} = \mathbb{I}$, this is, all the variables are independent and have standard univariate normal probability distributions.

- **Stochastic process**: a stochastic or random process is a collection of random variables indexed by some mathematical set, with each random variable uniquely associated with an element in the set. The mathematical set could be, for example, the points comprised inside a spatial region, and the random variables could correspond to the values of a certain field in the corresponding points.

- **Variance**: The variance of a random value is the expected value of its squared deviation from the mean.

$$\mathrm{var}[X] = \mathbb{E}[X - \mathbb{E}[X]]. \tag{F.9}$$

The variance can be interpreted as a special case of the covariance: the covariance of a random variable with itself.

Appendix G

The bare CN-BPT molecule

Here we describe the vibrational spectrum of the bare 4’-cyanobiphenyl-4-thiol molecule in the interval between 1000 cm^{-1} and 2400 cm^{-1}, as computed with the formalism presented in Section 2.3 of this thesis, which is used as a reference in Chapter 5. We first represent all the vibrational modes whose excitation energies are located in the aforementioned interval in Fig. G.1a, where the red (blue) arrows indicate the displacements of the hydrogen (carbon) atoms. The 21 modes displayed in the figure of a total of 72 modes are labeled in ascending energy order, and the Raman active modes are identified with colored numbers. In Fig. G.1b, we plot the Raman spectrum of the molecule in that spectral range, highlighting the main peaks in the color of the corresponding active Raman mode. Finally, the bar plot in Fig. G.1c represents the Raman intensity for each of the modes in G.1a. Table G.1 displays the vibrational mode frequencies and the infrared intensities and dipole moments for the Raman active modes.

Mode	ν_n $[cm^{-1}]$	$I_{IR,n}$ $[(D/\text{Å})^2\text{amu}^{-1}]$	p_n $[D]$
43	1084.9	2.098	0.0571
46	1170.8	0.135	0.0139
47	1184.4	0.368	0.0229
50	1276.5	0.234	0.0176
60	1580.4	3.288	0.0592
61	1597.6	0.397	0.0205
62	2230.5	1.856	0.0374

Table G.1: Information regarding the Raman active modes of the bare CN-BPT molecule. From left to right: vibrational mode number, excitation frequency, infrared intensity, and infrared transition dipole moment.

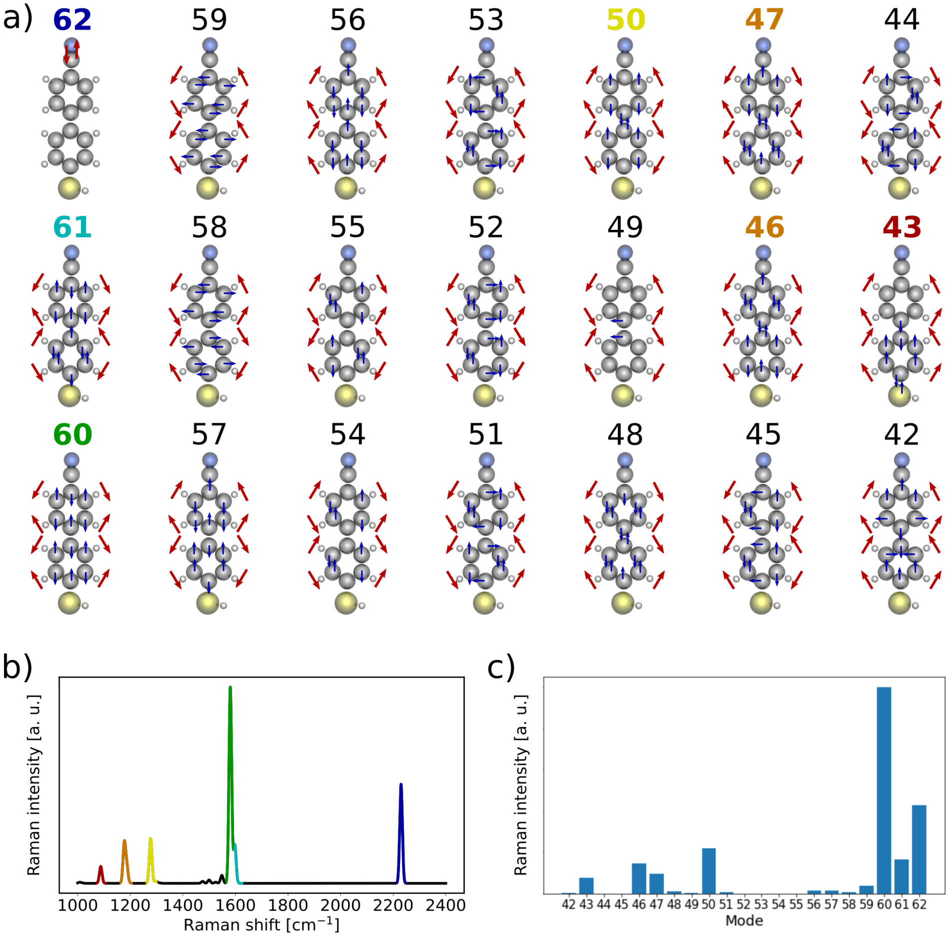

Figure G.1: a) Representation of the vibrational modes ν_n of the bare CN-BPT molecule with excitation energies in the $1000 - 2400$ cm^{-1} range. The modes are labeled with numbers corresponding to the ordering of their excitation energies. The arrows indicate the displacements of the molecule atoms. b) Raman spectrum of the bare CN-BPT molecule, with the main peaks marked with different colors, according to the colors of the corresponding mode labels in a). c) Plot of the normalized Raman intensities of the vibrational modes in a).

List of publications

Most of the results discussed in this thesis are based on the following publications:

1. **B. Candelas**, N. Zabala, P. Koval, A. Babaze, D. Sánchez-Portal, and J. Aizpurua: "Influence of atomistic features in plasmon–exciton coupling and charge transfer driven by a single molecule in a metallic nanocavity", *J. Chem. Phys.* **161**, 044707 (2024).
https://doi.org/10.1063/5.0216464

2. R. A. Boto, R. Esteban, **B. Candelas**, and J. Aizpurua: "Theoretical Procedure for Precise Evaluation of Chemical Enhancement in Molecular Surface-Enhanced Raman Scattering", *J. Phys. Chem. C* **128**, 43, 18293–18304 (2024).
https://doi.org/10.1021/acs.jpcc.4c03491

3. **B. Candelas**, M. Urbieta, A. Babaze, E. Ogando, A. G. Borisov, N. Zabala, and J. Aizpurua: "*Ab initio* Atomistic Characterization of Confined Bulk and Bennett Plasmons in Metallic Nanoparticles as Probed by Penetrating Electrons", *J. Phys. Chem. Lett.* **16**, 2965–2971, (2025).
https://doi.org/10.1021/acs.jpclett.5c00157

4. **B. Candelas**, N. Zabala, R. A. Boto, J. Löfgren, P. Rinke, T. Rossi, and J. Aizpurua: "*Ab initio* study of Surface-Enhanced Raman Spectroscopy of optimized cyanobiphenyl-4-thiol Self-Assembled Monolayers on Au(111)", In preparation.

Bibliography

[1] A. Hon., “The Relation of Aperture and Power in the Microscope (continued).” Journal of the Royal Microscopical Society **2**, 460–473 (1882).

[2] J. A. Schuller, E. S. Barnard, W. Cai, Y. C. Jun, J. S. White, and M. L. Brongersma, “Plasmonics for extreme light concentration and manipulation”, Nature Mater **9**, 193–204 (2010).

[3] J. Langer *et al.*, “Present and Future of Surface-Enhanced Raman Scattering”, ACS Nano **14**, 28–117 (2020).

[4] E. Fort and S. Grésillon, “Surface enhanced fluorescence”, J. Phys. D: Appl. Phys. **41**, 013001 (2007).

[5] T. L. Doane and C. Burda, “The unique role of nanoparticles in nanomedicine: imaging, drug delivery and therapy”, Chem. Soc. Rev. **41**, 2885–2911 (2012).

[6] W. Carvalho and J. R. Mejía-Salazar, “Plasmonics for Telecommunications Applications”, Sensors **20** (2020), 10.3390/s20092488.

[7] H. C. Zhang, L. P. Zhang, P. H. He, J. Xu, C. Qian, F. J. Garcia-Vidal, and T. J. Cui, “A plasmonic route for the integrated wireless communication of subdiffraction-limited signals”, Light Sci Appl **9**, 113 (2010).

[8] J. D. Jackson, *Classical Electrodynamics* (John Wiley & Sons, 1998).

[9] H. Song, M. A. Reed, and T. Lee, “Single Molecule Electronic Devices”, Adv. Mater. **23**, 1583–1608 (2011).

[10] J. Zuloaga, E. Prodan, and P. Nordlander, “Quantum Description of the Plasmon Resonances of a Nanoparticle Dimer”, Nano Lett. **9**, 887–891 (2009).

[11] K. J. Savage, M. M. Hawkeye, R. Esteban, J. Aizpurua, and J. J. Baumberg, “Revealing the quantum regime in tunnelling plasmonics”, Nature **491**, 574–577 (2012).

[12] J. A. Scholl, A. García-Etxarri, A. L. Koh, and J. A. Dionne, “Observation of Quantum Tunneling between Two Plasmonic Nanoparticles”, Nano Lett. **13**, 564–569 (2013).

[13] M. L. Perrin, E. Galan, R. Eelkema, F. Grozema, J. M. Thijssen, and H. S. J. van der Zant, “Single-Molecule Resonant Tunneling Diode”, J. Phys. Chem. C **119**, 5697–5702 (2015).

[14] F. J. García de Abajo, “Nonlocal effects in the plasmons of strongly interacting nanoparticles, dimers, and waveguides”, J. Phys. Chem. C **112**, 17983–17987 (2008).

[15] T. V. Teperik, P. Nordlander, J. Aizpurua, and A. G. Borisov, “Quantum effects and nonlocality in strongly coupled plasmonic nanowire dimers”, Opt. Express **21**, 27306–27325 (2013).

[16] A. Babaze, T. Neuman, R. Esteban, J. Aizpurua, and A. G. Borisov, “Dispersive surface-response formalism to address nonlocality in extreme plasmonic field confinement”, Nanophotonics **12**, 3277–3289 (2023).

[17] P. Apell and A. Ljungbert, “Red shift of surface plasmons in small metal particles”, Solid State Commun. **44**, 1367–1369 (1982).

[18] A. Liebsch, “Dynamical screening at simple-metal surfaces”, Phys. Rev. B **36**, 7378–7388 (1987).

[19] A. Varas, P. García-González, J. Feist, F. García-Vidal, and A. Rubio, “Quantum plasmonics: from jellium models to ab initio calculations”, Nanophotonics **5**, 409–426 (2016).

[20] M. Barbry, *Plasmons in nanoparticles: atomistic Ab Initio theory for large systems*, Ph.D. thesis, University of the Basque Country, UPV/EHU (2018).

[21] A. Babaze, *Quantum Many-Body Effects in the Optoelectronic Response of Plasmonic Nanostructures and their Coupling to Quantum Emitters*, Ph.D. thesis, University of the Basque Country, UPV/EHU (2023).

[22] M. Urbieta, M. Barbry, Y. Zhang, P. Koval, D. Sánchez-Portal, N. Zabala, and J. Aizpurua, “Atomic-Scale Lightning Rod Effect in Plasmonic Picocavities: A Classical View to a Quantum Effect”, ACS Nano **12**, 585–595 (2018).

[23] F. Marchesin, P. Koval, M. Barbry, J. Aizpurua, and D. Sánchez-Portal, “Plasmonic Response of Metallic Nanojunctions Driven by Single Atom Motion: Quantum Transport Revealed in Optics”, ACS Photonics **3**, 269–277 (2016).

[24] T. P. Rossi, T. Shegai, P. Erhart, and T. J. Antosiewicz, “Strong plasmon-molecule coupling at the nanoscale revealed by first-principles modeling”, Nat Commun **10**, 3336 (2019).

[25] M. Kuisma, B. Rousseaux, K. M. Czajkowski, T. P. Rossi, T. Shegai, P. Erhart, and T. J. Antosiewicz, “Ultrastrong Coupling of a Single Molecule to a Plasmonic Nanocavity: A First-Principles Study”, ACS Photonics **9**, 1065–1077 (2022).

[26] T. P. Rossi, P. Erhart, and M. Kuisma, "Hot-Carrier Generation in Plasmonic Nanoparticles: The Importance of Atomic Structure", ACS Nano **14**, 9963–9971 (2020).

[27] M. Barbry, P. Koval, F. Marchesin, R. Esteban, A. G. Borisov, J. Aizpurua, and D. Sánchez-Portal, "Atomistic Near-Field Nanoplasmonics: Reaching Atomic-Scale Resolution in Nanooptics", Nano Lett. **15**, 3410–3419 (2015).

[28] P. Törmä and W. L. Barnes, "Strong coupling between surface plasmon polaritons and emitters: a review", Rep. Prog. Phys. **78**, 013901 (2014).

[29] J. A. Hutchison, T. Schwartz, C. Genet, E. Devaux, and T. W. Ebbesen, "Modifying Chemical Landscapes by Coupling to Vacuum Fields", Angew. Chem. Int. Ed. **51**, 1592–1596 (2012).

[30] F. J. Garcia-Vidal, C. Ciuti, and T. W. Ebbesen, "Manipulating matter by strong coupling to vacuum fields", Science **373**, eabd0336 (2021).

[31] F. Herrera and F. C. Spano, "Cavity-Controlled Chemistry in Molecular Ensembles", Phys. Rev. Lett. **116**, 238301 (2016).

[32] J. Galego, F. J. Garcia-Vidal, and J. Feist, "Suppressing photochemical reactions with quantized light fields", Nat Commun **7**, 13841 (2016).

[33] Y. Kim, A. Barulin, S. Kim, L. P. Lee, and I. Kim, "Recent advances in quantum nanophotonics: plexcitonic and vibro-polaritonic strong coupling and its biomedical and chemical applications", Nanophotonics **12**, 413–439 (2023).

[34] T. B. Hoang, G. M. Akselrod, and M. H. Mikkelsen, "Ultrafast Room-Temperature Single Photon Emission from Quantum Dots Coupled to Plasmonic Nanocavities", Nano Lett. **16**, 270–275 (2016).

[35] K. Miwa, S. Sakamoto, and A. Ishizaki, "Control and Enhancement of Single-Molecule Electroluminescence through Strong Light–Matter Coupling", Nano Lett. **23**, 3231–3238 (2023).

[36] M. Wang, T. Wang, O. S. Ojambati, T. J. Duffin, K. Kang, T. Lee, E. Scheer, D. Xiang, and C. A. Nijhuis, "Plasmonic phenomena in molecular junctions: principles and applications", Nano Lett. **6**, 681–704 (2022).

[37] K. Kneipp, Y. Wang, H. Kneipp, L. T. Perelman, I. Itzkan, R. R. Dasari, and M. S. Feld, "Single Molecule Detection Using Surface-Enhanced Raman Scattering (SERS)", Phys. Rev. Lett. **78**, 1667–1670 (1997).

[38] H. Xu, E. J. Bjerneld, M. Käll, and L. Börjesson, "Spectroscopy of Single Hemoglobin Molecules by Surface Enhanced Raman Scattering", Phys. Rev. Lett. **83**, 4357–4360 (1999).

[39] Y. Zhu, H. Kuang, L. Xu, W. Ma, C. Peng, Y. Hua, L. Wang, and C. Xu, "Gold nanorod assembly based approach to toxin detection by SERS", J. Mater. Chem. **22**, 2387–2391 (2012).

[40] H. Karabeber, R. Huang, P. Iacono, J. M. Samii, K. Pitter, E. C. Holland, and M. F. Kircher, "Guiding Brain Tumor Resection Using Surface-Enhanced Raman Scattering Nanoparticles and a Hand-Held Raman scanner", ACS Nano **8**, 9755–9766 (2014).

[41] L. Jensen, C. M. Aikens, and G. C. Schatz, "Electronic structure methods for studying surface-enhanced Raman scattering", Chem. Soc. Rev. **37**, 1061–1073 (2008).

[42] A. Ulman, "Formation and Structure of Self-Assembled Monolayers", Chem. Rev. **96**, 1533–1554 (1996).

[43] W. Peng, J.-W. Zhou, M.-L. Li, L. Sun, Y.-J. Zhang, and J.-F. Li, "Construction of nanoparticle-on-mirror nanocavities and their applications in plasmon-enhanced spectroscopy", Chem. Sci. **15**, 2697–2711 (2024).

[44] F. Benz, M. K. Schmidt, A. Dreismann, R. Chikkaraddy, Y. Zhang, A. Demetriadou, C. Carnegie, H. Ohadi, B. de Nijs, R. Esteban, J. Aizpurua, and J. J. Baumberg, "Single-molecule optomechanics in "picocavities"", Science **354**, 726–729 (2016).

[45] Y. Zhang, R. Esteban, R. A. Boto, M. Urbieta, X. Arrieta, C. Shan, S. Li, J. J. Baumberg, and J. Aizpurua, "Addressing molecular optomechanical effects in nanocavity-enhanced raman scattering beyond the single plasmonic mode", Nanoscale **13**, 1938–1954 (2021).

[46] P. E. Batson, N. Dellby, and O. L. Krivanek, "Sub-ångstrom resolution using aberration corrected electron optics", Nature **418**, 617–620 (2002).

[47] P. D. Nellist, M. F. Chisholm, N. Dellby, O. L. Krivanek, M. F. Murfitt, Z. S. Szilagyi, A. R. Lupini, A. Borisevich, W. H. Sides, and S. J. Pennycook, "Direct Sub-Angstrom Imaging of a Crystal Lattice", Science **305**, 1741–1741 (2004).

[48] S. Lazar, G. Botton, and H. Zandbergen, "Enhancement of resolution in core-loss and low-loss spectroscopy in a monochromated microscope", Ultramicroscopy **106**, 1091–1103 (2006).

[49] J. L. Hart, A. C. Lang, A. C. Leff, P. L. adn Colin Trevor, R. D. Twesten, and M. L. Taheri, "Direct Detection Electron Energy-Loss Spectroscopy: A Method to Push the Limits of Resolution and Sensitivity", Sci Rep **7**, 8243 (2017).

[50] M.-W. Chu, V. Myroshnychenko, C. H. Chen, J.-P. Deng, C.-Y. Mou, and F. J. García de Abajo, “Probing Bright and Dark Surface-Plasmon Modes in Individual and Coupled Noble Metal Nanoparticles Using an Electron Beam”, Nano Lett. **9**, 399–404 (2009).

[51] A. L. Koh, K. Bao, I. Khan, W. E. Smith, G. Kothleitner, P. Nordlander, S. A. Maier, and D. W. McComb, “Electron Energy-Loss Spectroscopy (EELS) of Surface Plasmons in Single Silver Nanoparticles and Dimers: Influence of Beam Damage and Mapping of Dark Modes”, ACS Nano **3**, 3015–3022 (2009).

[52] R. Ruppin, “Optical Properties of a Plasma Sphere”, Phys. Rev. Lett. **31**, 1434–1437 (1973).

[53] J. A. Scholl, A. L. Koh, and J. A. Dionne, “Quantum plasmon resonances of individual metallic nanoparticles”, Nature **483**, 421–427 (2012).

[54] S. Raza, N. Stenger, S. Kadkhodazadeh, S. V. Fischer, N. Kostesha, A.-P. Jauho, A. Burrows, M. Wubs, and N. A. Mortensen, “Blueshift of the surface plasmon resonance in silver nanoparticles studied with EELS”, Nanophotonics **2**, 131–138 (2013).

[55] A. Campos, N. Troc, E. Cottancin, M. Pellarin, H.-C. Weissker, J. Lermé, M. Kociak, and M. Hillenkamp, “Plasmonic quantum size effects in silver nanoparticles are dominated by interfaces and local environments”, Nat. Phys. **15**, 275–280 (2019).

[56] I. Lindau and P. O. Nilsson, “Experimental Verification of Optically Excited Longitudinal Plasmons”, Phys. Scr. **3**, 87 (1971).

[57] T. Christensen, W. Yan, S. Raza, A.-P. Jauho, N. A. Mortensen, and M. Wubs, “Nonlocal Response of Metallic Nanospheres Probed by Light, Electrons, and Atoms”, ACS Nano **8**, 1745–1758 (2014).

[58] R. v. Baltz, M. P. Mensch, and H. Zohm, “Longitudinal electric response and loss-function of metallic microspheres and voids”, Z. Physic B - Condensed Matter **98**, 151–161 (1995).

[59] A. Rivacoba, “Electron spill-out effects in plasmon excitations by fast electrons”, Ultramicroscopy **207**, 112835 (2019).

[60] M. Brack, “The physics of simple metal clusters: self-consistent jellium model and semiclassical approaches”, Rev. Mod. Phys. **65**, 677 (1993).

[61] A. Borisov, D. Sánchez-Portal, R. D. M. no, and P. Echenique, “Building up the screening below the femtosecond scale”, Chem. Phys. Lett. **387**, 95–100 (2004).

[62] L. Novotny and B. Hecht, *Principles of Nano-Optics* (Cambridge University Press, 2012).

[63] N. A. Mortensen, "Mesoscopic electrodynamics at metal surfaces: — From quantum-corrected hydrodynamics to microscopic surface-response formalism", Nanophotonics **10**, 2563–2616 (2021).

[64] P. Drude, "Zur Elektronentheorie der Metalle", Ann. Phys. **306**, 566–613 (1900).

[65] N. W. Ashcroft and N. D. Mermin, *Solid State Physics* (HRW international editions, 1976).

[66] G. Toscano, *Semiclassical theory of nonclocal plasmonic excitation in metallic nanostructures*, Ph.D. thesis, Technical University of Denmark (2013).

[67] U. Muniain, *Quantum-mechanical study of optical excitations in nanoscale systems: first-principles description of plasmons, tunneling-induced light emission and ultrastrong light-matter interaction*, Ph.D. thesis, University of the Basque Country, UPV/EHU (2023).

[68] J. M. Pitarke, V. M. Silkin, E. V. Chulkov, and P. M. Echenique, "Theory of surface plasmons and surface-plasmon polaritons", Rep. Prog. Phys. **70**, 1 (2006).

[69] B. Hecht, H. Bielefeldt, L. Novotny, Y. Inouye, and D. W. Pohl, "Local Excitation, Scattering, and Interference of Surface Plasmons", Phys. Rev. Lett. **77**, 1889–1892 (1996).

[70] A. Otto, "Excitation of nonradiative surface plasma waves in silver by the method of frustrated total reflection", Z. Physik **216**, 398–410 (1968).

[71] E. Kretschmann and H. Raether, "Notizen: Radiative Decay of Non Radiative Surface Plasmons Excited by Light", Zeitschrift für Naturforschung A **23**, 2135–2136 (1968).

[72] Y.-Y. Teng and E. A. Stern, "Plasma Radiation from Metal Grating Surfaces", Phys. Rev. Lett. **19**, 511–514 (1967).

[73] G. Mie, "Beiträge zur Optik trüber Medien, speziell kolloidaler Metallösungen", Ann. Phys. **330**, 377–445 (1908).

[74] C. F. Bohren and D. R. Huffman, *Absorption and scattering of light by small particles* (John Wiley & Sons, 2008).

[75] V. Myroshnychenko, J. Rodríguez-Fernández, I. Pastoriza-Santos, A. M. Funston, C. Novo, P. Mulvaney, L. M. Liz-Marzán, and F. J. García de Abajo, "Modelling the optical response of gold nanoparticles", Chem. Soc. Rev. **37**, 1792–1805 (2008).

[76] R. C. Monreal, T. J. Antosiewicz, and S. P. Apell, "Competition between surface screening and size quantization for surface plasmons in nanoparticles", New J. Phys. **15**, 083044 (2013).

[77] P. A. D. Gonçalves, T. Christensen, N. Rivera, A.-P. Jauho, N. A. Mortensen, and M. Soljačić, "Plasmon–emitter interactions at the nanoscale", Nat Commun **11**, 366 (2020).

[78] L. Novotny and N. van Hulst, "Antennas for light", Nature Photon **5**, 83–90 (2011).

[79] E. Castanié, R. Vincent, R. Pierrat, and R. Carminati, "Absorption by an Optical Dipole Antenna in a Structured Environment", International Journal of Optics **2012**, 452047 (2012).

[80] J. J. Mock, M. Barbic, D. R. Smith, D. A. Schultz, and S. Schultz, "Shape effects in plasmon resonance of individual colloidal silver nanoparticles", J. Chem. Phys. **116**, 6755–6759 (2002).

[81] F. Hao, C. L. Nehl, J. H. Hafner, and P. Nordlander, "Plasmon Resonances of a Gold Nanostar", Nano Lett. **7**, 729–732 (2007).

[82] M. Pelton, J. Aizpurua, and G. Bryant, "Metal-nanoparticle plasmonics", Laser & Photon. Rev. **2**, 136–159 (2008).

[83] R. Vogelgesang and A. Dmitriev, "Real-space imaging of nanoplasmonic resonances", Analyst **135**, 1175–1181 (2010).

[84] A. Taflove and S. Hagness, *Computational electrodynamics: the finite-difference time-domain method. 2nd ed*, Vol. 67–106 (Artech House, 2000).

[85] M. S. Gockenbach, *Understanding and Implementing the Finite Element Method* (Society for Industrial and Applied Mathematics, Philadelphia, PA, 2006).

[86] B. T. Draine and P. J. Flatau, "Discrete-Dipole Approximation For Scattering Calculations", J. Opt. Soc. Am. A **11**, 1491–1499 (1994).

[87] F. J. García de Abajo and A. Howie, "Retarded field calculation of electron energy loss in inhomogeneous dielectrics", Phys. Rev. B **65**, 115418 (2002).

[88] U. Hohenester and A. Trügler, "MNPBEM – A Matlab toolbox for the simulation of plasmonic nanoparticles", Comput. Phys. Commun. **183**, 370–381 (2012).

[89] E. Prodan, C. Radloff, N. J. Halas, and P. Nordlander, "A Hybridization Model for the Plasmon Response of Complex Nanostructures", Science **302**, 419–422 (2003).

[90] P. Nordlander, C. Oubre, E. Prodan, K. Li, and M. I. Stockman, "Plasmon Hybridization in Nanoparticle Dimers", Nano Lett. **4**, 899–903 (2004).

[91] P. Mühlschlegel, H.-J. Eisler, O. J. F. Martin, B. Hecht, and D. W. Pohl, "Resonant Optical Antennas", Science **308**, 1607–1609 (2005).

[92] I. Romero, J. Aizpurua, G. W. Bryant, and F. J. G. de Abajo, "Plasmons in nearly touching metallic nanoparticles: singular response in the limit of touching dimers", Opt. Express **14**, 9988–9999 (2006).

[93] R. Alvarez-Puebla, L. M. Liz-Marzán, and F. J. García de Abajo, "Light Concentration at the Nanometer Scale", J. Phys. Chem. Lett. **1**, 2428–2434 (2010).

[94] O. Pérez-González, N. Zabala, A. G. Borisov, N. J. Halas, P. Nordlander, and J. Aizpurua, "Optical Spectroscopy of Conductive Junctions in Plasmonic Cavities", Nano Lett. **10**, 3090–3095 (2010).

[95] F. Benz, C. Tserkezis, L. O. Herrmann, B. de Nijs, A. Sanders, D. O. Sigle, L. Pukenas, S. D. Evans, J. Aizpurua, and J. J. Baumberg, "Nanooptics of Molecular-Shunted Plasmonic Nanojunctions", Nano Lett. **15**, 669–674 (2015).

[96] R. Esteban, A. G. Borisov, P. Nordlander, and J. Aizpurua, "Bridging quantum and classical plasmonics with a quantum-corrected model", Nat Commun **3**, 825 (2012).

[97] C. Ciracì and F. Della Sala, "Quantum hydrodynamic theory for plasmonics: Impact of the electron density tail", Phys. Rev. B **93**, 205405 (2016).

[98] P. Koval, M. Barbry, and D. Sánchez-Portal, "PySCF-NAO: An efficient and flexible implementation of linear response time-dependent density functional theory with numerical atomic orbitals", Comput. Phys. Commun. **236**, 188–204 (2019).

[99] T. P. Rossi, A. Zugarramurdi, M. J. Puska, and R. M. Nieminen, "Quantized Evolution of the Plasmonic Response in a Stretched Nanorod", Phys. Rev. Lett. **115**, 236804 (2015).

[100] M. Anderegg, B. Feuerbacher, and B. Fitton, "Optically Excited Longitudinal Plasmons in Potassium", Phys. Rev. Lett. **27**, 1565–1568 (1971).

[101] M. M. Özer, E. J. Moon, A. G. Eguiluz, and H. H. Weitering, "Plasmon Response of a Quantum-Confined Electron Gas Probed by Core-Level Photoemission", Phys. Rev. Lett. **106**, 197601 (2011).

[102] M. S. Sander, R. Gronsky, Y. M. Lin, and M. S. Dresselhaus, "Plasmon excitation modes in nanowire arrays", J. Appl. Phys. **89**, 2733–2736 (2001).

[103] T. Hanrath and B. A. Korgel, "A Comprehensive Study of Electron Energy Losses in Ge Nanowires", Nano Lett. **4**, 1455–1461 (2004).

[104] Y. W. Wang, J. S. Kim, G. H. Kim, and K. S. Kim, "Quantum size effects in the volume plasmon excitation of bismuth nanoparticles investigated by electron energy loss spectroscopy", Appl. Phys. Lett. **88**, 143106 (2006).

[105] R. Borja-Urby, S. P. Paredes-Carrera, H. Viltres-Cobas, P. Santiago-Jacinto, F. Paraguay-Delgado, G. Herrera-Pérez, L. Rendón-Vázquez, J. C. Sánchez-Ochoa, and D. Morales-Cruz, “Confined volume plasmon spatial distribution by low-loss EELS on self-assemble bismuth nanoparticles”, J. Electron Spectrosc. Relat. Phenom. **237**, 146891 (2019).

[106] R. G. Hobbs, V. R. Manfrinato, Y. Yang, S. A. Goodman, L. Zhang, E. A. Stach, and K. K. Berggren, “High-Energy Surface and Volume Plasmons in Nanopatterned Sub-10 nm Aluminum Nanostructures”, Nano Lett. **16**, 4149–4157 (2016).

[107] J. L. Gervasoni and N. R. Arista, “Plasmon excitations in cylindrical wires by external charged particles”, Phys. Rev. B **68**, 235302 (2003).

[108] S. Segui, J. Gervasoni, and N. Arista, “Impact parameter dependence of plasmon excitations in cylindrical nanostructures”, Nucl. Instrum. Methods Phys. Res. B **233**, 227–231 (2005).

[109] J. Aizpurua and A. Rivacoba, “Nonlocal effects in the plasmons of nanowires and nanocavities excited by fast electron beams”, Phys. Rev. B **78**, 035404 (2008).

[110] S. Raza, G. Toscano, A.-P. Jauho, M. Wubs, and N. A. Mortensen, “Unusual resonances in nanoplasmonic structures due to nonlocal response”, Phys. Rev. B **84**, 121412 (2011).

[111] J. M. Soler, E. Artacho, J. D. Gale, A. García, J. Junquera, P. Ordejón, and D. Sánchez-Portal, “The SIESTA method for ab initio order-N materials simulation”, J. Phys.: Condens. Matter **14**, 2745 (2002).

[112] B. H. Stuart, *Infrared Spectroscopy: Fundamentals and Applications* (Wiley, 2004).

[113] C. V. Raman and K. S. Krishnan, “A New Type of Secondary Radiation”, Nature **121**, 501–502 (1928).

[114] E. Condon, “A Theory of Intensity Distribution in Band Systems”, Phys. Rev. **28**, 1182–1201 (1926).

[115] W. E. Moerner and D. P. Fromm, “Methods of single-molecule fluorescence spectroscopy and microscopy”, Rev. Sci. Instrum. **74**, 3597–3619 (2003).

[116] D. A. Wheeler and J. Z. Zhang, “Exciton Dynamics in Semiconductor Nanocrystals”, Adv. Mater. **25**, 2878–2896 (2013).

[117] G. Zengin, M. Wersäll, S. Nilsson, T. J. Antosiewicz, M. Käll, and T. Shegai, “Realizing Strong Light-Matter Interactions between Single-Nanoparticle Plasmons and Molecular Excitons at Ambient Conditions”, Phys. Rev. Lett. **114**, 157401 (2015).

[118] R. Chikkaraddy, B. de Nijs, F. Benz, S. J. Barrow, O. A. Scherman, E. Rosta, A. Demetriadou, P. Fox, O. Hess, and J. J. Baumberg, "Single-molecule strong coupling at room temperature in plasmonic nanocavities", Nature **535**, 127–130 (2016).

[119] J. M. Winkler, F. T. Rabouw, A. A. Rossinelli, S. V. Jayanti, K. M. McPeak, D. K. Kim, B. le Feber, F. Prins, and D. J. Norris, "Room-Temperature Strong Coupling of CdSe Nanoplatelets and Plasmonic Hole Arrays", Nano Lett. **19**, 108–115 (2019).

[120] L. Novotny, "Strong coupling, energy splitting, and level crossings: A classical perspective", Am. J. Phys. **78**, 1199–1202 (2010).

[121] X. Wu, S. K. Gray, and M. Pelton, "Quantum-dot-induced transparency in a nanoscale plasmonic resonator", Opt. Express **18**, 23633–23645 (2010).

[122] R. Esteban, J. Aizpurua, and G. W. Bryant, "Strong coupling of single emitters interacting with phononic infrared antennae", New J. Phys. **16**, 013052 (2014).

[123] E. Waks and J. Vuckovic, "Dipole Induced Transparency in Drop-Filter Cavity-Waveguide Systems", Phys. Rev. Lett. **96**, 153601 (2006).

[124] N. Liu, L. Langguth, T. Weiss, J. Kästel, M. Fleischhauer, T. Pfau, and H. Giessen, "Plasmonic analogue of electromagnetically induced transparency at the Drude damping limit", Nature Mater **8**, 758–762 (2009).

[125] M. Barra-Burillo, U. Muniain, S. Catalano, M. Autore, F. Casanova, L. E. Hueso, J. Aizpurua, R. Esteban, and R. Hillenbrand, "Microcavity phonon polaritons from the weak to the ultrastrong phonon–photon coupling regime", Nat Commun **12**, 6206 (2021).

[126] A. C. Ferrari and D. M. Basko, "Raman spectroscopy as a versatile tool for studying the properties of graphene", Nature Nanotech **8**, 235–246 (2013).

[127] T. Vankeirsbilck, A. Vercauteren, W. Baeyens, G. V. der Weken, F. Verpoort, G. Vergote, and J. Remon, "Applications of Raman spectroscopy in pharmaceutical analysis", TrAC Trends Anal. Chem. **21**, 869–877 (2002).

[128] L.-P. Choo-Smith, H. G. M. Edwards, H. P. Endtz, J. M. Kros, F. Heule, H. Barr, J. S. Robinson Jr., H. A. Bruining, and G. J. Puppels, "Medical applications of Raman spectroscopy: From proof of principle to clinical implementation", Biopolymers **67**, 1–9 (2002).

[129] A. Candeias and J. M. Madariaga, "Applications of Raman spectroscopy in art and archaeology", J Raman Spectrosc. **50**, 137–142 (2019).

[130] R. L. McCreery, *Raman Spectroscopy for Chemical Analysis* (John Wiley & Sons, 2000).

[131] L. A. Nafie, “Recent advances in linear and nonlinear Raman spectroscopy. Part VI”, J Raman Spectrosc. **43**, 1845–1863 (2012).

[132] M. J. Frisch *et al.*, “Gaussian 16 Revision B.01”, (2016), gaussian Inc. Wallingford CT.

[133] R. A. Boto, R. Esteban, B. Candelas, and J. Aizpurua, “Theoretical Procedure for Precise Evaluation of Chemical Enhancement in Molecular Surface-Enhanced Raman Scattering”, J. Phys. Chem. C **128**, 18293–18304 (2024).

[134] E. C. Le Ru and P. G. Etchegoin, *Principles of Surface-Enhanced Raman Spectroscopy* (Elsevier, 2009).

[135] Y. Zhang, B. Yang, A. Ghafoor, Y. Zhang, Y.-F. Zhang, R.-P. Wang, J.-L. Yang, Y. Luo, Z.-C. Dong, and J. G. Hou, “Visually constructing the chemical structure of a single molecule by scanning Raman picoscopy”, National Science Review **6**, 1169–1175 (2019).

[136] Y. Kumamoto, Y. Harada, T. Takamatsu, and H. Tanaka, “Label-free Molecular Imaging and Analysis by Raman Spectroscopy”, ACTA HISTOCHEMICA ET CYTOCHEMICA **51**, 101–110 (2018).

[137] M. Fleischmann, P. Hendra, and A. McQuillan, “Raman spectra of pyridine adsorbed at a silver electrode”, Chem. Phys. Lett. **26**, 163–166 (1974).

[138] A. S. D. S. Indrasekara and L. Fabris, “Sers-Based Approaches Toward Genetic Profiling”, Bioanalysis **7**, 263–278 (2015).

[139] Y. Zhang, X. Mi, X. Tan, and R. Xiang, “Recent Progress on Liquid Biopsy Analysis using Surface-Enhanced Raman Spectroscopy”, Theranostics **9**, 491–525 (2019).

[140] W. Ma, M. Sun, L. Xu, L. Wang, H. Kuang, and C. Xu, “A SERS active gold nanostar dimer for mercury ion detection”, Chem. Commun. **49**, 4989–4991 (2013).

[141] V. M. Szlag, R. S. Rodriguez, J. He, N. Hudson-Smith, H. Kang, N. Le, T. M. Reineke, and C. L. Haynes, “Molecular Affinity Agents for Intrinsic Surface-Enhanced Raman Scattering (SERS) Sensors”, ACS Appl. Mater. Interfaces **10**, 31825–31844 (2018).

[142] E. Bailo and V. Deckert, “Tip-enhanced Raman scattering”, Chem. Soc. Rev. **37**, 921–930 (2008).

[143] B. Küstner, M. Gellner, M. Schütz, F. Schöppler, A. Marx, P. Ströbel, P. Adam, C. Schmuck, and S. Schlücker, “SERS Labels for Red Laser Excitation: Silica-Encapsulated SAMs on Tunable Gold/Silver Nanoshells”, Angew. Chem. Int. Ed. **48**, 1950–1953 (2009).

[144] S. Barbosa, A. Agrawal, L. Rodríguez-Lorenzo, I. Pastoriza-Santos, R. A. Alvarez-Puebla, A. Kornowski, H. Weller, and L. M. Liz-Marzán, "Tuning Size and Sensing Properties in Colloidal Gold Nanostars", Langmuir **26**, 14943–14950 (2010).

[145] L. Polavarapu, A. L. Porta, S. M. Novikov, M. Coronado-Puchau, and L. M. Liz-Marzán, "Pen-on-Paper Approach Toward the Design of Universal Surface Enhanced Raman Scattering Substrates", Small **10**, 3065–3071 (2014).

[146] E. Ruska, "The development of the electron microscope and of electron microscopy", Rev. Mod. Phys. **59**, 627–638 (1987).

[147] M. Haider, S. Uhlemann, E. Schwan, H. Rose, B. Kabius, and K. Urban, "Electron microscopy image enhanced", Nature **392**, 768–769 (1998).

[148] P. Hawkes, "The correction of electron lens aberrations", Ultramicroscopy **156**, A1–A64 (2015).

[149] O. L. Krivanek, M. F. Chisholm, V. Nicolosi, T. J. Pennycook, G. J. Corbin, N. Bellby, M. F. Murfitt, C. S. Own, Z. S. Szilagyi, M. P. Oxley, S. T. Pntelides, and Pennycook, "Atom-by-atom structural and chemical analysis by annular dark-field electron microscopy", Nature **464**, 571–574 (2010).

[150] R. F. Egerton, *Electron Energy-Loss Spectroscopy in the Electron Microscope* (Springer New York, NY, 2011).

[151] O. L. Krivanek, T. C. Lovejoy, N. Dellby, T. Aoki, R. W. Carpenter, P. Rez, E. Soignard, J. Zhu, P. E. Batson, M. J. Lagos, R. F. Egerton, and P. A. Crozier, "Vibrational spectroscopy in the electron microscope", Nature **514**, 209–212 (2014).

[152] R. G. Ricarte, T. P. Lodge, and M. A. Hillmyer, "Nanoscale Concentration Quantification of Pharmaceutical Actives in Amorphous Polymer Matrices by Electron Energy-Loss Spectroscopy", Langmuir **32**, 7411–7419 (2016).

[153] Y. Wu, G. Li, and J. P. Camden, "Probing Nanoparticle Plasmons with Electron Energy Loss Spectroscopy", Chem. Rev. **118**, 2994–3031 (2018).

[154] N. Browning, M. Chisholm, and S. Pennycook, "Atomic-resolution chemical analysis using a scanning transmission electron microscope", Nature **366**, 143–146 (1993).

[155] P. Batson, "Simultaneous STEM imaging and electron energy-loss spectroscopy with atomic-column sensitivity", Nature **366**, 727–728 (1993).

[156] D. Pines, "Collective Energy Losses in Solids", Rev. Mod. Phys. **28**, 184–198 (1956).

[157] R. H. Ritchie, "Plasma Losses by Fast Electrons in Thin Films", Phys. Rev. **106**, 874–881 (1957).

[158] X. Ke, C. Bittencourt, and G. V. Tendeloo, “Possibilities and limitations of advanced transmission electron microscopy for carbon-based nanomaterials”, Beilstein J. Nanotechnol. **6**, 1541–1557 (2015).

[159] M. J. Lagos, A. Trügler, U. Hohenester, and P. E. Batson, “Mapping vibrational surface and bulk modes in a single nanocube”, Nature **543**, 529–539 (2017).

[160] A. A. Govyadinov, A. Konečná, A. Chuvilin, S. Vélez, I. Dolado, A. Y. Nikitin, S. Lopatin, F. Casanova, L. E. Hueso, J. Aizpurua, and R. Hillenbrand, “Probing low-energy hyperbolic polaritons in van der Waals crystals with an electron microscope”, Nat Commun **8**, 95 (2017).

[161] P. M. Zeiger and J. Rusz, “Efficient and Versatile Model for Vibrational STEM-EELS”, Phys. Rev. Lett. **124**, 025501 (2020).

[162] P. Rez, K. Aoki, Toshihiro adn March, D. Gur, o. L. Krivanek, N. Dellby, T. C. Lovejoy, S. G. Wolf, and H. Cohen, “Damage-free vibrational spectroscopy of biological materials in the electron microscope”, Nat Commun **7**, 10945 (2016).

[163] J. A. Hachtel, J. Huang, I. Popovs, S. Jansone-Popova, J. K. Keum, J. Jakowski, T. C. Lovejoy, N. Dellby, O. L. Krivanek, and J. C. Idrobo, “Identification of site-specific isotopic labels by vibrational spectroscopy in the electron microscope”, Science **363**, 525–528 (2019).

[164] N. Jiang, D. Su, J. C. Spence, S. Zhou, and J. Qiu, “Volume plasmon of bismuth nanoparticles”, Solid State Commun. **149**, 111–114 (2009).

[165] S. Raza, S. Kadkhodazadeh, T. Christensen, M. D. Vece, M. Wubs, N. A. Mortensen, and N. Stenger, “Quantum plasmon resonances of individual metallic nanoparticles”, Nat Commun **6**, 8788 (2015).

[166] F. J. García de Abajo, “Optical excitations in electron microscopy”, Rev. Mod. Phys. **82**, 209–275 (2010).

[167] D. E. Gómez, Z. Q. Teo, M. Altissimo, T. J. Davis, S. Earl, and A. Roberts, “The Dark Side of Plasmonics”, Nano Lett. **13**, 3722–3728 (2013).

[168] F. Hao, E. M. Larsson, T. A. Ali, D. S. Sutherland, and P. Nordlander, “Shedding light on dark plasmons in gold nanorings”, Chem. Phys. Lett. **458**, 262–266 (2008).

[169] L. Stella, P. Zhang, F. J. García-Vidal, A. Rubio, and P. García-González, “Performance of Nonlocal Optics When Applied to Plasmonic Nanostructures”, J. Phys. Chem. C **117**, 8941–8949 (2013).

[170] U. Hohenester, *Nano and Quantum Optics* (Springer Cham, 2019).

[171] M. Schmeits, “Inelastic scattering of fast electrons by spherical surfaces”, J. Phys. C: Solid State Phys. **14**, 1203 (1981).

[172] T. L. Ferrell and P. M. Echenique, “Generation of Surface Excitations on Dielectric Spheres by an External Electron Beam”, Phys. Rev. Lett. **55**, 1526–1529 (1985).

[173] M. Todorović, M. U. Gutmann, J. Corander, and P. Rinke, “Bayesian inference of atomistic structure in functional materials”, npj Comput Mater **5**, 35 (2019).

[174] C. Cohen-Tannoudji, B. Diu, and F. Laloë, *Quantum Mechanics, Volume 1: Basic Concepts, Tools, and Applications* (Wiley, 2019).

[175] M. Born and R. Oppenheimer, “Zur Quantentheorie der Molekeln”, Annalen der Physik **389**, 457–484 (1927).

[176] P. Hohenberg and W. Kohn, “Inhomogeneous Electron Gas”, Phys. Rev. **136**, B864–B871 (1964).

[177] W. Kohn and L. J. Sham, “Self-Consistent Equations Including Exchange and Correlation Effects”, Phys. Rev. **140**, A1133–A1138 (1965).

[178] R. O. Jones and O. Gunnarsson, “The density functional formalism, its applications and prospects”, Rev. Mod. Phys. **61**, 689–746 (1989).

[179] K. Burke, “Perspective on density functional theory”, J. Chem. Phys. **136**, 150901 (2012).

[180] J. P. Perdew and A. Zunger, “Self-interaction correction to density-functional approximations for many-electron systems”, Phys. Rev. B **23**, 5048–5079 (1981).

[181] J. P. Perdew, K. Burke, and M. Ernzerhof, “Generalized Gradient Approximation Made Simple”, Phys. Rev. Lett. **77**, 3865–3868 (1996).

[182] Z. Wu and R. E. Cohen, “More accurate generalized gradient approximation for solids”, Phys. Rev. B **73**, 235116 (2006).

[183] S. Grimme, “Semiempirical GGA-type density functional constructed with a long-range dispersion correction”, J. Comput. Chem. **27**, 1787–1799 (2006).

[184] J. C. Phillips and L. Kleinman, “New Method for Calculating Wave Functions in Crystals and Molecules”, Phys. Rev. **116**, 287–294 (1959).

[185] P. E. Blöchl, “Projector augmented-wave method”, Phys. Rev. B **50**, 17953–17979 (1994).

[186] A. García *et al.*, “Siesta: Recent developments and applications”, J. Chem. Phys. **152**, 204108 (2020).

[187] J. Enkovaara *et al.*, “Electronic structure calculations with GPAW: a real-space implementation of the projector augmented-wave method”, J. Phys.: Condens. Matter **22**, 253202 (2010).

[188] J. J. Mortensen *et al.*, “GPAW: An open Python package for electronic structure calculations”, J. Chem. Phys. **160**, 092503 (2024).

[189] E. Runge and E. K. U. Gross, “Density-Functional Theory for Time-Dependent Systems”, Phys. Rev. Lett. **52**, 997–1000 (1984).

[190] P. Elliott, F. Furche, and K. Burke, “Excited States from Time-Dependent Density Functional Theory”, in *Reviews in Computational Chemistry* (John Wiley & Sons, Ltd, 2008) Chap. 3, pp. 91–165.

[191] M. A. Marques, N. T. Maitra, F. M. Nogueira, E. Gross, and A. Rubio, eds., *Fundamentals of Time-Dependent Density Functional Theory* (Springer Berlin, Heidelberg, 2012).

[192] M. Petersilka, U. J. Gossmann, and E. K. U. Gross, “Excitation Energies from Time-Dependent Density-Functional Theory”, Phys. Rev. Lett. **76**, 1212–1215 (1996).

[193] P. Koval, F. Marchesin, D. Foerster, and D. Sánchez-Portal, “Optical response of silver clusters and their hollow shells from linear-response TDDFT”, J. Phys.: Condens. Matter **28**, 214001 (2016).

[194] M. Urbieta, M. Barbry, P. Koval, A. Rivacoba, D. Sánchez-Portal, J. Aizpurua, and N. Zabala, “Footprints of atomic-scale features in plasmonic nanoparticles as revealed by electron energy loss spectroscopy”, Phys. Chem. Chem. Phys. **26**, 14991–15004 (2024).

[195] D. Foerster, “Elimination, in electronic structure calculations, of redundant orbital products”, J. Chem. Phys. **128**, 034108 (2008).

[196] P. Koval, D. Foerster, and O. Coulaud, “A Parallel Iterative Method for Computing Molecular Absorption Spectra”, J. Chem. Theory Comput. **6**, 2654–2668 (2010).

[197] A. Taghizadeh, U. Leffers, T. G. Pederson, and K. S. Thygesen, “A library of ab initio Raman spectra for automated identification of 2D materials”, Nat Commun **11**, 3011 (2020).

[198] H. J. Monkhorst and J. D. Pack, “Special points for Brillouin-zone integrations”, Phys. Rev. B **13**, 5188–5192 (1976).

[199] E. Merzbacher, *Quantum Mechanics* (Wiley, 1998).

[200] U. Aseginolaza, *Anharmonic Effects in Thermoelectric and 2D Materials*, Ph.D. thesis, University of the Basque Country, UPV/EHU (2020).

[201] F. Giustino, “Electron-phonon interactions from first principles”, Rev. Mod. Phys. **89**, 015003 (2017).

[202] R. Saito, M. Hofmann, G. Dresselhaus, A. Jorio, and M. S. Dresselhaus, “Raman spectroscopy of graphene and carbon nanotubes”, Advances in Physics **60**, 413–550 (2011).

[203] J. Mattiat and S. Luber, “Comparison of Length, Velocity, and Symmetric Gauges for the Calculation of Absorption and Electric Circular Dichroism Spectra with Real-Time Time-Dependent Density Functional Theory”, J. Chem. Theory Comput. **18**, 5513–5526 (2022).

[204] A. Taghizadeh, F. Hipolito, and T. G. Pedersen, “Linear and nonlinear optical response of crystals using length and velocity gauges: Effect of basis truncation”, Phys. Rev. B **96**, 195413 (2017).

[205] Y. Gillet, M. Giantomassi, and X. Gonze, “First-principles study of excitonic effects in Raman intensities”, Phys. Rev. B **88**, 094305 (2013).

[206] G. Grosso and G. P. Parravicini, *Solid State Physics* (Academic Press, 2000).

[207] P. Y. Yu and M. Cardona, *Fundamentals of Semiconductors* (Springer Berlin, Heidelberg, 2010).

[208] D. Alfè, “PHON: A program to calculate phonons using the small displacement method”, Comput. Phys. Commun. **180**, 2622–2633 (2009), 40 YEARS OF CPC: A celebratory issue focused on quality software for high performance, grid and novel computing architectures.

[209] A. H. Larsen *et al.*, “The atomic simulation environment–a Python library for working with atoms”, J. Phys.: Condens. Matter **29**, 273002 (2017).

[210] K. Kaasbjerg, K. S. Thygesen, and K. W. Jacobsen, “Phonon-limited mobility in n-type single-layer MoS_2 from first principles”, Phys. Rev. B **85**, 115317 (2012).

[211] R. Garnett, *Bayesian Optimization* (Cambridge University Press, 2023).

[212] M. U. Gutmann and J. Corander, “Bayesian Optimization for Likelihood-Free Inference of Simulator-Based Statistical Models”, J. Mach. Learn. Res. **17**, 1–47 (2016).

[213] C. E. Rasmussen and C. K. I. Williams, *Gaussian Processes for Machine Learning* (The MIT Press, 2006).

[214] J. Schachenmayer, C. Genes, E. Tignone, and G. Pupillo, “Cavity-Enhanced Transport of Excitons”, Phys. Rev. Lett. **114**, 196403 (2015).

[215] P. Anger, P. Bharadwaj, and L. Novotny, “Enhancement and Quenching of Single-Molecule Fluorescence”, Phys. Rev. Lett. **96**, 113002 (2006).

[216] T. Neuman, R. Esteban, D. Casanova, F. J. Carcía-Vidal, and J. Aizpurua, "Coupling of Molecular Emitters and Plasmonic Cavities beyond the Point-Dipole Approximation", Nano Lett. **18**, 2358–2364 (2018).

[217] Y. Zhang, Z. C. Dong, and J. Aizpurua, "Influence of the Chemical Structure on Molecular Light Emission in Strongly Localized Plasmonic Fields", J. Phys. Chem. C **124**, 4674–4683 (2020).

[218] G. Toscano, J. Strauble, A. Kwiatkowski, C. Rockstuhl, F. Evers, H. Xu, N. A. Mortensen, and M. Wubs, "Resonance shifts and spill-out effects in self-consistent hydrodinamic nanoplasmonics", Nat Commun **6**, 7132 (2015).

[219] T. V. Teperik, P. Nordlander, J. Aizpurua, and A. G. Borisov, "Robust Subnanometric Plasmon Ruler by Rescaling of the Nonlocal Optical Response", Phys. Rev. Lett. **110**, 263901 (2013).

[220] A. Babaze, E. Ogando, P. E. Stamatopoulou, C. Tserkezis, N. A. Mortensen, J. Aizpurua, A. G. Borisov, and R. Esteban, "Quantum surface effects in the electromagnetic coupling between a quantum emitter and a plasmonic nanoantenna: time-dependent density functional theory vs. semiclassical Feibelman approach", Opt. Express **30**, 21159–21183 (2022).

[221] D. C. Marinica, A. K. Kazansky, P. Nordlander, J. Aizpurua, and A. G. Borisov, "Quantum Plasmonics: Nonlinear Effects in the Field Enhancement of a Plasmonic Nanoparticle Dimer", Nano Lett. **12**, 1333–1339 (2012).

[222] M. Sánchez-Barquilla, A. I. Fernández-Domínguez, J. Feist, and F. J. García-Vidal, "A Theoretical Perspective on Molecular Polaritonics", ACS Photonics **9**, 1830–1841 (2022).

[223] M. Ruggentahler, D. Sidler, and A. Rubio, "Understanding Polaritonic Chemistry from Ab Initio Quantum Electrodynamics", Chem. Rev. **123**, 11191–11229 (2023).

[224] G. Parolin, N. Peruffo, F. Mancin, E. Collini, and S. Corni, "Molecularly Detailed View of Strong Coupling in Supramolecular Plexcitonic Nanohybrids", Nano Lett. **24**, 2273–2281 (2024).

[225] P. Zhang, J. Feist, A. Rubio, P. García-González, and F. J. García-Vidal, "Ab initio nanoplasmonics: The impact of atomic structure", Phys. Rev. B **90**, 161407 (2014).

[226] P. Song, P. Nordlander, and S. Gao, "Quantum mechanical study of the coupling of plasmon excitations to atomic-scale electron transport", J. Chem. Phys. **134**, 074701 (2011).

[227] V. Kulkarni and A. Manjavacas, "Quantum Effects in Charge Transfer Plasmons", ACS Photonics **2**, 987–992 (2015).

[228] A. S. Fedorov, M. A. Visotin, A. V. Lukyanenko, V. S. Gerasimov, and A. S. Aleksandrovsky, “Intense charge transfer plasmons in golden nanoparticle dimers connected by conductive molecular linkers”, J. Chem. Phys. **160**, 084110 (2024).

[229] S. Corni and J. Tomasi, “Theoretical evaluaion of Raman spectra and enhancement factors for a molecule adsorbed on a complex-shaped metal particle”, Chem. Phys. Lett. **342**, 135–140 (2001).

[230] K. Kluczyk-Korch and T. J. Antosiewicz, “Hot carrier generation in a strongly coupled molecule-plasmonic nanoparticle system”, Nanophotonics **12**, 1711–1722 (2023).

[231] A. Babaze, R. Esteban, A. G. Borisov, and J. Aizpurua, “Electronic Exciton–Plasmon Coupling in a Nanocavity Beyond the Electromagnetic Interaction Picture”, Nano Lett. **21**, 8466–8473 (2021).

[232] A. Varas, P. García-González, F. J. García-Vidal, and A. Rubio, “Anisotropy Effects on the Plasmonic Response of Nanoparticle Dimers”, J. Phys. Chem. Lett. **6**, 1891–1898 (2015).

[233] J. P. K. Doye and D. J. Wales, “Global minima for transition metal clusters described by Sutton–Chen potentials”, New J. Chem. **22**, 733–744 (1998).

[234] Y. He and T. Zeng, “First-Principles Study and Model of Dielectric Functions of Silver Nanoparticles”, J. Phys. Chem. C **114**, 18023–18030 (2010).

[235] F. Tran, R. Laskowski, P. Blaha, and K. Schwarz, “Performance on molecules, surfaces, and solids of the Wu-Cohen GGA exchange-correlation energy functional”, Phys. Rev. B **75**, 115131 (2007).

[236] A. Liebsch, “Surface-plasmon dispersion and size dependence of Mie resonance: Silver versus simple metals”, Phys. Rev. B **48**, 11317–11328 (1993).

[237] K.-P. Charlé, L. König, S. Nepijko, I. Rabin, and W. Schulze, “The Surface Plasmon Resonance of Free and Embedded Ag-Clusters in the Size Range 1,5 nm $< D <$ 30 nm”, Cryst. Res. Technol. **33**, 1085–1096 (1998).

[238] S. Singh, A. Aggarwal, N. V. S. D. K. Bhupathiraju, G. Arianna, K. Tiwari, and C. M. Drain, “Glycosylated Porphyrins, Phthalocyanines, and Other Porphyrinoids for Diagnostics and Therapeutics”, Chem. Rev. **115**, 10261–10306 (2015).

[239] A. R. Sekhar, Y. Chitose, J. Janoš, S. I. Dangoor, A. Ramundo, R. Satchi-Fainaro, P. Slavíček, P. Klán, and R. Weinstain, “Porphyrin as a versatile visible-light-activatable organic/metal hybrid photoremovable protecting group”, Nat Commun **13**, 3614 (2022).

[240] D. C. Marinica, H. Luorenço-Martins, J. Aizpurua, and A. G. Borisov, "Plexciton Quenching by Resonant Electron Transfer from Quantum Emitter to Metallic Nanoantenna", Nano Lett. **13**, 5972—5978 (2013).

[241] P. Garcia-Gonzalez, A. Varas, F. J. Garcia-Vidal, and A. Rubio, "Single-atom control of the optoelectronic response in sub-nanometric cavities", arXiv , 1903.08443 (2019).

[242] W. E. Pickett, S. C. Erwin, and E. C. Ethridge, "Reformulation of the LDA+U method for a local-orbital basis", Phys. Rev. B **58**, 1201 (1998).

[243] M. Cococcioni and S. de Gironcoli, "Linear response approach to the calculation of the effective interaction parameters in the LDA+U method", Phys. Rev. B **71**, 035105 (2005).

[244] S. F. Tan, L. Wu, J. K. Yang, P. Bai, M. Bosman, and C. A. Nijhuis, "Quantum Plasmon Resonances Controlled by Molecular Tunnel Junctions", Science **343**, 1496–1499 (2014).

[245] M. Mecklenburg, W. A. Hubbard, E. R. White, R. Dhall, S. B. Cronin, S. Aloni, and B. C. Regan, "Nanoscale temperature mapping in operating microelectronic devices", Science **347**, 629–632 (2015).

[246] M. Mecklenburg, B. Zutter, and B. C. Regan, "Thermometry of Silicon Nanoparticles", Phys. Rev. Appl. **9**, 014005 (2018).

[247] C. Wang, W.-C. D. Yang, D. Raciti, A. Bruma, R. Marx, A. Agrawal, and R. Sharma, "Endothermic reaction at room temperature enabled by deep-ultraviolet plasmons", Nat. Mater. **20**, 346–352 (2021).

[248] P. E. Stamatopoulou, W. Zhao, A. Rodríguez Echarri, N. A. Mortensen, K. Busch, C. Tserkezis, and C. Wolff, "Electron beams traversing spherical nanoparticles: Analytic and numerical treatment", Phys. Rev. Res. **6**, 013239 (2024).

[249] B. Candelas, N. Zabala, P. Koval, A. Babaze, D. Sánchez-Portal, and J. Aizpurua, "Influence of atomistic features in plasmon–exciton coupling and charge transfer driven by a single molecule in a metallic nanocavity", J. Chem. Phys. **161**, 044707 (2024).

[250] R. C. Monreal, S. P. Apell, and T. J. Antosiewicz, "Quantum-size effects in visible defect photoluminescence of colloidal ZnO quantum dots: a theoretical analysis", Nanoscale **10**, 7016–7025 (2018).

[251] A. Liebsch, *Electronic excitations at metal surfaces* (Springer Science & Business Media, 2013).

[252] E. G. Noya, J. Doye, and D. Wales, "Geometric magic numbers of sodium clusters: Interpretation of the melting behaviour", Eur. Phys. J. D **43**, 57–60 (2007).

[253] C. Yannouleas, E. Vigezzi, and R. A. Broglia, “Evolution of the optical properties of alkali-metal microclusters towards the bulk: The matrix random-phase-approximation description”, Phys. Rev. B **47**, 9849–9861 (1993).

[254] T. P. Rossi, M. Kuisma, M. J. Puska, R. M. Nieminen, and P. Erhart, “Kohn–Sham Decomposition in Real-Time Time-Dependent Density-Functional Theory: An Efficient Tool for Analyzing Plasmonic Excitations”, J. Chem. Theory and Comput. **13**, 4779–4790 (2017).

[255] A. J. Bennett, “Influence of the Electron Charge Distribution on Surface-Plasmon Dispersion”, Phys. Rev. B **1**, 203 (1970).

[256] K.-D. Tsuei, E. W. Plummer, A. Liebsch, K. Kempa, and P. Bakshi, “Multipole plasmon modes at a metal surface”, Phys. Rev. Lett. **64**, 44–47 (1990).

[257] W. Yan, “Hydrodynamic theory for quantum plasmonics: Linear-response dynamics of the inhomogeneous electron gas”, Phys. Rev. B **91**, 115416 (2015).

[258] E. Artacho, D. Sánchez-Portal, P. Ordejón, A. García, and J. M. Soler, “Linear-Scaling ab-initio Calculations for Large and Complex Systems”, phys. stat. sol. (b) **215**, 809–817 (1999).

[259] M. Urbieta, *Theoretical approach to atomic-scale nanoplasmonics as probed by light and swift electrons*, Ph.D. thesis, University of the Basque Country, UPV/EHU, Spain (2021).

[260] A. Borisov, J. Gauyacq, and S. Shabanov, “Wave packet propagation study of the charge transfer interaction in the F–Cu(111) and –Ag(111) systems”, Surface Sci. **487**, 243–257 (2001).

[261] M. Zapata Herrera, J. Aizpurua, A. K. Kazansky, and A. G. Borisov, “Plasmon Response and Electron Dynamics in Charged Metallic Nanoparticles”, Langmuir **32**, 2829–2840 (2016).

[262] C. Noguez, “Surface Plasmons in Metal Nanoparticles: The Influence of Shape and Physical Environment”, J. Phys. Chem. C **111**, 3806–3819 (2007).

[263] L. Stella, P. Zhang, F. J. García-Vidal, A. Rubio, and P. García-González, “Performance of Nonlocal Optics When Applied to Plasmonic Nanostructures”, J. Phys. Chem. C **117**, 8941–8949 (2013).

[264] S. Casalini, C. A. Bortolotti, F. Leonardi, and F. Biscarini, “Self-assembled monolayers in organic electronics”, Chem. Soc. Rev. **46**, 40–71 (2017).

[265] D. Kos, G. D. Martino, A. Boehmke, B. de Nijs, D. Berta, T. Földes, S. Sangtarash, E. Rosta, H. Sadeghi, and J. J. Baumberg, “Optical probes of molecules as nano-mechanical switches”, Nat Commun **11**, 5905 (2020).

[266] H. Chen and J. F. Stoddart, “From molecular to supramolecular electronics”, Nat Rev Mater **6**, 804–828 (2021).

[267] J. Rickert, T. Weiss, and W. Göpel, “Self-assembled monolayers for chemical sensors: molecular recognition by immobilized supramolecular structure”, Sens. Actuators, B **31**, 45–50 (1996), materials for Sensors: Functional Nanoscaled Structures of the 1995 E-MRS Spring Conference.

[268] Y. Wang, Y. Zhou, J. Sokolov, B. Rigas, K. Levon, and M. Rafailovich, “A potentiometric protein sensor built with surface molecular imprinting method”, Biosens. Bioelectron. **24**, 162–166 (2008).

[269] D. Mandler and S. Kraus-Ophir, “Self-assembled monolayers (SAMs) for electrochemical sensing”, J Solid State Electrochem **15**, 1535–1558 (2011).

[270] G. Pieters and L. J. Prins, “Catalytic self-assembled monolayers on gold nanoparticles”, New J. Chem. **36**, 1931–1939 (2012).

[271] C. A. Schoenbaum, D. K. Schwartz, and J. W. Medlin, “Controlling the Surface Environment of Heterogeneous Catalysts using Self-Assembled Monolayers”, Acc. Chem. Res. **47**, 1438–1445 (2014).

[272] J. A. Mennel, H. Pan, S. W. Palladino, and C. J. Barile, “Electrocatalytic CO2 Reduction by Self-Assembled Monolayers of Metal Porphyrins”, J. Phys. Chem. C **124**, 19716–19724 (2020).

[273] S. Frey, V. Stadler, K. Heister, W. Eck, M. Zharnikov, M. Grunze, B. Zeysing, and A. Terfort, “Structure of Thioaromatic Self-Assembled Monolayers on Gold and Silver”, Langmuir **17**, 2408–2415 (2001).

[274] D. G. Matei, H. Muzik, and A. Turchanin, “Structural Investigation of 1,1’-Biphenyl-4-thiol Self-Assembled Monolayers on Au(111) by Scanning Tunneling Microscopy and Low-Energy Electron Diffraction”, Langmuir **28**, 13905–13911 (2012).

[275] N. Ballav, B. Schüpbach, O. Dethloff, P. Feulner, A. Terfort, and M. Zharnikov, “Direct Probing Molecular Twist and Tilt in Aromatic Self-Assembled Monolayers”, J. Am. Chem. Soc. **129**, 15416–15417 (2007).

[276] H. Hamoudi, P. Kao, A. Nefedov, D. L. Allara, and M. Zharnikov, “X-ray spectroscopy characterization of self-assembled monolayers of nitrile-substituted oligo(phenylene ethynylene)s with variable chain length”, Beilstein J. Nanotechnol. **3**, 12–24 (2012).

[277] N. Biere, S. Koch, P. Stohmann, V. Walhorn, A. Gölzhäuser, and D. Anselmetti, “Resolving the 3D Orientation of Terphenylthiol Molecules on Noble Metals with Kelvin Probe Force Microscopy”, J. Phys. Chem. C **123**, 19659–19667 (2019).

[278] F. Cecchet, D. Lis, J. Guthmuller, B. Champagne, G. Fonder, Z. Mekhalif, Y. Caudano, A. A. Mani, P. A. Thiry, and A. Peremans, "Theoretical Calculations and Experimental Measurements of the Vibrational Response of p-NTP SAMs: An Orientational Analysis", J. Phys. Chem. C **114**, 4106–4113 (2010).

[279] J. Löfgren, H. Grönbeck, K. Moth-Poulsen, and P. Erhart, "Understanding the Phase Diagram of Self-Assembled Monolayers of Alkanethiolates on Gold", J. Phys. Chem. C **120**, 12059–12067 (2016).

[280] J.-J. Sun, H.-S. Su, H.-L. Yue, S.-C. Huang, T.-X. Huang, S. Hu, M. M. Sartin, J. Cheng, and B. Ren, "Role of Adsorption Orientation in Surface Plasmon-Driven Coupling Reactions Studied by Tip-Enhanced Raman Spectroscopy", J. Phys. Chem. Lett. **10**, 2306–2312 (2019).

[281] R. Zhang, Y. Zhang, Z. C. Dong, S. Jiang, C. Zhang, L. G. Chen, L. Zhang, Y. Liao, J. Aizpurua, Y. Luo, J. L. Yang, and J. G. Hou, "Chemical mapping of a single molecule by plasmon-enhanced Raman scattering", Nature **498**, 82–86 (2013).

[282] J. Griffiths, T. Földes, B. de Nijs, R. Chikkaraddy, D. Wright, W. M. Deacon, D. Berta, C. Readman, D.-B. Grys, E. Rosta, and J. J. Baumberg, "Resolving sub-angstrom ambient motion through reconstruction from vibrational spectra", Nat Commun **12**, 6759 (2021).

[283] Y. Zhang, J. Aizpurua, and R. Esteban, "Optomechanical Collective Effects in Surface-Enhanced Raman Scattering from Many Molecules", ACS Photonics **7**, 1676–1688 (2020).

[284] T. P. Gray, J. Nishida, S. C. Johnson, and M. B. Raschke, "2D Vibrational Exciton Nanoimaging of Domain Formation in Self-Assembled Monolayers", Nano Lett. **21**, 5754–5759 (2021).

[285] N. S. Mueller, R. Arul, L. A. Jakob, M. O. Blunt, T. Földes, E. Rosta, and J. J. Baumberg, "Collective Mid-Infrared Vibrations in Surface-Enhanced Raman Scattering", Nano Lett. **22**, 7254–7260 (2022).

[286] J. C. Love, L. A. Estroff, J. K. Kriebel, R. G. Nuzzo, and G. M. Whitesides, "Self-Assembled Monolayers of Thiolates on Metals as a Form of Nanotechnology", Chem. Rev. **105**, 1103–1170 (2005).

[287] O. Azzaroni, M. Cipollone, M. E. Vela, and R. C. Salvarezza, "Protective Properties of Dodecanethiol Layers oc Copper Surfaces: The Effect of Chloride Anions in Aqueous Environments", Langmuir **17**, 1483–1487 (2001).

[288] A. C. Templeton, W. P. Wuelfing, and R. W. Murray, "Monolayer-Protected Cluster Molecules", Acc. Chem. Res. **33**, 27–36 (2000).

[289] R. Jin, “Quantum sized, thiolate-protected gold nanoclusters”, Nanoscale **2**, 343–362 (2010).

[290] R. A. van Delden, M. K. J. ter Wiel, M. M. Pollard, J. Vicario, N. Koumura, and B. L. Feringa, “Unidirectional molecular motor on a gold surface”, Nature **437**, 1337–1340 (2005).

[291] C. Jehn, B. Küstner, P. Adam, A. Marx, P. Ströbel, C. Schmuck, and S. Schlücker, “Water soluble SERS labels comprising a SAM with dual spacers for controlled bioconjugation”, Phys. Chem. Chem. Phys. **11**, 7499–7504 (2009).

[292] J. J. Baumberg, J. Aizpurua, M. H. Mikkelsen, and D. R. Smith, “Extreme nanophotonics from ultrathin metallic gaps”, Nat. Mater. **18**, 668–678 (2019).

[293] H. Häkkinen, “The gold–sulfur interface at the nanoscale”, Nature Chem. **4**, 443–455 (2012).

[294] P. E. Laibinis, G. M. Whitesides, D. L. Allara, Y. T. Tao, A. N. Parikh, and R. G. Nuzzo, “Comparison of the structures and wetting properties of self-assembled monolayers of n-alkanethiols on the coinage metal surfaces, copper, silver, and gold”, J. Am. Chem. Soc. **113**, 7152–7167 (1991).

[295] L. H. Dubois, B. R. Zegarski, and R. G. Nuzzo, “Molecular ordering of organosulfur compounds on Au(111) and Au(100): Adsorption from solution and in ultrahigh vacuum”, J. Chem. Phys. **98**, 678–688 (1993).

[296] C. A. Widrig, C. Chung, and M. D. Porter, “The electrochemical desorption of n-alkanethiol monolayers from polycrystalline Au and Ag electrodes”, J. Electroanal. Chem. **310**, 335–359 (1991).

[297] D. P. Woodruff, “The interface structure of n-alkylthiolate self-assembled monolayers on coinage metal surfaces”, Phys. Chem. Chem. Phys. **10**, 7211–7221 (2008).

[298] P. Maksymovych, O. Voznyy, D. B. Dougherty, D. C. Sorescu, and J. T. Yates, “Gold adatom as a key structural component in self-assembled monolayers of organosulfur molecules on Au(111)”, Prog. Surf. Sci. **85**, 206–240 (2010).

[299] E. A. Wood, “Vocabulary of Surface Crystallography”, J. Appl. Phys. **35**, 1306–1312 (1964).

[300] L. Merz and K.-H. Ernst, “Unification of the matrix notation in molecular surface science”, Surf. Sci. **604**, 1049–1054 (2010).

[301] J. Klimeš, D. R. Bowler, and A. Michaelides, “Chemical accuracy for the van der Waals density functional”, J. Phys.: Condens. Matter **22**, 022201 (2009).

[302] L. Bengtsson, “Dipole correction for surface supercell calculations”, Phys. Rev. B **59**, 12301–12304 (1999).

[303] C. Carnegie, J. Griffiths, B. de Nijs, C. Readman, R. Chikkaraddy, W. M. Deacon, Y. Zhang, I. Szabó, E. Rosta, J. Aizpurua, and J. J. Baumberg, “Room-Temperature Optical Picocavities below 1 nm^3 Accessing Single-Atom Geometries”, J. Phys. Chem. Lett. **9**, 7146–7151 (2018).

[304] P. Maksymovych, D. C. Sorescu, and J. T. Yates, “Gold-Adatom-Mediated Bonding in Self-Assembled Short-Chain Alkanethiolate Species on the Au(111) Surface”, Phys. Rev. Lett. **97**, 146103 (2006).

[305] J. C. Slater, “A Simplification of the Hartree-Fock Method”, Phys. Rev. **81**, 385–390 (1951).

[306] D. M. Ceperley and B. J. Alder, “Ground State of the Electron Gas by a Stochastic Method”, Phys. Rev. Lett. **45**, 566–569 (1980).

[307] M. Dion, H. Rydberg, E. Schröder, D. C. Langreth, and B. I. Lundqvist, “Van der Waals Density Functional for General Geometries”, Phys. Rev. Lett. **92**, 246401 (2004).

[308] C. Fiolhais, F. Nogueira, and M. A. L. Marques, *A Primer in Density Functional Theory* (Springer Berlin, Heidelberg, 2003).

[309] W. Yang, “Direct calculation of electron density in density-functional theory”, Phys. Rev. Lett. **66**, 1438–1441 (1991).

[310] W. Kohn, “Density Functional and Density Matrix Method Scaling Linearly with the Number of Atoms”, Phys. Rev. Lett. **76**, 3168–3171 (1996).

[311] S. Goedecker, “Linear scaling electronic structure methods”, Rev. Mod. Phys. **71**, 1085–1123 (1999).

[312] P. Haynes and M. Payne, “Localised spherical-wave basis set for O(N) total-energy pseudopotential calculations”, Comput. Phys. Commun. **102**, 17–27 (1997).

[313] E. Hernández, M. J. Gillan, and C. M. Goringe, “Basis functions for linear-scaling first-principles calculations”, Phys. Rev. B **55**, 13485–13493 (1997).

[314] J. R. Chelikowsky, N. Troullier, and Y. Saad, “Finite-difference-pseudopotential method: Electronic structure calculations without a basis”, Phys. Rev. Lett. **72**, 1240–1243 (1994).

[315] S. F. Boys and A. C. Egerton, “Electronic wave functions - I. A general method of calculation for the stationary states of any molecular system”, Proc. R. Soc. Lond. A **200**, 542–554 (1950).

[316] E. Van Lenthe and E. J. Baerends, “Optimized Slater-type basis sets for the elements 1–118”, J. Comput. Chem. **24**, 1142–1156 (2003).

[317] R. M. Martin, *Electronic Structure: Basic Theory and Practical Methods* (Cambridge University Press, 2004).

[318] D. R. Hamann, M. Schlüter, and C. Chiang, “Norm-Conserving Pseudopotentials”, Phys. Rev. Lett. **43**, 1494–1497 (1979).

[319] C. Rostgaard, *The Projector Augmented-wave Method* (2010).

[320] A. H. Larsen, M. Vanin, J. J. Mortensen, K. S. Thygesen, and K. W. Jacobsen, “Localized atomic basis set in the projector augmented wave method”, Phys. Rev. B **80**, 195112 (2009).